Atmospheric Pressure Plasmas Driven By Tailored Voltage Waveforms

Layla Ahmed A Alelyani

PhD

University of York

Physics

March 2018

Abstract

This thesis presents the dynamics of capacitively coupled atmospheric pressure plasmas driven by tailored voltage waveforms (TVW). They are composed of a fundamental frequency (13.56 MHz) and a number of harmonics varied from 2-5.

This work concentrated on studying the electron excitation dynamics obtained experimentally in helium-nitrogen admixtures and helium-oxygen electronegative plasmas. Peaks-type waveforms and sawtooth-type waveforms operate plasma with different numbers of harmonics. The electron impact excitation dynamics are extracted from the emission of plasma photon through the use of phase-resolved optical emission spectroscopy (PROES). As the electron dynamics are influenced by the transition of the plasma boundary sheath, however, a field reversal builds up in the plasma because the reduction of electron motion due to the collisions. Consequently, the electric field initiates an acceleration of electrons toward the electrode and therefore contribute to ionisation or excitation mechanisms. This electric field was observed through the application of peaks or valleys waveforms, either via helium-nitrogen or helium-oxygen. Electron impact excitations are influenced by two parameters used in this work. First, with more harmonics applied, the excitation rates increase. This is applicable on all types of TVW used here. Therefore, the plasma density increases as observed from the thickness of the plasma sheath being smaller with more harmonics applied. The second factor affecting electron dynamics is the variation of the molecular gases used (nitrogen and oxygen). In electro-negative plasma (He-O_2), the transition from sheath expansion-dominated excitation to sheath collapse-dominated excitation occurs when adding more admixtures of oxygen. However, this kind of transition is not fulfilled in the case of helium-nitrogen plasmas. When operating the helium-oxygen plasma, the resultant effluent was exploited to measure the ozone density. In all cases ozone densities rise with more concentrations of oxygen.

Contents

Abstract……2

Contents……..3

List of Figures……..……..5

Acknowledgements……11

Declaration……13

Chapter 1 Introduction……14
1.1 Motivation……14
1.2 Thesis outline……...17

Chapter 2 Theoretical Background……18
2.1 Concept of plasma……18
2.2. Low-temperature Plasmas……...20
2.3 Plasma Sheath……..21
2.4 Electrical Breakdown and Plasma Formation……..22
2.4.1 DC plasmas……...22
2.4.2 Radio frequency plasmas……..24
2.4.2.1 Atmospheric pressure plasma and plasma jets……...27
2.4.2.2. Micro-atmospheric plasma jets (μ-APPJ)……28
2.5 Electron Excitation Dynamics……..31
2.6 Tailored Waveform Frequency Coupling in CCPs……...……...34

Chapter 3 Experiment and Diagnostics……..37
3.1 APPJ and Related Equipment……..38
3.2 The Electrical Set Up and Diagnostics……...……39
3.2.1 Driving Tailored Voltage Waveforms……..41
3.3 Optical Diagnostics……45

3.4 Ozone Detection……..49

Chapter 4 Tailored Voltage Waveforms Coupling In a He-N_2 RF APP…….50

4.1 Peaks-type Waveforms…….51

4.1.1 Excitation dynamics with N_2 variations……51

4.1.2 Electrical asymmetry effect (EAE)……...69

4.2 Sawtooth-type Waveforms……...72

4.2.1 Investigation of Excitation Dynamics……..72

4.2.2 DC self-bias with harmonics number and N_2 variations……104

4.3 Summary……107

Chapter 5 The Electro-negative Character of He-O_2 RF-APPs Driven by TVWs…...109

5.1 Peak-type waveforms…….……110

5.1.1 Investigation of excitation dynamics…….…110

5.1.2 Electrical asymmetry effect of peaks-type waveforms on electronegative plasma.122

5.2 Sawtooth-type waveforms……..124

5.2.1 Excitation dynamics……124

5.2.2 Electrical asymmetry effect……149

5.3 Ozone species measurements……152

5.4 Summary……155

Chapter 6 Conclusion and Future Work……...157

6.1 Conclusion……157

6.2 Future work……...158

List of symbols Abbreviations……159

References list……..162

List of Figures

Figure 2.1: Illustration of the plasma sheath…….....22

Figure 2.2: Voltage-current features of a DC discharge [26]……..…….23

Figure 2.3: Typical capacitively coupled RF plasma set up……..…….....25

Figure 2.4: Illustration of electron oscillating in the plasma bulk during the applied RF sine waveform……..……26

Figure 2.5: A sketch of a typical Paschen curve for most gases. The breakdown voltage is illustrated on the y-axis while the distance between the electrodes *d* and the gas pressure *p* are illustrated on x-axis……...……28

Figure 2.6 Micro-atmospheric pressure plasma jet……...……30

Figure 2.7: Electron impact excitation out of the ground state and subsequent decay to a lower level with the emission of a photon…….....32

Figure 3.1: The experimental set up…….….38

Figure 3.2: Tailored voltage waveforms: (a) 'peaks' and (b) 'valleys' type waveforms for a consecutive number of harmonics from one to five harmonics and 480 peak-to-peak voltage……..….43

Figure 3.3: Tailored voltage waveforms: (a) 'Sawtooth-up' and (b) 'sawtooth-down' type waveforms for a consecutive number of harmonics from one to five harmonics and 480 peak-to-peak voltage……..….45

Figure 3.4: Diagram illustrating the principle of PROES……..…47

Figure 3.5: Illustration of larger μ-APPJ with front view and side view [86]…….……49

Figure 4.1: Spatiotemporal excitation rates obtained from the measurement of the emission line at 750.4 nm using PROES and applying peaks waveform with n=2-5 harmonics (the top part of each image) applied on a gas mixture of He with 0.05 % Ar. The peak-to-peak voltage waveform (set at 470 V_{pp}) and the corresponding current waveforms for each harmonic are presented in the lower part of each image……53

Figure 4.2: Spatiotemporal electron impact excitation obtained from measurement of the emission line at 750.4 nm using PROES and applying peaks waveform with n=2-5 harmonics

applied on a gas mixture of He with 0.05 % Ar and N_2 mixture 0.05 % driven by 480 V_{pp} are presented in the upper part of each image. The peak-to-peak voltage waveform and the corresponding current waveforms for each harmonic are presented in the lower part of each image……57

Figure 4.3 Spatiotemporal electron impact excitation obtained from measurement of the emission line at 750.4 nm using PROES and applying peaks waveform with n=2-5 harmonics applied on a gas mixture of He with 0.05 % Ar and N_2 mixture 0.1 % driven by 490 V_{pp} are presented in the upper part of each image. The peak-to-peak voltage waveform and the corresponding current waveforms for each harmonic are presented in the lower part of each image……59

Figure 4.4 Summary of excitation rate as a function of the applied number of harmonics for different N_2 mixtures when applying peaks waveforms……60

Figure 4.5: Spatiotemporal excitation rates obtained from measurement of the emission line at 750.4 nm using PROES and applying valleys waveform with n=2-5 harmonics (the top part of each image) applied on a gas mixture of He with 0.05 % Ar. The peak-to-peak voltage waveform (set at 470 $_{Vpp}$) and the corresponding current waveforms for each harmonic are presented in the lower part of each image……63

Figure 4.6: Spatiotemporal electron impact excitation obtained from measurement of the emission line at 750.4 nm using PROES and applying valleys waveform with n=2-5 harmonics applied on a gas mixture of He with 0.05 % Ar and N_2 mixture 0.05 % driven by 480 V_{pp} are presented in the upper part of each image. The peak-to-peak voltage waveform and the corresponding current waveforms for each harmonic are presented in the lower part of each image……65

Figure 4.7 Spatiotemporal electron impact excitation obtained from measurement of the emission line at 750.4 nm using PROES and applying valleys waveform with n=2-5 harmonics applied on a gas mixture of He with 0.05 % Ar and N_2 mixture 0.1 % driven by 490 V_{pp} are presented in the upper part of each image. The peak-to-peak voltage waveform and the corresponding current waveforms for each harmonic are presented in the lower part of each image……67

Figure 4.8 Summary of excitation rate as a function of the applied number of harmonics for different N_2 mixtures when applying valleys waveforms……69

Figure 4.9: DC self-bias voltages measured as a function of n = 1-5 for peaks waveforms (blue) and valleys waveforms (red) at (a) 470 V_{pp} with 0 % N_2, (b) 480 V_{pp} with 0.05 % N_2 and (c) 490 V_{pp} with 0.1 % N_2. Error bars show the standard error of the DC-bias voltages…….71

Figure 4.10: Spatiotemporal excitation rates obtained from measurement of the emission line at 750.4 nm using PROES and applying sawtooth up waveform with n=2-5 harmonics (the top part of each image) applied on a gas mixture of He with 0.05 % Ar. The peak-to-peak voltage waveform (set at 470 v_{pp}) and the corresponding current waveforms for each harmonic are presented in the lower part of each image……..74

Figure 4.11 Spatiotemporal excitation rates obtained from measurement of the emission line at 750.4 nm using PROES and applying sawtooth-up waveform with n=2-5 harmonics (the top part of each image) applied on a gas mixture of He with 0.05 % Ar and 0.05 % N_2. The peak-to-peak voltage waveform (set at 480 V_{pp}) and the corresponding current waveforms for each harmonic are presented in the lower part of each image……78

Figure 4.12 Spatiotemporal excitation rates obtained from measurement of the emission line at 750.4 nm using PROES and applying sawtooth-up waveform with n=2-5 harmonics (the top part of each image) applied on a gas mixture of He with 0.05 % Ar and 0.1 % N_2. The peak-to-peak voltage waveform (set at 540 V_{pp}) and the corresponding current waveforms for each harmonic are presented in the lower part of each image……80

Figure 4.13 Spatiotemporal excitation rates obtained from measurement of the emission line at 750.4 nm using PROES and applying sawtooth-up waveform with n=2-5 harmonics (the top part of each image) applied on a gas mixture of He with 0.05 % Ar and 0.2 % N_2. The peak-to-peak voltage waveform (set at 570 V_{pp}) and the corresponding current waveforms for each harmonic are presented in the lower part of each image……82

Figure 4.14 Spatiotemporal excitation rates obtained from measurement of the emission line at 750.4 nm using PROES and applying sawtooth-up waveform with n=2-5 harmonics (the top part of each image) applied on a gas mixture of He with 0.05 % Ar and 0.3 % N_2. The peak-to-peak voltage waveform (set at 580 V_{pp}) and the corresponding current waveforms for each harmonic are presented in the lower part of each image……84

Figure 4.15: Spatiotemporal excitation rates obtained from measurement of the emission line at 750.4 nm using PROES and applying sawtooth-up waveform with n=2-5 harmonics (the top part of each image) applied on a gas mixture of He with 0.05 % Ar and 0.5 % N_2. The peak-to-peak voltage waveform (set at 615 V_{pp}) and the corresponding current waveforms for each harmonic are presented in the lower part of each image……86

Figure 4.16 Summary of excitation rates as a function of the applied harmonics numbers 2-5 for when sawtooth-up waveforms applied on the plasma with different percentages of N_2 admixtures……88

Figure 4.17 The emission ratio of the dense excitation structures as a function of N_2 admixture for the used harmonics in the application of sawtooth-up waveforms……89

Figure 4.18: Spatiotemporal excitation rates obtained from measurement of the emission line at 750.4 nm using PROES and applying sawtooth-down waveform with n=2-5 harmonics (the top part of each image) applied on a gas mixture of He with 0.05 % Ar. The peak-to-peak voltage waveform (set at 470 V_{pp}) and the corresponding current waveforms for each harmonic are presented in the lower part of each image……91

Figure 4.19 Spatiotemporal excitation rates obtained from measurement of the emission line at 750.4 nm using PROES and applying sawtooth-down waveforms with n=2-5 harmonics (the top part of each image) applied on a gas mixture of He with 0.05 % Ar and 0.05 % N_2. The peak-to-peak voltage waveform (set at 480 V_{pp}) and the corresponding current waveforms for each harmonic are presented in the lower part of each image……94

Figure 4.20 Spatiotemporal excitation rates obtained from measurement of the emission line at 750.4 nm using PROES and applying sawtooth-down waveforms with n=2-5 harmonics (the top part of each image) applied on a gas mixture of He with 0.05 % Ar and 0.1 % N_2. The peak-to-peak voltage waveform (set at 540 V_{pp}) and the corresponding current waveforms for each harmonic are presented in the lower part of each image……96

Figure 4.21 Spatiotemporal excitation rates obtained from measurement of the emission line at 750.4 nm using PROES and applying sawtooth-down waveforms with n=2-5 harmonics (the top part of each image) applied on a gas mixture of He with 0.05 % Ar and 0.2 % N_2. The peak-to-peak voltage waveform (set at 570 V_{pp}) and the corresponding current waveforms for

each harmonic are presented in the lower part of each image……98

Figure 4.22 Spatiotemporal excitation rates obtained from measurement of the emission line at 750.4 nm using PROES and applying sawtooth-down waveforms with n=2-5 harmonics (the top part of each image) applied on a gas mixture of He with 0.05 % Ar and 0.3 % N_2. The peak-to-peak voltage waveform (set at 580 V_{pp}) and the corresponding current waveforms for each harmonic are presented in the lower part of each image……100

Figure 4.23: Spatiotemporal excitation rates obtained from measurement of the emission line at 750.4 nm using PROES and applying sawtooth-down waveforms with n=2-5 harmonics (the top part of each image) applied on a gas mixture of He with 0.05 % Ar and 0.5 % N_2. The peak-to-peak voltage waveform (set at 615 V_{pp}) and the corresponding current waveforms for each harmonic are presented in the lower part of each image……102

Figure 4.24 Summary of excitation rates as a function of the applied harmonics numbers 2-5 for when sawtooth-down waveforms are applied on the plasma with different percentages of N_2 admixtures……103

Figure 4.25 The emission ratio of the dense excitation structures as a function of N_2 admixture for the used harmonics in the application of sawtooth-down waveforms……104

Figure 4.26 DC self-bias voltages measured as a function of n being varied from 1 to 5 harmonics for sawtooth-up waveforms (blue) and sawtooth-down waveforms (red) at (a) 470 V_{pp} with 0 % N_2, (b) 480 V_{pp} with 0.05 % N_2, (c) 540 V_{pp} with 0.1 % N_2, (d) 570 V_{pp} with 0.2 % N_2, (e) 580 V_{pp} with 0.3 % N_2 and (f) 615 V_{pp} with 0.5 % N_2. Error bars show the standard error of the DC-bias voltages……106

Figure 5.1: Spatio-temporal excitation rates obtained from measurement of the emission line at 750.4 nm using PROES and applying peaks waveforms with n = 2-5 harmonics applied on a gas mixture of He with 0.05 % Ar and O_2 mixture 0.05 %. The peak-to-peak voltage waveform and the corresponding current waveforms for each harmonic are presented in the lower part of each image……..113

Figure 5.2 Spatio-temporal excitation rates obtained from measurement of the emission line at 750.4 nm using PROES and applying peaks waveforms with n = 2-5 harmonics applied on a gas mixture of He with 0.05 % Ar and O_2 mixture 0.1 %. The peak-to-peak voltage waveform and the corresponding current waveforms for each harmonic are presented in the lower part of each image……..115

Figure 5.3 Summary of excitation rates as a function of the applied harmonics numbers 2-5 when peaks waveforms applied on the plasma with different percentages of O_2 admixtures……...117

Figure 5.4: Spatiotemporal excitation rates obtained from measurement of the emission line at 750.4 nm using PROES and applying valleys waveforms with n=2-5 harmonics applied on a gas mixture of He with 0.05 % Ar and O_2 mixture 0.05 %. The peak-to-peak voltage waveform and the corresponding current waveforms for each harmonic are presented in the lower part of each image……119

Figure 5.5 Spatio-temporal excitation rates obtained from measurement of the emission line at 750.4 nm using PROES and applying valleys waveforms with n = 2-5 harmonics applied on a gas mixture of He with 0.05 % Ar and O_2 mixture 0.1 %. The peak-to-peak voltage waveform and the corresponding current waveforms for each harmonic are presented in the lower part of each image……..121

Figure 5.6 Summary of excitation rates as a function of the applied harmonics numbers 2-5 when valleys waveforms applied on the plasma with different percentages of O_2 admixtures……..122

Figure 5.7: DC self-bias voltages measured as a function of harmonics varied between 1 to 5 harmonics for peaks waveforms (blue) and valleys waveforms (red) at (a) 480 V_{pp} with 0.05 % O_2 and (b) 490 V_{pp} with 0.1 % O_2……123

Figure 5.8 Spatio-temporal excitation rates obtained from measurement of the emission line at 750.4 nm using PROES and applying sawtooth-up waveforms with n = 2-5 harmonics applied on a gas mixture of He with 0.05 % Ar and O_2 mixture 0.05 %. The peak-to-peak voltage waveform and the corresponding current waveforms for each harmonic are presented in the lower part of each image……126

Figure 5.9 Spatio-temporal excitation rates obtained from measurement of the emission line at 750.4 nm using PROES and applying sawtooth-up waveforms with n = 2-5 harmonics applied on a gas mixture of He with 0.05 % Ar and O_2 mixture 0.1 %. The peak-to-peak voltage waveform and the corresponding current waveforms for each harmonic are presented in the lower part of each image……128

Figure 5.10 Spatio-temporal excitation rates obtained from measurement of the emission line at 750.4 nm using PROES and applying sawtooth-up waveforms with n = 2-5 harmonics applied on a gas mixture of He with 0.05 % Ar and O_2 mixture 0.2 %. The peak-to-peak voltage waveform and the corresponding current waveforms for each harmonic are presented in the lower part of each image……..130

Figure 5.11 Spatio-temporal excitation rates obtained from measurement of the emission line at 750.4 nm using PROES and applying sawtooth-up waveforms with n = 2-5 harmonics applied on a gas mixture of He with 0.05 % Ar and O_2 mixture 0.3 %. The peak-to-peak voltage waveform and the corresponding current waveforms for each harmonic are presented in the lower part of each image……..132

Figure 5.12 Spatio-temporal excitation rates obtained from measurement of the emission line at 750.4 nm using PROES and applying sawtooth-up waveforms with n = 2-5 harmonics applied on a gas mixture of He with 0.05 % Ar and O_2 mixture 0.5 %. The peak-to-peak voltage waveform and the corresponding current waveforms for each harmonic are presented in the lower part of each image……..134

Figure 5.13 Summary of excitation rates as a function of the applied harmonics numbers 2-5 when sawtooth-up waveforms applied on the plasma with different percentages of O_2 admixtures……..136

Figure 5.14 The emission ratio of the dense excitation structures as a function of O_2 admixture for the used harmonics in the application of sawtooth-up waveforms……...137

Figure 5.15 Spatio-temporal excitation rates obtained from measurement of the emission line at 750.4 nm using PROES and applying sawtooth-down waveforms with n = 2-5 harmonics applied on a gas mixture of He with 0.05 % Ar and O_2 mixture 0.05 %. The peak-to-peak voltage waveform and the corresponding current waveforms for each harmonic are presented in the lower part of each image……...139

Figure 5.16 Spatio-temporal excitation rates obtained from measurement of the emission line at 750.4 nm using PROES and applying sawtooth-down waveforms with n = 2-5 harmonics applied on a gas mixture of He with 0.05 % Ar and O_2 mixture 0.1 %. The peak-to-peak

voltage waveform and the corresponding current waveforms for each harmonic are presented in the lower part of each image……..141

Figure 5.17 Spatio-temporal excitation rates obtained from measurement of the emission line at 750.4 nm using PROES and applying sawtooth-down waveforms with n = 2-5 harmonics applied on a gas mixture of He with 0.05 % Ar and O_2 mixture 0.2 %. The peak-to-peak voltage waveform and the corresponding current waveforms for each harmonic are presented in the lower part of each image……143

Figure 5.18 Spatio-temporal excitation rates obtained from measurement of the emission line at 750.4 nm using PROES and applying sawtooth-down waveforms with n = 2-5 harmonics applied on a gas mixture of He with 0.05 % Ar and O_2 mixture 0.3 %. The peak-to-peak voltage waveform and the corresponding current waveforms for each harmonic are presented in the lower part of each image……145

Figure 5.19 Spatio-temporal excitation rates obtained from measurement of the emission line at 750.4 nm using PROES and applying sawtooth-down waveforms with n = 2-5 harmonics applied on a gas mixture of He with 0.05 % Ar and O_2 mixture 0.5 %. The peak-to-peak voltage waveform and the corresponding current waveforms for each harmonic are presented in the lower part of each image……147

Figure 5.20 Summary of excitation rates as a function of the applied harmonics numbers 2-5 when sawtooth-down waveforms are applied on the plasma with different percentages of O_2 admixtures……...148

Figure 5.21 The emission ratio of the dense excitation structures as a function of O_2 admixture for the used harmonics in the application of sawtooth-down waveforms……..149

Figure 5.22: DC self-bias voltages measured as a function of n = 1-5 for sawtooth-up waveforms (blue) and sawtooth-down waveforms (red) at (a) 480 V_{pp} with 0.05 % O_2, (b) 540 V_{pp} with 0.1 % O_2, (c) 570 V_{pp} with 0.2 % O_2, (d) 580 V_{pp} with 0.3 % O_2 and (e) 615 V_{pp} with 0.5 % O_2……..151

Figure 5.23: Ozone density as a function of the number of harmonics 1-5 by applying peaks and valleys waveforms using 0.05 % and 0.1 % of O_2……..153

Figure 5.24: Ozone density as a function of the number of harmonics 1-5 by applying sawtooth-up waveforms with oxygen concentrations 0.05 %, 0.1 %, 0.2 %, 0.3 %, and 0.5 % O_2……154

Acknowledgements

This work would not have been possible without the encouragement and support of others.

First and foremost, I would like to acknowledge the Ministry of Higher Education in Saudi Arabia or the financial support during my study abroad.

My sincere thanks go to my Supervisor Dr. Deborah O'Connell. Thank you, Deborah, for giving me the opportunity to study at York University under your tutelage, the continued encouragement, enthusiasm, the helpful discussion and patience particularly at the start of my PhD when I knew next to nothing about plasma physics. Special thanks need to be expressed to my co-supervisor Dr. James Dedrick for your contribution on TVW experiment and enduring help. My gratitude to Dr. Kari Niemi and Richard Armitage for their technical expertise in the lab. My deepest thanks to Dr. Jerome Bredin for his knowledge and assistance on my experiments and his skills in matlab, I really learned a lot of his expertise. It is my pleasure to extend my thanks to all people in TVW group, Proffesor Timo Gans, Dr. Julian Schulze, Dr. Andrew Gibson and Scott Doyle for your cooperation. Special thanks go to Dr. Zoltan Donko for your time devoted on TVW numerical simulations. Great thanks also to all my colleagues and the member of staff in York plasma institute and labs who made the work environment extremely cooperative and enjoyable.

To all of my friends specially, Dr. Reem Alradadi, Sarah Alotaibi, Khadija Algamdi and Njwa

Gaffar, I would like to say thank you very much for your amazing friendship, academic and emotional support during my PhD journey.

I am particularly thankful to all of my family members for their motivation and believing in me. My special heartfelt thanks expressed to my parents Ahmed Alelyani and Aliah Alelyani for their continued encouragement, support and praying for me to achieve my dream, I will be forever grateful.

To my husband, Magbool Alelyani whom deserves the most thanks I would say thank you for your invaluable support, patience, encouragement and love. You have sacrificed so many things to help me to achieve this goal; I will always be in your debt.

Finally, the deepest thanks go to my lovely kids, Lujain and Khalid who made my life full of love and happiness. It was really nice having you around me, thank you for your encouragement by always saying 'do not give up mum'!

Declaration

I declare that the work presented in this thesis, except where it is otherwise stated, is generated based on my own research and all other sources including figures or diagrams which have been copied from academic articles, books and internet website are acknowledged by explicit references. This thesis has not previously been accepted and is not being concurrently submitted for any degree other than Doctor of Philosophy of the University of York. All practical experiments and subsequent data collection and analysis were carried out only by the author.

In chapter 4, the experimental results of studying electron dynamics in He-N_2 driven by tailored voltage waveforms have been published in the article Gibson, A.R., et al., *Disrupting the spatio-temporal symmetry of the electron dynamics in atmospheric pressure plasmas by voltage waveform tailoring.* Plasma Sources Science and Technology, 2018.

Chapter 1 Introduction

1.1 Motivation

Plasmas play an important role in technological and biomedical aspects of modern life. They have enabled our everyday lives as they are used for lighting, plasma displays, semiconductor device fabrication, surface cleaning, sterilisation, wound healing and much more. It is said that about 99% of matter in the universe is plasma [1]. By definition, plasma is a quasi-neutral partially or fully ionised gas consisting of negative particles (electrons and ions), positive ions and neutral particles, which exhibit collective behaviour. Based on the temperature distribution among the plasma species, plasma can be categorised as thermal or non-thermal plasmas. In high-temperature plasmas, typically a large amount of gas is ionised and the plasma components are in thermal equilibrium; therefore, they can be described by a typical temperature ranging from several thousands Kelvin to millions of Kelvin [2]. Such thermal plasmas are significant in transferring heat to surfaces in welding applications as well as to convert energy in fusion experiments [3-6]. In contrast, in non-thermal (low temperatures) plasmas, plasma particles are not in thermal equilibrium, and are described as being partially ionized due to a small fraction of gas being ionized. In such low-temperature plasmas, the much lighter electrons exhibit much greater temperatures (> 10,000 K) compared to the temperature of the heavier particles (ions and neutrals), which remain roughly at room temperature (~ 300 K). Non-thermal plasmas utilised in technology applications can be produced by the implementation of radio frequency (RF) electric

fields, typically 13.56 MHz, which is allowed by international communication laws. This high frequency is less than the electron frequency but higher than the ion frequency, allowing the coupling of the applied electric field into the lighter electrons while the heavier ions stay cold.

Recently, interest has increased in low-temperature plasmas operating at atmospheric pressure. Atmospheric pressure plasma jet (APPJ) driven by radio frequency (RF) is an efficient source of chemically reactive species which are widely used for a variety of industrial and biological applications. Examples of such applications include etching, deposition, surfaces modifications and biomedical treatments [7-10].

Atmospheric pressure plasmas (APPs) are characterised by ability to work in ambient air; therefore, they do not require expensive vacuums systems in comparison to low-pressure plasmas [11-13]. Thermal instabilities are possible to initiate in plasma at atmospheric pressure [14]; however, this issue can be overcome through the coupling of radio frequency electric fields. As the diagnostics of APPs is challenging due to the highly collisional environment in a small scale of confining reactor, using such probes as the Langmuir probe to diagnose the plasma is not applicable, as it will disturb the plasma discharge. However, phase-resolved optical emission spectroscopy (PROES), used in this work, is a robust diagnostic tool, which can provide direct information with high spatial and temporal resolution of the plasma parameters from the emitted photons without any disturbance to the plasma processes [15].

In this work, APPJ operated in helium with different amounts of nitrogen/ oxygen admixtures to generate reactive oxygen and nitrogen species (RONS), which are important for many biomedical applications. These reactive species are mainly produced through the processes of electron excitation and dissociation of the admixed molecules. Controlling electron energy distribution function (EEDF) leads to controlling electron dynamics, and associated chemical kinetics governs

the applications, which is the aim of this thesis. In APPs, the EEDF can be controlled through the operating parameters i.e. the driving frequency. AAPs driven by a single radio frequency have been investigated, showing the fundamental of electron dynamics depending on electron heating [16, 17]. Non-linear radiofrequency represented in dual frequency (consisting of two disparate radio frequencies coupled into the plasma simultaneously) proved that the EEDF can be tailored due to the confinement of electron heating in a small spatio-temporal region [18-20]. Tailored voltage waveforms comprising a fundamental radio frequency summed with its harmonics provides more control over the plasma parameters, as extensively studied for low pressure RF plasmas [21, 22]. To date, the role of atmospheric pressure plasmas driven by tailored voltage waveforms is not known and became a topic of current research.

This work represents electron impact excitation induced by tailored voltage waveforms driving APPs. Increasing the number of harmonics influences the plasma sheath behaviour and consequently electron heating mechanisms, which, in turn, affect the production of reactive species. The density of produced reactive oxygen species (ROS)—namely ozone which results from the dissociation of oxygen molecules in the neutral gas and from the excitation of oxygen atoms—was detected from the plasma effluent.

1.2 Thesis outline

This thesis is organised as follows:

Chapter 2 contains a brief introduction of the fundamental background associated with non-thermal APPs with regard to CC-RF plasmas, plasma sheath and electron excitation dynamics. The chapter ends with an overview of μ-APPJ and tailored voltage waveforms (TVW) coupling.

Chapter 3 introduces the experimental setup including the electrical and optical equipment and their related diagnostics techniques. It is also includes an illustration of the monitor used to measure ozone density and description of the methods followed to measure the ozone concentration in the plasma which operated in helium with an oxygen admixture. The methods used to measure phase and space resolved excitation mechanisms are also presented. The production of TVWs used in this work is described.

Chapter 4 investigates the influence of applying TVW, Peaks-type waveform and Sawtooth-type waveforms on He-N_2 APPs. The DC-bias voltages initiated from electrical asymmetry effect are also measured with different harmonics and different amounts of nitrogen. The spatio-temporal electron impact excitation as a result of the application of TVW is demonstrated.

Chapter 5 focuses on the influence of TVW on electron dynamics in electro-negative He-O_2 plasmas. The DC-bias voltages are measured as well. These two parameters were investigated through variations in the number of harmonics and the different amounts of oxygen being added to the plasma. The electronegative species, namely ozone, produced from oxygen admixtures, is also measured and described at different TVWs.

Chapter 6 summarises the main conclusions and presents an outlook on possible future research.

Chapter 2 Theoretical Background

2.1 Concept of plasma

The state of any matter can change by adding more energy; this is how a solid becomes a liquid and a liquid becomes a gas. Applying sufficient energy leads to the breakdown of a gas whereby ionisation can occur. Plasmas are simply ionised gas, and thus can be defined as a fourth state of matter. However, there are some criteria for the ionised gas to be classified as plasma. As cited by Chen, 'plasma is a quasineutral gas of charged and neutral particles which exhibit collective behaviour' [1, 23].

In neutral gas, particles move undisturbed until they collide with each other, producing positive and negative charged particles. The density of positive charge $n+$ must balance the density of negative charge $n-$ that results in a zero net charge in the system, leading to the concept of **quasi-neutrality**.

Due to the presence of the charged particles which arise due to collisions in the plasma, electromagnetic fields can be introduced, affecting the motion of other charged particles of long range. This means that each particle interacts with many other particles in its vicinity and not just with its neighbouring ones, and this satisfies the meaning of **collective behaviour**.

Another fundamental characteristic of plasma exhibited by the interaction of charged species and the ability of plasma to shield out applied external electric fields, called Debye shielding. The

distance over which significant charge separation can occur is known as Debye length $\lambda_{D,}$ and is given as:

$$\lambda_D = \left(\frac{\varepsilon_0 k_B T_e}{n_e^2}\right)^{1/2} \tag{2.1}$$

In this equation, ε_0 refers to the permittivity of a free vacuum, k_B is the Boltzmann constant and e is the elementary charge. Due to the greater mobility of electrons compared to the heavier ions, which are approximately static, only the electron temperature T_e and electron number density n_e are taken into consideration.

The more energy the electrons have, $k_B\ T_e$, the larger plasma dimensions L must be to screen charges. On the other hand, the more charge carriers n_e are present in the plasma, the more effective the plasma is at screening charge and the Debye length is smaller [1, 24].

The final condition for the ionised gas to be classified as plasma includes what is called plasma frequency ω_p. In a plasma, if ions and electrons are separated by a small distance, an internal electric field initiates to iterate the plasma to a quasi-neutrality state. The electrons oscillate around the equilibrium position due to their mobility compared to the ions. The characteristics of these oscillations are known as the plasma frequency.

$$\omega_p = \sqrt{\frac{n_e e^2}{m_e\ \varepsilon_0}} \tag{2.3}$$

Here, the plasma frequency shown in equation 2.3 as a function of the number density $n_e$and the mass of the electron m_e [25] .The symbol ε_0 refers to the permittivity of a free vacuum and e is the electron charge.

In a quasi-neutral plasma, the electron density is equivalent to the ion density, so the relationship between the plasma frequency and ions equals that for electrons. However, as the energetic electrons govern the plasma dynamics, the plasma frequency describes the electron plasma frequency ω_{pe}. The frequency of an applied external electric field must be less than the plasma frequency.

2.2. Low-temperature Plasmas

A plasma can be categorised as thermal or non-thermal based on the associated temperatures of the electrons, ions and neutrals within the plasma. In non-thermal plasma, the ions and electrons are not in thermal equilibrium with each other. Temperature is a measure of the average thermal kinetic energy per particle. Since the transfer of energy depends on the mass ratio of the colliding particles, the energy transfer between the heavier particles (ions and neutrals) and the lighter and more mobile electron is inefficient. Electrons respond to the rapid varying applied electric field compared to the ions and are accelerated to temperature ~ 1 – 5 eV whereas ions and neutrals' temperature is usually lower and close to the ambient temperature ~ 300 K. Therefore, the ions and neutrals are not in thermal equilibrium with electrons. Hence, the gas temperature does not increase although the collisions present at atmospheric pressure increase, and this is due to the inefficient energy transfer between the hot electron and lower temperature ions and neutrals. Electrons govern the plasma chemistry through various collisional processes such as ionisation, excitation and dissociation. The percentage of atoms or molecules in a plasma in an ionised state is defined as the degree of ionisation I where n_e is the electron density and n_0 is the number density of background gas neutral species.

$$I = \frac{n_e}{n_e + n_0} \tag{2.4}$$

In high temperature plasmas such as sun or nuclear fusion the plasma is fully ionised and $I \approx 1$. However, low-temperature plasmas are weakly ionised, normally $I << 1$, and this is the basis of technological processing plasmas. This is also a key property to create a unique chemically reactive species by a plasma, with a high electron temperature, without causing corresponding thermal damage to a sample.

2.3 Plasma Sheath

To satisfy the condition of quasi-neutrality in a plasma, the fluxes of positively charged ions (Γ_{+i}) and negatively charged ions and electrons ($\Gamma_{-i} + \Gamma_e \approx \Gamma_e$, mainly determined by electron), leaving the plasma toward the surrounding surface, must be equal ($\Gamma_i + \Gamma_e$). Consequently, this leads to a potential gradient, and the condition of quasi-neutrality close to the vicinity of the surface deviates. Due to the difference of mass and thermal velocity between electrons and ions, the lighter electrons are able to leave the plasma toward the surface much more easily than the ions leaving a net positive charge near the edge of the plasma. Therefore, the quasi-neutrality breaks down. The space of positive charges repels the electrons back into the plasma bulk.

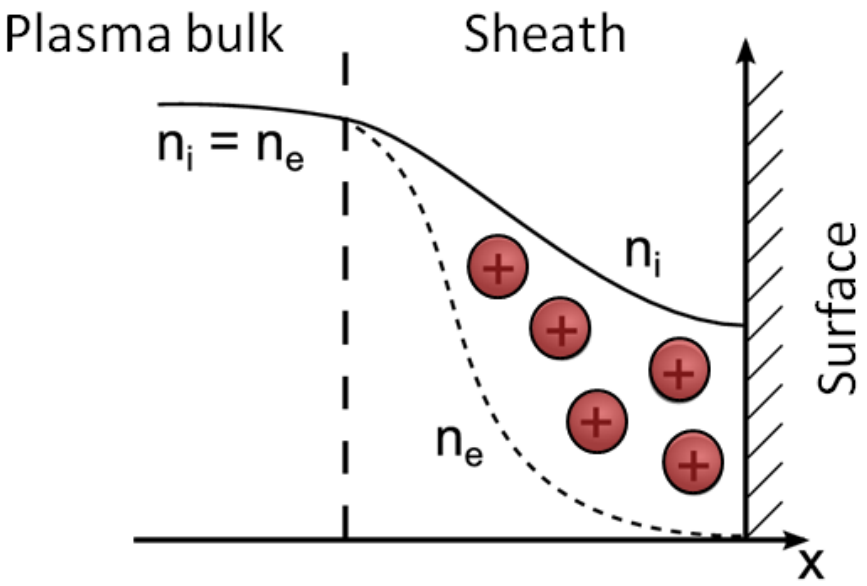

Figure 2.1: Illustration of the plasma sheath.

The effect of imbalance of charge results in a region with very low electron density and higher ion density as shown in figure 2.1. This region is known as a plasma sheath [26].

2.4 Electrical Breakdown and Plasma Formation

Low-temperature plasmas can be produced depending on the means of electrical power coupling. There are two distinct approaches to generate and sustain low-temperature plasmas. Firstly, and the simplest way is through the application of DC voltage while the second way is the application of alternating current (AC) on a neutral gas. These discharges will be illustrated in the following sections.

2.4.1 DC plasmas

The simplest approach to generate and sustain a non-thermal plasma is through the application of a DC voltage electric field across one or more electrodes which are separated by a gap filled with

neutral gas given that the system operates at low pressure. Free electrons present in the background gas, e.g. from cosmic radiation, are accelerated by the applied electric field. The kinetic energy of these electrons is increased, allowing them to collide with atoms and molecules in the gas, thereby causing ionisation. Each ionisation event produces one new electron-ion pair as a simple approximation. Subsequently, these new electron-ion pairs are accelerated into other particles resulting in the multiplication of the number of free electrons and the formation of an electron avalanche. The evolution of this avalanche is given by the first Townsend coefficient α that specifies the degree of electron amplification in the plasma. The plasma formation depends on the quantity of initial free charges, which are supplied by the external electron source; otherwise, the plasma diminishes after the electron avalanche reaches the anode. Since this mode of discharge depends strictly on the external electric field, they are also called non-self sustained or Townsend discharges. This is shown in region (A) in figure 2.2, which indicates the relation between the current and voltage of the discharge [26]. The discharges are sustained due to the emission of secondary electrons that are driven by the applied electric field.

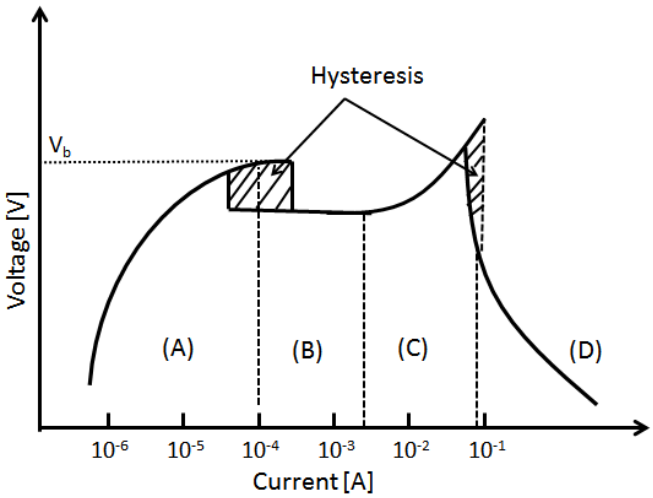

Figure 2.2: Voltage-current features of a DC discharge [26].

Secondary electrons are emitted through ion impacts at the cathode, and this is described by the so-called second Townsend coefficient γ. These glowing discharges are called glow discharges, and this is represented in region (B) on the V-I curve figure 2.2. At the normal glow mode, the voltage needed to sustain the discharge is at the minimum and the discharge cover the entire electrodes keeping the current density constant. When the current increases beyond the point whereby the complete electrode surfaces area is filled by the discharge, the discharge enters the abnormal glow mode as illustrated in region (C) where there is an obvious increase in the voltage as shown in figure 2.2. With increasing current, the voltage rapidly decreases and the discharge reaches an arc discharge mode as shown in region (D) in figure 2.2.

At the transition between the different discharges modes, hysteresis effects might exist (indicated by the dashed regions in figure 2.2), showing that the discharges can be sustained by lower voltages.

2.4.2 Radio frequency plasmas

The DC discharges use most of the input power to sustain the discharge, and this, in turn, causes complications [27]. Another alternative and more energy efficient way to operate low-temperature plasmas is through the application of alternating current (AC). The charge carriers are trapped in the plasma; hence, a higher number density of particles can be achieved in comparison with the DC discharge wherein the carrier discharge is lost at the electrodes. The method of electrical power coupling is related to the electron plasma frequency. If the external driven frequency is lower than the electron plasma frequency, the electrons can easily respond to the changing electric field and hence couple the electrical energy into the electrons. The typical excitation frequency is in the range of $1 < f < 500$ MHz and the most prominent frequency used is 13.56 MHz. The

plasmas driven by radiofrequency are known as radiofrequency plasmas or RF plasmas [25]. RF plasma plays a key role in industrial plasmas used for deposition and etching applications [28-30].

One of the most prominent RF plasmas is the capacitively coupled plasma CCP. The typical configuration of the CCP, illustrated in figure 2.3, consists of two plane parallel electrodes. One electrode is powered by a siousoidal RF voltage through a matching network while the other electrode is grounded. The matching network ensures an efficient power coupling into the discharge by matching the impedance of the discharge to the output impedance of the RF power generator.

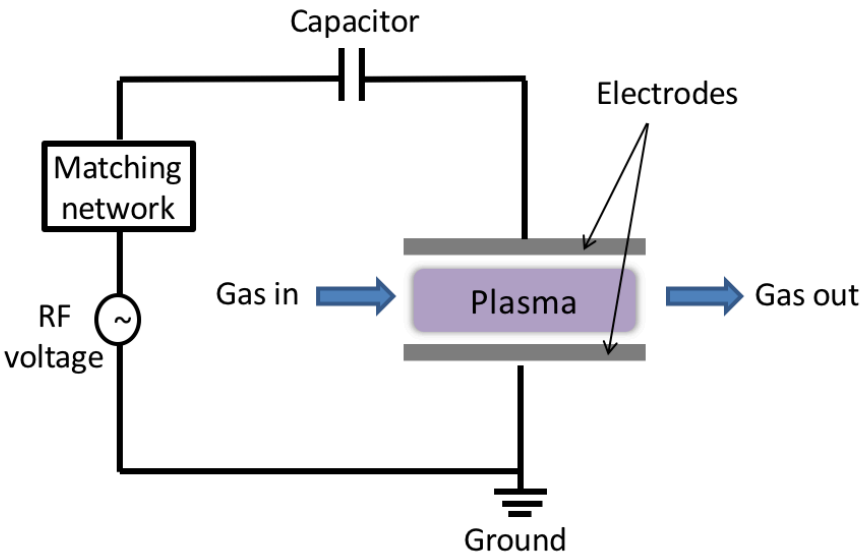

Figure 2.3: Typical capacitively coupled RF plasma set up.

A blocking capacitor is connected between the powered electrode and the matching network but often it is included within the matching network. This blocking capacitor guarantees the transportation of net charge across the discharge over an RF cycle is avoided; therefore, the flux of electrons and ions are balanced. However, due to the higher mobility of electrons compared to the lower mobility of ions, a higher voltage sheath forms close to the electrodes. The sheath region

does not contain electrons as they are repelled back to the plasma bulk and the ion density is uniform across the discharge [31].

According to the symmetry ratio of the two electrodes areas in the CCP system, the discharge can be considered a symmetric or an asymmetric discharge. The discharge is symmetric when the electrodes areas are equal. As a result, the potential difference across both sheaths is equal; therefore, the level of ion bombardment is equal for both electrodes. The asymmetric discharge initiates when the electrodes areas are different. At the smaller electrode, the potential difference is higher than that at the larger electrode. Consequently, the level of ion bombardment is greater at the smaller electrode. DC self-biasing is generated due to the different potential at the two sheaths, and this plays a key role in asymmetric plasmas [32].

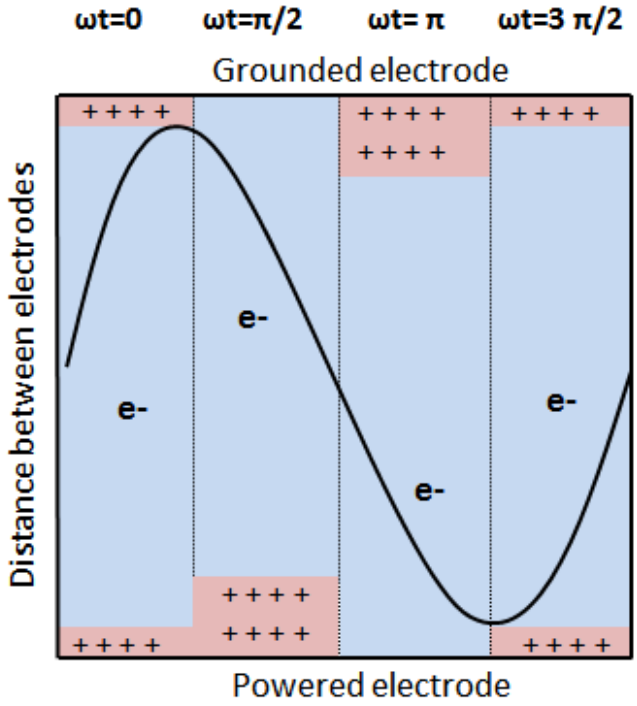

Figure 2.4: Illustration of electron oscillating in the plasma bulk during the applied RF sine waveform.

In order to shield the plasma from the fast-changing RF potential, the electrons oscillate between the two electrodes due to the high voltage plasma sheath expanding and collapsing with the

applied RF voltage. A simple illustration of electron oscillation between the electrodes by the RF plasma sheath is shown in figure 2.4.

There are two distinct modes to operate RF-driven CCPs based on the discharge conditions [33, 34]. These modes are similar to the Townsend discharge and glow discharge modes of the DC discharges. At higher RF voltages, ion bombardment of the electrodes increases by the higher sheath voltages; hence, secondary electrons are produced and accelerated into the plasma bulk by the sheath electric field, thus causing efficient ionization. Here, the plasma is sustained by the γ-mode. At lower driving voltage, the plasma is sustained by plasma bulk free electrons, which are accelerated by the fast moving sheath in front of the electrodes. This is similar to the first Townsend coefficient in DC discharges; therefore, the plasma operates in α-mode.

2.4.2.1 Atmospheric pressure plasma and plasma jets

Low-temperature plasmas operating at atmospheric pressure (APPs) have been developed over the last few decades [35-37]. They are attractive due to their ability to produce chemically reactive species which are of significant interest in many technological and medical applications. Moreover, APPs are distinguished by the elimination of the requirement of the expensive vacuum chamber that is needed in low-pressure plasmas. The voltage at which the plasma can be sustained is referred to as the breakdown voltage. The breakdown voltage depends on the product of the distance between the electrodes d and the gas pressure p as shown in figure 2.5 depending on Paschen's law. Increasing the values of p and d, when the mean free path between collisions and the electric field decreases respectively, leads to linear increases in the applied voltage. On the other hand, at minimum values of pd, the breakdown voltage reaches a minimum point required

for plasma ignition, and, at voltages less than this point, breakdown is not possible. The minimum breakdown voltage and the related *pd* value is optimal for plasma operation.

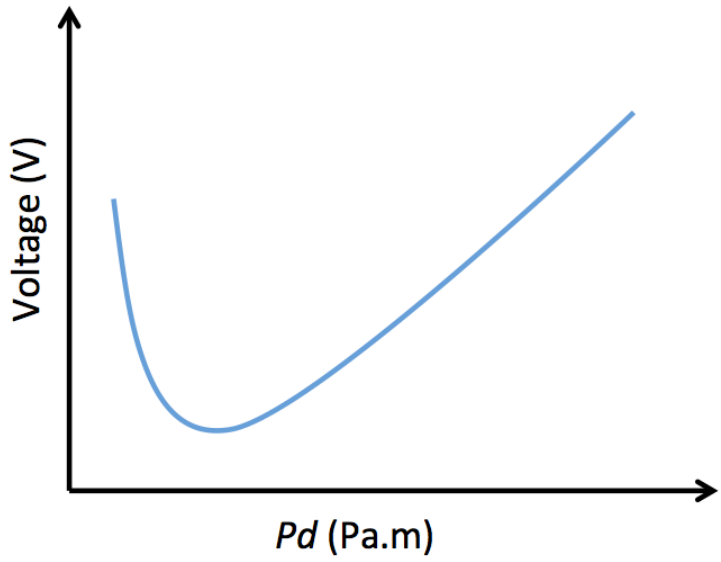

Figure 2.5: A sketch of a typical Paschen curve for most gases. The breakdown voltage is illustrated on the y-axis while the distance between the electrodes *d* and the gas pressure *p* are illustrated on x-axis.

Atmospheric pressure plasmas can be scaled for treating larger working areas as reported in [38]. Consequently, this characteristic allows the plasma to reach large areas such as surface treatments, solar cells and fabrics [39-41]. On the other side, many applications need focused plasma treatments, such as etching [42, 43], deposition [44-46] and biomedical applications such as cancer treatments [47, 48].

2.4.2.2. Micro-atmospheric plasma jets (µ-APPJ)

The RF-driven atmospheric pressure plasma jet (APPJ) was first introduced by Selwyn et al. [38]. The atmospheric pressure plasma jet presented in this work is classified as a micro-atmospheric pressure plasma jet (µ-APPJ) due to the small scale of its discharge gap. A schematic diagram of the µ-APPJ is shown in figure 2.6. Based on the concept of APPJ reported by Selwyn, it was developed by Schulz-von der Gathen, et al. [49, 50]. It does not need a vacuum chamber as in low-

pressure plasma, making it easy to move for different applications. It is also designed to provide ideal optical access to the plasma core, allowing the study of some plasma properties. Homogenous non-thermal plasma operating in μ-APPJ maintains the compact between two symmetric parallel electrodes (3 cm length x 1 mm thickness x 1 mm gap in between). Both electrodes and the gap are enclosed by two quartz windows which offer a good optical access to the electromagnetic spectrum in the range between infrared and ultraviolet. However, using physical probes to obtain plasma parameters is not applicable due to the small dimensions of the plasma channel. On the other hand, if the probe could be used, it would disturb the collisional plasma. Therefore, investigating such plasma depends on optical diagnostics. An example of these optical diagnostic techniques is Tow Photon Absorption Laser Induced Fluorescence (TALIF) that is used to obtain the density of the neutral species. Another example, used in this work to study electron dynamics, is Phase Resolved Optical Emission Spectroscopy (PROES).

Working gases flow into the jet channel through a flexible pipe connected to the plasma jet. The gas flow rate is regulated using mass flow controller (MFC). The plasma is driven by 13.56 MHz and its harmonics, as allowed by International Telecommunications Union, can be used for technological and medical applications. The RF voltage is coupled into the powered electrode from an RF generator. The second electrode is grounded through the shielding of a coaxial cable connected into the device. The configuration of the two electrodes acts as a capacitor. The RF generator is designed to provide an optimum power transfer coupled into 50 Ω loads. Therefore, a matching network is installed between the jet and the generator to match 50 Ω of the jet load to 50 Ω of the generator. Also, the matching network prevents power from being reflected back to the generator, which would damage it.

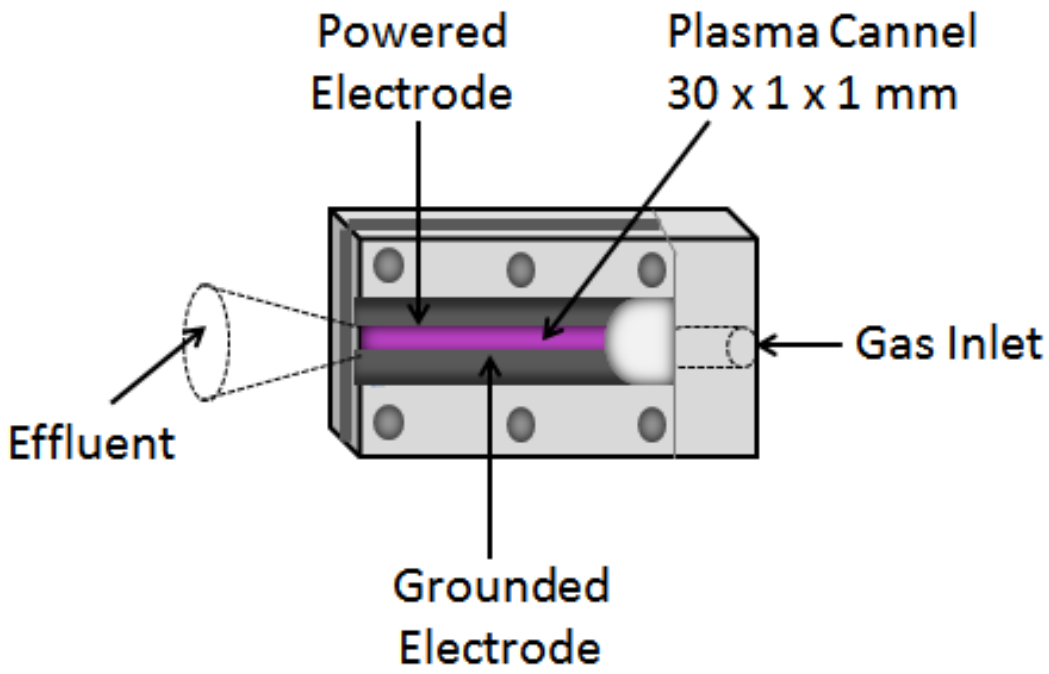

Figure 2.6 Micro-atmospheric pressure plasma jet.

The μ-APPJ can be classified as a cross-field jet. This means that the electric field applied between the two electrodes is orthogonal per the direction of the gas flow [51]. As a result, the core plasma is kept compact into the jet channel and only the neutral species can leave the jet and interact with a substrate at the channel exit, without a charged species. The region outside the jet—where the neutral species leaves the jet—is called plasma effluent. In the case of the applied electric field being parallel to the gas flow, the plasma expands into the open air beyond the plasma channel. It appears in a visible emission and usually interacts with a substrate and this region is referred to as the afterglow.

In the μ-APPJ, the plasma is operated in a non-thermal homogenous glow mode. The gas temperature is typically below 100 ^{o}C; therefore, the μ-APPJ is considered a cold device. This is beneficial for the treatments of some thermosensitive substrates that would be negatively affected

by high temperatures, e.g. biological materials. The high temperature of neutral species can be avoided by controlling the power applied from the RF generator.

2.5 Electron Excitation Dynamics

The population dynamics of excited states can be described by what is called an equilibrium model, which relies on the assumption that the plasma components are characterised by distribution functions. Maxwell-Boltzmann distributions are the most distinct functions for describing the velocity and population distribution of all components of a plasma. However, they can be applied only to a plasma with high electron density. Low-temperature plasmas with low electron density $\leq 10^{13}$ cm^{-3} can be described by the so-called corona model and collisional radiative model [52, 53].

The simplest form of corona model can be an electron impact excitation out of the ground state into an observed excitation state *i* following the spontaneous emission of photons due to the de-excitation process into lower state *k* as shown in figure 2.7.

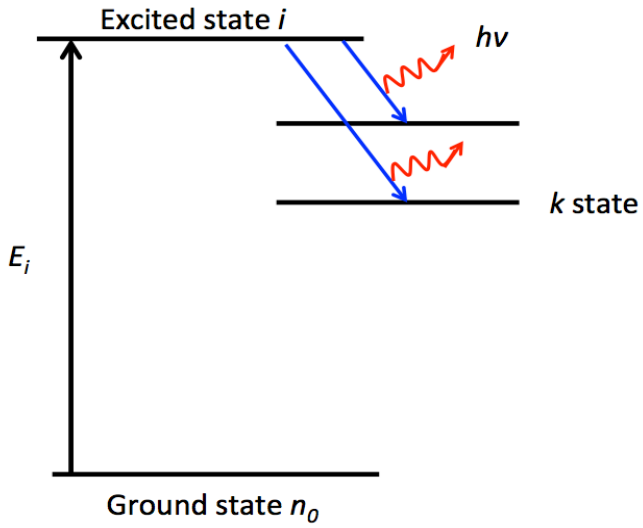

Figure 2.7: Electron impact excitation out of the ground state and subsequent decay to a lower level with the emission of a photon.

These transitions influence the population dynamics of the excited state i with population density n_i as described by the rate equation 2.5 as following:

$$\frac{dn_i(t)}{dt} = n_0 E_i(t) - \sum_k A_{ik} n_i(t) \tag{2.5}$$

Here, n_0 is the ground state population density, E_i is the electron impact excitation from the ground state into the excitation state i. A_{ik} is the Einstein coefficient which describes the probability of optical transition for the spontaneous emission of a photon from the excited state i to a lower energy level k. Electron impact excitation out of the ground state depends on the electron density n_e, the cross section of the energy dependant on electron impact excitation $\sigma_i(\epsilon)$ and the normalised electron energy distribution function $f(\epsilon)$ as shown in the following equation.

$$E_i(t) = n_e \int_0^\infty \sigma_i(\epsilon) \sqrt{\frac{2\varepsilon}{m_e}} f(\epsilon) d\epsilon \tag{2.6}$$

In a steady state, the population density of the excited state reaches equilibrium between the processes of excitation and de-excitation where:

$$\frac{dn_i(t)}{dt} = 0 \tag{2.7}$$

Hence, the equation 2.5 can be simplified as following:

$$n_i = \frac{n_0 E_i}{\sum_k A_{ik}} \tag{2.8}$$

The time constant to reach steady state is the radiative lifetime τ_i, of the excited state, and it is shown in the following equation:

$$\tau_i = \frac{1}{\sum_k A_{ik}} \tag{2.9}$$

In the corona model, it is assumed that there is no more additional excitation or de-excitation processes, which can affect the population density of an excited state. However, the corona model can be extended to include additional excitation and de-excitation mechanisms, and this is covered by the so-called collisional radiative model. These additional processes include the population of cascade processes out of higher excited states, electron impact excitation out of lower metastable states or collisional de-excitation, which is known as quenching. These additional excitation processes are explained via equation (2.10) as following:

$$\frac{dn_i}{dt} = n_0 E_i + A_{ci} n_c + n_m E_{mi} - A_i n_i \tag{2.10}$$

Here, the term $A_{ci} n_c$ represents additional excitation processes out of cascades from higher states c into the observed level *i* of population density n_c. A_{ci} is the transition rate from the cascade level c into level *i*. The term $n_m E_{mi}$ describes the electron impact excitation out of metastable states into the observed state *i*, E_{mi} of population density n_m. The symbol A_i denotes the effective decay rate which takes into consideration the radiation reabsorption and radiationless collisional de-excitation mechanisms known as quenching. The effective decay rate is represented as:

$$A_i = \frac{1}{\tau} = \sum_k A_{ik} g_{ik} + \sum_q k_q n_q \tag{2.11}$$

The reabsorption of radiation introduced in equation 2.11 is indicated by the so-called escape factors g_{ik} which describe the probability of emitted photons leaving the plasma without being absorbed by other particles during the transition from level *i* into level *k*. Reabsorption leads to overpopulated ground state; hence, the plasma described as optically thick. However, in optically thin plasma where ($g_{ik} = 0$), the absorption is neglected, the effective decay rate decreases while the effective lifetime increases.

Equation 2.11 also includes quenching which is described by the sum of the products of quenching coefficients k_q and the corresponding density $n_q$of the collision partners. In the collisional de-excitation processes, originated by quenching, the energy is transferred into the collision partners' internal energy. Therefore, increasing quenching results in increasing the effective decay rate and consequently decreasing the lifetime which affects the emission intensity [54, 55].

2.6 Tailored Waveform Frequency Coupling in CCPs

Non-sinusoidal RF waveforms can be referred to as dual frequency whereby two distinct frequencies are applied to the plasma. In the case of applying multiple frequencies, the non-sinusoidal waveforms are typically referred to as tailored voltage waveforms (TVWs). The TVWs mainly comprise a fundamental frequency ranging from hundreds of kHz up to the excitation frequency of 13.56 MHz. The fundamental frequency with its harmonics is summed and coupled into the powered electrode of the plasma simultaneously. Non-linear radio frequencies coupling into CCPs have attracted attention due to increasing opportunities in providing additional control of plasmas properties.

In CCPs geometrically symmetric reactors driven by a single radio frequency, the ion flux and ion energy are both controlled by the applied voltage whereby increasing the voltage amplitude leads to increasing both ion flux (and plasma density) and ion bombardment energy. This in turn makes it challenging for some industrial applications due to the strong coupling between ion energy and ion flux. However, researcher have investigated applying two different excitation frequencies, wherein with a large difference between the two frequencies can be used to achieve good separate control of ion flux and ion energy [56-59]. The ion flux can be changed while the ion energy is kept low, through the application of a higher frequency, and this has been applied for thin film deposition applications [60, 61]. On the other hand, a lower frequency allows for changing the ion energy while minimising the ion flux, and this is favourable for etching applications [62]. Although using two distinct excitation frequencies operating the plasma simultaneously shows more control of the plasma properties (ion flux and ion energy independently of one another) over the use of single radio frequency, this also introduces some disadvantages related to the wide distribution of the ion energy (IED) obtained. In addition, researchers have found that total collisionless heating result from dual frequency is greater than the collisionless heating results when applying the two frequencies separately [26, 63, 64]. Therefore, a possible solution to overcome such drawbacks of dual frequency is the application of tailored voltage waveforms. Improved control can be achieved by applying a fundamental frequency with its first harmonic instead of two frequencies that are widely separated as stated above in the case of the conventional dual frequency [22, 65, 66].

In CCPs, geometrically symmetric reactor AAPs driven by a single radio frequency produce identical spatio-temporal features [67, 68]. This indicates symmetric behaviours of electron heating and thus densities and fluxes of charged particles. The symmetry pattern observed in the application of a single frequency is disrupted when the plasma driven by non-linear voltage

waveforms is applied into the plasma simultaneously [18]. As mentioned previously, electron in radiofrequency-driven atmospheric pressure plasma governs most plasma processes. The driving frequency is a crucial parameter that efficiently influences the nature of discharge. Synergetic effect of coupling two different excitation frequencies can be used to achieve good independent control over the mean electron energy and the electron density through governing the operation parameters. Consequently, the effected electron energy distribution function (EEDF) is influenced and therefore the control of the chemical kinetics when enhanced for different applications. Here, dual frequency operation produced high electron density while the mean electron energy shows little to no change [20, 69] . Separate control between electron density and electron temperature is investigated through the application of nonlinear frequency whereas such control is not possible in the case of single-frequency-driven plasma. In single-frequency applications, the electron density increases linearly with increasing the input power while the electron temperature is almost constant. However, coupling dual frequencies shows an increase in electron density and a decrease in electron temperature [70]. Whereas the electron density increases with more frequencies coupling into the APPs, the gas temperature remains low, and this, in turn, is beneficial in some specific applications such as cancer treatments. All of these studies discussed above indicate that the nonlinear frequency coupling into APPs allows a variety of electron characteristics and therefore different applications.

Chapter 3 Experiment and Diagnostics

In this chapter, the experimental set up and diagnostics techniques used for studying electron dynamics in the plasma are discussed. Firstly, the atmospheric pressure plasma jet and the peripheral equipment are introduced. Then, electrical setup and diagnostics are also presented here. Finally, the optical emission spectroscopy diagnostic techniques are discussed.

3.1 APPJ and Related Equipment

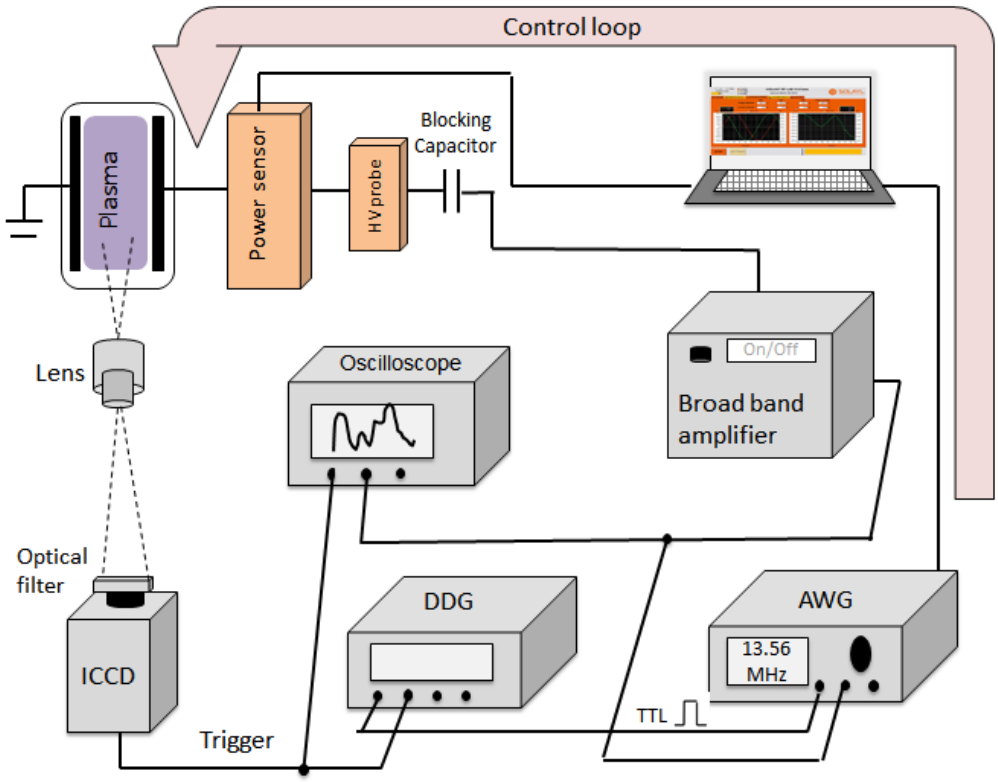

Figure 3.1: The experimental set up.

A schematic diagram of the experimental setup and diagnostic equipment used in this work is shown in figure 3.1. This specific design, used in this work, is based on the geometry of the micro scale atmospheric pressure plasma jet (μ-APPJ), as developed by Schulz-von der Gathen et al. [49, 50] as mentioned in chapter 2. It consists of two parallel, symmetric areas, stainless steel electrodes with length of 30 mm and thickness of 1 mm and a distance of 1 mm separating them. The electrodes are enclosed between two quartz windows offering good optical observation of the plasma core and allowing measurement of a wide range of the electromagnetic spectrum from infrared to the ultraviolet range. Therefore, a confined discharge with a cross section of 1 x 1 mm^2 results between the electrodes and the quartz windows. One electrode is grounded while the other one is powered, and the latter is driven by a fundamental frequency of 13.56 MHz and its higher

harmonics. The gas flow is regulated by control unit MKS type 247 four-channel readout, which are connected to three MKS mass flow controllers (MFC) for helium, nitrogen/ oxygen and argon gas with flow rate up to 10 slm, 10 sccm and 5 sccm respectively used for the micro atmospheric pressure plasma jet. The MFC calibrated based on various gases correction factors as illustrated in [71]. The working gas used is helium as a carrier gas and molecular admixture of nitrogen / oxygen of order of < 1% and this will be specified in chapters 4 and 5 respectively. Also, a small amount of argon gas < 1% was added to the gas mixture as a tracer gas which is known to not change the charge dynamics. The gas mixtures are fed through a 50 cm in length PFA tube which has a chemical resistance property connected to the stainless steel tube that is fixed at the back of the APPJ [67, 72].

3.2 The Electrical Set Up and Diagnostics

The setup of electrical devices used to operate and monitor electrical parameters of the plasma is also illustrated in figure 3.1. Applying an RF signal of frequency of 13.56 MHz to the powered electrode generates the plasma. The RF signal can be either a single sinusoidal waveform or tailored waveforms. The sinusoidal waveform is used as reference for comparison with the tailored waveforms. A computer-controlled arbitrary function generator (AFG, KEYSIGHT 33600A) was used to generate the input voltage waveform. The output signal is amplified by a broadband amplifier (Prana GN 500, 100 KHz – 200MHz, 500 W). The fundamental sine waveform operates with a matching network being connected between the amplifier output and the powered electrode, which is important to ensure the efficient coupling of power between the generator and the discharge reactor. This power is used to produce and sustain the plasma through the ionization processes. The amplifier is connected to the powered electrode through a series of elements. The output signal goes through a blocking capacitor which has a capacitance of 2000 PF

± 20% to block out any DC current. Then a high voltage oscilloscope probe (Solayl 1000X voltage attenuation from DC to RF) connected directly to the blocking capacitor by a coaxial connector is used for measuring the DC self-bias generated from the application of asymmetric voltage waveforms on symmetric plasma source. The DC-bias is monitored by a digital oscilloscope (LeCroy WaveSurfer 104 MXs-B 1 GHz). The DC self-bias is the extracted time averaged of the waveform displayed in the oscilloscope. A Vigilant Power Monitor (Solayl, frequency band 1-150 MHz, max power 10 kW +/- 2%, max voltage 5kV, max current 100A**)** is connected inline to the high voltage probe and then to the powered electrode. It measures the absolute parameters of the plasma such as voltage, current and power through PC software, which works in a feedback loop with the AFG [73]. In the case of operating the plasma by non-sinusoidal waveforms, many frequency components present and no matching network was used. Therefore, coupling power and matching impedance could be an issue as the plasma impedance is highly reactive. Without the matching network, up to 15 % of the incident power can be coupled into the plasma. The oversized amplifier used is required to strike and maintain the plasma by applying a high voltage and tolerating at the high reflected power. In addition, the stray impedances of the reactor and the cables around the discharge can perform as a partial matching without a real matching unit. A digital delay generator (Standford Research System DG645) is linked between the AFG and the ICCD camera to produce a synchronised trigger signal between the ICCD camera and the plasma voltage. The ICCD camera is capable of being triggered at a frequency no more than 500 kHz, which is lower than the driving frequency of 13.56 MHz. Therefore, a frequency of 452 kHz is found to be suitable as a trigger signal to be sent to the camera in each 30 RF cycles of the driving frequency.

In this work when applying tailored waveform to generate the plasma in the presence of the utilized gas mixture that consists of helium gas with small amount of molecular gas (~ 0.05 %)

flowing into the plasma jet, a big instantaneous arcing occurs which might damage the plasma jet. This results from the high voltage breakdown applied into the helium dominant discharge. This issue can be overcome by following a consistent method relay on the concept of Paschen's law that determines the breakdown voltage of different gases [74]. Molecular gas such as nitrogen or oxygen can be fed into the plasma jet continually when applying the tailoring mode on the RF signal and after getting stable voltage in the plasma until stopping the signal-tailoring mode; helium gas can then be used. An additional benefit of this approach besides avoiding the arc phenomenon is reducing the chance of air diffusion into the plasma jet and the gas tubes.

The applied RF voltages used in this thesis are varied depending on different molecular admixtures and the different waveforms. These voltages are high enough to break down the gas mixtures and produce a homogenous discharge filling the entire channel. At these voltages the plasma operated and sustained at α-mode. Further higher voltages lead to the generation of an arcing mode which means higher gas temperature and this is avoided due to the negative application of high gas temperatures on thermosensetive surfaces as well as damaging the plasma jet.

3.2.1 Driving Tailored Voltage Waveforms

An advanced control of plasma properties can be achieved by applying a promising method: driving the plasma with tailored voltage waveforms. These waveforms basically consist of a fundamental radio frequency of 13.56 MHz and a superposition of multiple harmonics. Different tailored waveforms can be discriminated by adjusting their phases or amplitudes as shown in equation 3.1.

$$\phi(t) = \sum_{k=1}^{n} \phi_k \cos(2\pi k f t + \theta_k) \qquad (3.1)$$

Where ϕ is the voltage applied to the powered electrode, k is the harmonics index (k = 1,….,n) and n is the number of harmonics (in this work it varied between 1 to 5 harmonics), f is the fundamental frequency (13.56 MHz), θ_k is the phase shift of the harmonics and ϕ_k is the amplitude of every individual harmonic. The amplitude of each harmonic is given by the

$$\phi_k = \phi_0 \frac{2(n-k+1)}{(n+1)^2} \qquad (3.2)$$

following equation:

Where ϕ_0 is the peak-to-peak voltage, which can be adjusted to have the desired values.

In this work, different types of tailored voltage waveforms that were used to drive capacitively coupled atmospheric pressure plasma: peaks, valleys, sawtooth-up and sawtooth-down waveforms.

(i) ‘Peaks’ and ‘valleys’ waveforms are generated depending on equations (3.1) and (3.2) and examples of these tailored waveforms are shown in figure (3.1).

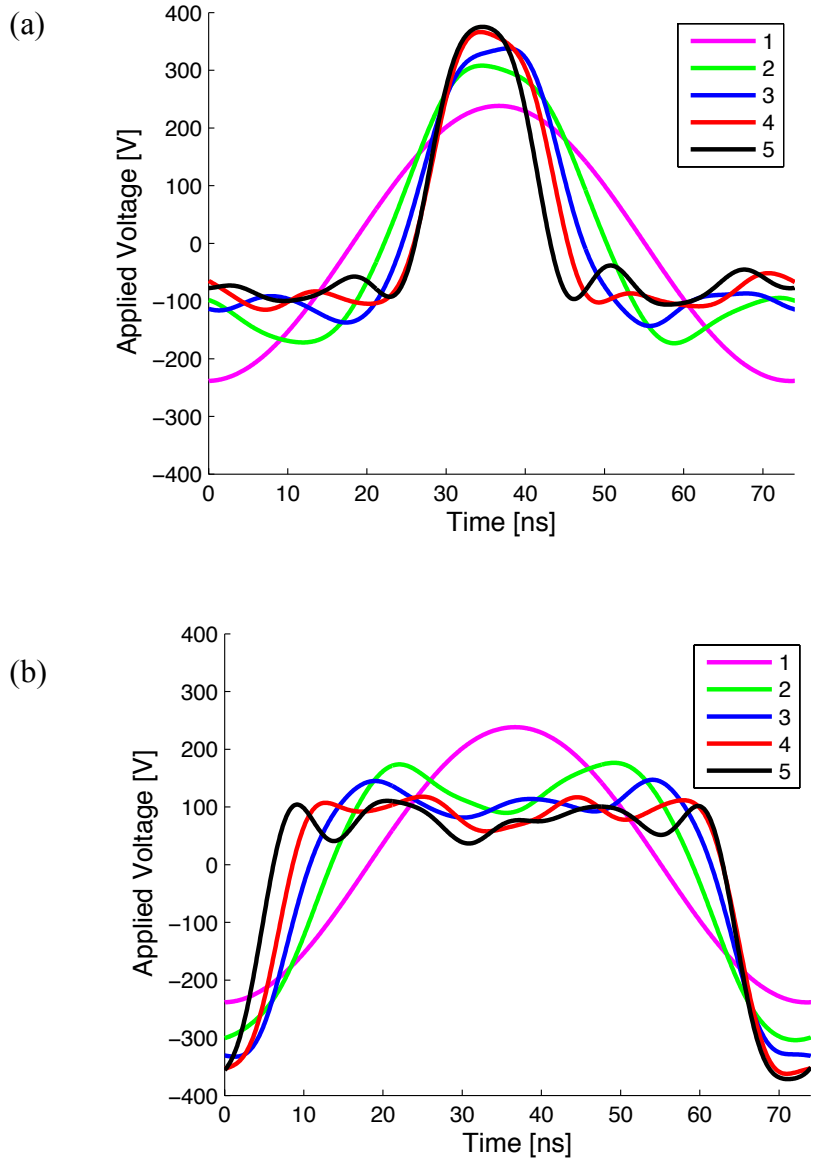

Figure 3.2: Tailored voltage waveforms: (a) 'peaks' and (b) 'valleys' type waveforms for a consecutive number of harmonics from one to five harmonics and 480 peak-to-peak voltage.

Peaks waveforms are obtained by setting the phase θ_k for all harmonics to zero while valleys waveforms are obtained by setting the phase angle to π. Peaks waveform-driven plasma mirrors valleys waveform-driven plasma with respect to the discharge gap between the two electrodes in the geometrically symmetric plasma jet. Peaks and valleys waveforms consist of high peak / valley followed by small peaks / valleys respectively and the number of peaks/ valleys is related to the number of harmonics. The voltage amplitude of the dominant peak/valley becomes higher with an

increase in the number of harmonics.

(ii) The sawtooth-type waveform can be obtained from the following formula:

$$\phi(t) = \pm\phi_0 \sum_{k=1}^{n} \frac{1}{k} \sin(2\pi k f t) \tag{3.3}$$

The minus and plus sign indicate sawtooth-down and sawtooth-up waveforms respectively. Examples of sawtooth-up and sawtooth-down are illustrated in figure (3.3) with a fundamental frequency of 13.56 MHz for number of harmonics from one to five at 480 Vpp. Sawtooth-up waveforms consist of a slow positive slope and a fast negative slope and the vice versa is illustrated in the case of sawtooth-down waveforms.

(a)

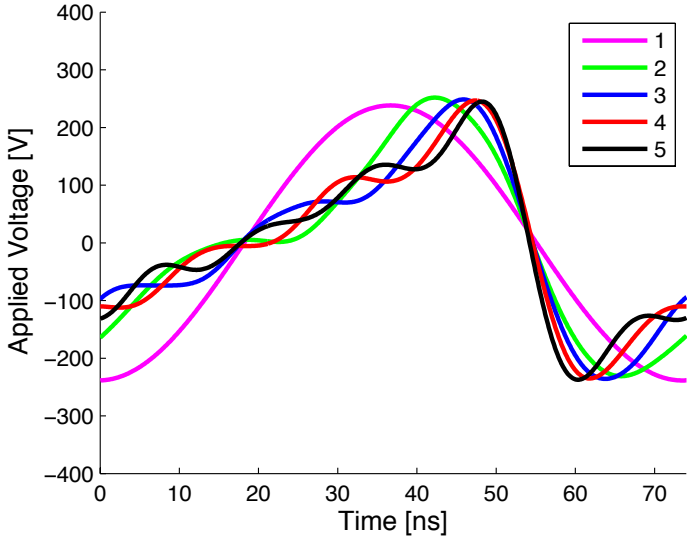

(b)

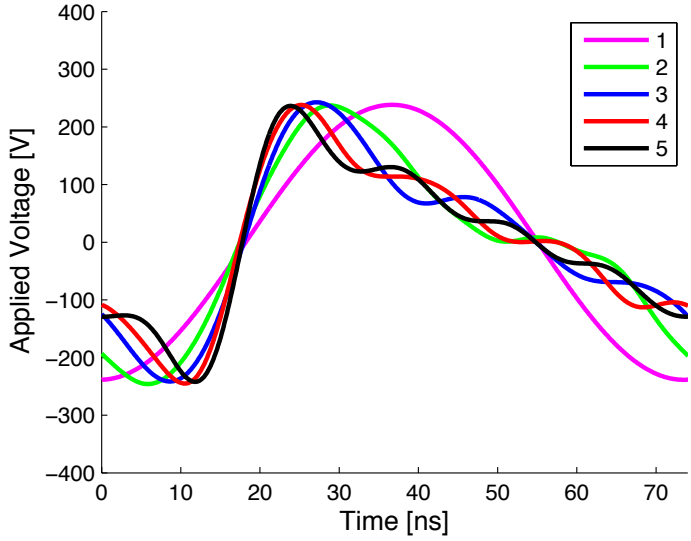

Figure 3.3: Tailored voltage waveforms: (a) 'Sawtooth-up' and (b) 'sawtooth-down' type waveforms for a consecutive number of harmonics from one to five harmonics and 480 peak-to-peak voltage.

Sawtooth-up waveform-driven plasma mirrors sawtooth-down waveform-driven plasma with respect to the discharge gap between the two electrodes in the geometrically symmetric plasma jet. The slow positive slope in the case of sawtooth-up and the reverse fast negative slope in the case of sawtooth-down waveforms increase according to the number of harmonics. In increasing the number of harmonics, the phase between each harmonic is changed and this effect can be indicated as slope asymmetry effect (SAE).

3.3 Optical Diagnostics

There has been a great number of optical diagnostic techniques and appropriate equipment created to study the physical and chemical properties of plasma [75-79]. The most prominent experimental optical diagnostic techniques are the active and passive methods. Active diagnostic techniques are based on using special instruments, such as probes, introduced into the plasma to study the plasma parameters. However, as these instruments are in direct interaction with the plasma components, their presence influences the plasma state. On the other hand, passive diagnostic techniques imply

using external optical sources to study plasma properties without interrupting the plasma. It is most efficient to detect the plasma that operating in a system with small dimensions where using probe is not applicable such as APPJ. The most distinct passive diagnostic method is optical emission spectroscopy (OES). It is characterised by examining the plasma properties from the emitted photons with high spatial and temporal resolution. It also provides information about the population density of excited states through the emission intensities of different species in the discharge [80, 81]. From the emission lines' profiles, many plasma parameters can be deduced e.g. the neutral particles temperatures can be acquired from Doppler broadening and electron density from Stark broadening.

The optical emission spectroscopy used in this work is phase-resolved optical emission spectroscopy (PROES), a powerful optical diagnostic technique that allows the study of fast processes of excitation dynamics caused by electrons from the emission intensity [77, 82, 83]. This needs the use of a fast gateable (nanosecond timescale) intensified coupled charge camera (ICCD) (Andor Istar, DH334T-18U-C3, 1024 x 1024) with high repetition rate. A gate width of 2 ns time was used to measure the phase resolved of the full RF cycle ($\approx$ 73.75 ns). The plasma emission is focused, with high spatial resolution, by using a lens (SIGMA DC 18 - 200 mm- 1:3.5 – 6.3II) mounted between the plasma and the ICCD camera. An optical interference filter (Andover corporation optical filter - 750 nm FWHM) of 10 nm bandwidth is used to discriminate different emission lines in the discharge.

The ICCD is synchronised with the driving RF frequency of 13.56 MHz, and, in the case of dual or multi frequencies, the camera is synchronised with the fundamental frequency. The concept of phase-resolved optical emission is illustrated in figure (3.4). The delay generator produces a trigger signal, through PC serial commands, by a fixed delay times. The trigger pulse activates the

ICCD camera intensifier gate allowing for an image to be taken each 30 RF cycle which is equivalent to 452 kHz. In the ICCD camera integration window, the obtained emission is integrated over thousands of RF cycles relying on variable exposure times of several seconds to produce a high signal-to-noise ratio, which then results in image data. After a sequence of increments in the variable delay by step equal to 2 ns, the camera gate delay increases consequently within the RF period. Therefore, phase-resolved emission is achieved via the entire RF cycle with 37 images in total.

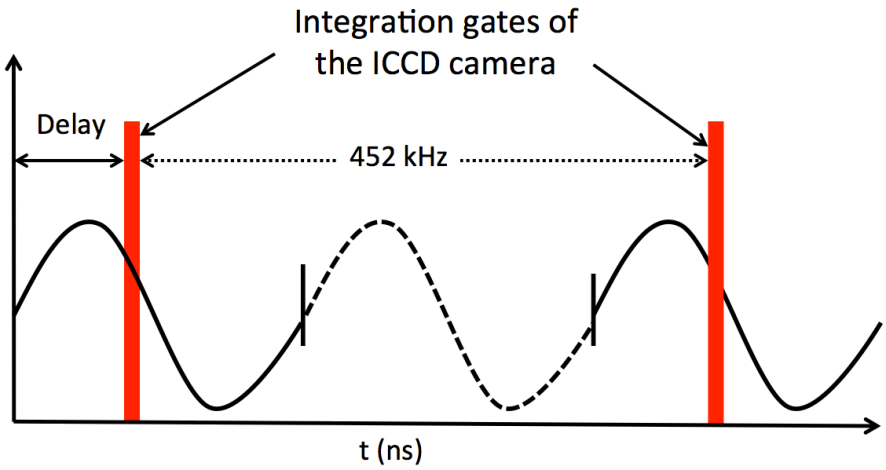

Figure 3.4: Diagram illustrating the principle of PROES.

Spatio-temporal electron impact excitation rate can be calculated from the gained spatio-temporal emission, which is proportional to the population density of the observed excited state, and this is given by the excitation function illustrated in equation (3.4) [84].

$$E_i(t) = \frac{1}{n_0}\left(\frac{dn_i(t)}{dt} + \frac{1}{\tau_{eff}} n_i(t)\right) \qquad (3.4)$$

$$\frac{1}{\tau_{eff}} = \frac{1}{\tau} + \sum_q k_q \, n_q \qquad (3.5)$$

The excitation can be obtained taking into account the effective lifetime τ_{eff}, which is proportional to the radiative lifetime τ and the quenching coefficient k_q of species q with the density of n_q of the observed excited state.

The spectroscopic data include wavelength, natural radiative lifetimes, quenching coefficients and transitions of the atomic states at atmospheric pressure and room temperature of 300 K are illustrated in table (3.2).

Table 3.1: The wavelength, observed atomic state, radiative lifetime and quenching coefficients of Ar (2p1) atom by different gases.

Wavelength (nm)	Atomic state	Lifetime (ns)	Quenching coefficient (10^{-10} cm^3 s^{-1})			
			Ar	He	N_2	O_2
750.4	Ar ($2p_1$)	22.5	0.16 [67]	0.0031 [67]	0.32 [85]	7.6 [67]

In this work, gas mixtures consist of helium as working gas with small admixture of molecular gases nitrogen / oxygen and argon as a tracer gas. An interference filter of width of 750 nm is used to detect the plasma dynamic via the 750.4 nm emission line. The radiative lifetime and quenching coefficients are calculated for argon as a quenching partner. The natural lifetime of Ar ($2p_1$) is calculated from the atomic database NIST as 22.5 ns and in comparison with the natural lifetimes obtained in [67].

3.4 Ozone Detection

A gas mixture of helium with 0.05 % argon and oxygen admixtures were operated through the application of tailored voltage waveforms. Therefore, ozone species densities are measured. The gas flow is regulated by control unit MKS type 247 four-channel readout, which are connected to three MKS mass flow controllers (MFC) for helium, oxygen and argon gas with flow rate up to 50 slm, 50 sccm and 50 sccm respectively.

The plasma jet used in this case is basically a μ-APPJ but 11 times larger than the standard μ-APPJ; it is shown in figure 3.5. This plasma jet is 1 mm x 30 mm x 11mm, channel width, channel length and depth respectively. It is totally sealed, and the gas inlet and outlet tubes are PFA tubes are connected to the jet body properly. This makes it more beneficial over the standard jet as the air diffusion back into the plasma core is reduced.

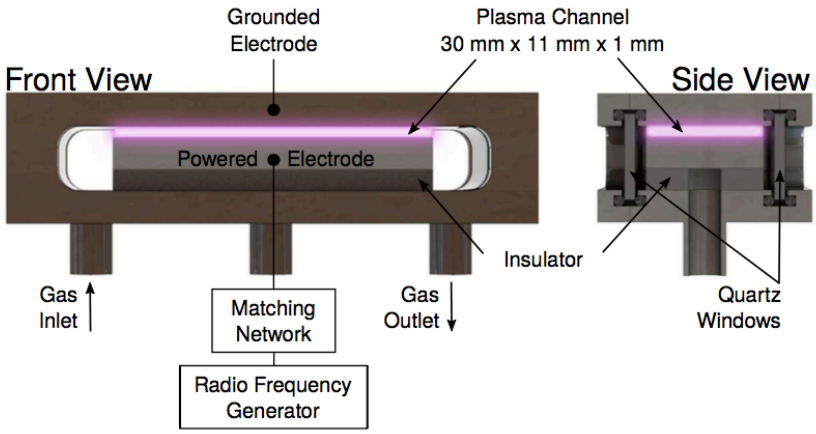

Figure 3.5: Illustration of larger μ-APPJ with front view and side view [86].

The gas outlet tube is connected to an ozone monitor (Model 106-L). It provides an accurate and precise reading of ozone concentrations up to 100,000 ppb. The measurements are based on UV absorption, and they can easily be taken from the monitor display.

Chapter 4 Tailored Voltage Waveforms Coupling In a He-N_2 RF APP

Atmospheric pressure plasma driven by radio frequencies are known as efficient sources for the production of chemically reactive species depending on the used gas components, the plasma volume and the operating parameters. Atomic nitrogen and its family species are valuable for many plasma applications. For instance, nitric oxide (NO), which is one of the most important nitrogen compounds, is used for biomedical therapy such as cancer treatment [87, 88] and wound healing [89, 90]. In addition, it plays a key role in industrial plasma processes. Delicate materials treatment such as polymers are an example [91].

Studying plasma properties is a significant way to provide control of these chemically reactive species. Tailored voltage waveforms (TVW) are considered as a promising approach to control plasma characteristics over single and dual frequencies. In this chapter, the experimental results of atmospheric pressure plasmas excited by tailored voltage waveforms are presented. The tailored voltage waveforms are applied on helium as a background gas with small amounts of argon 0.05 % used only for optical diagnostic purposes, which do not affect plasma interactions, as well as different amounts of nitrogen from 0.05 % - 0.5 %. The impact of TVW coupling through the variations of the nitrogen admixtures, different types of TVW and their harmonics and the preliminary measurements of DC self-bias voltages are investigated. Therefore, electron impact excitation in such plasma is discussed.

4.1 Peaks-type Waveforms

4.1.1 Excitation dynamics with N_2 variations

Atmospheric pressure plasmas operated in He with a small admixture of nitrogen < 1 % have been studied in single and dual frequencies [17, 18, 20]. It was found that the nitrogen admixture is of major importance as the Penning ionization of nitrogen by helium metastable is the dominant ionization mechanism to sustain the discharge ($He^* + N_2 \rightarrow He + N_2^* + e$) and this exceeds the direct ionisation of helium ($He + e \rightarrow He^+ + 2e$) [92].

The spatio-temporal electron-impact excitation into Ar ($2p_1$) state obtained from phase and space optical emission line at 750.4 nm for a gas mixture including He with 0.05 % Ar-driven by peaks waveforms is illustrated in figure 4.1. The fundamental frequency of 13.56 MHz and its harmonics n = 2-5 are applied. This is represented in the upper part of each image, and the colour bar at the top of each image shows the excitation rate, and the higher rate is represented in dark red. The y-axis represents the distance between the two electrodes. The grounded electrode is located at 0 mm while the powered electrode is located at 1 mm. The x-axis, shared for the upper and the lower parts of each image, illustrates the time in ns, which include one cycle of the fundamental frequency. The lower part of each image comprises the peak-to-peak voltage waveforms on the left y-axis as well as the current waveforms on the right y-axis, and they are shown for references. The peak-to-peak voltage is set to 470 V_{pp}. The voltage waveforms represent the sheath motion in the plasma with the applied electric field.

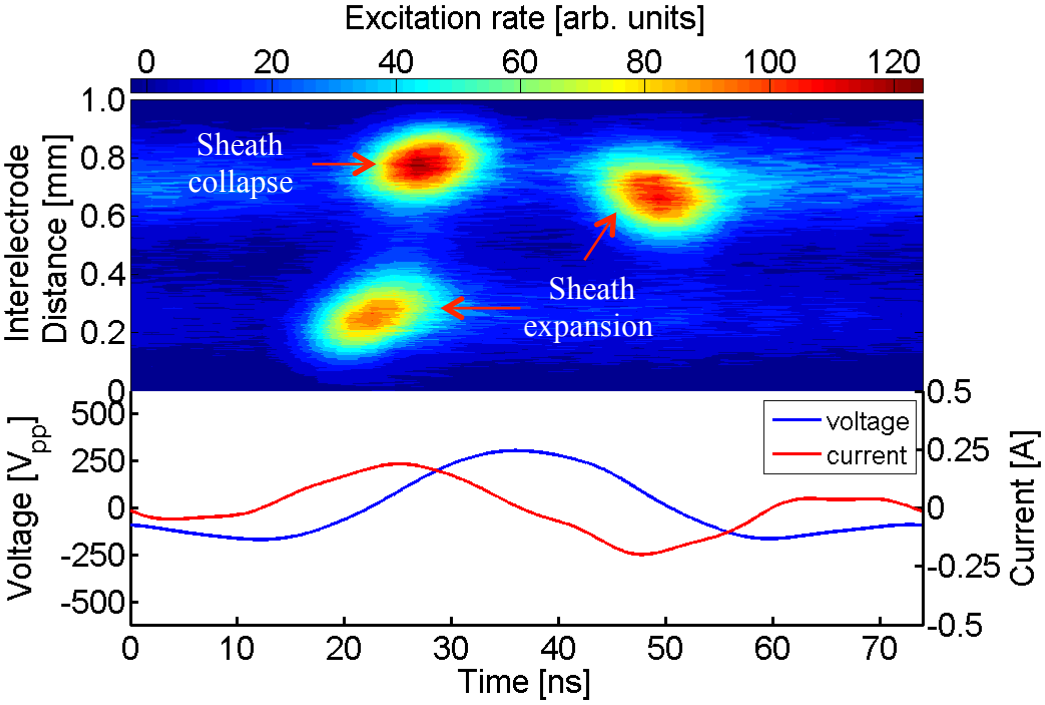
Excitation rate [arb. units]
0
20
40
60
80
100
120
Interelectrode Distance [mm]
1.0
0.8
0.6
0.4
0.2
0
Sheath collapse
Sheath expansion
Voltage [Vpp]
500
250
0
-250
-500
voltage
current
Current [A]
0.5
0.25
0
-0.25
-0.5
0
10
20
30
40
50
60
70
Time [ns]

n = 2

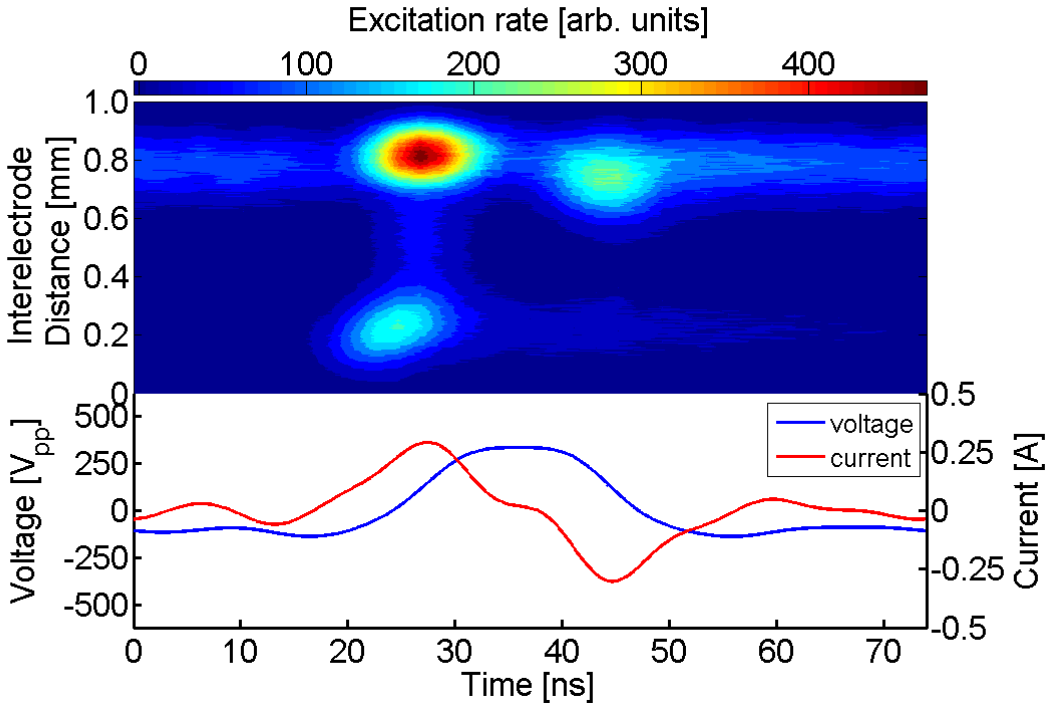
Excitation rate [arb. units]
0
100
200
300
400
Interelectrode Distance [mm]
1.0
0.8
0.6
0.4
0.2
0
Voltage [Vpp]
500
250
0
-250
-500
voltage
current
Current [A]
0.5
0.25
0
-0.25
-0.5
0
10
20
30
40
50
60
70
Time [ns]

n = 3

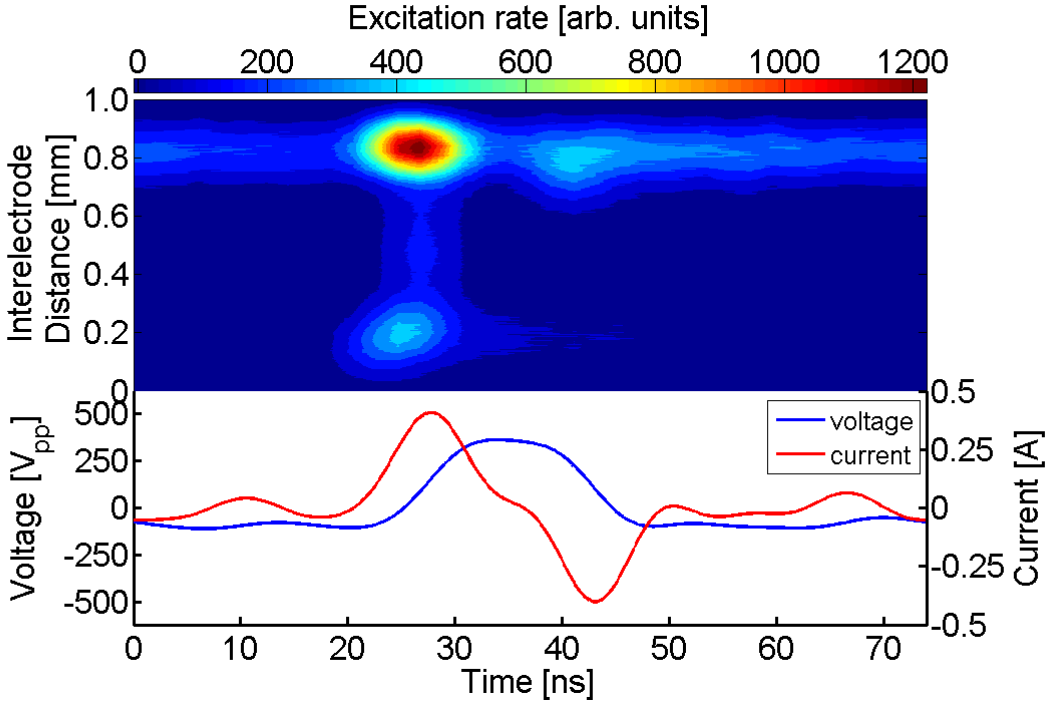

n = 4

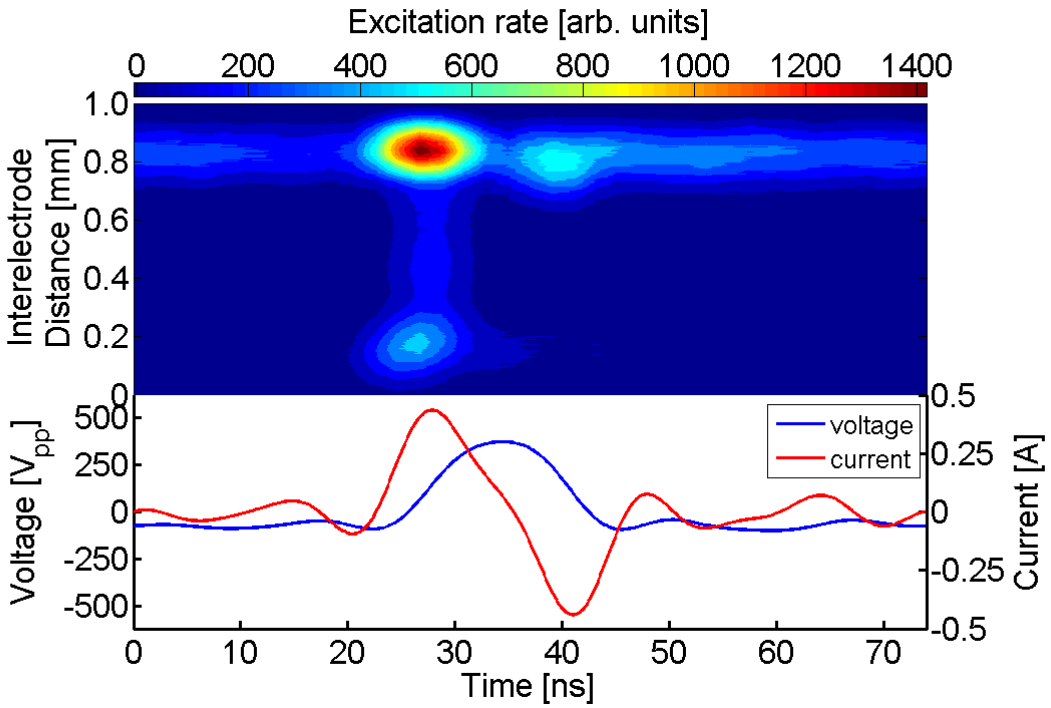

n = 5

Figure 4.1: Spatiotemporal excitation rates obtained from the measurement of the emission line at 750.4 nm using PROES and applying peaks waveform with n=2-5 harmonics (the top part of each image) applied on a gas mixture of He with 0.05 % Ar. The peak-to-peak voltage waveform (set at 470 V_{pp}) and the corresponding current waveforms for each harmonic are presented in the lower part of each image.

As one can see, at two harmonics, there are three excitation peaks: one at the grounded electrode while two excitation structures are observed at the powered electrode. This exhibits spatial and temporal asymmetry of the electron heating confinement. All these excitation peaks are different in intensity. At the powered electrode, the more intense excitation peaks is close to the electrode while the second excitation peak tends to propagate further toward the plasma bulk. The rapid increase in the voltage at time between ~ 20 to ~ 35 ns induces a fast sheath expansion at the grounded electrode where electrons are accelerated away from the electrode and then an excitation peak is initiated close to the grounded electrode. Almost at the same time, another excitation peak, located closer to the powered electrode, occurs through the intensive sheath collapse, which resulted from the rapid decrease in the voltage at the powered electrode. During sheath collapse, electrons cannot follow the fast change of the RF potential due to the collision condition; therefore, an electric field is initiated and hence accelerates electrons toward the powered electrode [93]. This electric field is similar to the so-called field reversal, which has been observed in hydrogen plasmas at low pressure driven by single frequency [54, 94] and using dual frequencies [95] and also by multi frequencies [96]. This phenomenon is also observed in helium with nitrogen plasma carried out in the case of sine waveform at atmospheric pressure [19]. At the powered electrode, there is also another excitation peak observed nearly in the plasma bulk at time between ~ 40 to ~ 55, and this occurs during sheath expansion at the powered electrode when the voltage decreases rapidly. However, the sheath is fully contracted at the grounded electrode; therefore, there is no field reversal produced at the grounded electrode. This excitation peak at the powered electrode is larger than the excitation peak at the grounded electrode. The amplitude of all of the excitation peaks mentioned above is correlated with the density of conduction current that represents the electron flux. The peak-to-peak voltage and the associated current increase by increasing the number of harmonics; therefore, the excitation maximum increases. There is a

structure alongside the powered electrode being more obvious with n = 3 up to n = 5 which might be described as a continuous excitation resulting from the minimum peaks of the applied voltage waveform. The spatial and temporal asymmetry of the electron heating confinement occurs due to long duration between sheath expansion and sheath collapse and also due the short time of the sheath collapse both at the powered electrode.

Here, different amounts of nitrogen < 0.05 % have been added; therefore, the electron impact excitation obtained by peaks waveforms has been investigated. Each set of gas mixture is driven by a fixed peak-to-peak voltage with harmonic numbers 2-5 harmonics. The nitrogen mixtures used are 0.05 % driven by 480 V_{pp} and 0.1 % driven by 490 V_{pp} respectively, and the results are shown in figures 4.2 and 4.3 respectively.

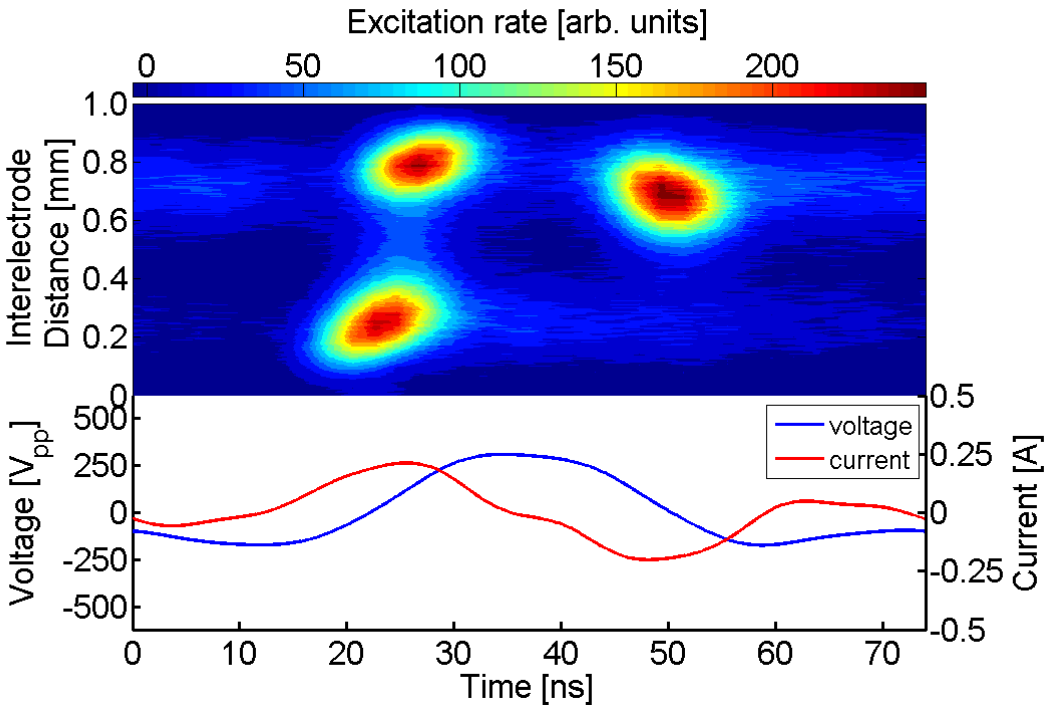

n = 2

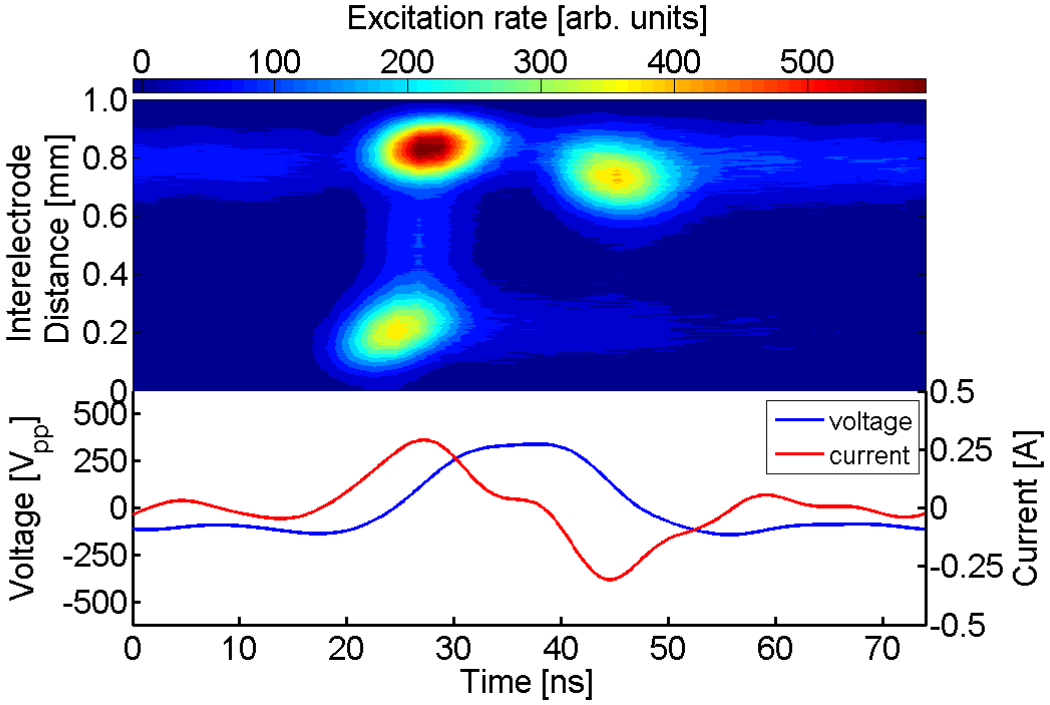
Excitation rate [arb. units]
0
100
200
300
400
500
Interelectrode Distance [mm]
1.0
0.8
0.6
0.4
0.2
0
Voltage [Vpp]
500
250
0
-250
-500
voltage
current
Current [A]
0.5
0.25
0
-0.25
-0.5
0
10
20
30
40
50
60
70
Time [ns]

n = 3

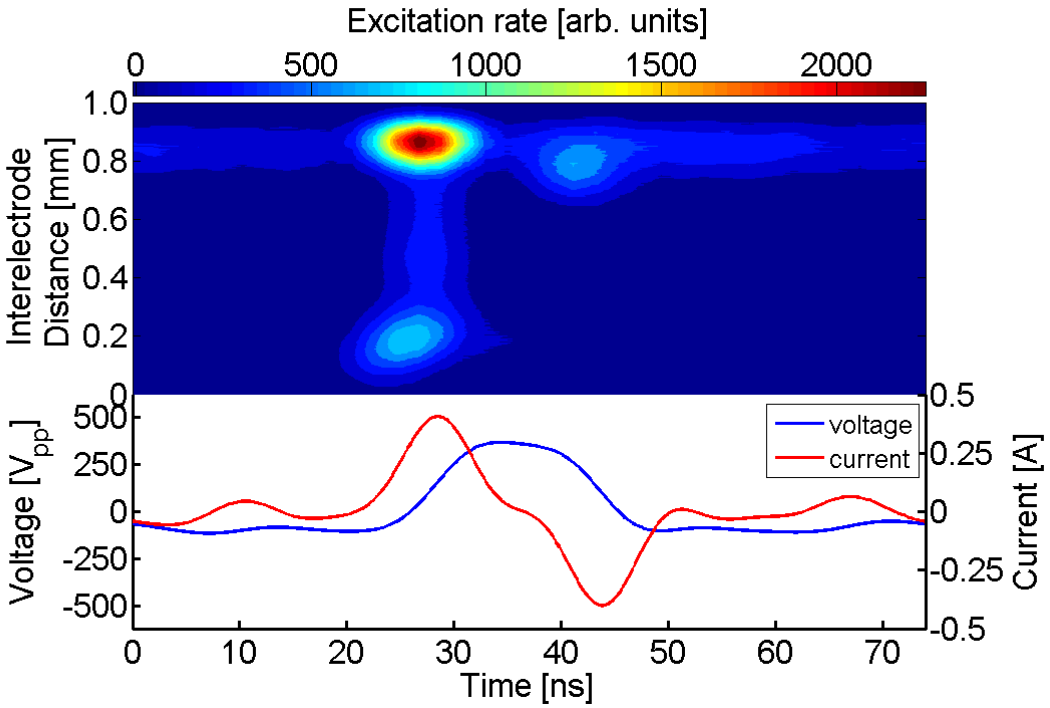
Excitation rate [arb. units]
0
500
1000
1500
2000
Interelectrode Distance [mm]
1.0
0.8
0.6
0.4
0.2
0
Voltage [Vpp]
500
250
0
-250
-500
voltage
current
Current [A]
0.5
0.25
0
-0.25
-0.5
0
10
20
30
40
50
60
70
Time [ns]

n = 4

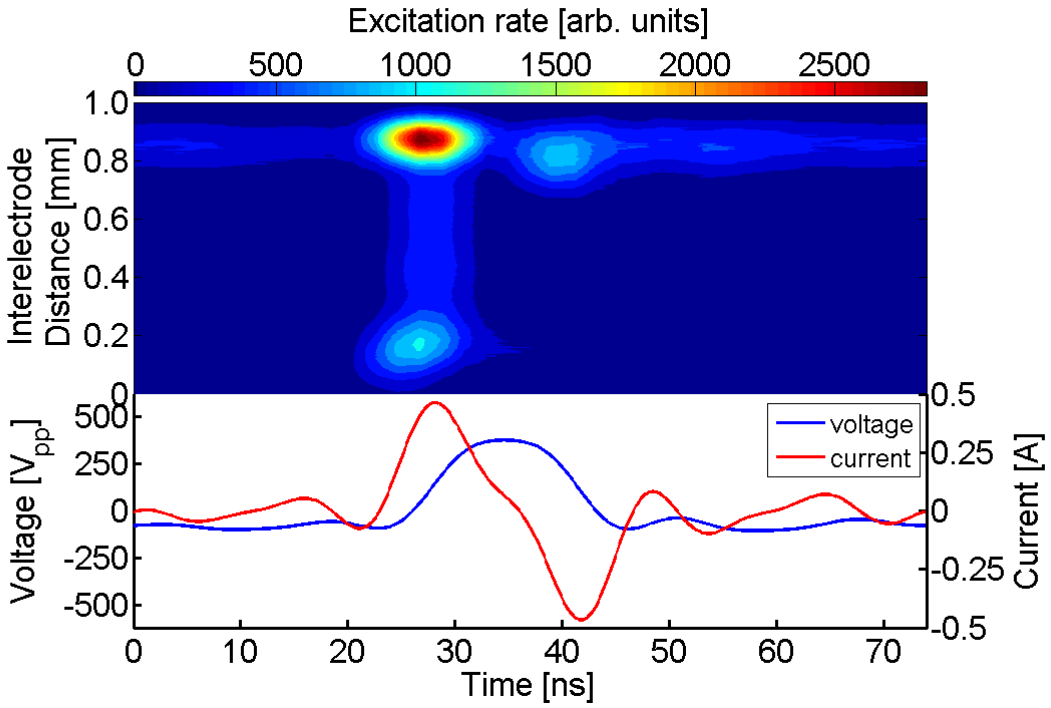

n = 5

Figure 4.2: Spatiotemporal electron impact excitation obtained from measurement of the emission line at 750.4 nm using PROES and applying peaks waveform with n=2-5 harmonics applied on a gas mixture of He with 0.05 % Ar and N_2 mixture 0.05 % driven by 480 V_{pp} are presented in the upper part of each image. The peak-to-peak voltage waveform and the corresponding current waveforms for each harmonic are presented in the lower part of each image.

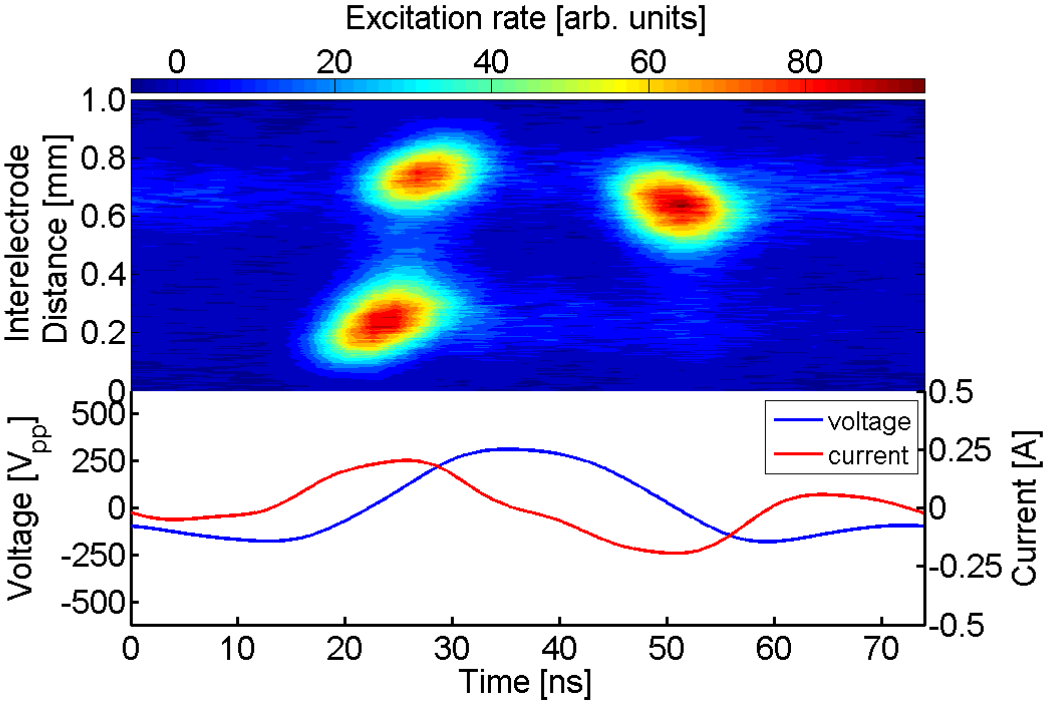
Excitation rate [arb. units]
0
20
40
60
80
Interelectrode Distance [mm]
1.0
0.8
0.6
0.4
0.2
0
Voltage [V_{pp}]
500
250
0
-250
-500
voltage
current
0.5
0.25
0
-0.25
-0.5
Current [A]
0
10
20
30
40
50
60
70
Time [ns]

n = 2

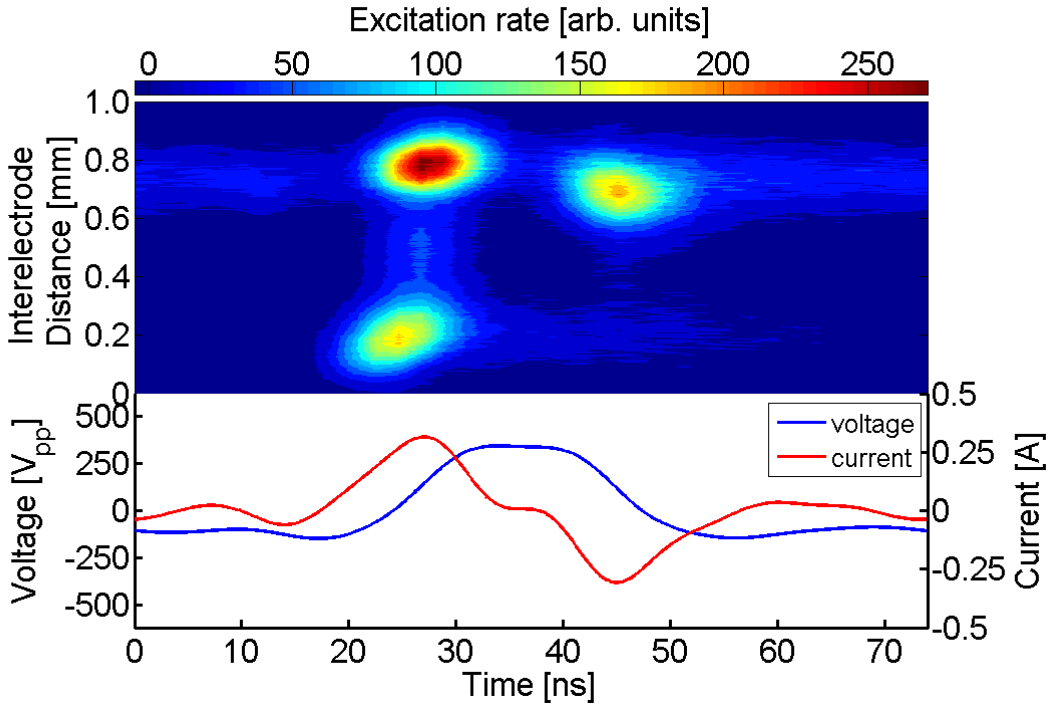
Excitation rate [arb. units]
0
50
100
150
200
250
Interelectrode Distance [mm]
1.0
0.8
0.6
0.4
0.2
0
Voltage [V_{pp}]
500
250
0
-250
-500
voltage
current
0.5
0.25
0
-0.25
-0.5
Current [A]
0
10
20
30
40
50
60
70
Time [ns]

n = 3

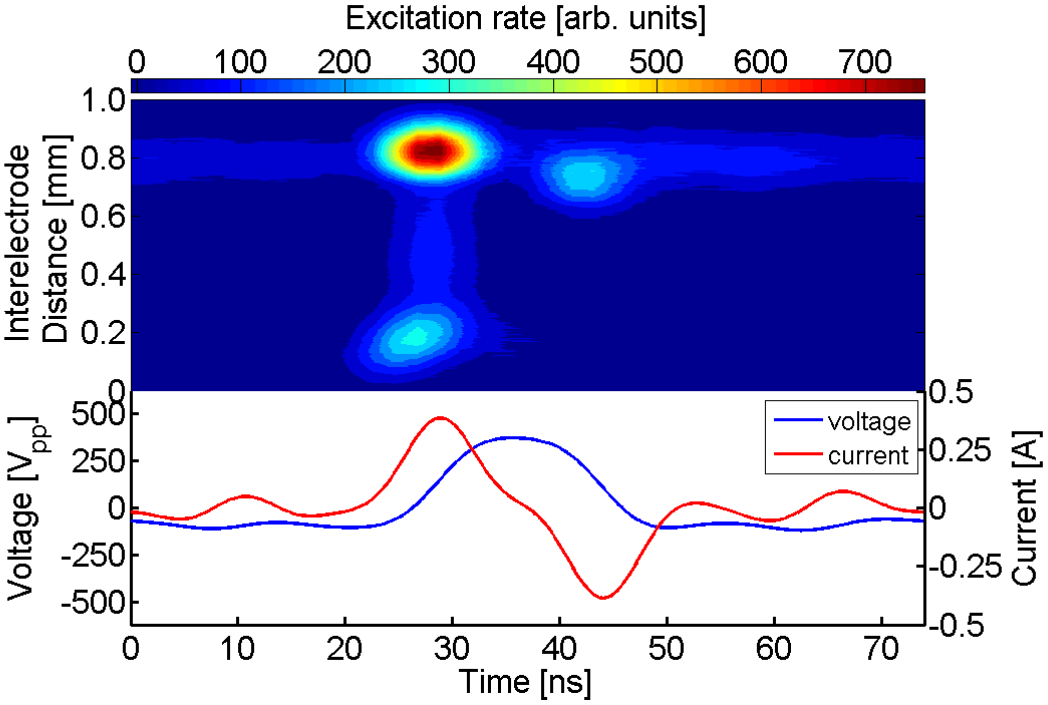

n = 4

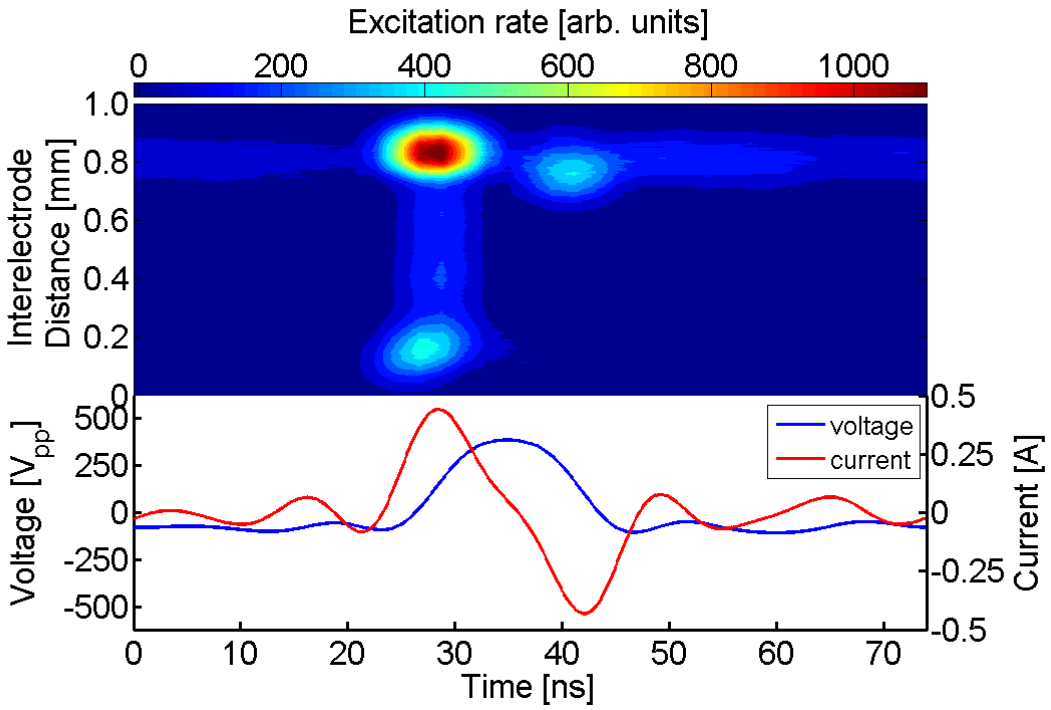

n = 5

Figure 4.3 Spatiotemporal electron impact excitation obtained from measurement of the emission line at 750.4 nm using PROES and applying peaks waveform with n=2-5 harmonics applied on a gas mixture of He with 0.05 % Ar and N_2 mixture 0.1 % driven by 490 V_{pp} are presented in the upper part of each image. The peak-to-peak voltage waveform and the corresponding current waveforms for each harmonic are presented in the lower part of each image.

The excitation peaks shown in figure 4.1 are also shown here quantitatively and qualitatively. In all results, the effect of increasing the number of harmonics and the nitrogen admixture are observed. For each individual set of nitrogen admixture, the excitation rates increase with more harmonics being added. This is extracted from the top colour bar of each image and summarised in figure 4.4. The sheath thicknesses become smaller with more harmonics being added, which indicates that the plasma density increases.

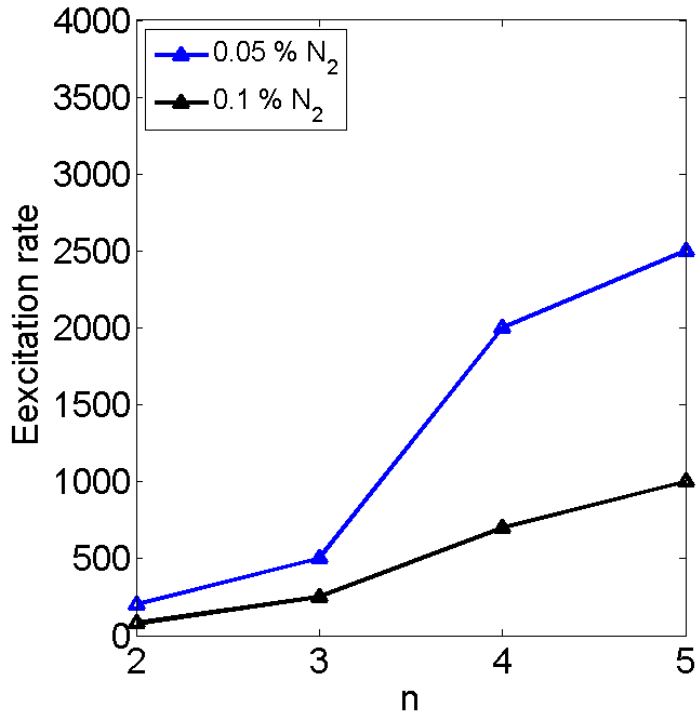

Figure 4.4 Summary of excitation rate as a function of the applied number of harmonics for different N_2 mixtures when applying peaks waveforms.

However, additional admixtures of nitrogen lead to a decrease in excitation rate. This is due to the excited state being quenched by the increasing number of nitrogen species according to equation 2.11 as mentioned in chapter 2 [97]. In addition, the energy is exploited for dissociating the additional amount of molecular nitrogen. The sheath thickness gets wider which indicating a decreasing in the plasma density.

In the case of valleys waveforms (when $\theta = \pi$), the spatio-temporal electron impact excitation of

applying valley waveforms with a voltage of 470 V_{pp} on a gas admixture of helium with 0.05 % of argon is shown in figure 4.5. Here, the images' specifications are the same as shown in figure 4.1. The behaviour of the plasma is almost the opposite of that in the case of peaks waveforms. It is also observed that there are three excitation peaks in each image in figure 4.5; two of them are at the grounded electrode while one is located at the powered electrode in contrast to peaks waveforms. The first excitation structure at the powered electrode at time between ~ 55 ns to ~ 70 ns occurs due to fast sheath expansion, which results from the increase in the voltage followed by fast sheath collapse at the grounded electrode resulted in an excitation peak due to the field reversal as mentioned in the case of peaks waveforms. Another excitation peak originates when the voltage increase induces fast sheath expansion at the grounded electrode.

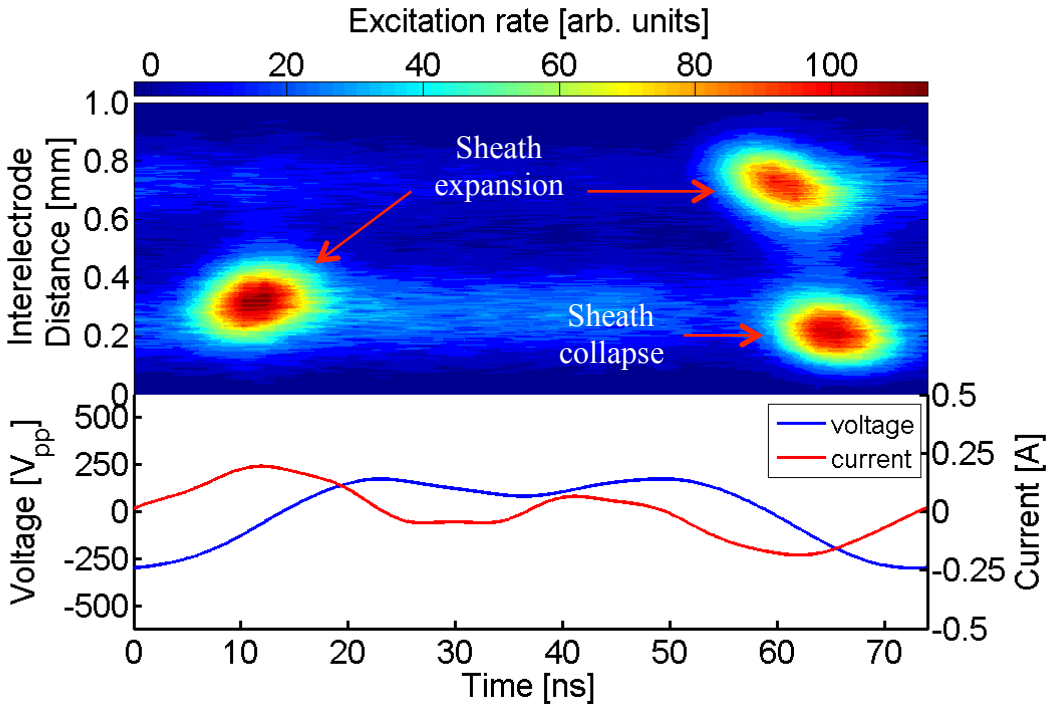

n = 2

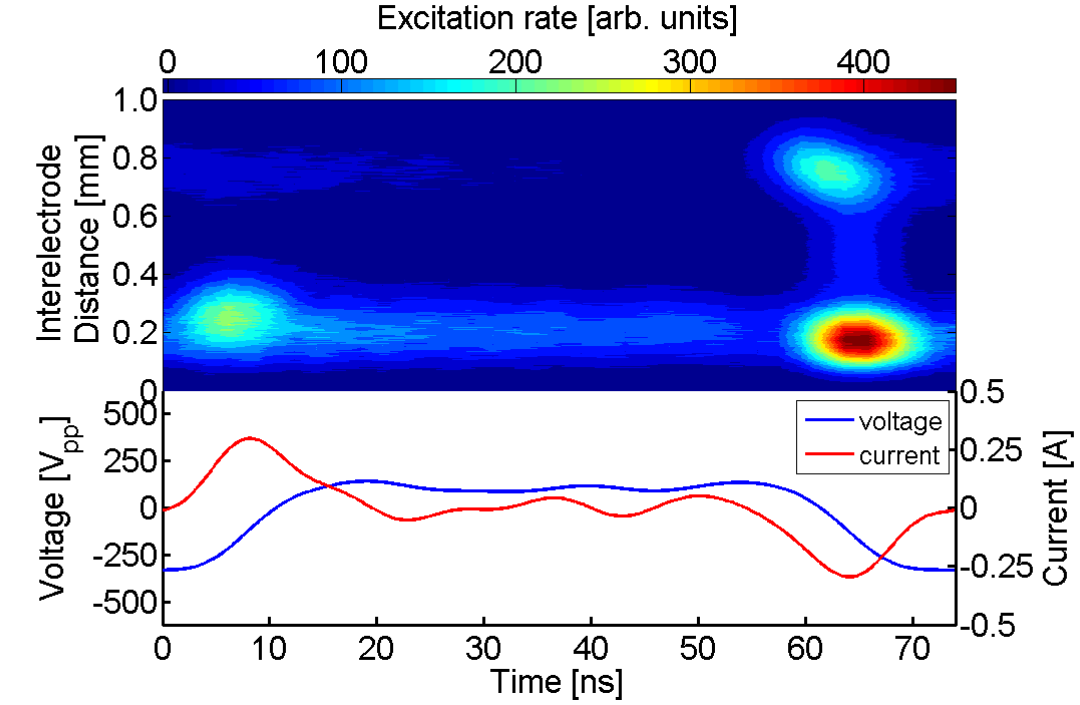
Excitation rate [arb. units]
0
100
200
300
400
Interelectrode Distance [mm]
1.0
0.8
0.6
0.4
0.2
0
Voltage [Vpp]
500
250
0
-250
-500
voltage
current
Current [A]
0.5
0.25
0
-0.25
-0.5
0
10
20
30
40
50
60
70
Time [ns]

n = 3

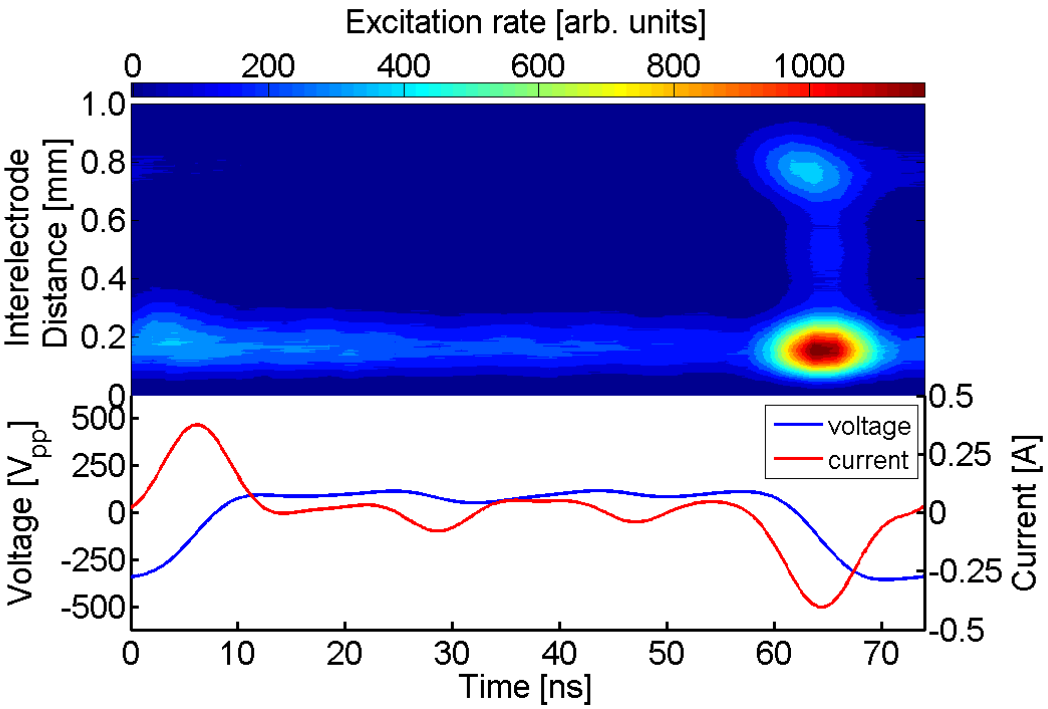
Excitation rate [arb. units]
0
200
400
600
800
1000
Interelectrode Distance [mm]
1.0
0.8
0.6
0.4
0.2
0
Voltage [Vpp]
500
250
0
-250
-500
voltage
current
Current [A]
0.5
0.25
0
-0.25
-0.5
0
10
20
30
40
50
60
70
Time [ns]

n = 4

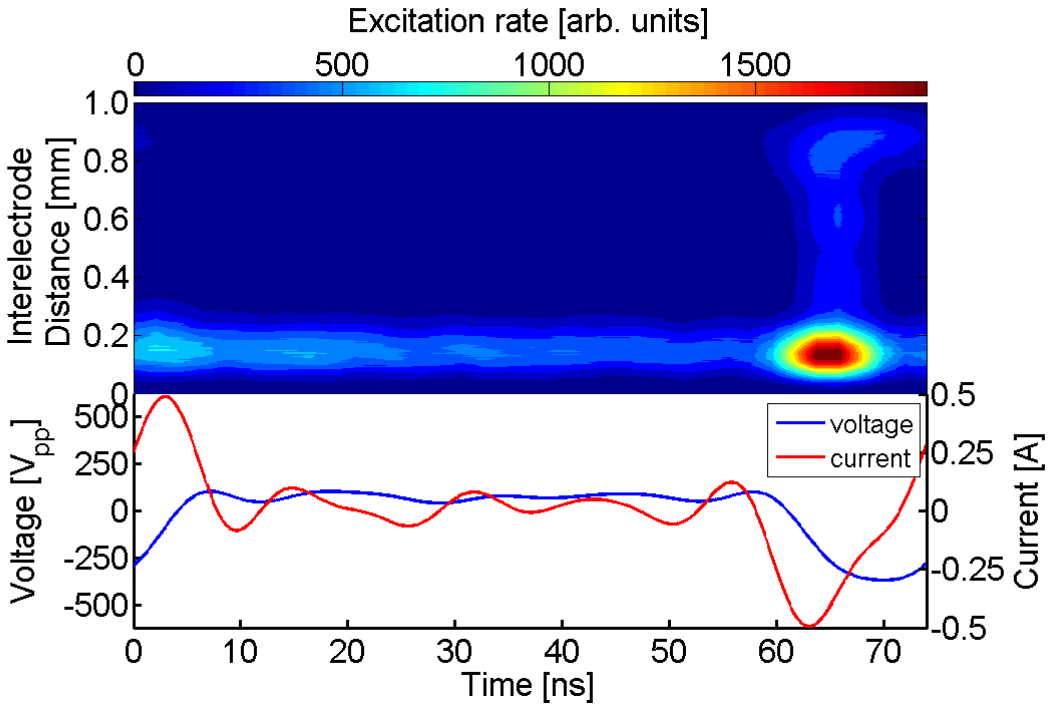

n = 5

Figure 4.5: Spatiotemporal excitation rates obtained from measurement of the emission line at 750.4 nm using PROES and applying valleys waveform with n=2-5 harmonics (the top part of each image) applied on a gas mixture of He with 0.05 % Ar. The peak-to-peak voltage waveform (set at 470 $_{Vpp}$) and the corresponding current waveforms for each harmonic are presented in the lower part of each image.

The influence of increasing the number of harmonics and the amount of nitrogen into the gas admixtures are also observed for the valley waveforms.

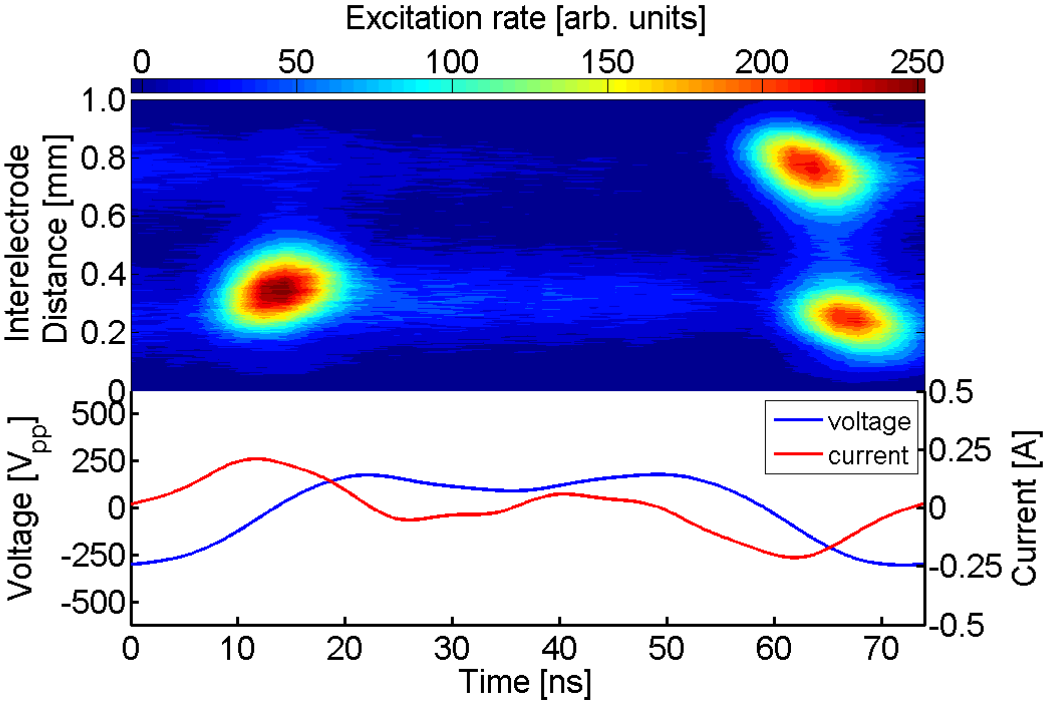
Excitation rate [arb. units]
0
50
100
150
200
250
Interelectrode Distance [mm]
1.0
0.8
0.6
0.4
0.2
0
Voltage [V_{pp}]
500
250
0
-250
-500
voltage
current
0.5
0.25
0
-0.25
-0.5
Current [A]
0
10
20
30
40
50
60
70
Time [ns]

n = 2

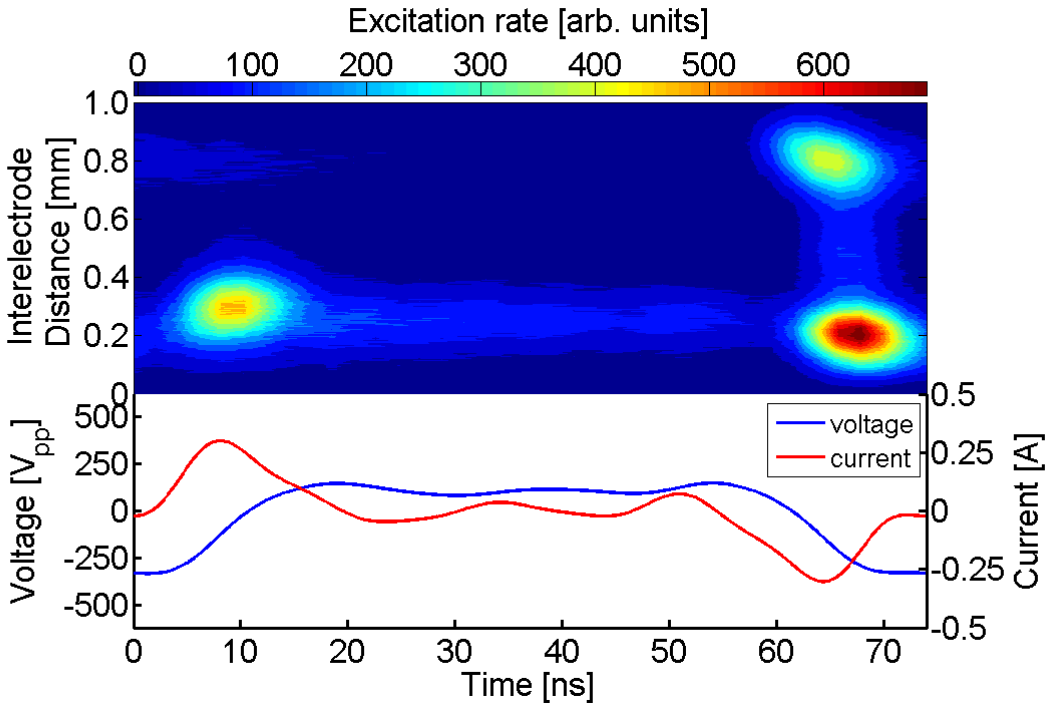
Excitation rate [arb. units]
0
100
200
300
400
500
600
Interelectrode Distance [mm]
1.0
0.8
0.6
0.4
0.2
0
Voltage [V_{pp}]
500
250
0
-250
-500
voltage
current
0.5
0.25
0
-0.25
-0.5
Current [A]
0
10
20
30
40
50
60
70
Time [ns]

n = 3

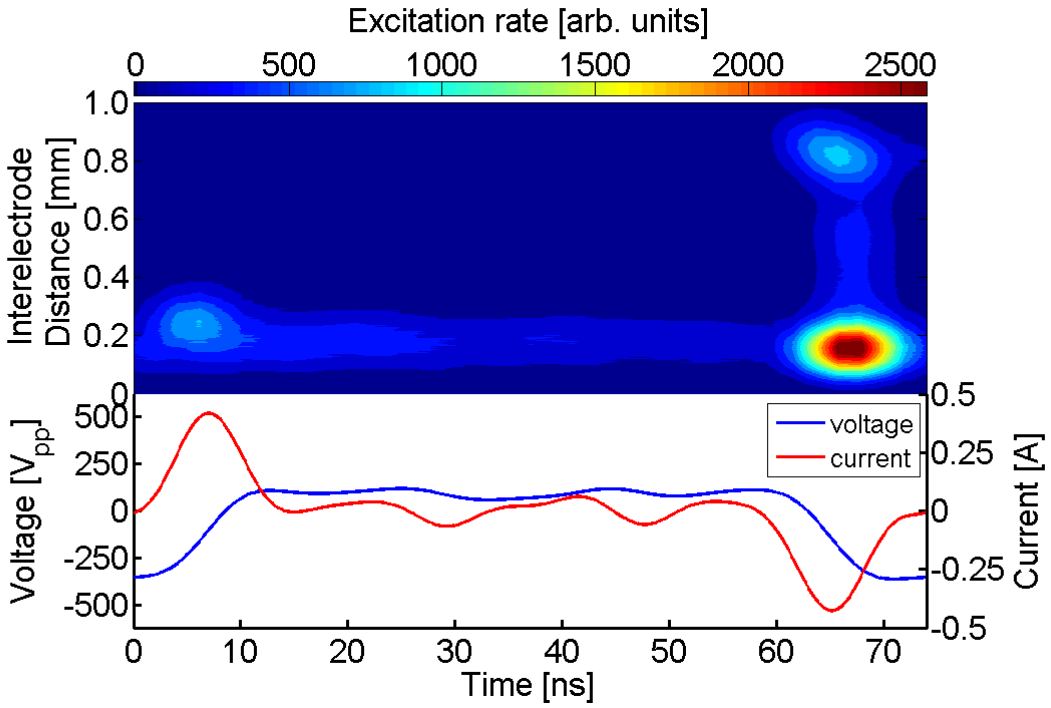

n = 4

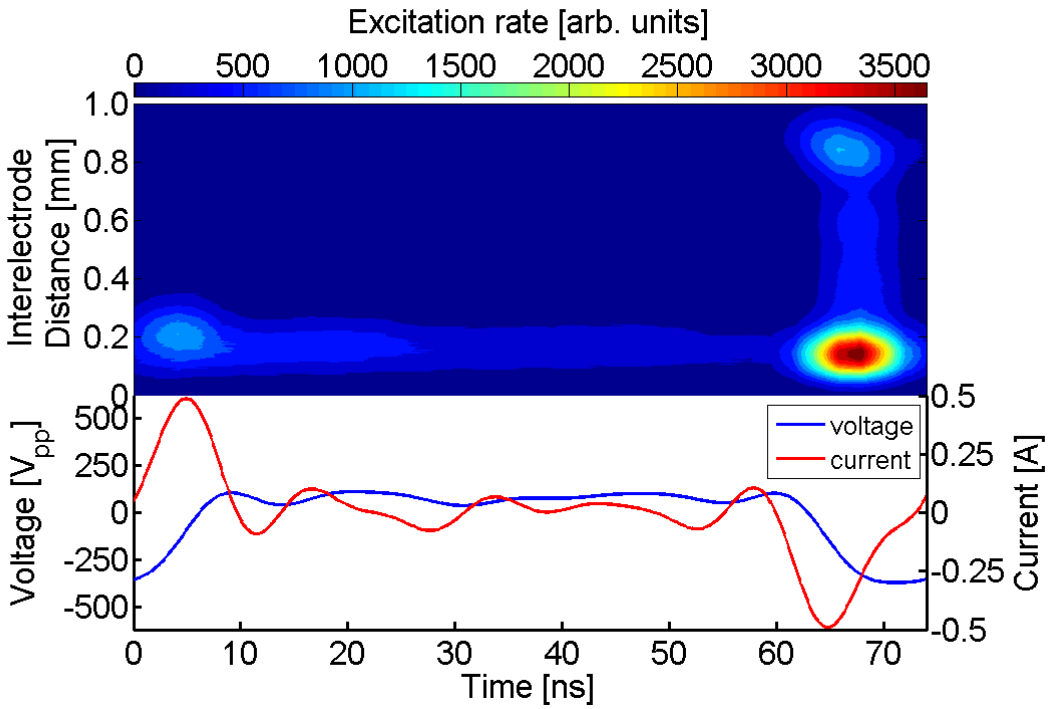

n = 5

Figure 4.6: Spatiotemporal electron impact excitation obtained from measurement of the emission line at 750.4 nm using PROES and applying valleys waveform with n=2-5 harmonics applied on a gas mixture of He with 0.05 % Ar and N_2 mixture 0.05 % driven by 480 V_{pp} are presented in the upper part of each image. The peak-to-peak voltage waveform and the corresponding current waveforms for each harmonic are presented in the lower part of each image.

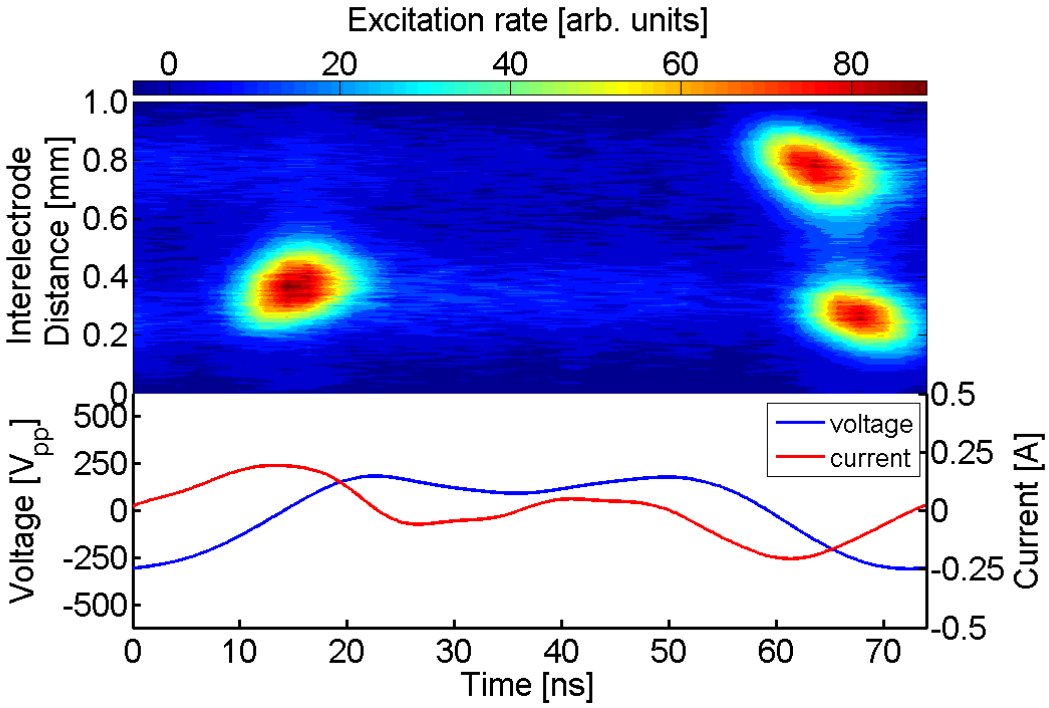
Excitation rate [arb. units]
0
20
40
60
80
Interelectrode Distance [mm]
1.0
0.8
0.6
0.4
0.2
0
Voltage [Vpp]
500
250
0
-250
-500
Current [A]
0.5
0.25
0
-0.25
-0.5
voltage
current
0
10
20
30
40
50
60
70
Time [ns]

n = 2

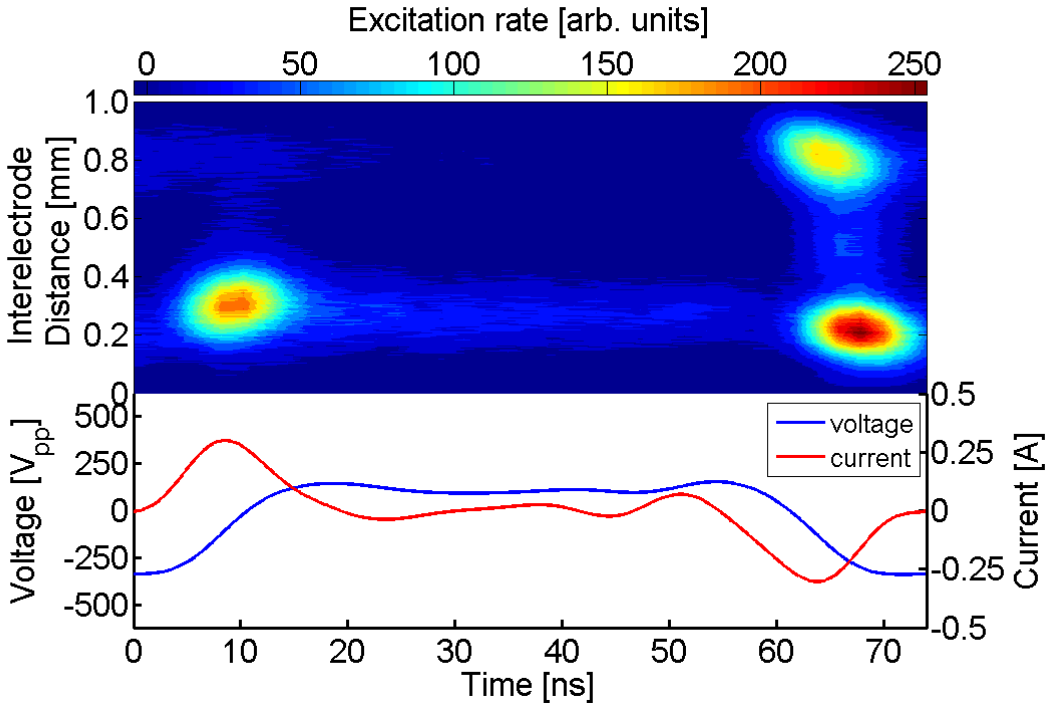
Excitation rate [arb. units]
0
50
100
150
200
250
Interelectrode Distance [mm]
1.0
0.8
0.6
0.4
0.2
0
Voltage [Vpp]
500
250
0
-250
-500
Current [A]
0.5
0.25
0
-0.25
-0.5
voltage
current
0
10
20
30
40
50
60
70
Time [ns]

n = 3

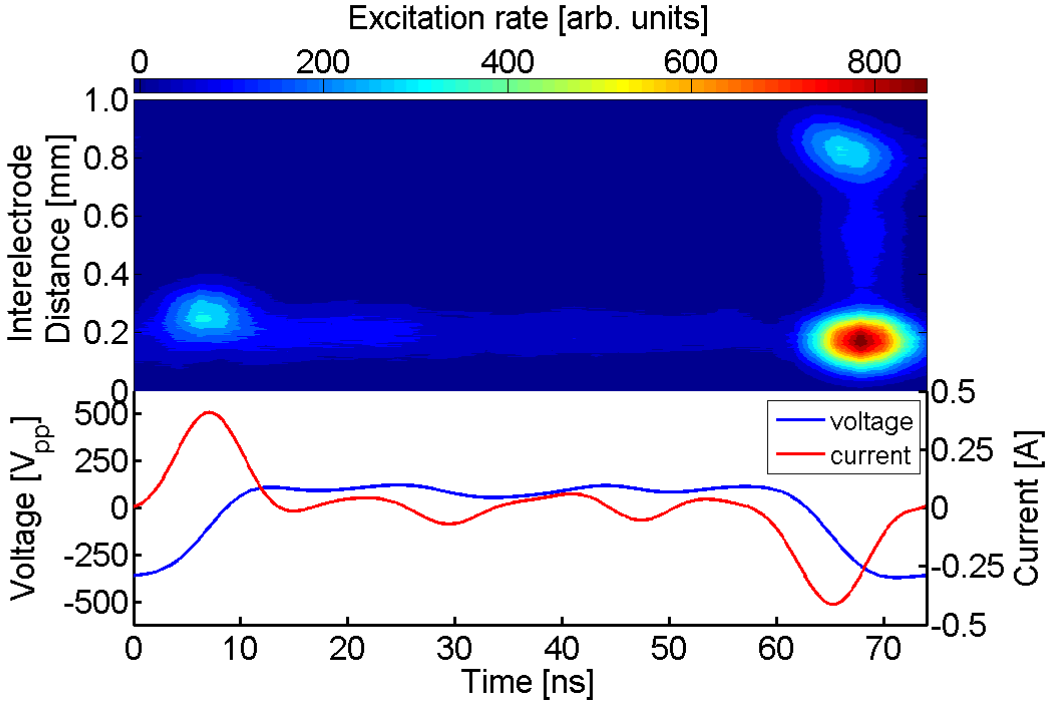

n = 4

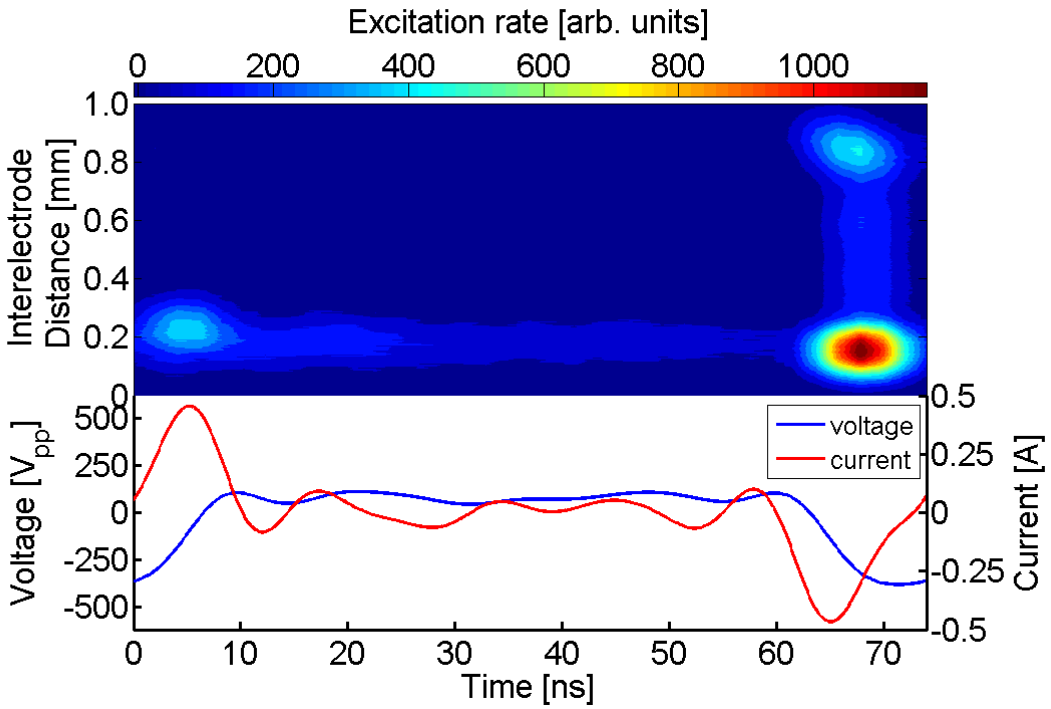

n = 5

Figure 4.7 Spatiotemporal electron impact excitation obtained from measurement of the emission line at 750.4 nm using PROES and applying valleys waveform with n=2-5 harmonics applied on a gas mixture of He with 0.05 % Ar and N_2 mixture 0.1 % driven by 490 V_{pp} are presented in the upper part of each image. The peak-to-peak voltage waveform and the corresponding current waveforms for each harmonic are presented in the lower part of each image.

In the case of applying valleys waveforms in APPs operating in helium with 0.05 % of argon and different concentrations of nitrogen, the space- and phase-resolved electron impact excitation obtained from PROES is illustrated in figure 4.6 and 4.7 with 0.05 % N_2 and 0.1 % N_2 respectively. By comparing each image with the same harmonic number, the influences of different amount of nitrogen effect on excitation dynamics are observed. Almost the same observations are consistent with that in the case of applying peaks waveforms. The excitation rates decrease with more nitrogen being added to the gas admixtures. Also, the sheath thicknesses (visually) are getting a bit wider, and this denotes that the plasma density decreases. The excitation rates increase with an increase in the number of harmonics. All these results are summarised and illustrated in figure 4.8.

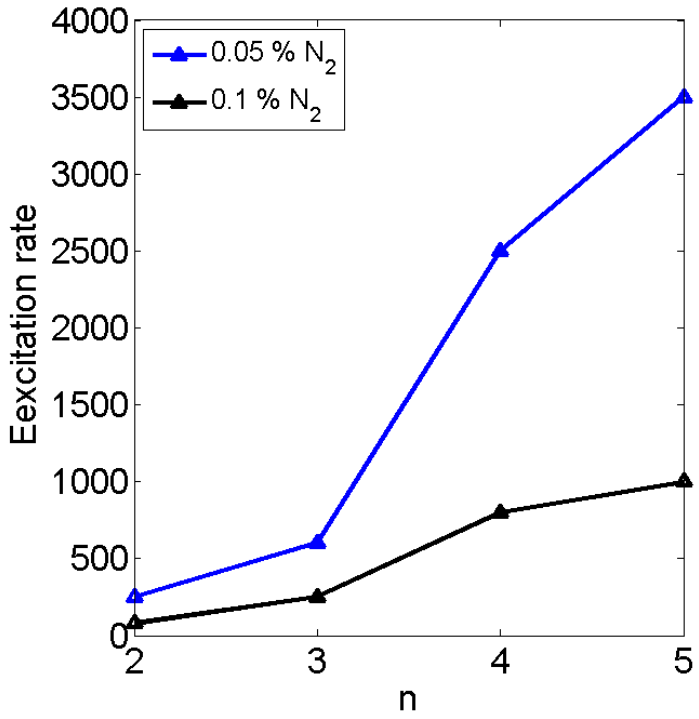

Figure 4.8 Summary of excitation rate as a function of the applied number of harmonics for different N_2 mixtures when applying valleys waveforms.

4.1.2 Electrical asymmetry effect (EAE)

The geometrical asymmetry of a reactor is not the only the factor in the production of asymmetric plasma and therefore forming a DC self-bias, as non-sinusoidal voltage waveforms coupling into geometrical symmetric reactors have been proven as generating DC self-bias electrically and not geometrically. This effect is the so-called electrical asymmetry effect (EAE). Applying non-sinusoidal arbitrary waveforms with different maximum and minimum excursions—namely peaks and valleys waveforms—represent an example of amplitude asymmetry effect (AAE) which is also a possible method to produce asymmetric plasmas. Tailored voltage waveforms coupled in geometrical symmetric μ-APPJ produce a DC self-bias. The DC self-bias voltages resulted from the non-uniformity of sheath voltages at each electrode.

DC self-bias voltages have been measured by applying peaks and valleys waveforms at different admixtures of nitrogen 0 %, 0.05 % and 0.1 %, and the applied peak-to-peak voltages are fixed at 470 V_{pp}, 480 V_{pp} and 490 V_{pp} respectively. The DC bias values, as a function of the number of applied harmonics (n = 1 - 5), are illustrated in figure 4.9.

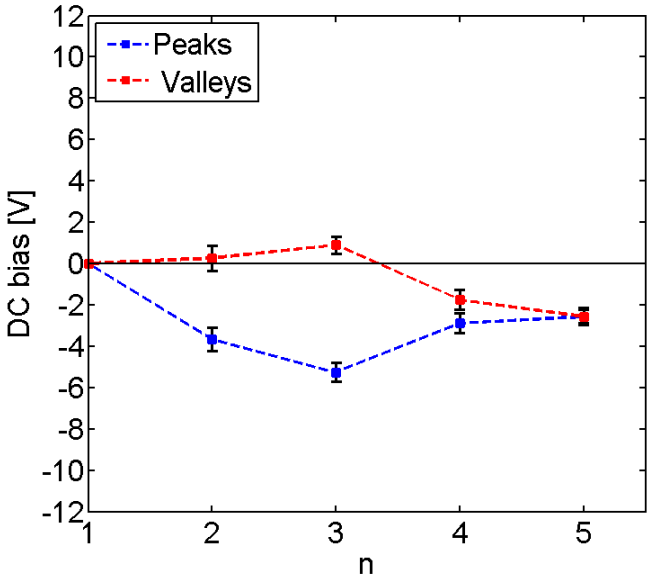

(a)

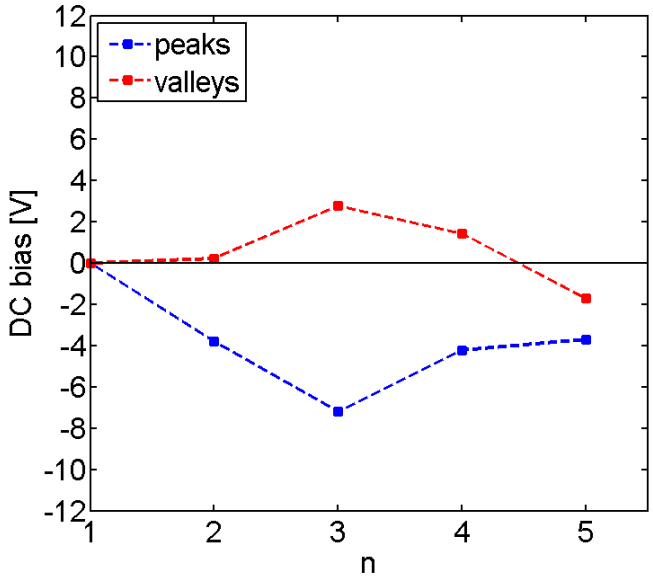

(b)

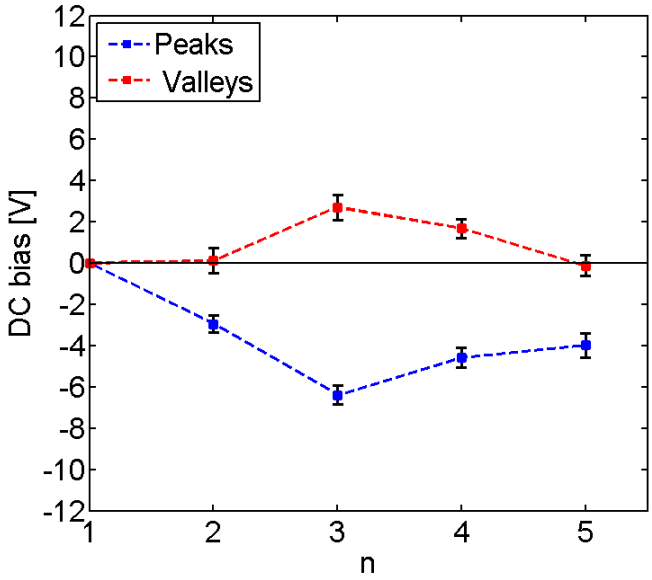

(c)

Figure 4.9: DC self-bias voltages measured as a function of n = 1-5 for peaks waveforms (blue) and valleys waveforms (red) at (a) 470 V_{pp} with 0 % N_2, (b) 480 V_{pp} with 0.05 % N_2 and (c) 490 V_{pp} with 0.1 % N_2. Error bars show the standard error of the DC-bias voltages.

In all images shown in figure 4.9, the numbers of harmonics used are on the x-axis while the y-axis indicates the DC bias voltages. The blue dashed line represents the DC self-bias obtained from applying peaks waveforms, while the red dashed line shows the DC self-bias resulting from the application of valleys waveforms on the plasma. The measured self-bias for the first harmonic has been shifted up by ~ 0.7 V which is originated from the uncertainty of the DC bias probe as well as the non-100 % symmetry of the reactor. The peaks waveforms show relatively negative self-bias while valleys waveforms show positive self-bias voltages. In all of these conditions, it is observed that the DC bias nearly follows the same trend starting with low values at n = 2 and increases to reach a maximum at n = 3 and then decreases at n = 4 down and reaches the minimum value at n = 5. The increment in the DC self-bias with increasing the number of harmonics up to 3 is consistent with studies into applying peaks waveforms on low-pressure plasma operating in argon [65] and hydrogen [98]. However, the decrease in the DC self-bias at higher harmonics follows almost the same trend as investigated in [99]. The measured DC self-bias values are small

compared to that obtained in low-pressure plasma [65, 98]. This is due to the nature of APPs as the DC self-bias is inversely proportional to the pressure: i.e. higher pressure results in lower DC bias voltages [100]. The higher DC bias voltage values are dominated by peaks waveforms although peaks and valleys waveforms both are operated at the same peak-to peak voltages.

4.2 Sawtooth-type Waveforms

Tailored voltage waveforms with the same maximum and minimum excursions but different slopes represent an example of slope asymmetry effect (SAE), which is considered an efficient factor in generating asymmetric plasmas. These types of waveforms are known as sawtooth-type waveforms. The slope of sawtooth up is positive while the sawtooth down slope is negative.

4.2.1 Investigation of Excitation Dynamics

The spatio-temporal electron-impact excitation into Ar ($2p_1$) state at 750.4 nm obtained from phase-resolved optical emission spectroscopy (PROES) for a gas mixture of He with 0.05 % Ar through the application of up sawtooth is illustrated in figure 4.10.

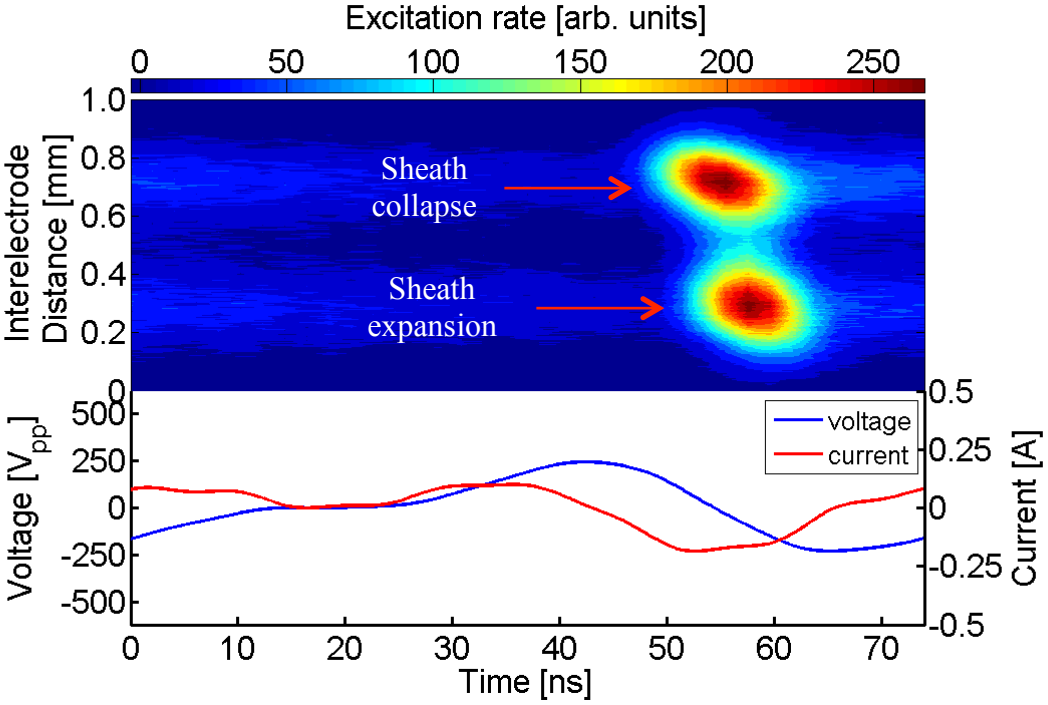
Excitation rate [arb. units]
0
50
100
150
200
250
Interelectrode Distance [mm]
1.0
0.8
0.6
0.4
0.2
0
Sheath collapse
Sheath expansion
Voltage [V_pp]
500
250
0
-250
-500
voltage
current
0.5
0.25
0
-0.25
-0.5
Current [A]
0
10
20
30
40
50
60
70
Time [ns]

n = 2

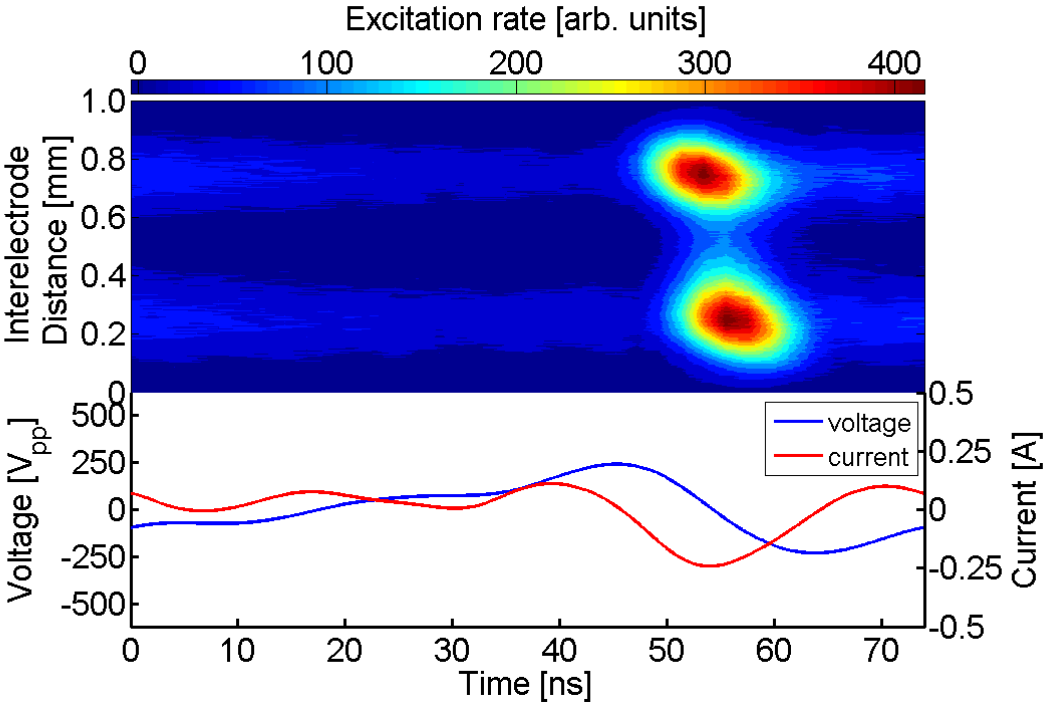
Excitation rate [arb. units]
0
100
200
300
400
Interelectrode Distance [mm]
1.0
0.8
0.6
0.4
0.2
0
Voltage [V_pp]
500
250
0
-250
-500
voltage
current
0.5
0.25
0
-0.25
-0.5
Current [A]
0
10
20
30
40
50
60
70
Time [ns]

n = 3

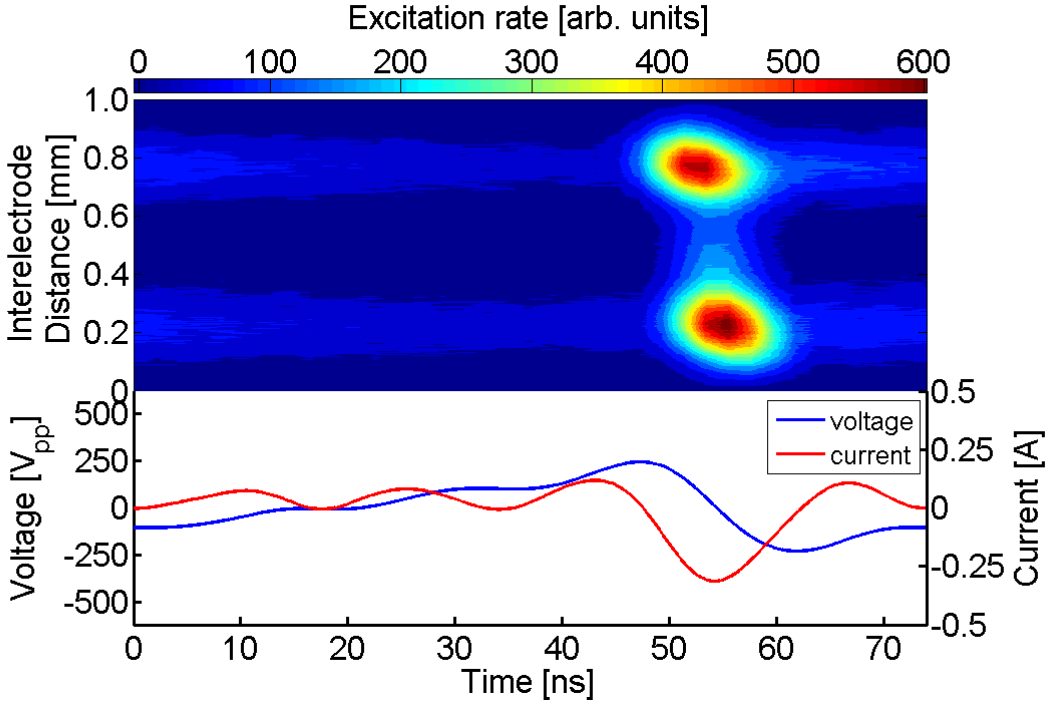

n = 4

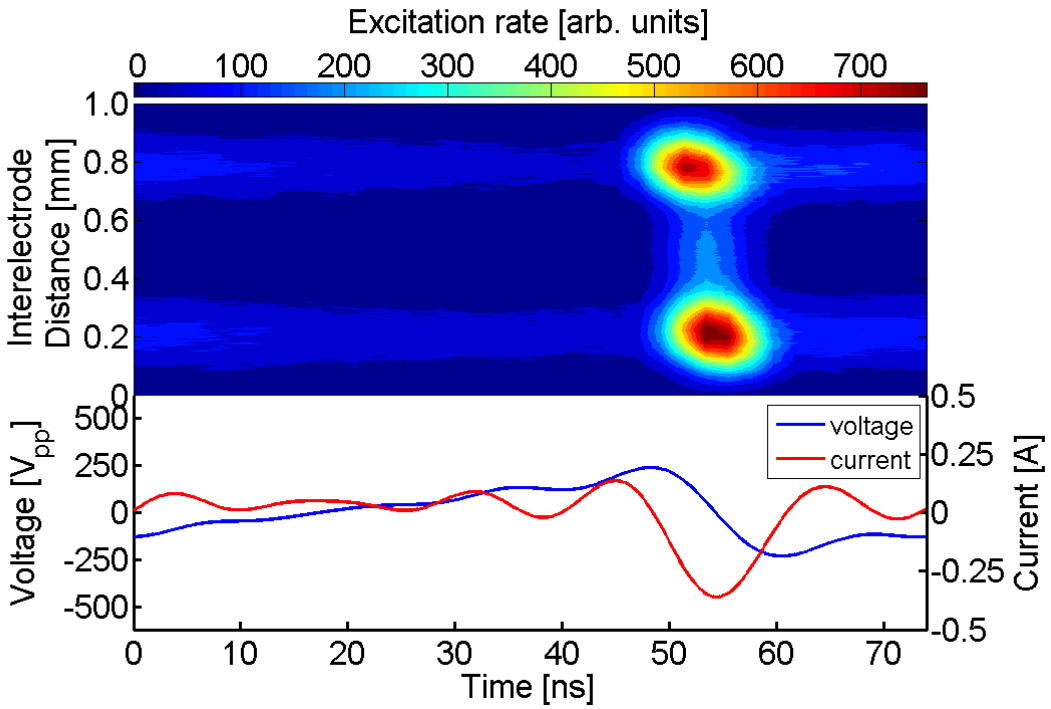

n = 5

Figure 4.10: Spatiotemporal excitation rates obtained from measurement of the emission line at 750.4 nm using PROES and applying sawtooth up waveform with n=2-5 harmonics (the top part of each image) applied on a gas mixture of He with 0.05 % Ar. The peak-to-peak voltage waveform (set at 470 v_{pp}) and the corresponding current waveforms for each harmonic are presented in the lower part of each image.

The image specifications mentioned in section 4.1.1 are repeated for image 4.10. In all cases, there are two excitation peaks: one at the grounded electrode while another excitation peak is located at the powered electrode. These excitation structures represent temporal asymmetry of electron heating. The rapid increase in the voltage at time between ~ 50 to ~ 65 ns induces a fast sheath expansion at the grounded electrode where electrons are accelerated away from the electrode toward the plasma bulk; therefore, an excitation peak is initiated close to the grounded electrode. Almost at the same time, another excitation peak located at the powered electrode occurs through the intensive sheath collapse, which results from the rapid decrease in the voltage at the powered electrode. Electron heating structures are spatially focused at the powered and grounded electrodes, which indicate higher electron density and this in turn, leads to reducing the production of the electric field.

The amplitude of all of the excitation peaks mentioned above is correlated with the density of conduction current that represents the electron flux. The peak-to-peak current increases by increasing the number of harmonics; therefore, the excitation maximum increases. There are structures spread along side each electrode and connected to the excitation peaks, and these structures might be explained as continuous excitation occurs from the small peaks in the applied voltage waveforms.

The spatio-temporal electron impact excitation is measured by applying sawtooth-types with adding different amounts of nitrogen, considered a significant factor for pinning ionization. Each set of gas mixture is driven by a fixed peak-to-peak voltage with consecutive harmonic numbers from two to five harmonics. The nitrogen mixtures used are 0.05 %, 0.1 %, 0.2 %, 0.3 % and 0.5 %, and they are driven by 480 V_{pp} and 540 V_{pp}, 570 $V_{pp,}$ 580 V_{pp} and 615 V_{pp} respectively. The space and phase excitation by applying sawtooth-up waveforms on APPs for each set of nitrogen

admixture is shown in figures 4.11, 4.12, 4.13, 4.14 and 4.15 respectively. The excitation dynamics in all conditions are exactly the same as described in the case of the gas mixture of helium with argon and without nitrogen. The excitation peaks at the grounded electrode occur as a result of sheath expansion during the increase of the voltage. On the other hand, during the sheath collapse, another excitation structure is produced at the powered electrode.

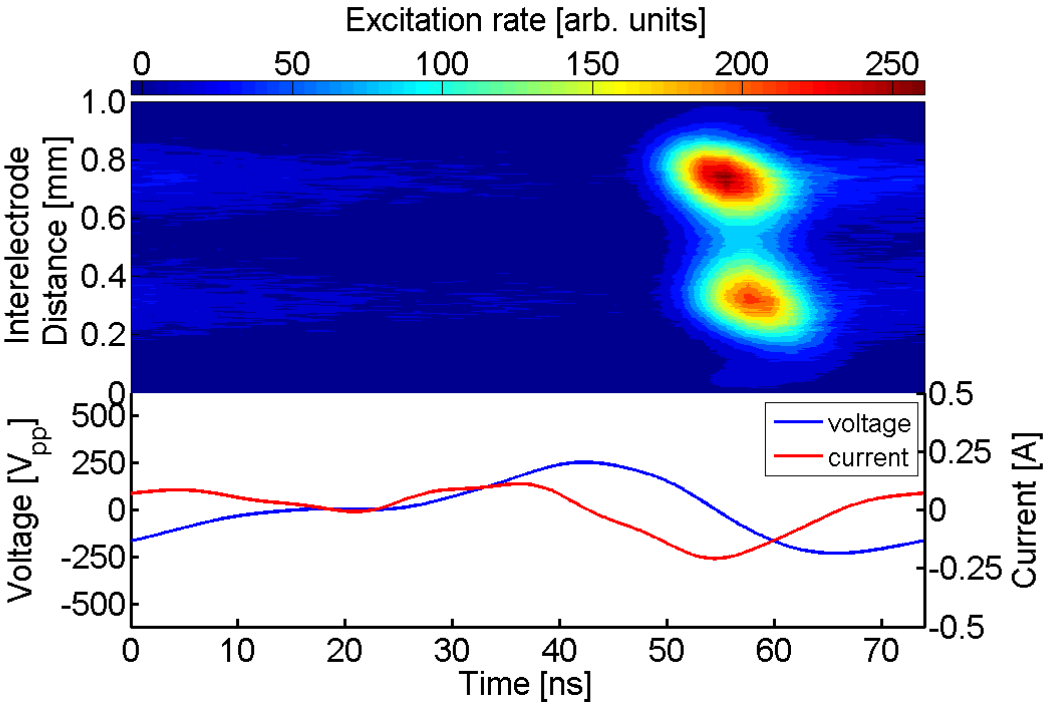

n = 2

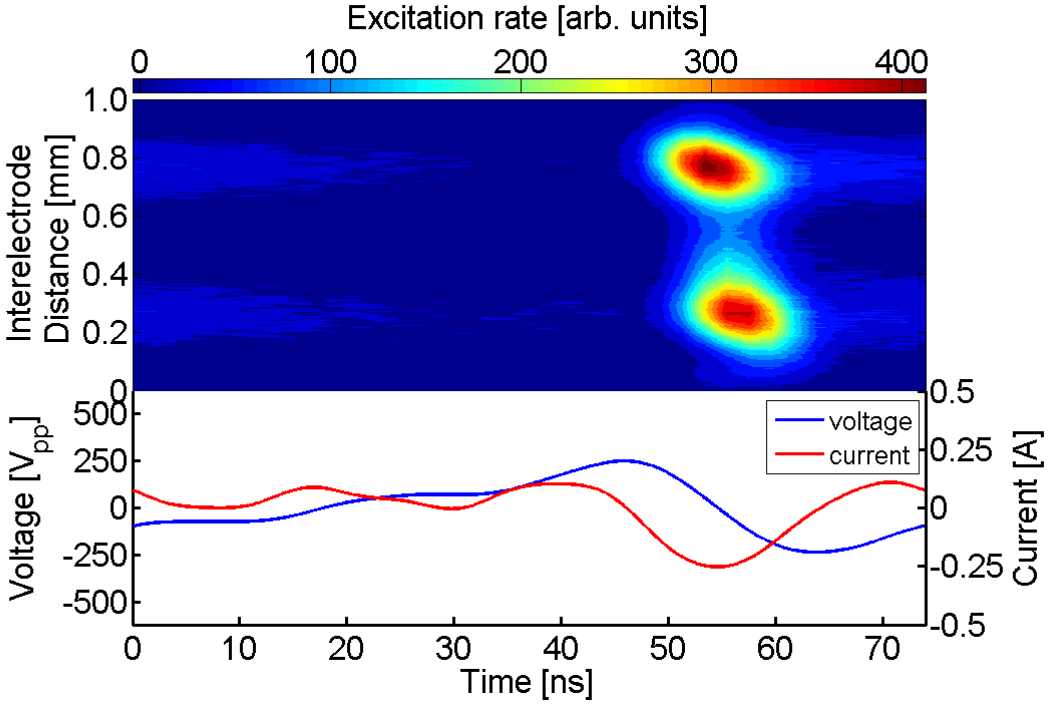
Excitation rate [arb. units]
0
100
200
300
400
Interelectrode Distance [mm]
1.0
0.8
0.6
0.4
0.2
0
Voltage [Vpp]
500
250
0
-250
-500
Current [A]
0.5
0.25
0
-0.25
-0.5
voltage
current
0
10
20
30
40
50
60
70
Time [ns]

n = 3

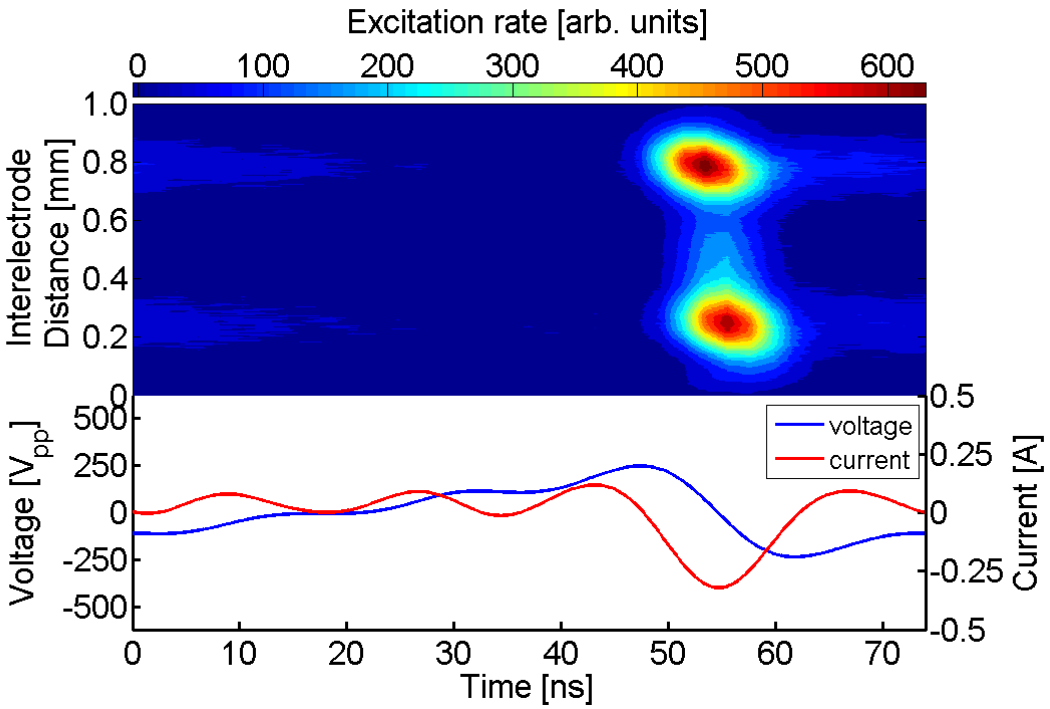
Excitation rate [arb. units]
0
100
200
300
400
500
600
Interelectrode Distance [mm]
1.0
0.8
0.6
0.4
0.2
0
Voltage [Vpp]
500
250
0
-250
-500
Current [A]
0.5
0.25
0
-0.25
-0.5
voltage
current
0
10
20
30
40
50
60
70
Time [ns]

n = 4

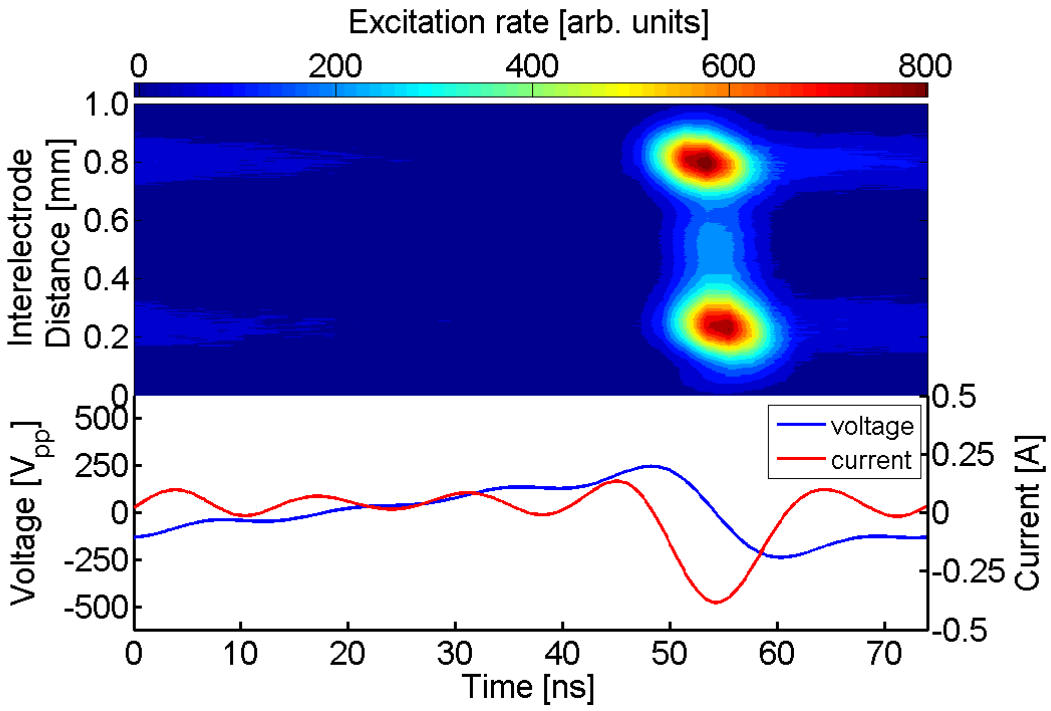

n = 5

Figure 4.11 Spatiotemporal excitation rates obtained from measurement of the emission line at 750.4 nm using PROES and applying sawtooth-up waveform with n=2-5 harmonics (the top part of each image) applied on a gas mixture of He with 0.05 % Ar and 0.05 % N_2. The peak-to-peak voltage waveform (set at 480 V_{pp}) and the corresponding current waveforms for each harmonic are presented in the lower part of each image.

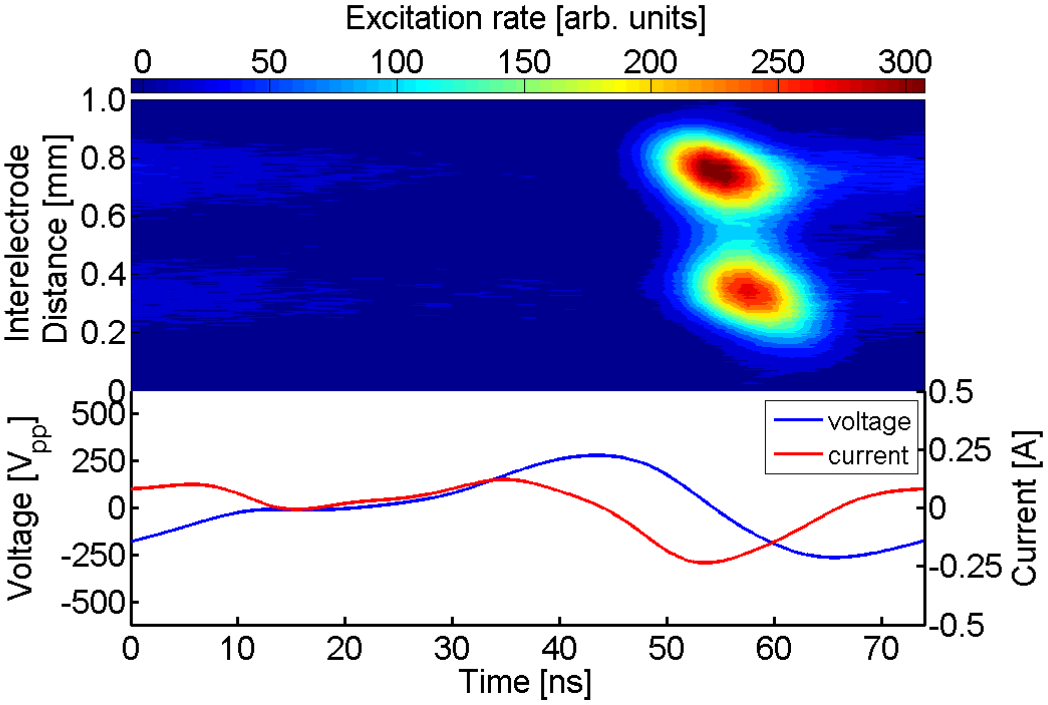
Excitation rate [arb. units]
0
50
100
150
200
250
300
Interelectrode Distance [mm]
1.0
0.8
0.6
0.4
0.2
0
Voltage [V_{pp}]
500
250
0
-250
-500
voltage
current
0.5
0.25
0
-0.25
-0.5
Current [A]
0
10
20
30
40
50
60
70
Time [ns]

n = 2

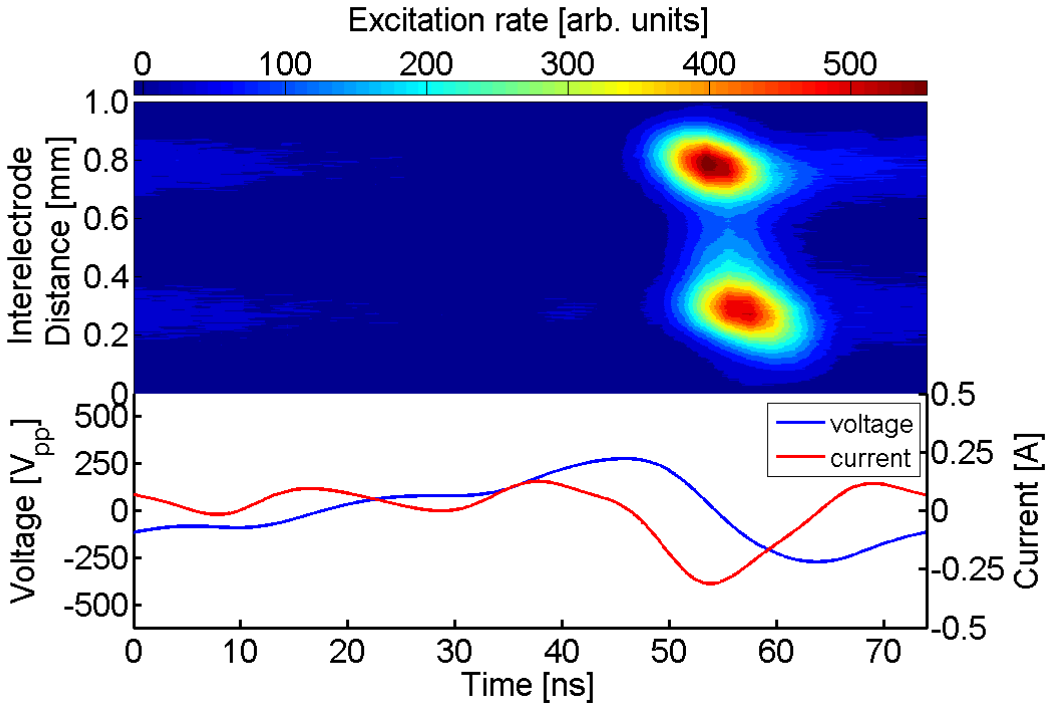
Excitation rate [arb. units]
0
100
200
300
400
500
Interelectrode Distance [mm]
1.0
0.8
0.6
0.4
0.2
0
Voltage [V_{pp}]
500
250
0
-250
-500
voltage
current
0.5
0.25
0
-0.25
-0.5
Current [A]
0
10
20
30
40
50
60
70
Time [ns]

n = 3

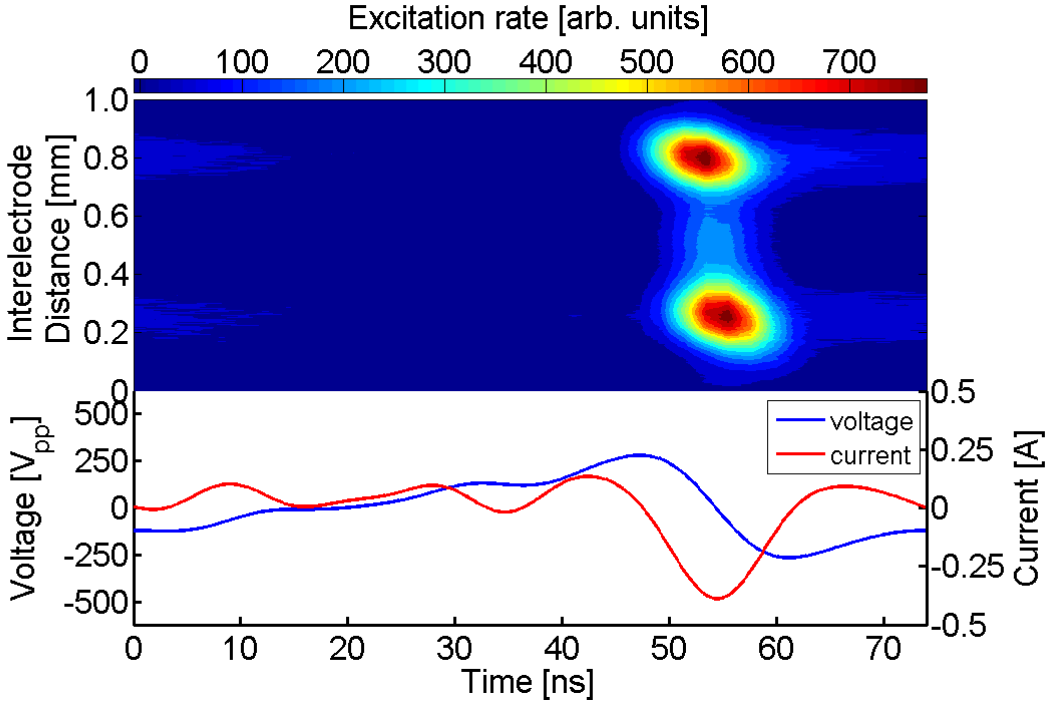

n = 4

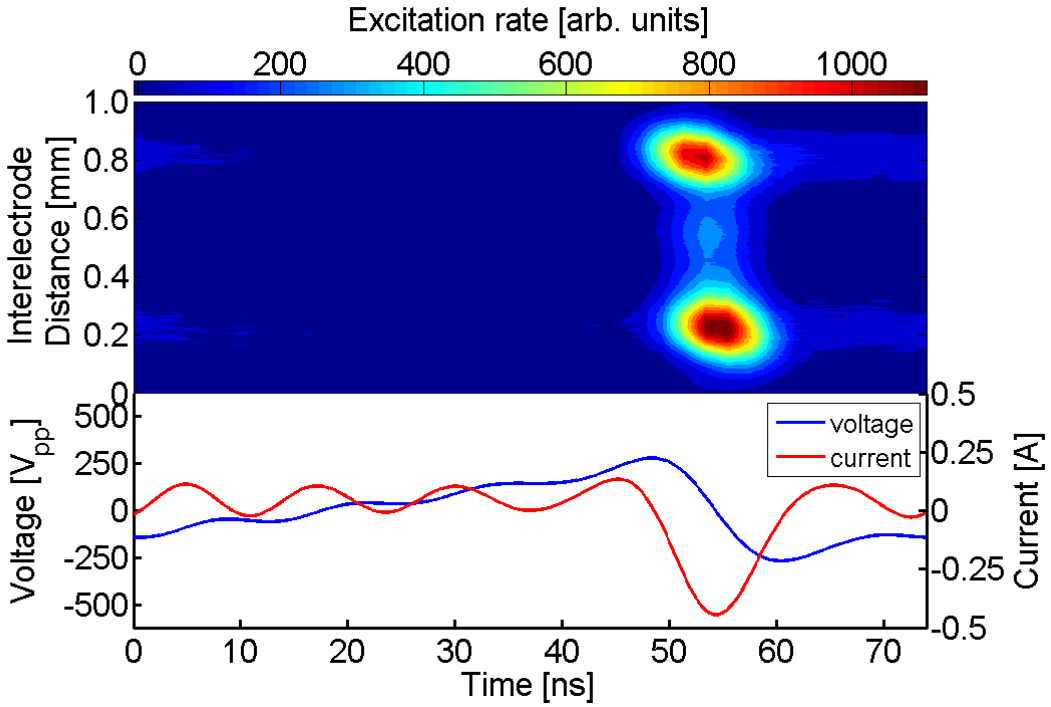

n = 5

Figure 4.12 Spatiotemporal excitation rates obtained from measurement of the emission line at 750.4 nm using PROES and applying sawtooth-up waveform with n=2-5 harmonics (the top part of each image) applied on a gas mixture of He with 0.05 % Ar and 0.1 % N_2. The peak-to-peak voltage waveform (set at 540 V_{pp}) and the corresponding current waveforms for each harmonic are presented in the lower part of each image.

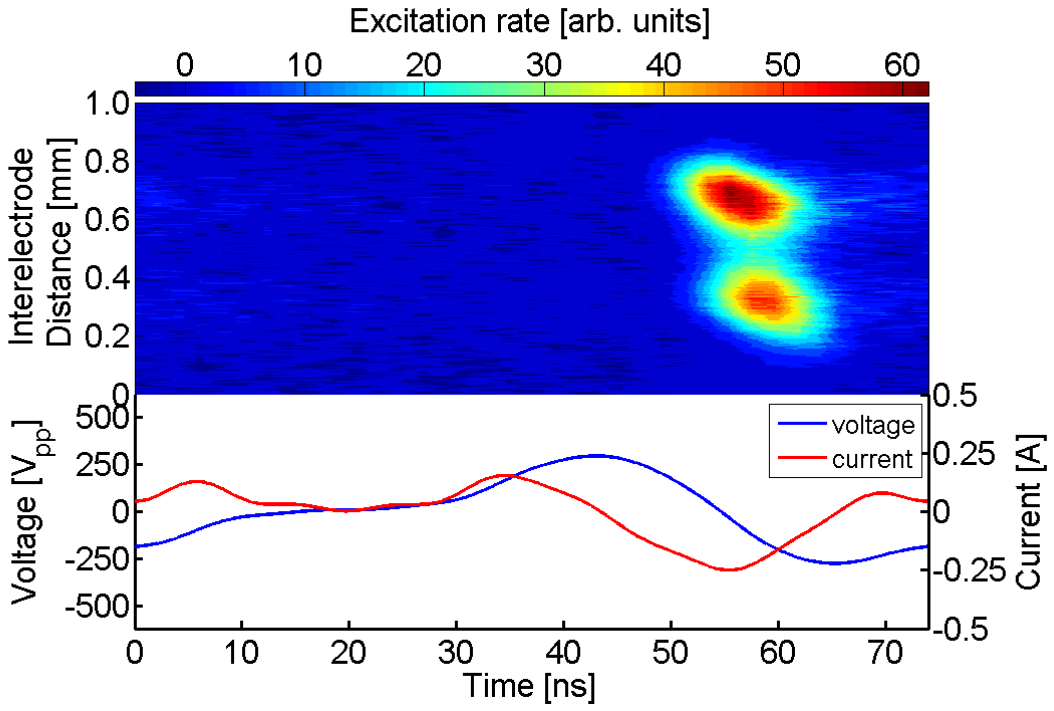
Excitation rate [arb. units]
0
10
20
30
40
50
60
Interelectrode Distance [mm]
1.0
0.8
0.6
0.4
0.2
0
Voltage [Vpp]
500
250
0
-250
-500
Current [A]
0.5
0.25
0
-0.25
-0.5
voltage
current
0
10
20
30
40
50
60
70
Time [ns]

n = 2

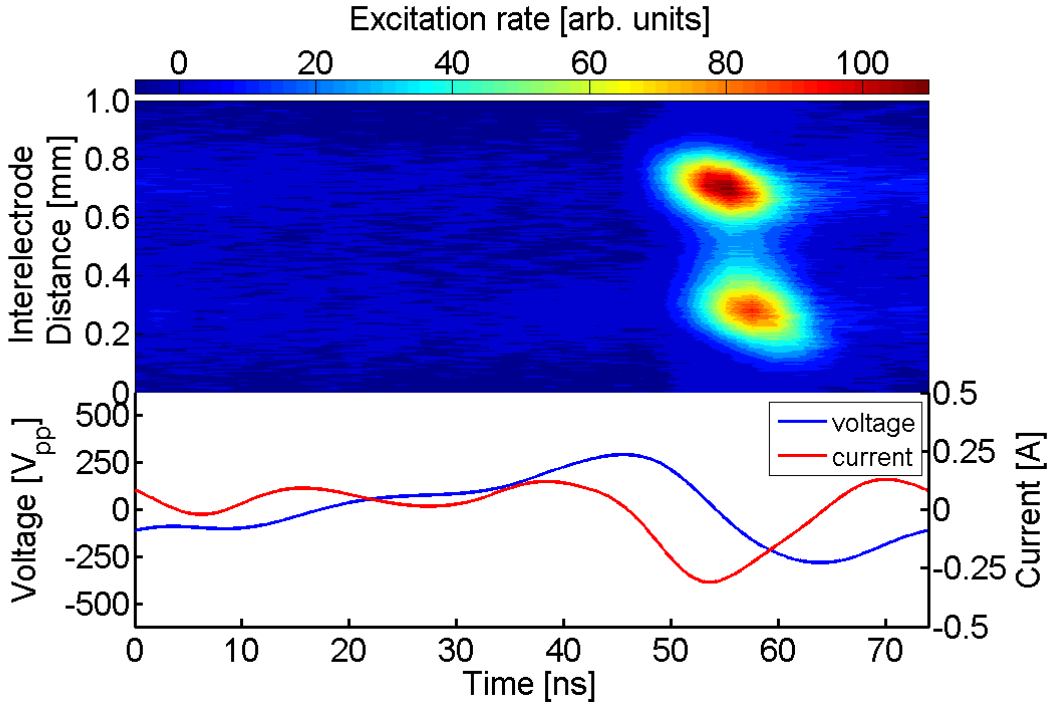
Excitation rate [arb. units]
0
20
40
60
80
100
Interelectrode Distance [mm]
1.0
0.8
0.6
0.4
0.2
0
Voltage [Vpp]
500
250
0
-250
-500
Current [A]
0.5
0.25
0
-0.25
-0.5
voltage
current
0
10
20
30
40
50
60
70
Time [ns]

n = 3

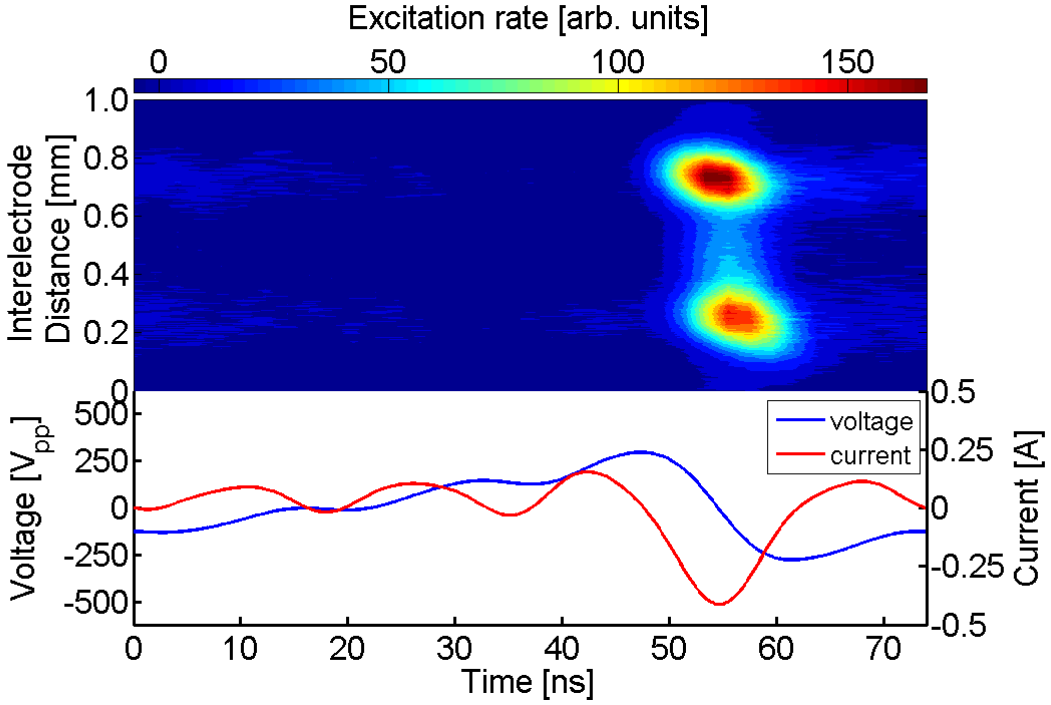

n = 4

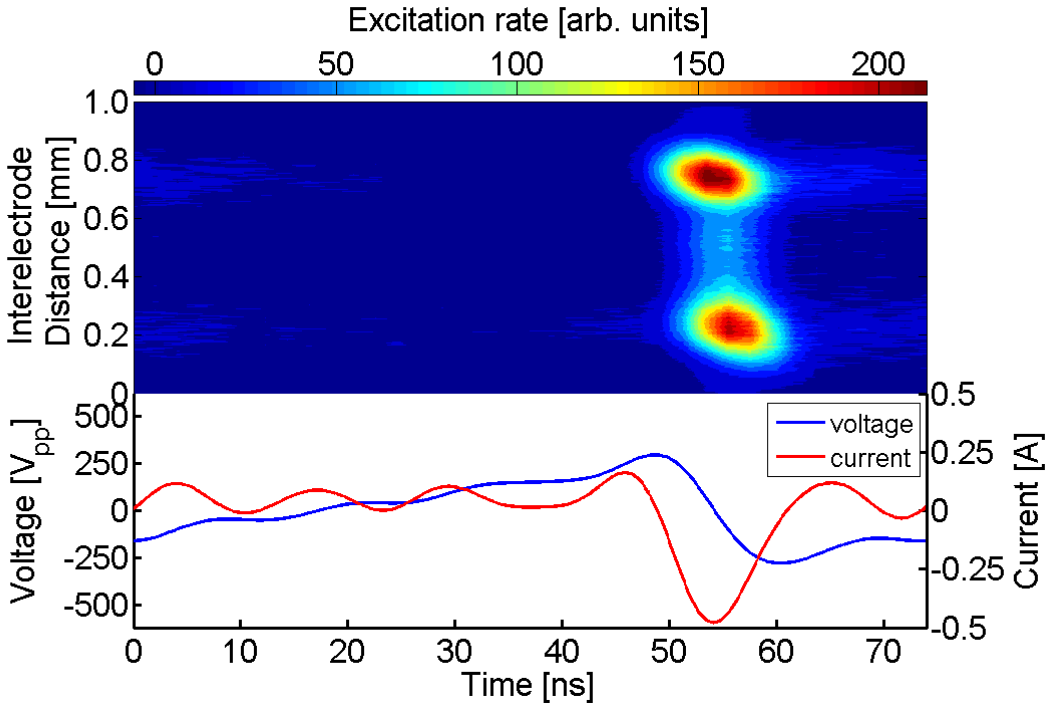

n = 5

Figure 4.13 Spatiotemporal excitation rates obtained from measurement of the emission line at 750.4 nm using PROES and applying sawtooth-up waveform with n=2-5 harmonics (the top part of each image) applied on a gas mixture of He with 0.05 % Ar and 0.2 % N_2. The peak-to-peak voltage waveform (set at 570 V_{pp}) and the corresponding current waveforms for each harmonic are presented in the lower part of each image.

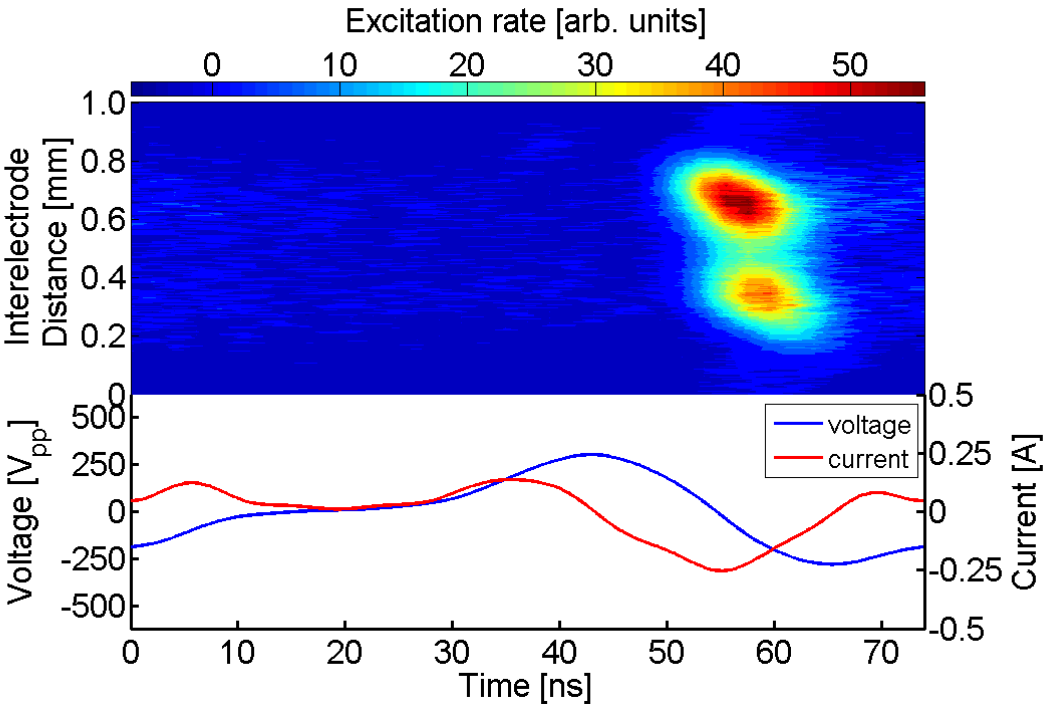
Excitation rate [arb. units]
0
10
20
30
40
50
Interelectrode Distance [mm]
1.0
0.8
0.6
0.4
0.2
0
Voltage [Vpp]
500
250
0
-250
-500
Current [A]
0.5
0.25
0
-0.25
-0.5
voltage
current
0
10
20
30
40
50
60
70
Time [ns]

n =2

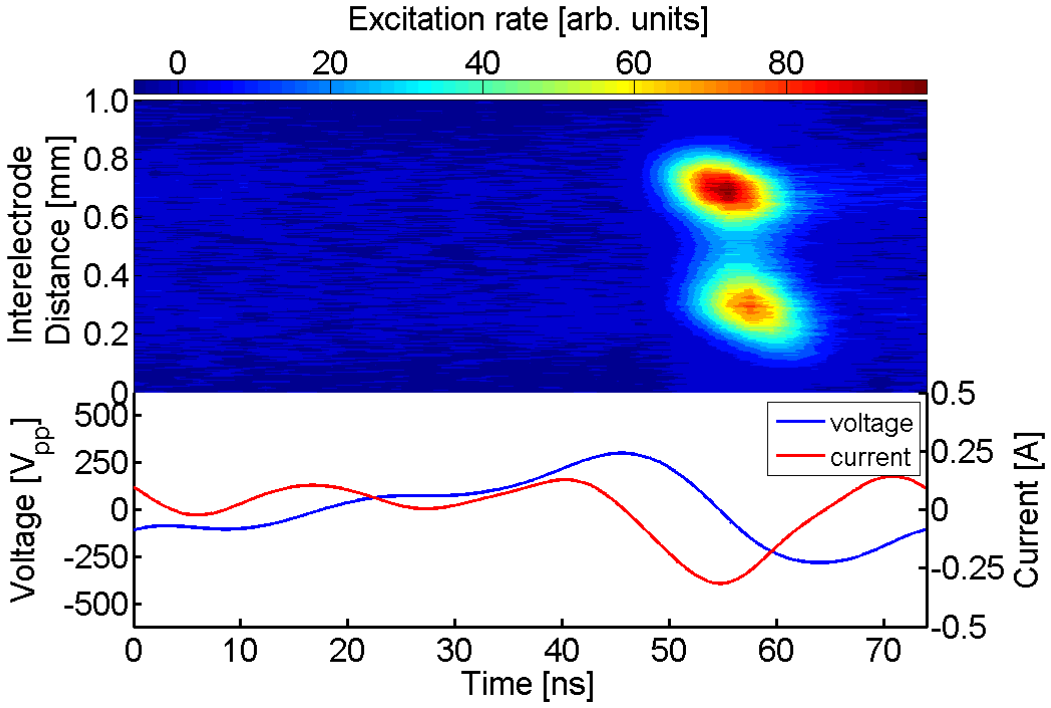
Excitation rate [arb. units]
0
20
40
60
80
Interelectrode Distance [mm]
1.0
0.8
0.6
0.4
0.2
0
Voltage [Vpp]
500
250
0
-250
-500
Current [A]
0.5
0.25
0
-0.25
-0.5
voltage
current
0
10
20
30
40
50
60
70
Time [ns]

n = 3

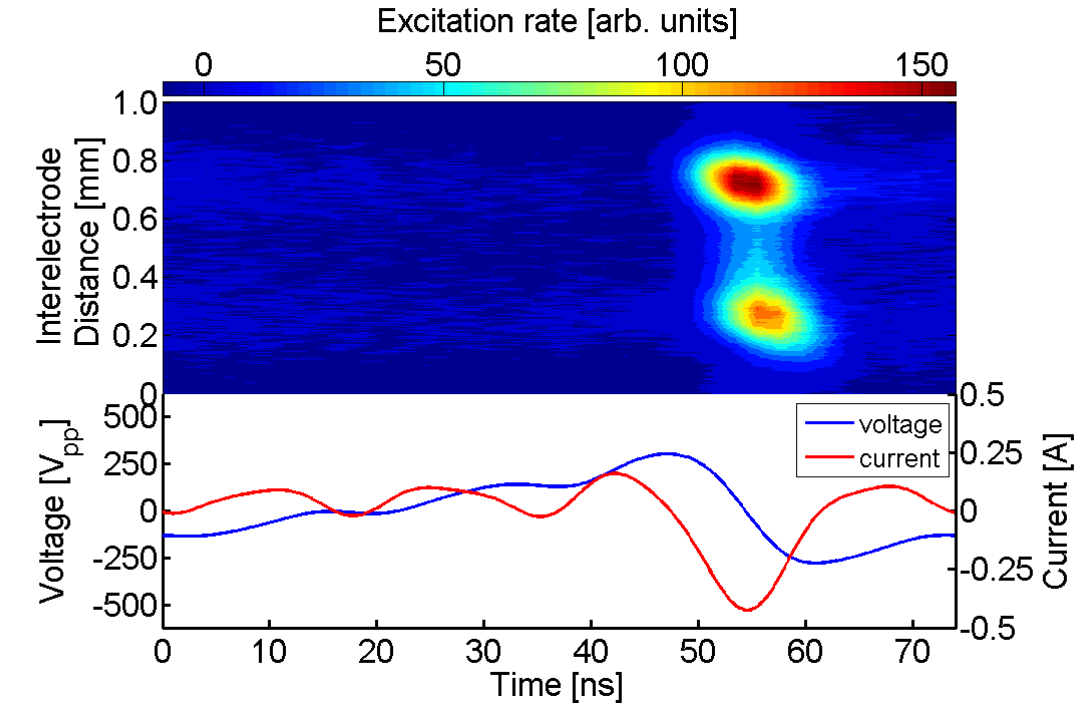

n = 4

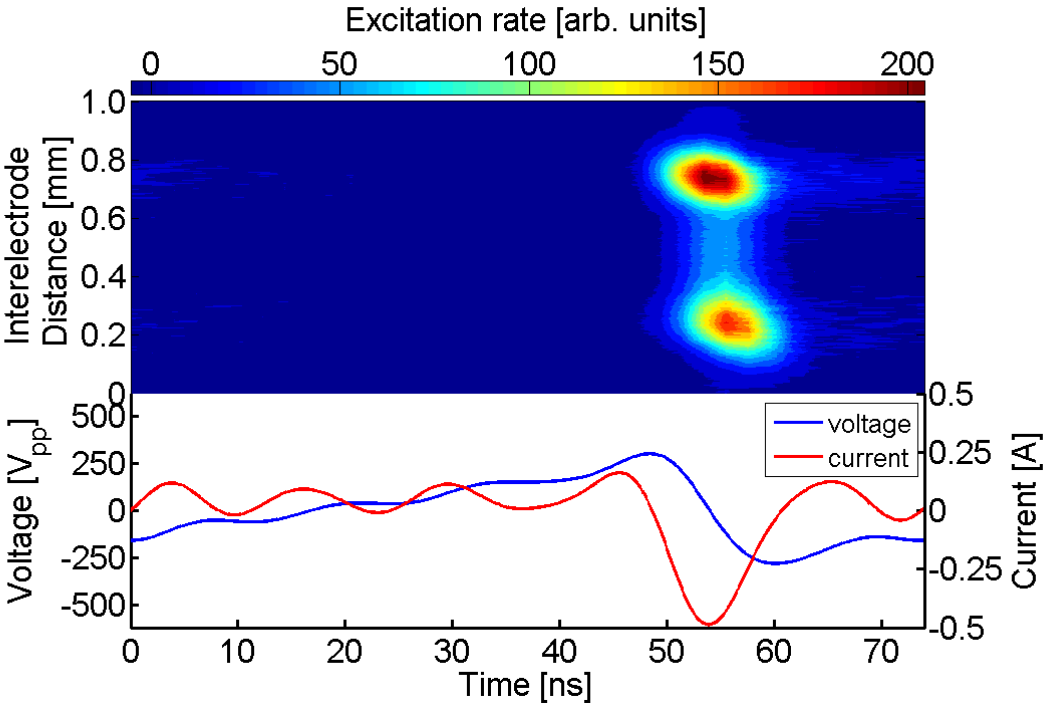

n = 5

Figure 4.14 Spatiotemporal excitation rates obtained from measurement of the emission line at 750.4 nm using PROES and applying sawtooth-up waveform with n=2-5 harmonics (the top part of each image) applied on a gas mixture of He with 0.05 % Ar and 0.3 % N_2. The peak-to-peak voltage waveform (set at 580 V_{pp}) and the corresponding current waveforms for each harmonic are presented in the lower part of each image.

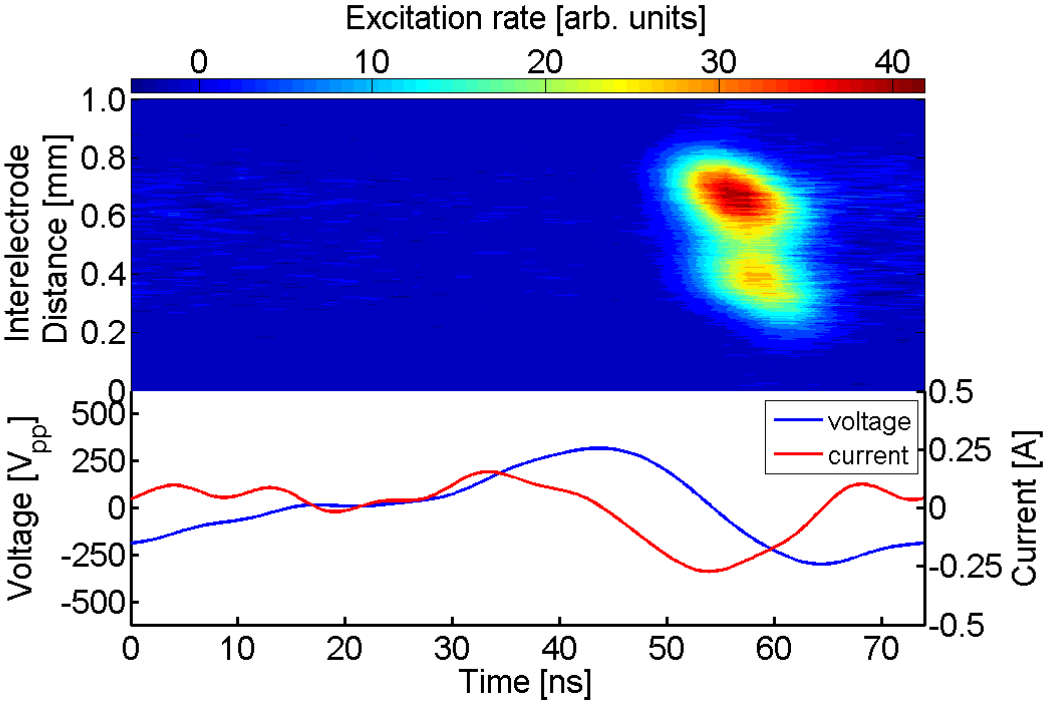
Excitation rate [arb. units]
0
10
20
30
40
Interelectrode Distance [mm]
1.0
0.8
0.6
0.4
0.2
0
Voltage [V_{pp}]
500
250
0
-250
-500
voltage
current
Current [A]
0.5
0.25
0
-0.25
-0.5
0
10
20
30
40
50
60
70
Time [ns]

n = 2

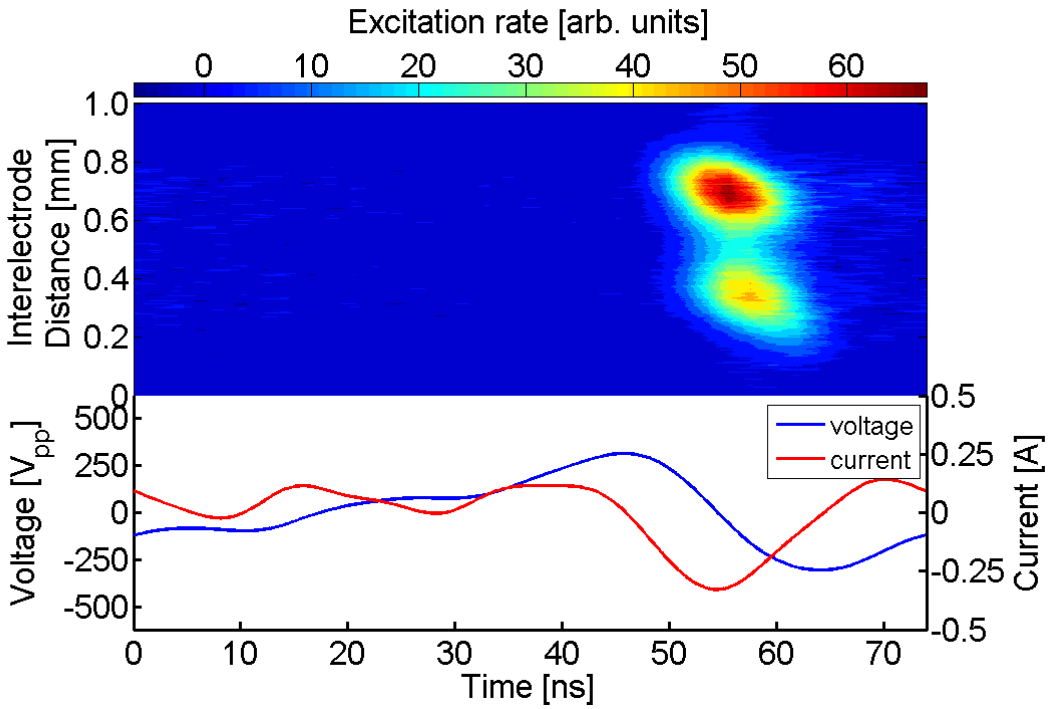
Excitation rate [arb. units]
0
10
20
30
40
50
60
Interelectrode Distance [mm]
1.0
0.8
0.6
0.4
0.2
0
Voltage [V_{pp}]
500
250
0
-250
-500
voltage
current
Current [A]
0.5
0.25
0
-0.25
-0.5
0
10
20
30
40
50
60
70
Time [ns]

n = 3

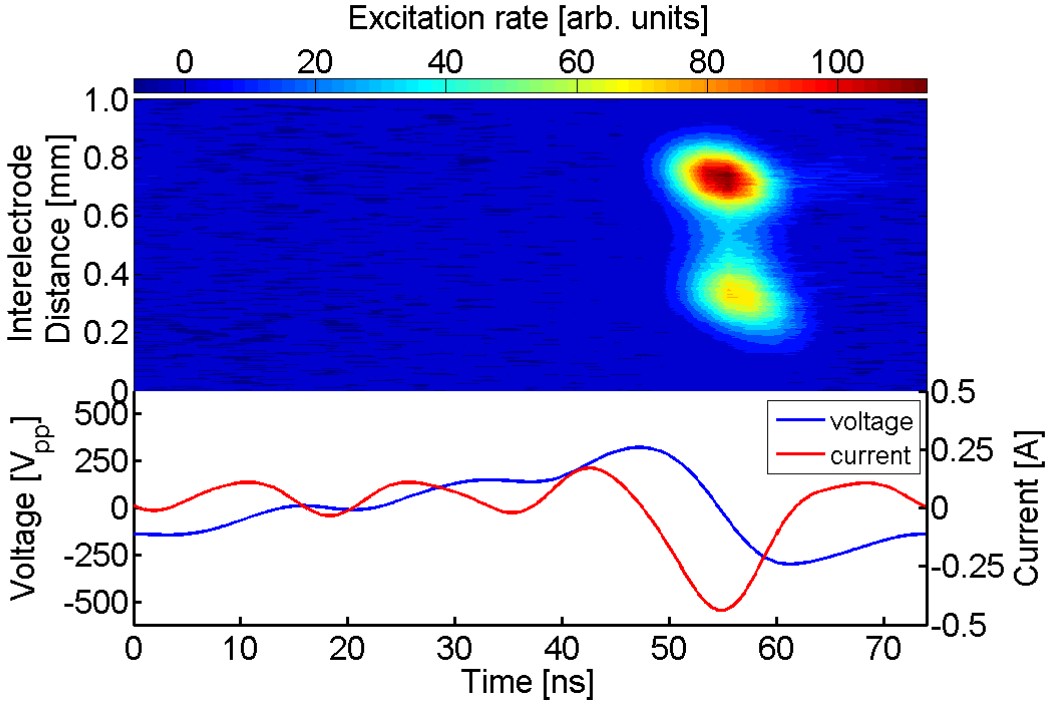

n = 4

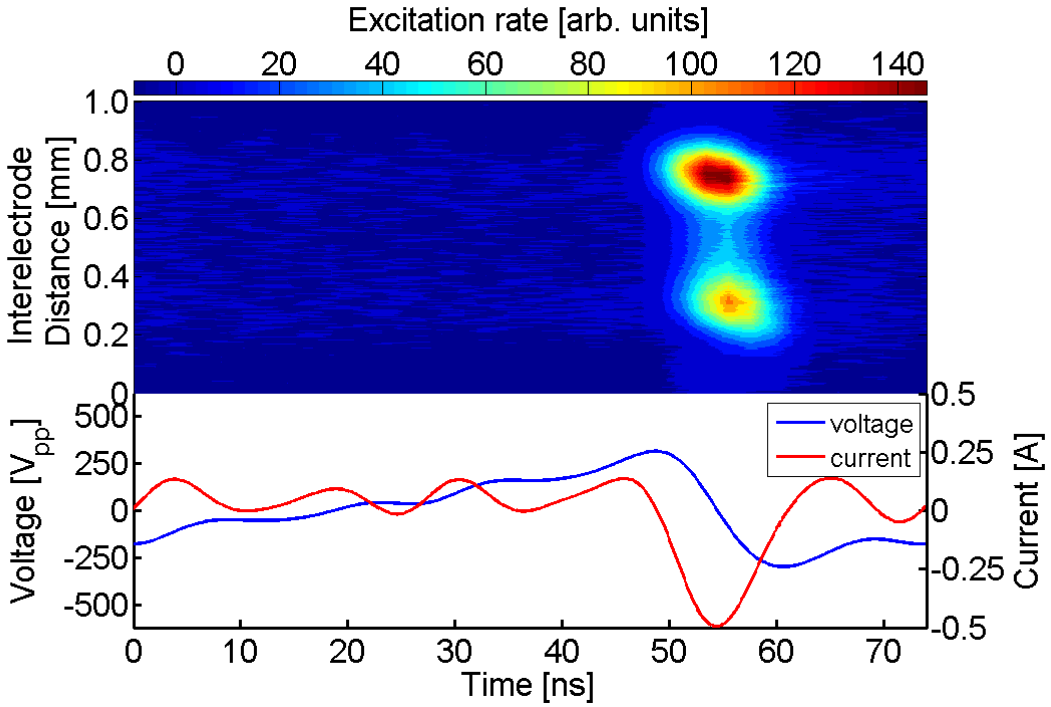

n = 5

Figure 4.15: Spatiotemporal excitation rates obtained from measurement of the emission line at 750.4 nm using PROES and applying sawtooth-up waveform with n=2-5 harmonics (the top part of each image) applied on a gas mixture of He with 0.05 % Ar and 0.5 % N_2. The peak-to-peak voltage waveform (set at 615 V_{pp}) and the corresponding current waveforms for each harmonic are presented in the lower part of each image.

The excitation structures tend to propagate toward plasma bulk when more nitrogen admixtures are added and the distance between the excitation peaks at the electrodes is reduced. The thickness of the plasma sheath depends on the plasma density; therefore, as the sheath thickness increased, the plasma density is decreased.

Increasing the nitrogen admixture affects the plasma dynamics. First, the excitation rate decreases with increasing the nitrogen admixture, and this might be due to the excited state becoming quenched by the nitrogen. It is also beneficial to mention that the excitation rate depends on the electron density as expressed in equation 2.6 in chapter 2. However, in the case of using 0.1% of N_2, the excitation rate is greater than that when using 0.05 % of N_2. This coincides with the results from [101]. These results are summarised in figure 4.16. It shows the relation between the excitation rates with the number of harmonics used at different N_2 admixtures.

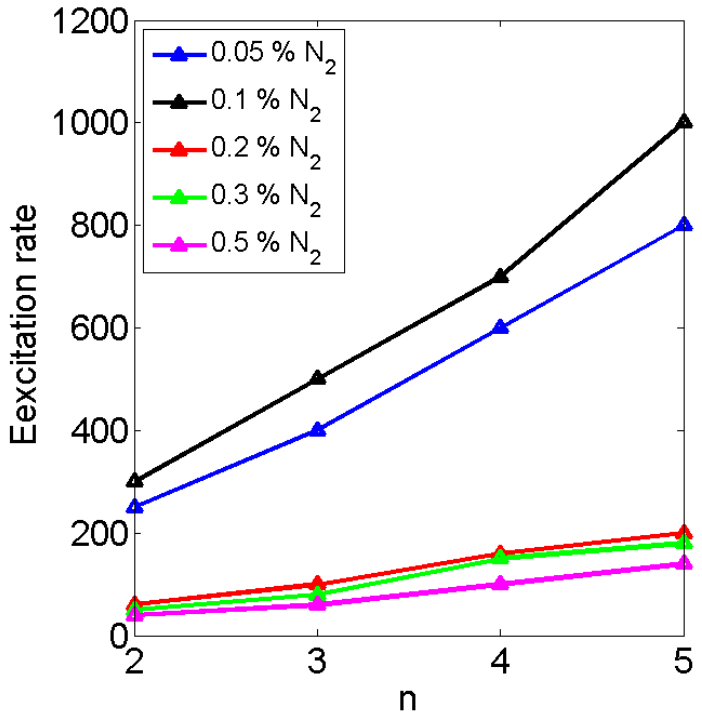

Figure 4.16 Summary of excitation rates as a function of the applied harmonics numbers 2-5 for when sawtooth-up waveforms applied on the plasma with different percentages of N_2 admixtures.

In all N_2 admixture sets, the denser excitation structures are located at the powered electrode. This is summarised and illustrated in figure 4.17. The intensities of emission ration are plotted as a function of the different amounts of N_2 for all used harmonics.

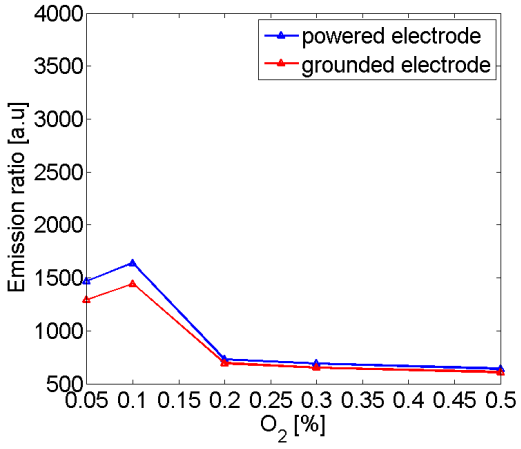

n = 2

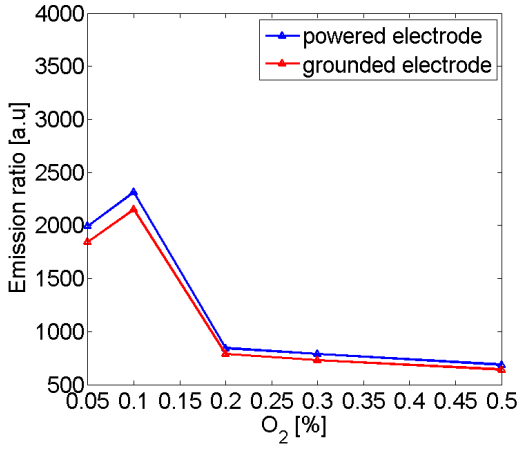

n = 3

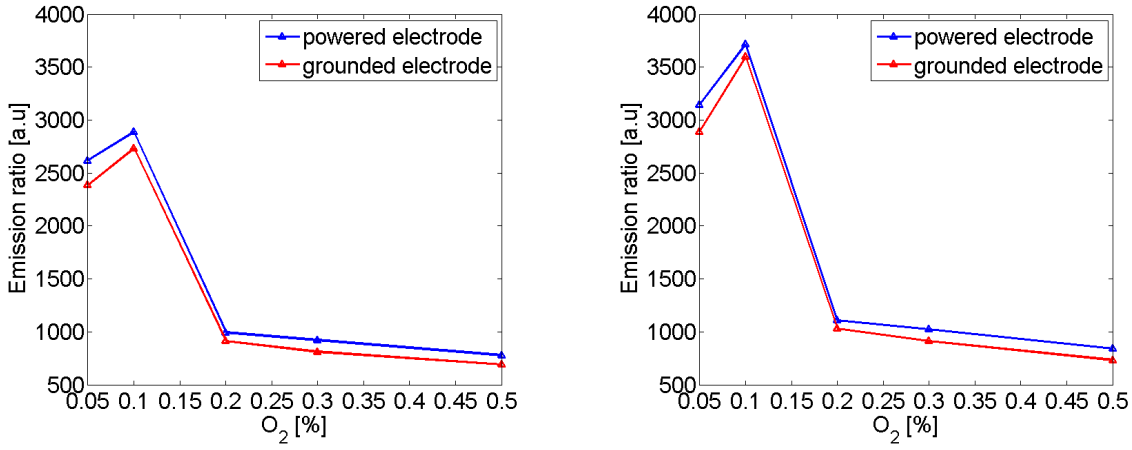

Figure 4.17 The emission ratio of the dense excitation structures as a function of N_2 admixture for the used harmonics in the application of sawtooth-up waveforms.

In the case of applying sawtooth-down waveforms, the spatio-temporal electron impact excitation with voltage of 470 V_{pp} on a gas admixture of helium with 0.05 % of argon is shown in figure 4.18. Here, the image specifications are the same as explained above in the case of sawtooth-up waveform. The plasma behaves similarly as that in sawtooth-up waveforms.

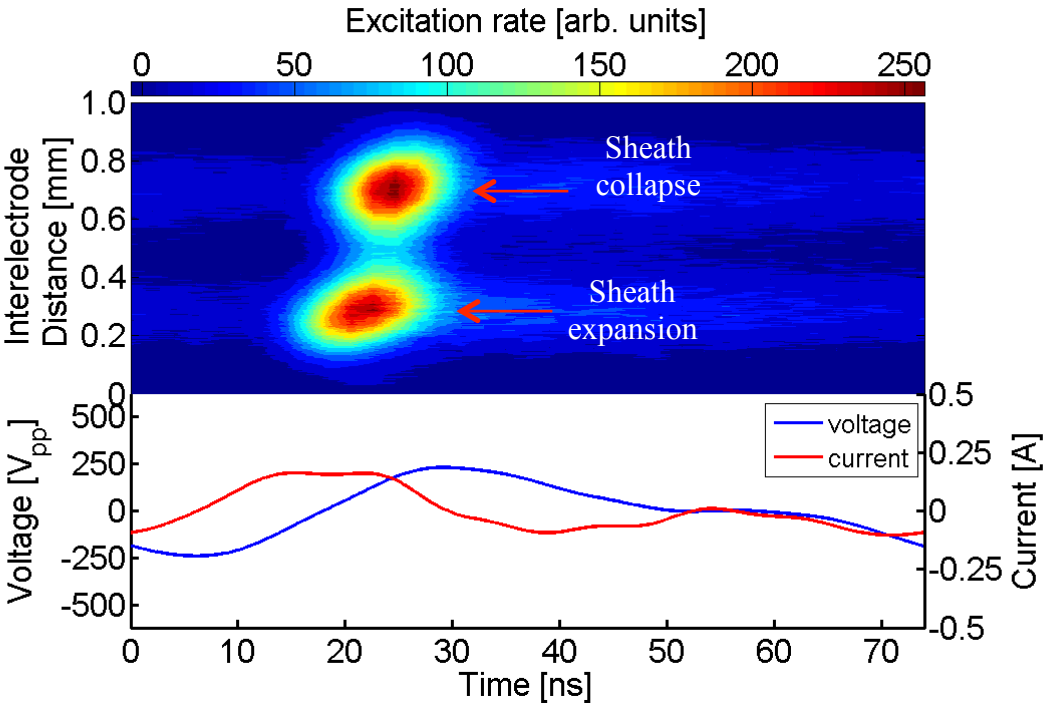
Excitation rate [arb. units]
0
50
100
150
200
250
Interelectrode Distance [mm]
1.0
0.8
0.6
0.4
0.2
0
Sheath collapse
Sheath expansion
Voltage [V_pp]
500
250
0
-250
-500
voltage
current
0.5
0.25
0
-0.25
-0.5
Current [A]
0
10
20
30
40
50
60
70
Time [ns]

n = 2

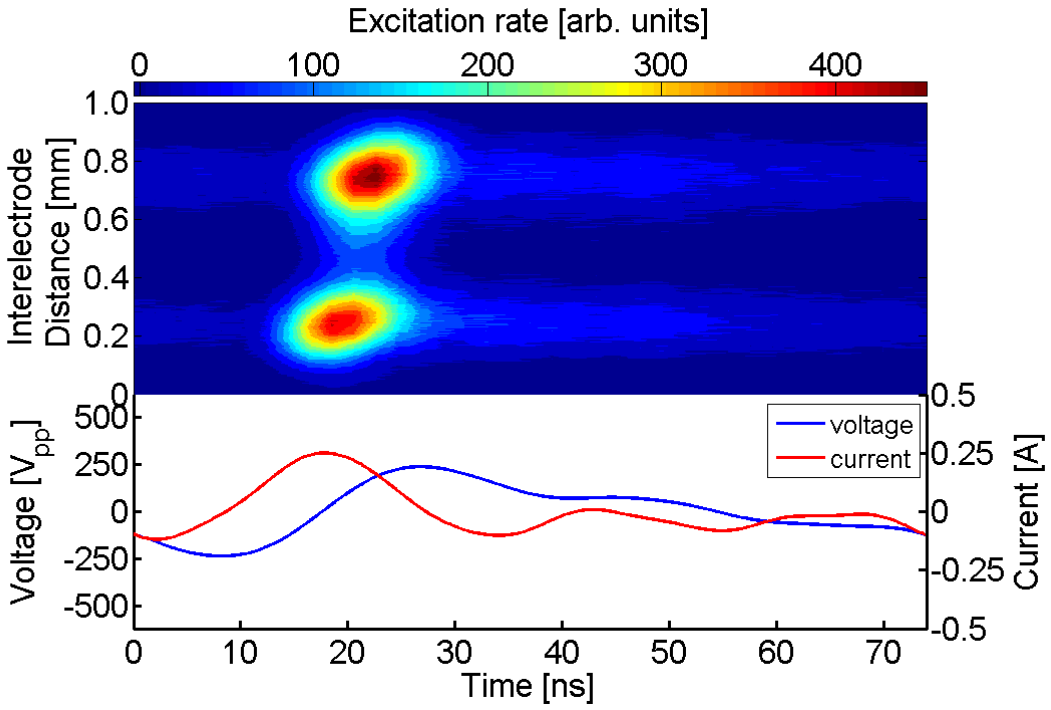
Excitation rate [arb. units]
0
100
200
300
400
Interelectrode Distance [mm]
1.0
0.8
0.6
0.4
0.2
0
Voltage [V_pp]
500
250
0
-250
-500
voltage
current
0.5
0.25
0
-0.25
-0.5
Current [A]
0
10
20
30
40
50
60
70
Time [ns]

n = 3

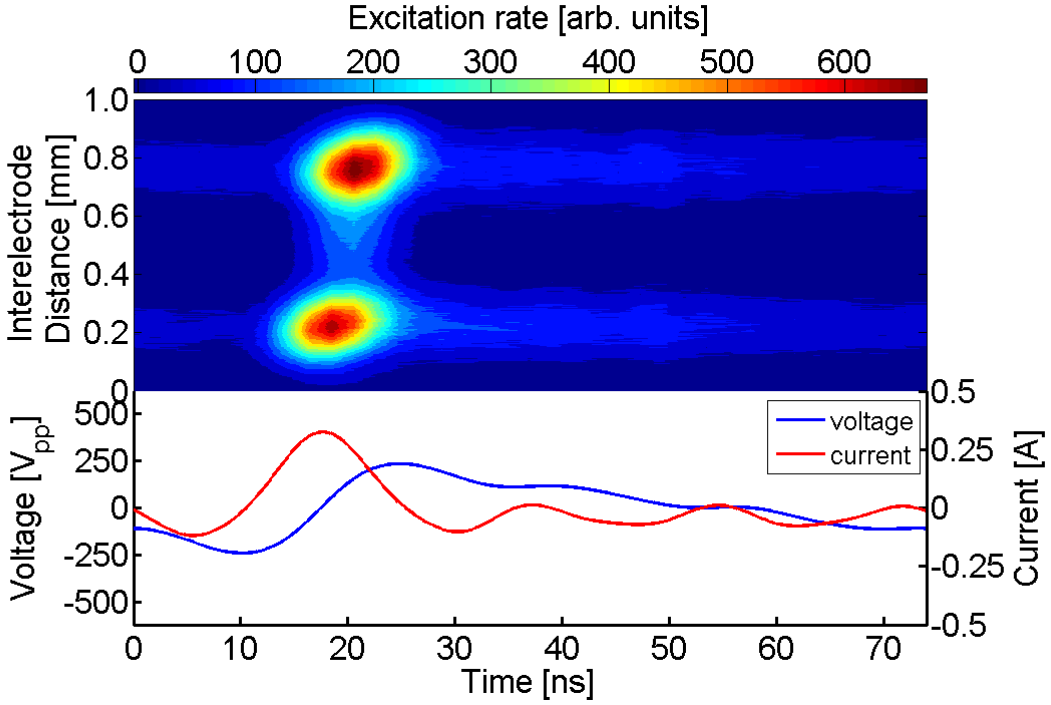

n = 4

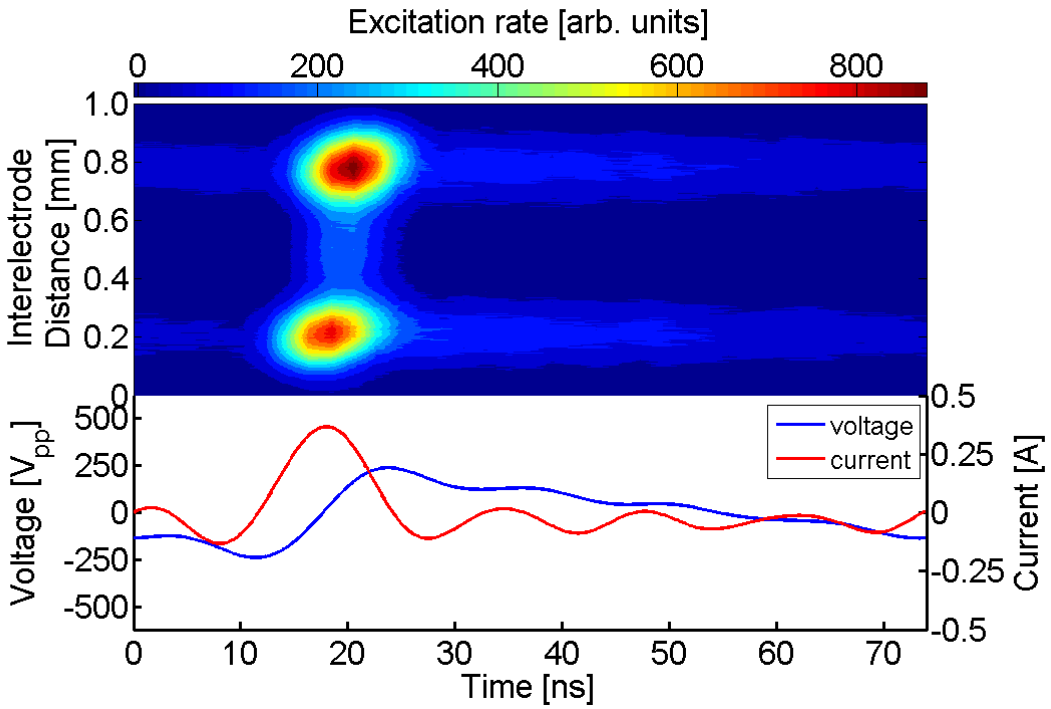

n = 5

Figure 4.18: Spatiotemporal excitation rates obtained from measurement of the emission line at 750.4 nm using PROES and applying sawtooth-down waveform with n=2-5 harmonics (the top part of each image) applied on a gas mixture of He with 0.05 % Ar. The peak-to-peak voltage waveform (set at 470 V_{pp}) and the corresponding current waveforms for each harmonic are presented in the lower part of each image.

It is also observed that there is two excitation structures in each image in figure 4.18: one at the grounded electrode while the second one is located at the powered electrode. The first excitation structure at the grounded electrode at time between ~ 10 ns to ~ 25 ns occurs due to the fast sheath expansion when the voltage rises and the electrons are accelerated into the plasma bulk producing strong impact excitation. This action is followed by a rapid decrease in the voltage during sheath collapse; therefore, the second excitation peak is initiated at the powered electrode. The influence of increasing the number of harmonics, observed in sawtooth-up waveforms, on the plasma sheaths, structure separation, increases in excitation rate and the current amplitude, are also observed in sawtooth-down waveforms.

The same method of applying sawtooth-up on the gas mixture with different concentrations of nitrogen is also repeated by driving the plasma through sawtooth-down waveforms. The nitrogen mixtures used are 0.05 %, 0.1 %, 0.2 %, 0.3 % and 0.5 % driven by 480 V_{pp} and 540 V_{pp}, 570 $V_{pp,}$ 580 V_{pp} and 615 V_{pp} respectively. The space and phase excitation by applying sawtooth-down waveforms on APPs for each set of nitrogen admixture is shown in figures 4.19, 4.20, 4.21, 4.22 and 4.23 respectively. The excitation dynamics when adding nitrogen to the gas mixture are the same as when applying sawtooth-down waveforms on a gas mixture of only helium with argon. In all cases, two excitation maxima are represented: one at the grounded electrode while the another one is located at the powered electrode. These structures are produced due to the action of sheath expansion and sheath collapse respectively.

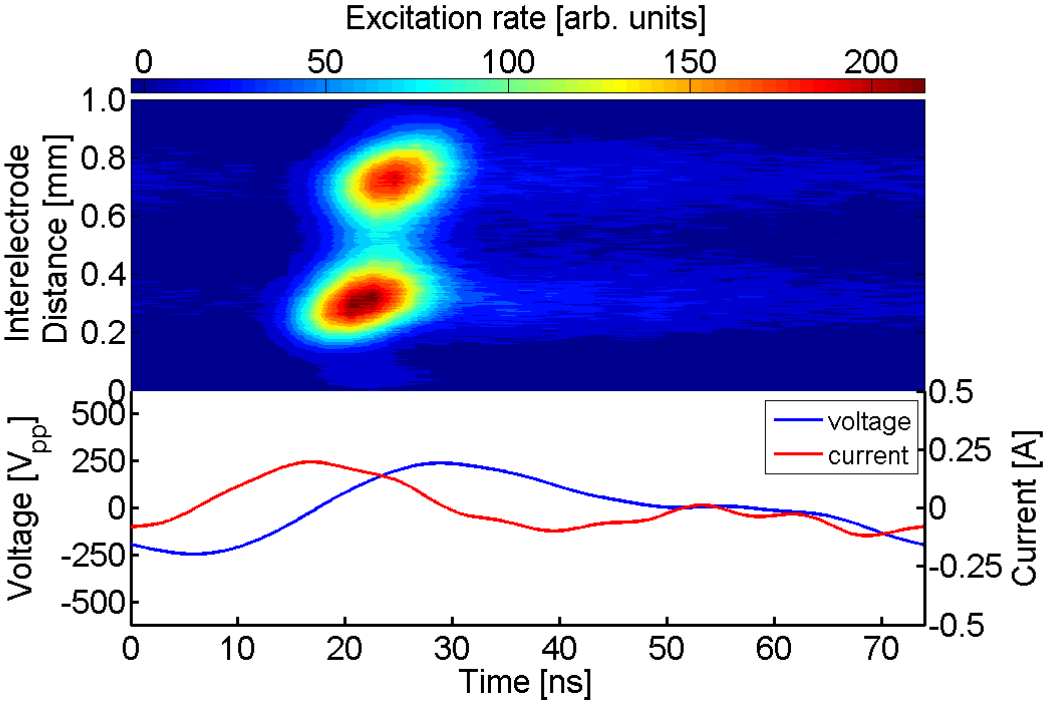
Excitation rate [arb. units]
0
50
100
150
200
Interelectrode Distance [mm]
1.0
0.8
0.6
0.4
0.2
0
Voltage [V_{pp}]
500
250
0
-250
-500
voltage
current
0.5
0.25
0
-0.25
-0.5
Current [A]
0
10
20
30
40
50
60
70
Time [ns]

n = 2

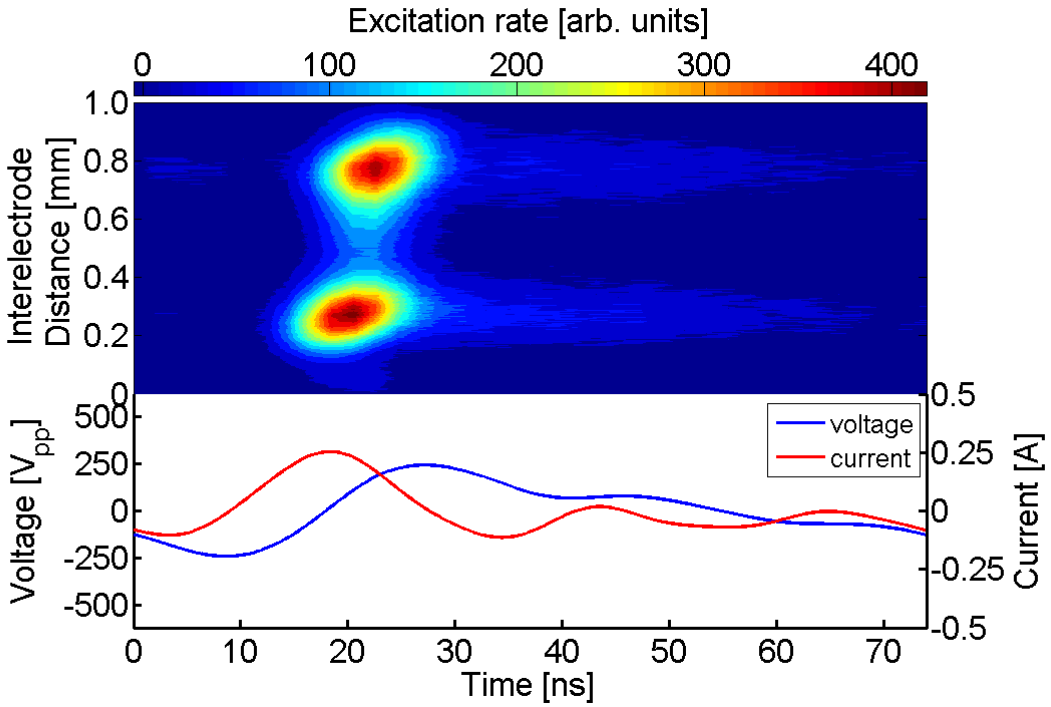
Excitation rate [arb. units]
0
100
200
300
400
Interelectrode Distance [mm]
1.0
0.8
0.6
0.4
0.2
0
Voltage [V_{pp}]
500
250
0
-250
-500
voltage
current
0.5
0.25
0
-0.25
-0.5
Current [A]
0
10
20
30
40
50
60
70
Time [ns]

n = 3

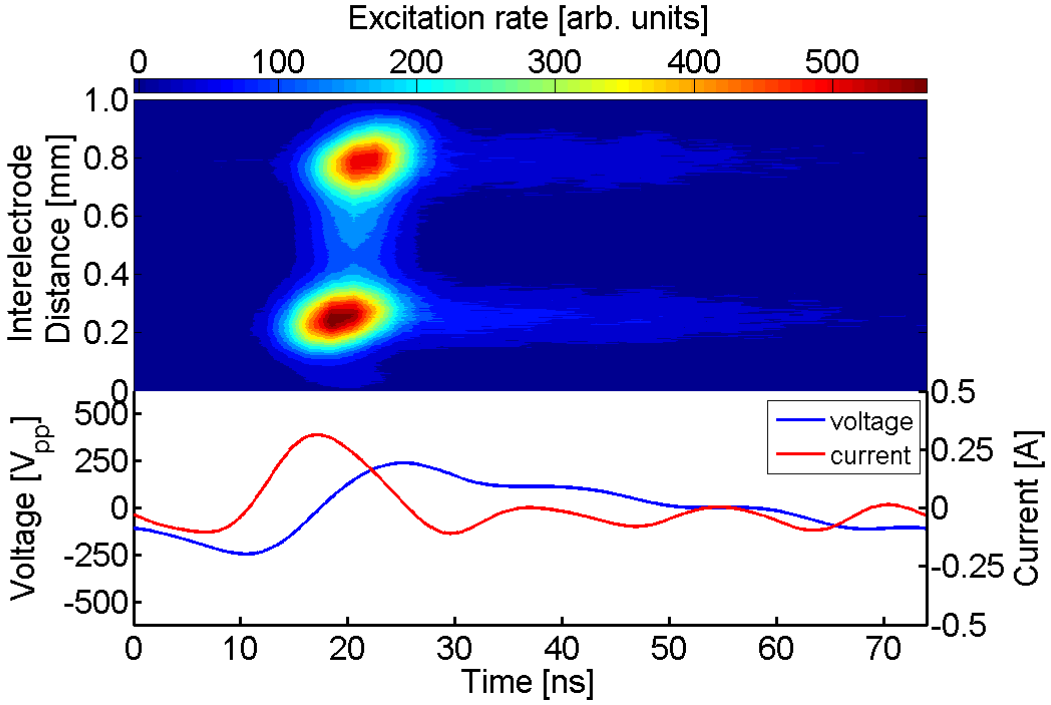

n = 4

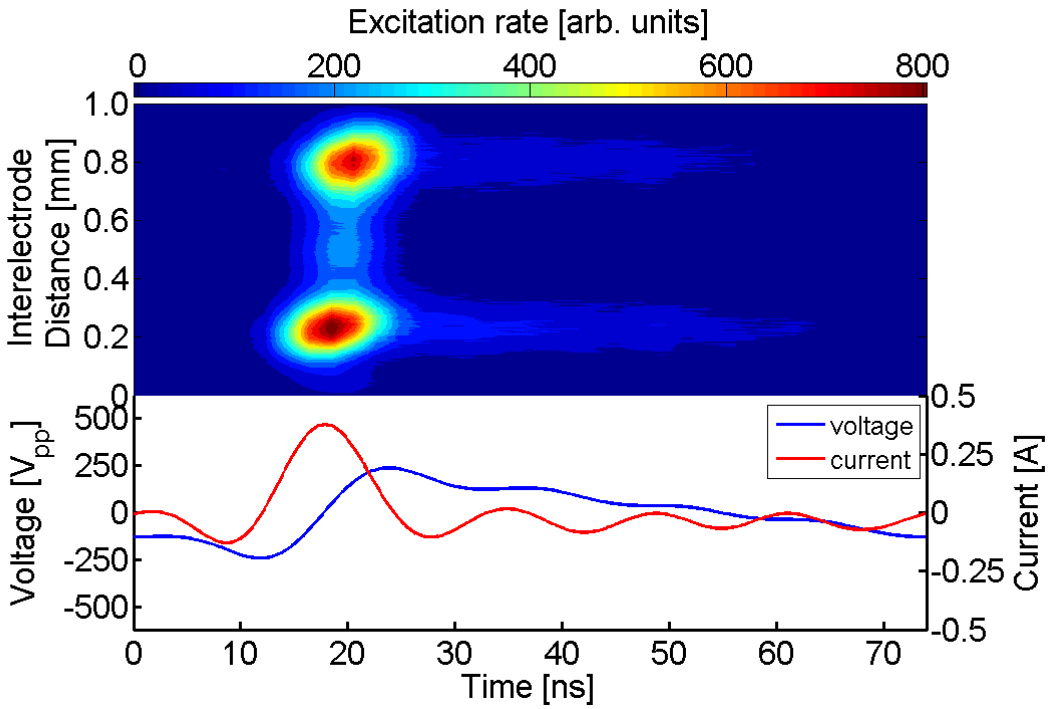

n = 5

Figure 4.19 Spatiotemporal excitation rates obtained from measurement of the emission line at 750.4 nm using PROES and applying sawtooth-down waveforms with n=2-5 harmonics (the top part of each image) applied on a gas mixture of He with 0.05 % Ar and 0.05 % N_2. The peak-to-peak voltage waveform (set at 480 V_{pp}) and the corresponding current waveforms for each harmonic are presented in the lower part of each image.

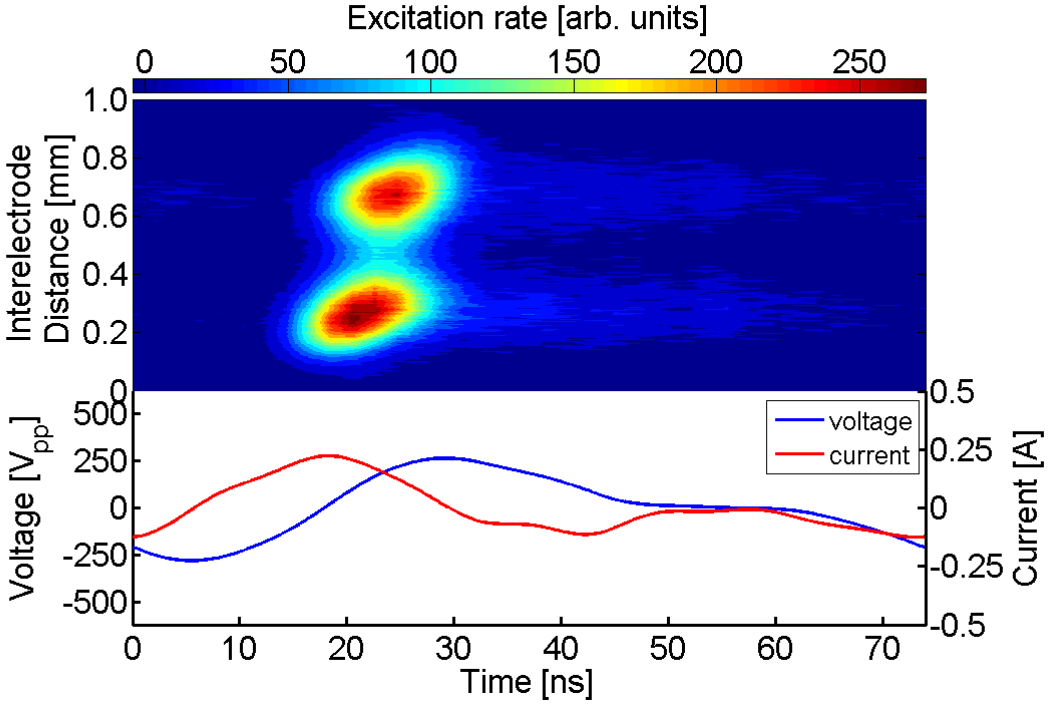
Excitation rate [arb. units]
0
50
100
150
200
250
Interelectrode Distance [mm]
1.0
0.8
0.6
0.4
0.2
0
Voltage [Vpp]
500
250
0
-250
-500
Current [A]
0.5
0.25
0
-0.25
-0.5
voltage
current
0
10
20
30
40
50
60
70
Time [ns]

n = 2

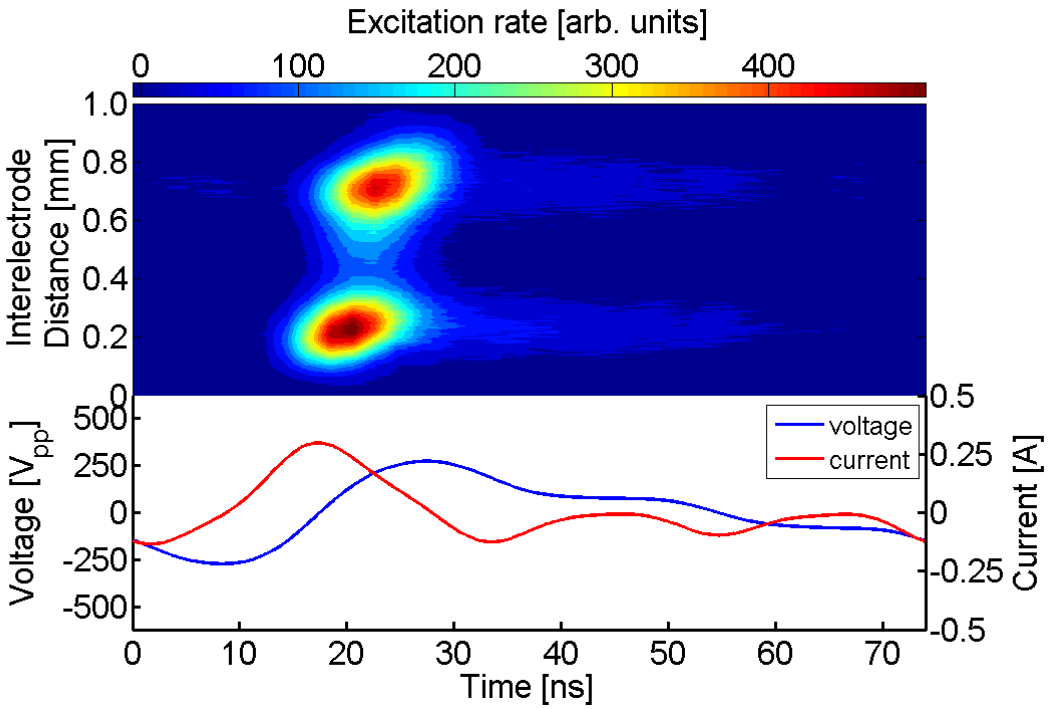
Excitation rate [arb. units]
0
100
200
300
400
Interelectrode Distance [mm]
1.0
0.8
0.6
0.4
0.2
0
Voltage [Vpp]
500
250
0
-250
-500
Current [A]
0.5
0.25
0
-0.25
-0.5
voltage
current
0
10
20
30
40
50
60
70
Time [ns]

n = 3

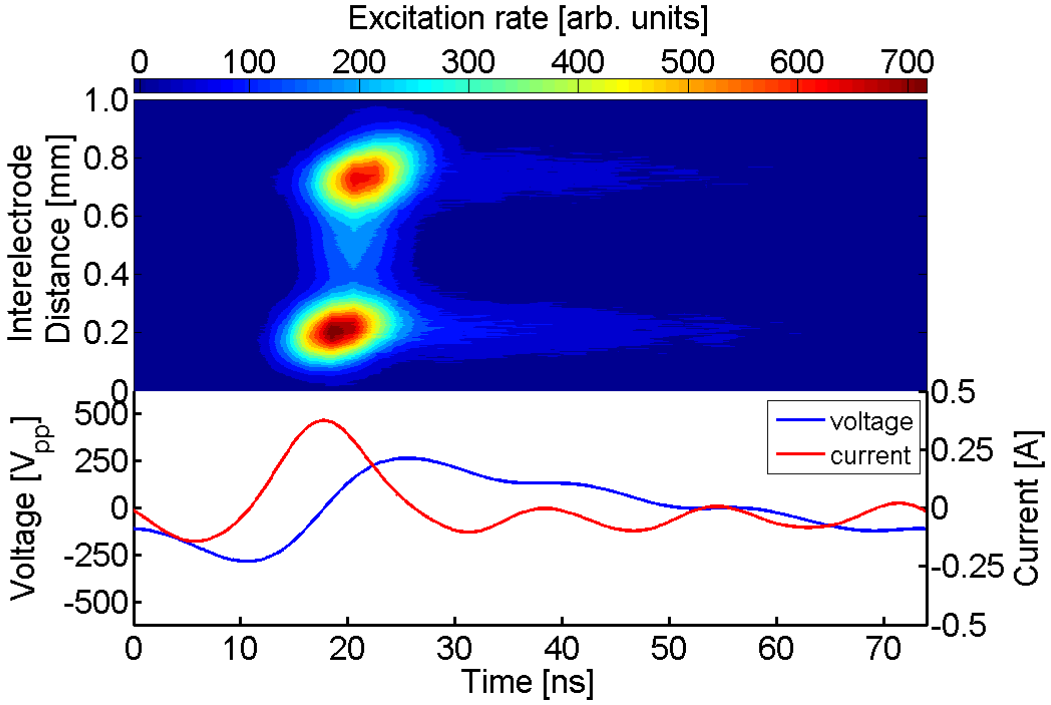

n = 4

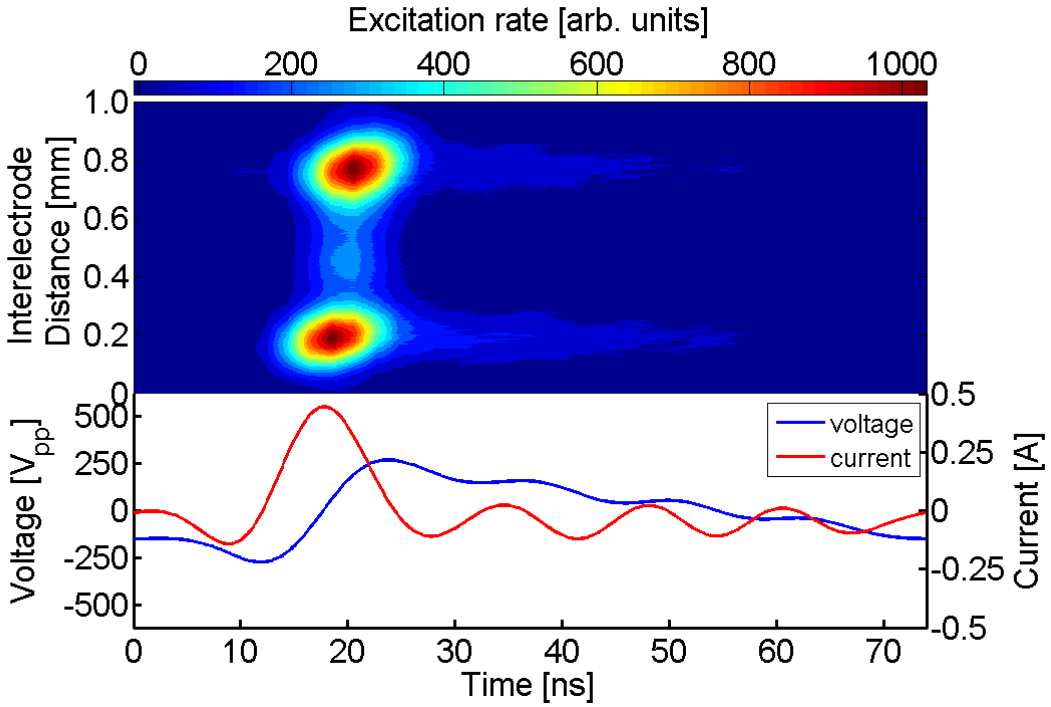

n = 5

Figure 4.20 Spatiotemporal excitation rates obtained from measurement of the emission line at 750.4 nm using PROES and applying sawtooth-down waveforms with n=2-5 harmonics (the top part of each image) applied on a gas mixture of He with 0.05 % Ar and 0.1 % N_2. The peak-to-peak voltage waveform (set at 540 V_{pp}) and the corresponding current waveforms for each harmonic are presented in the lower part of each image.

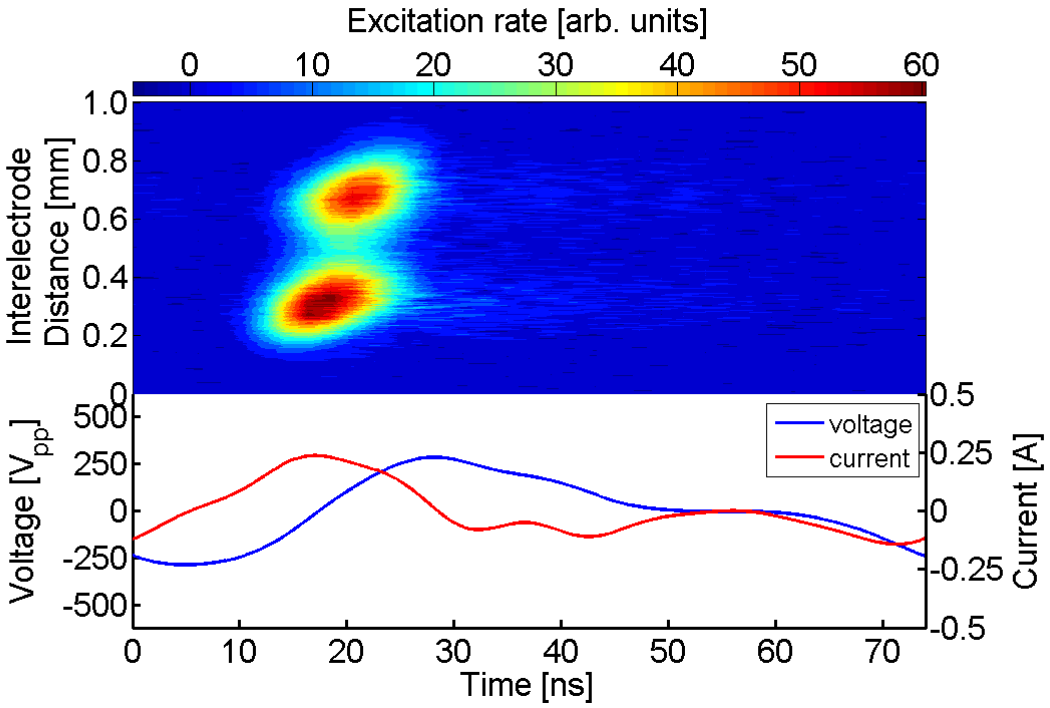
Excitation rate [arb. units]
0
10
20
30
40
50
60
Interelectrode Distance [mm]
1.0
0.8
0.6
0.4
0.2
0
Voltage [Vpp]
500
250
0
-250
-500
voltage
current
Current [A]
0.5
0.25
0
-0.25
-0.5
0
10
20
30
40
50
60
70
Time [ns]

n = 2

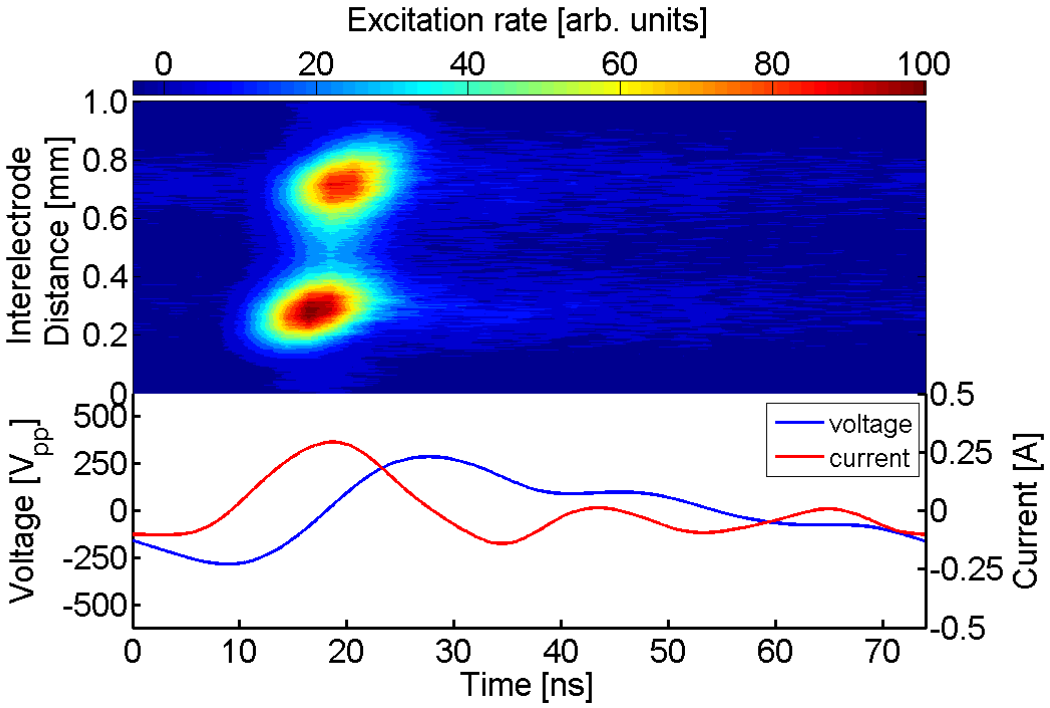
Excitation rate [arb. units]
0
20
40
60
80
100
Interelectrode Distance [mm]
1.0
0.8
0.6
0.4
0.2
0
Voltage [Vpp]
500
250
0
-250
-500
voltage
current
Current [A]
0.5
0.25
0
-0.25
-0.5
0
10
20
30
40
50
60
70
Time [ns]

n = 3

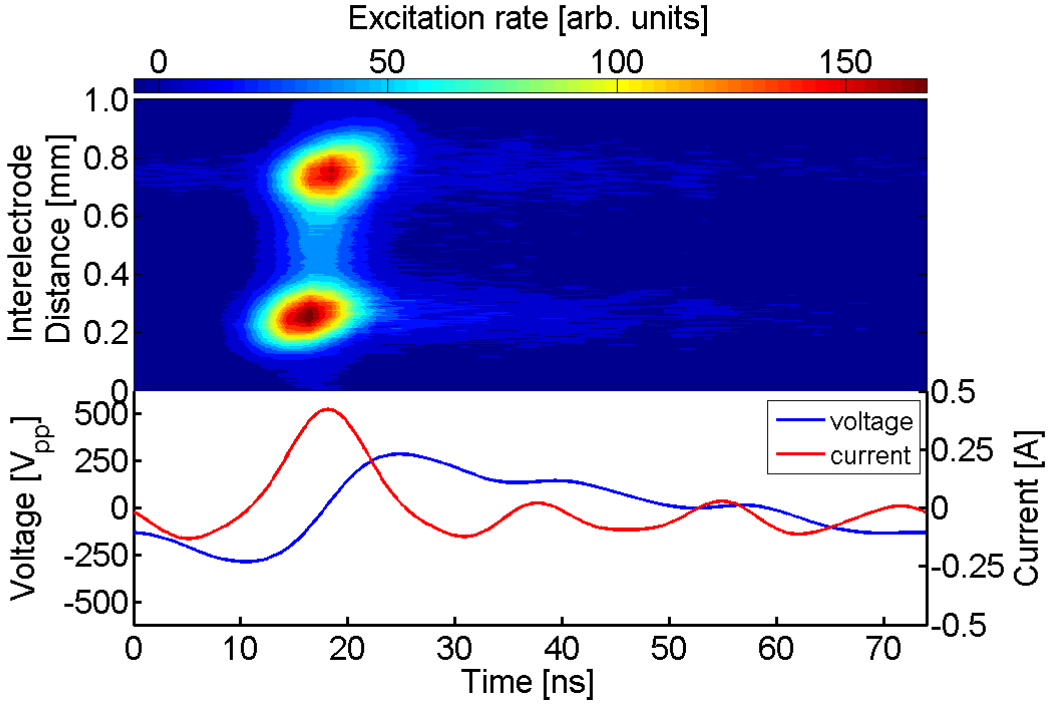

n = 4

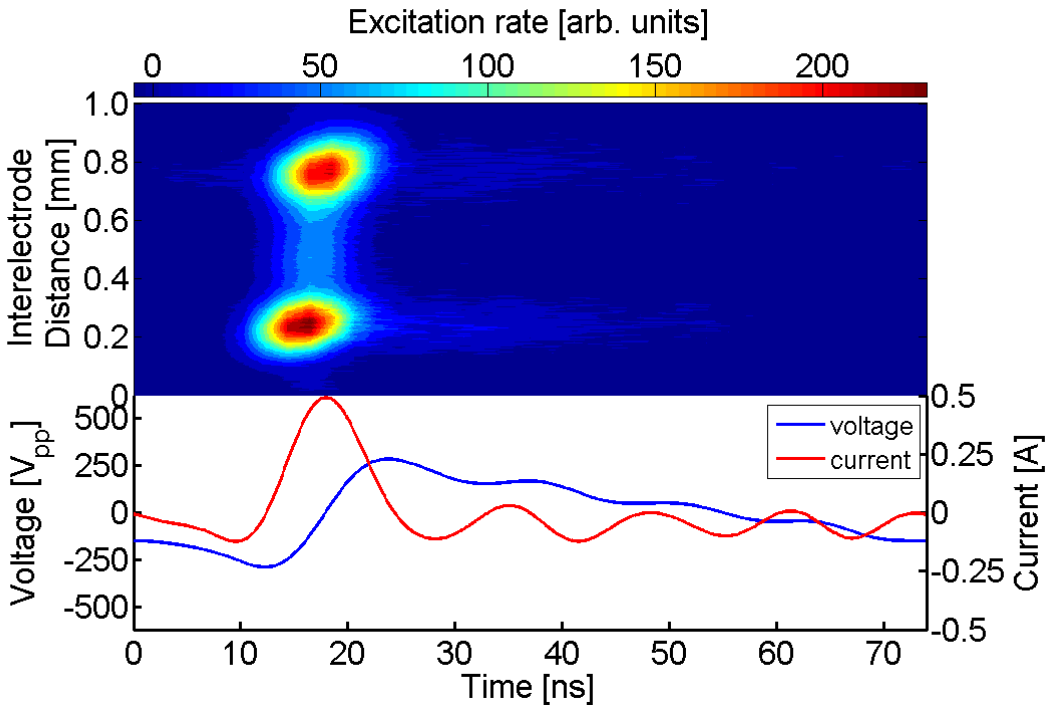

n = 5

Figure 4.21 Spatiotemporal excitation rates obtained from measurement of the emission line at 750.4 nm using PROES and applying sawtooth-down waveforms with n=2-5 harmonics (the top part of each image) applied on a gas mixture of He with 0.05 % Ar and 0.2 % N_2. The peak-to-peak voltage waveform (set at 570 V_{pp}) and the corresponding current waveforms for each harmonic are presented in the lower part of each image.

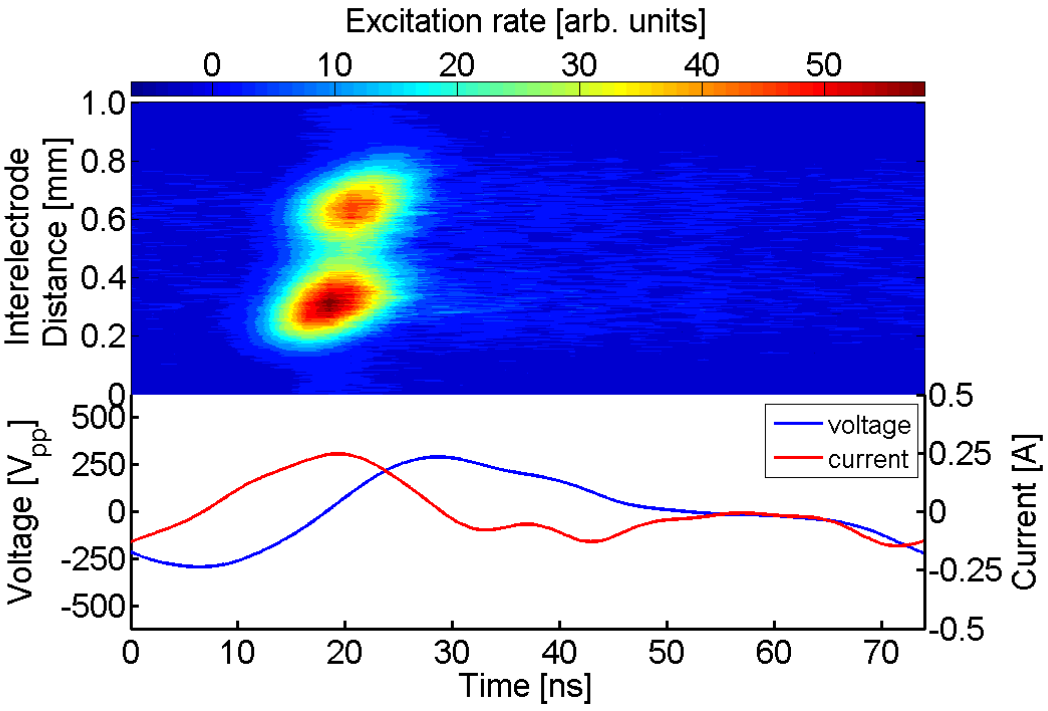
Excitation rate [arb. units]
0
10
20
30
40
50
Interelectrode Distance [mm]
1.0
0.8
0.6
0.4
0.2
0
Voltage [Vpp]
500
250
0
-250
-500
Current [A]
0.5
0.25
0
-0.25
-0.5
voltage
current
0
10
20
30
40
50
60
70
Time [ns]

n = 2

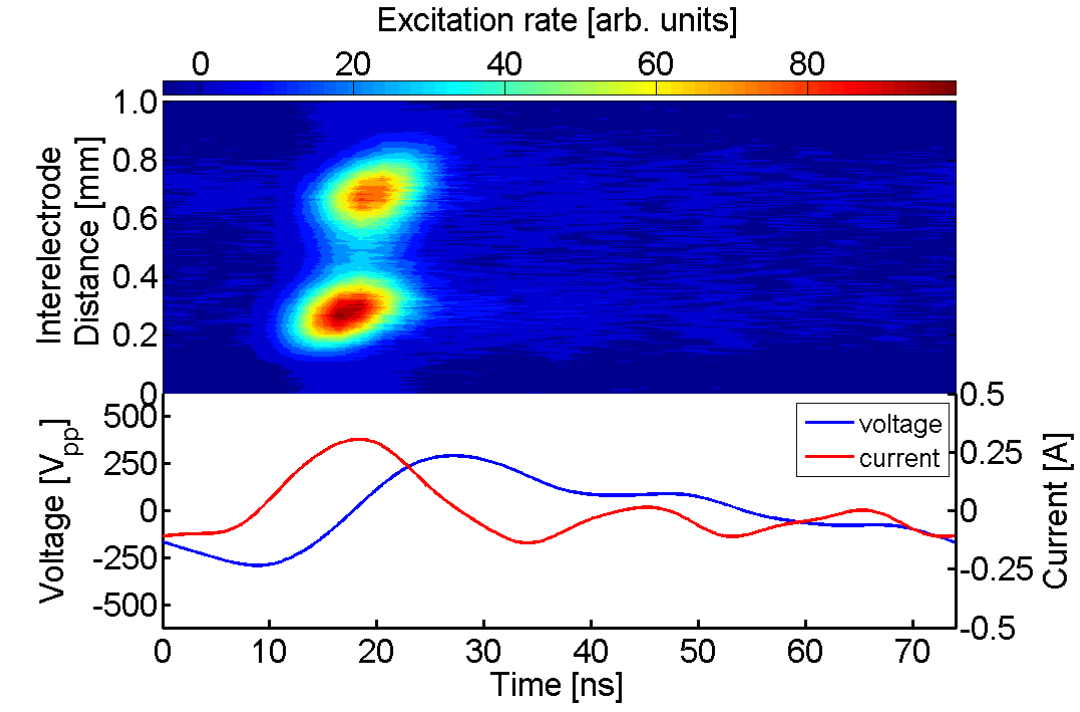
Excitation rate [arb. units]
0
20
40
60
80
Interelectrode Distance [mm]
1.0
0.8
0.6
0.4
0.2
0
Voltage [Vpp]
500
250
0
-250
-500
Current [A]
0.5
0.25
0
-0.25
-0.5
voltage
current
0
10
20
30
40
50
60
70
Time [ns]

n = 3

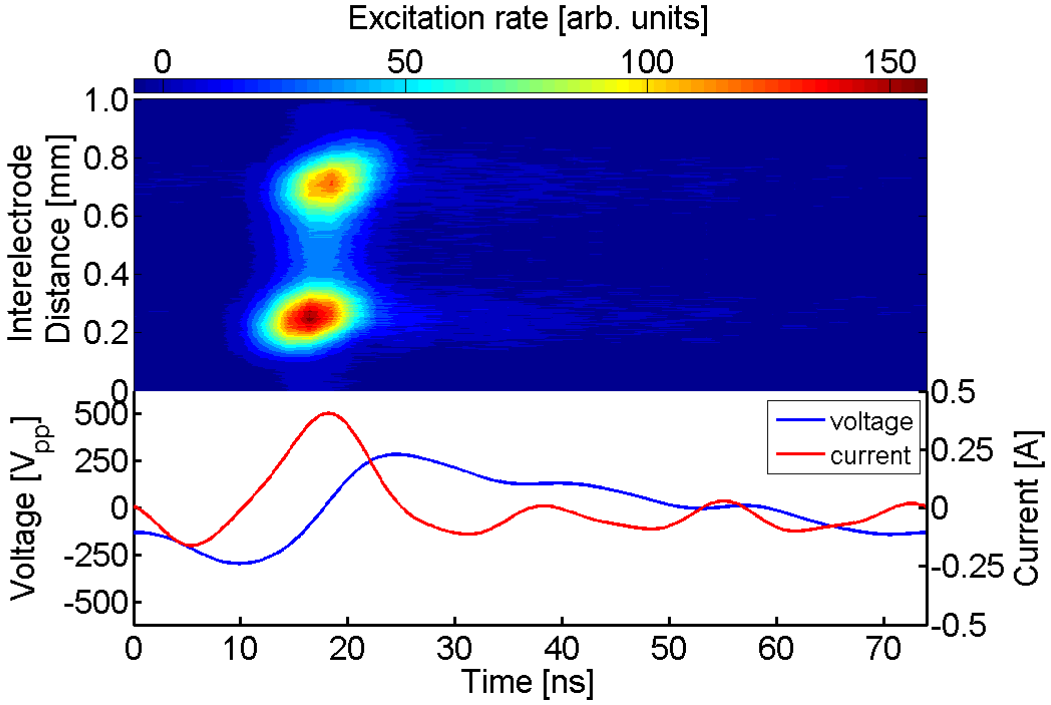

n = 4

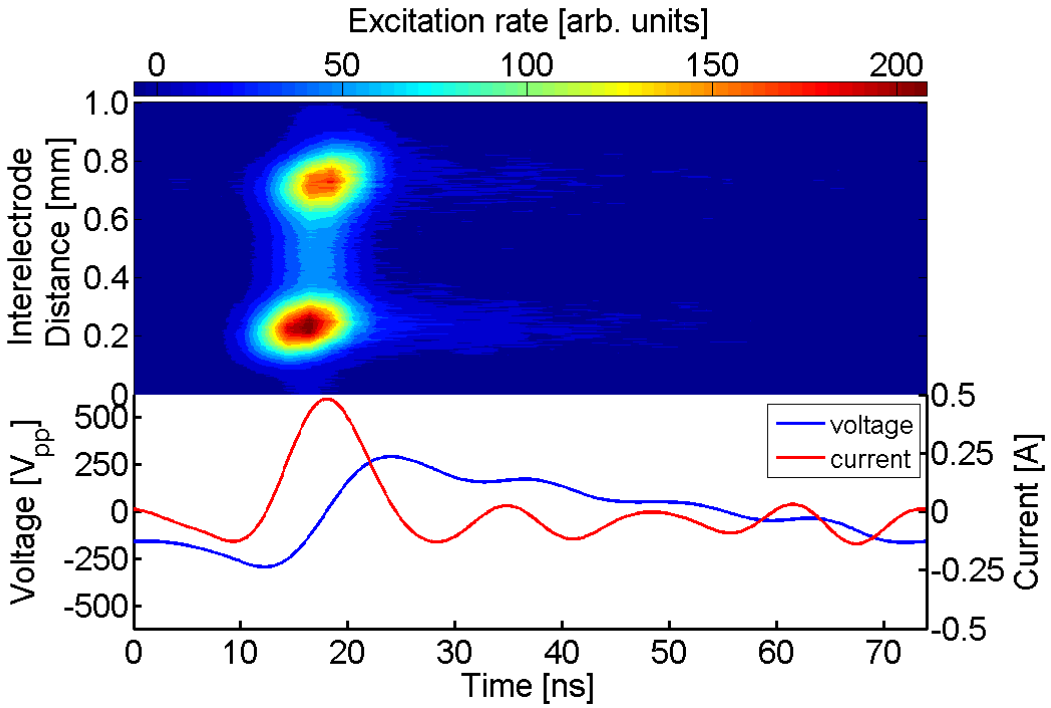

n = 5

Figure 4.22 Spatiotemporal excitation rates obtained from measurement of the emission line at 750.4 nm using PROES and applying sawtooth-down waveforms with n=2-5 harmonics (the top part of each image) applied on a gas mixture of He with 0.05 % Ar and 0.3 % N_2. The peak-to-peak voltage waveform (set at 580 V_{pp}) and the corresponding current waveforms for each harmonic are presented in the lower part of each image.

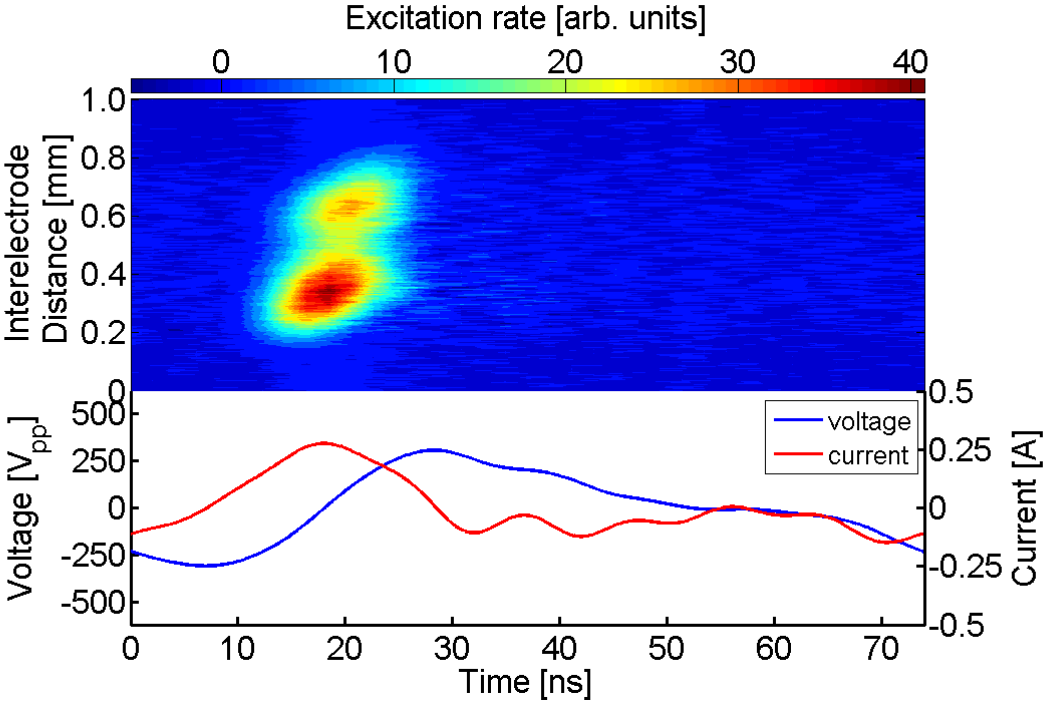
Excitation rate [arb. units]
0
10
20
30
40
Interelectrode Distance [mm]
1.0
0.8
0.6
0.4
0.2
0
Voltage [V_{pp}]
500
250
0
-250
-500
Current [A]
0.5
0.25
0
-0.25
-0.5
voltage
current
0
10
20
30
40
50
60
70
Time [ns]

n = 2

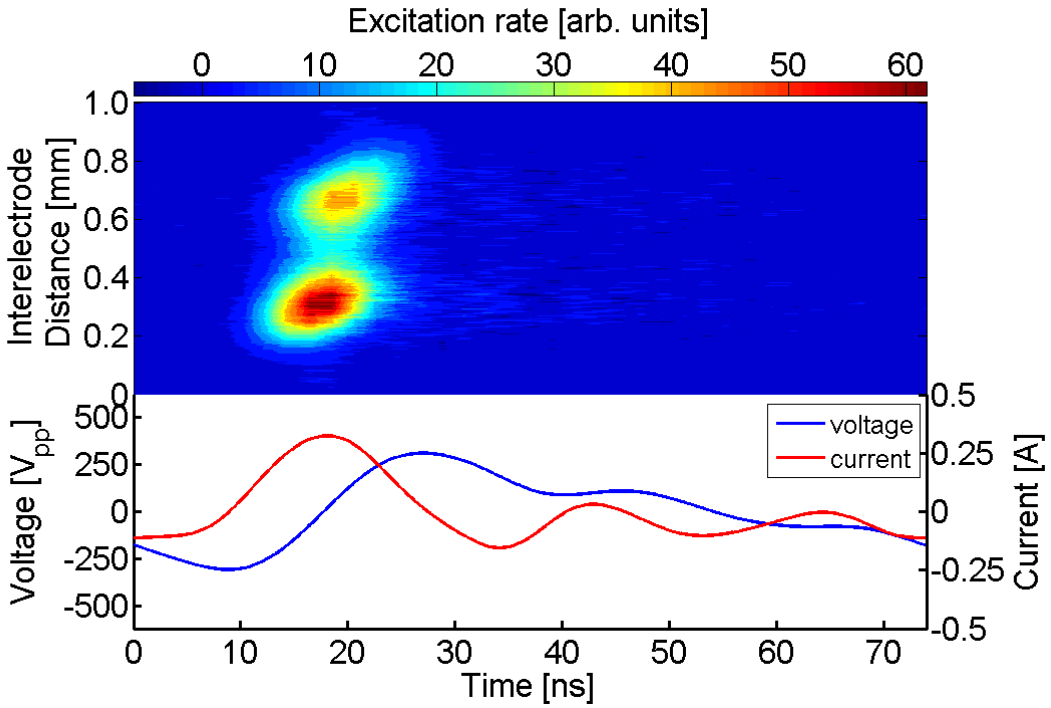
Excitation rate [arb. units]
0
10
20
30
40
50
60
Interelectrode Distance [mm]
1.0
0.8
0.6
0.4
0.2
0
Voltage [V_{pp}]
500
250
0
-250
-500
Current [A]
0.5
0.25
0
-0.25
-0.5
voltage
current
0
10
20
30
40
50
60
70
Time [ns]

n = 3

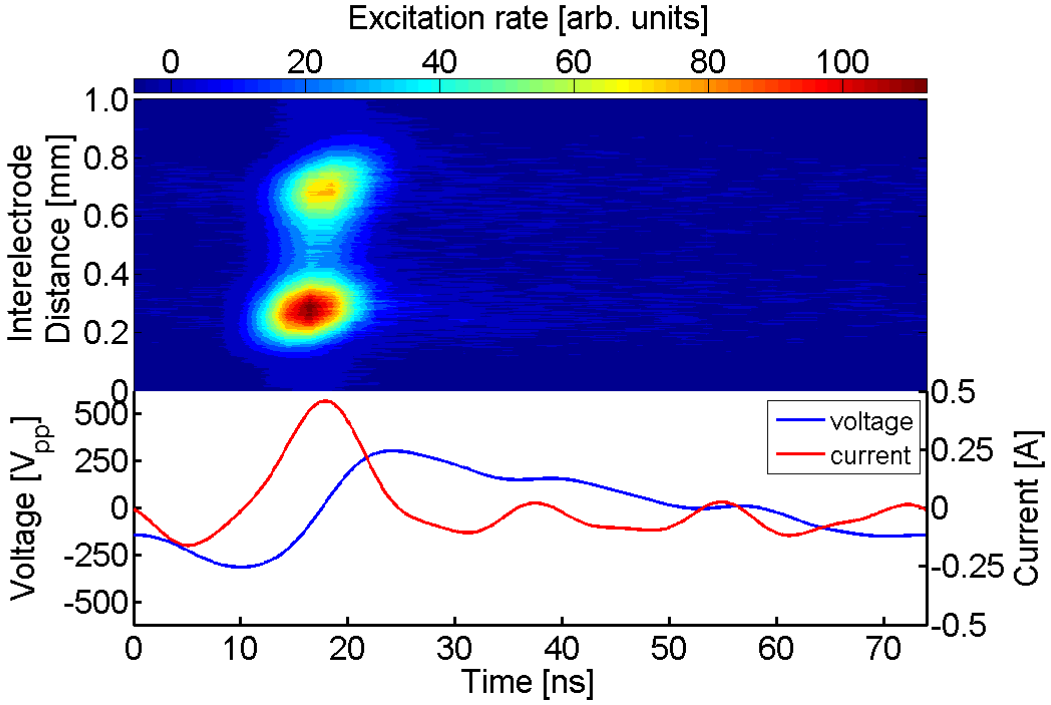

n = 4

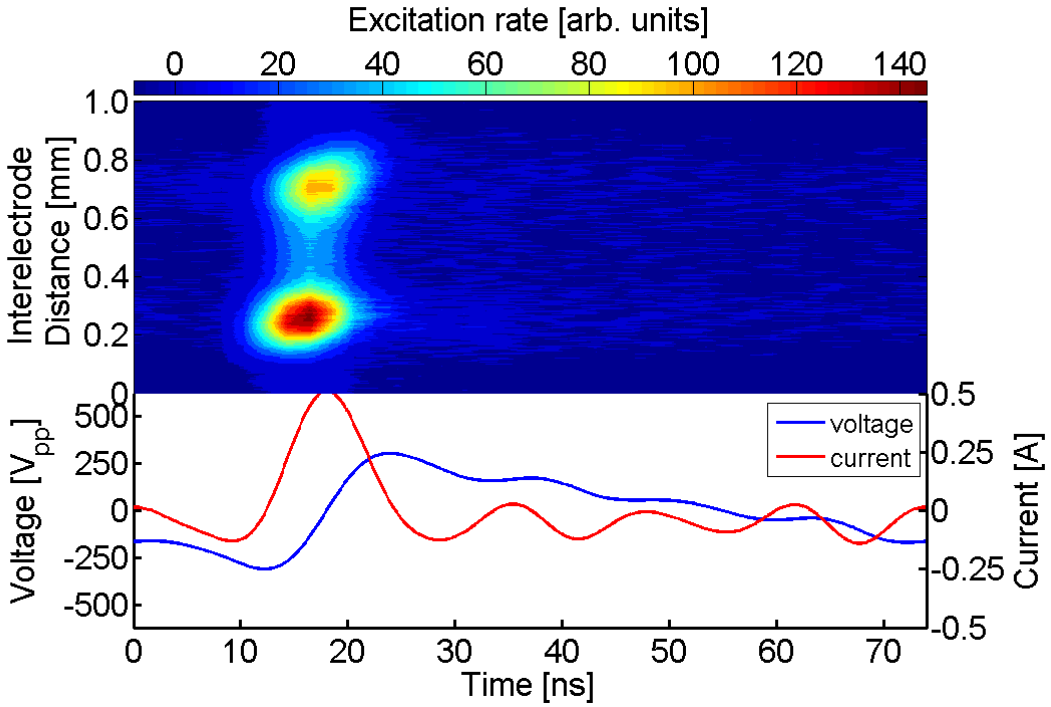

n = 5

Figure 4.23: Spatiotemporal excitation rates obtained from measurement of the emission line at 750.4 nm using PROES and applying sawtooth-down waveforms with n=2-5 harmonics (the top part of each image) applied on a gas mixture of He with 0.05 % Ar and 0.5 % N_2. The peak-to-peak voltage waveform (set at 615 V_{pp}) and the corresponding current waveforms for each harmonic are presented in the lower part of each image.

The impact of adding different concentrations of nitrogen to the plasma driven by sawtooth-down waveforms is noticed. The excitation structures are getting closer to each other toward the centre of the discharge by increasing the concentration of nitrogen; therefore, the plasma sheaths are getting thicker at the two electrodes. This denotes that the plasma density decreases. The excitation rates are also diminished with higher percentages of nitrogen being added to the plasma. In the case of using 0.1 % nitrogen, the results seem different than what other cases show. The excitation rate is higher than the excitation rate in the case of using 0.05 % of nitrogen. These results are shown in figure 4.24.

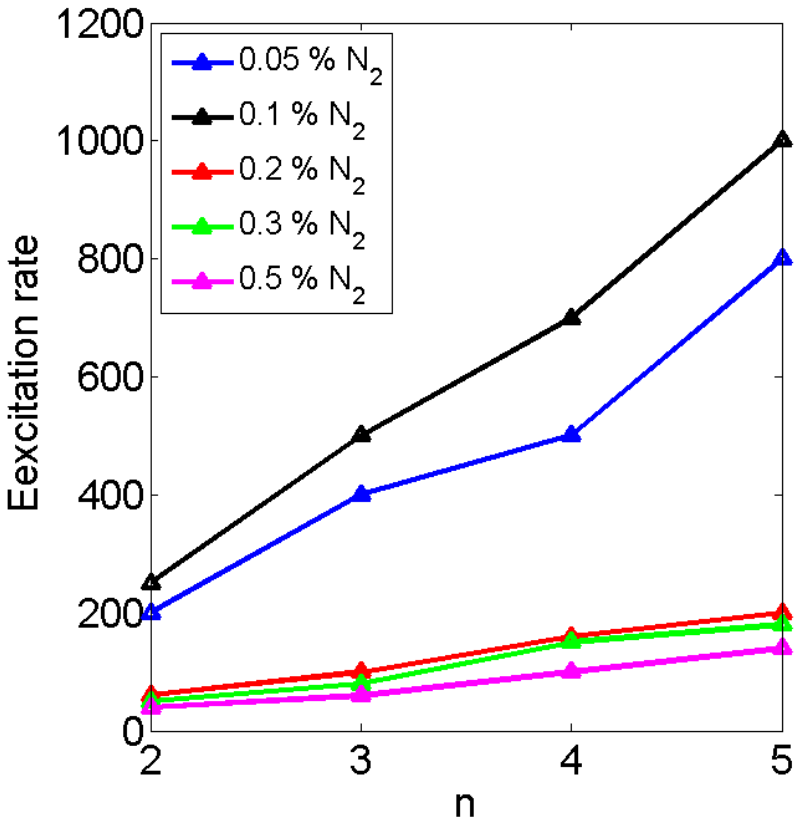

Figure 4.24 Summary of excitation rates as a function of the applied harmonics numbers 2-5 for when sawtooth-down waveforms are applied on the plasma with different percentages of N_2 admixtures.

In all N_2 admixture sets, the denser excitation structures are located at the grounded electrode. This is summarised and illustrated in figure 4.25. The intensities of emission ration are plotted as a function of the different amounts of N_2 for all used harmonics.

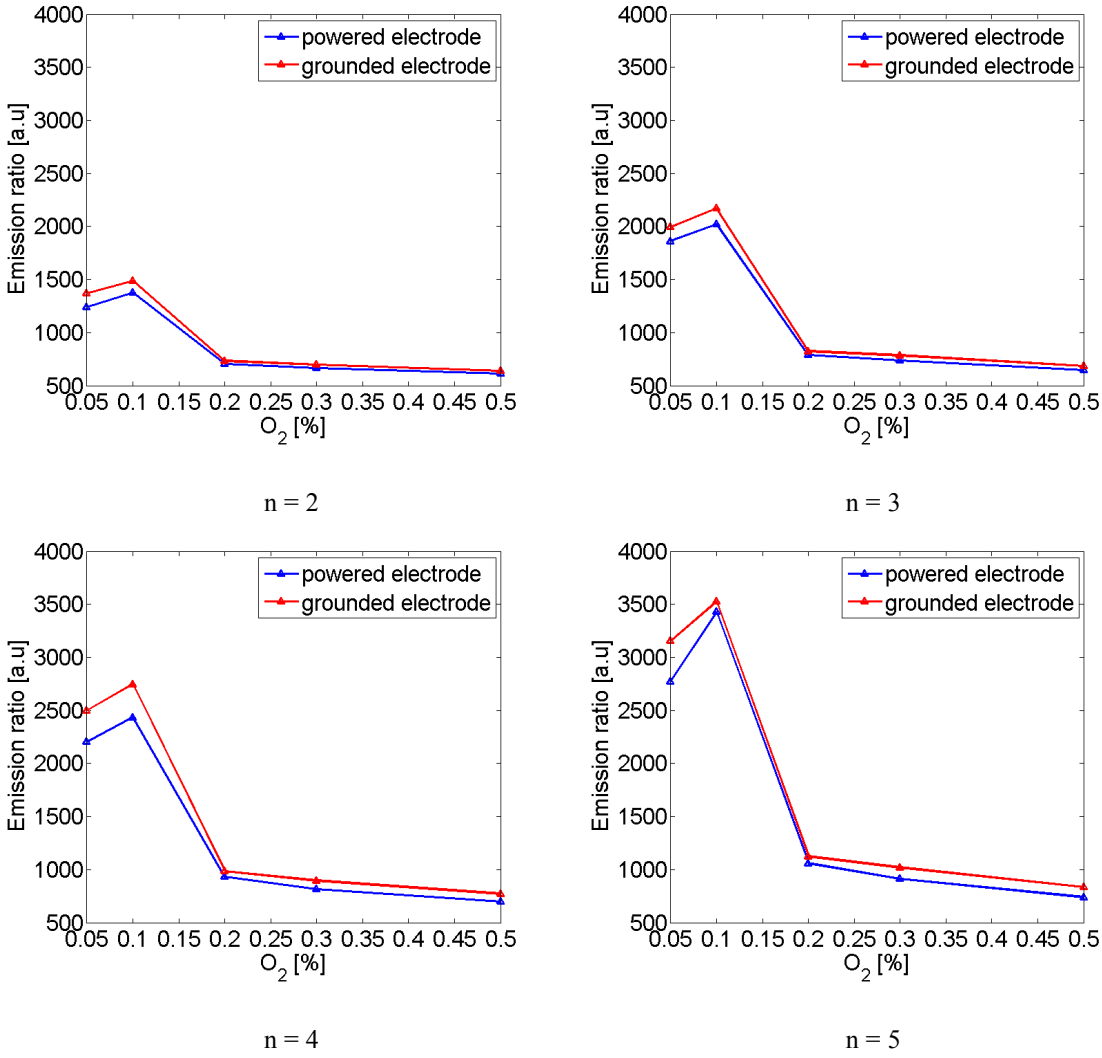

Figure 4.25 The emission ratio of the dense excitation structures as a function of N_2 admixture for the used harmonics in the application of sawtooth-down waveforms.

4.2.2 DC self-bias with harmonics number and N_2 variations

DC self-bias voltages were experimentally measured by applying sawtooth-up and sawtooth-down waveforms using different admixtures of nitrogen 0 %, 0.05 %, 0.1 %, 0.2 %, 0.3 % and 0.5 %,

and the applied peak-to-peak voltage was fixed at 470 V_{pp}, 480 V_{pp} and 540 V_{pp} , 570 V_{pp} , 580 V_{pp} and 615 V_{pp} respectively. The DC bias values as a function of the number of the applied harmonics varied from 1 to 5 are illustrated in figure 4.26.

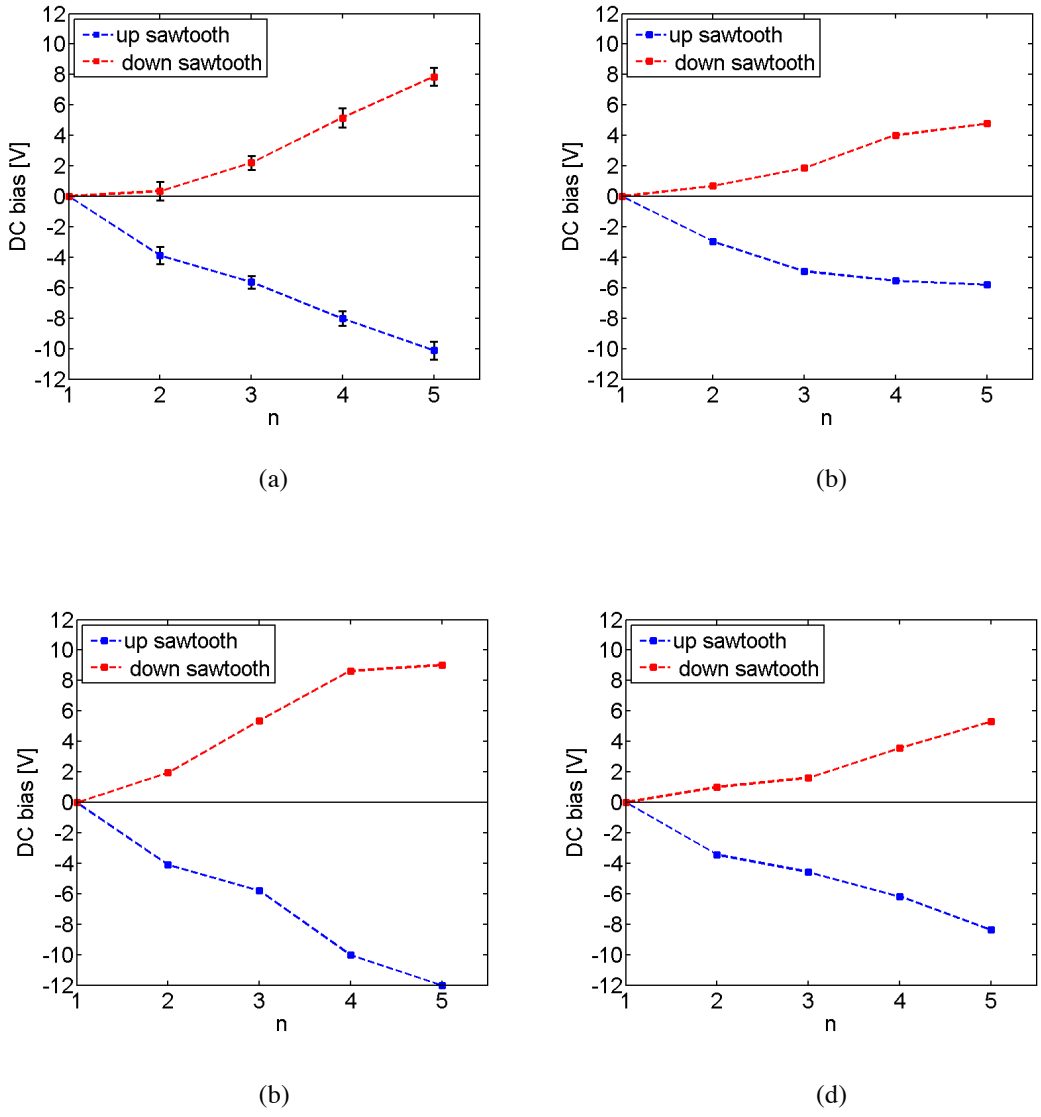

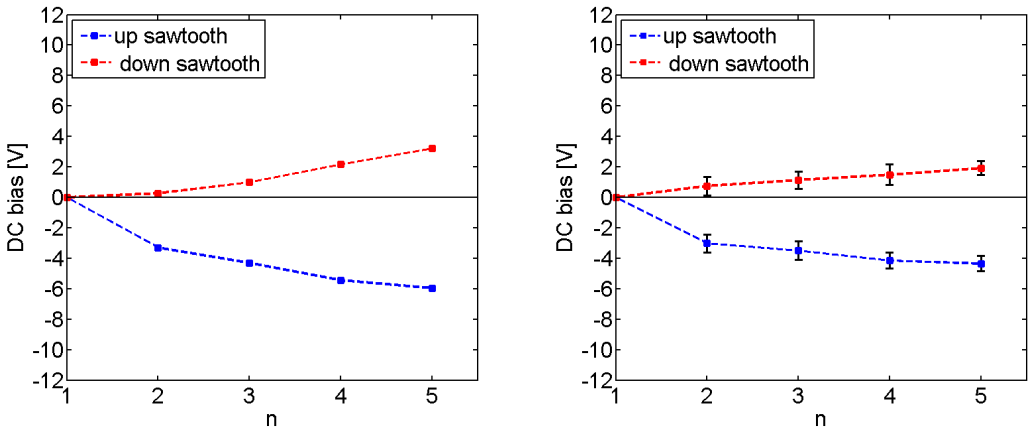

Figure 4.26 DC self-bias voltages measured as a function of n being varied from 1 to 5 harmonics for sawtooth-up waveforms (blue) and sawtooth-down waveforms (red) at (a) 470 V_{pp} with 0 % N_2, (b) 480 V_{pp} with 0.05 % N_2, (c) 540 V_{pp} with 0.1 % N_2, (d) 570 V_{pp} with 0.2 % N_2, (e) 580 V_{pp} with 0.3 % N_2 and (f) 615 V_{pp} with 0.5 % N_2. Error bars show the standard error of the DC-bias voltages.

The blue dashed line represents the DC self-bias obtained from the sawtooth-up waveform, while the red dashed line shows the DC self-bias resulted from the application of sawtooth- down waveform on the plasma. The measured self-bias for the first harmonic has been shifted up by ~ 0.8 V to correct for the uncertainty of the DC bias probe. The sawtooth-up waveforms show negative self-bias while sawtooth-down waveforms show positive self-bias voltages. The higher DC bias voltage values are dominated by sawtooth-up waveforms although sawtooth-up and sawtooth-down waveforms are both operated at the same peak-to-peak voltages. In all of these conditions, the DC bias nearly follows the same trend starts with low values and increases to reach the maximum at n = 5 and this shows a linear increase in the DC self-bias with respect to the number of harmonics. This trend is consistent with the DC self-bias obtained in some studies that were carried out in low-pressure plasma such as hydrogen plasma [66] and argon [22]. The values of the DC self-bias measured here are small in comparison with what were measured in argon; however, it is consistent with the small values obtained in from hydrogen plasma [66]. The DC self-bias voltages mostly tend to decrease with more concentrations of N_2.

4.3 Summary

Tailored voltage waveforms (TVW) are essentially a sine waveform of a fundamental frequency of 13.56 MHz comprising a number of harmonics. It is possible to produce asymmetric plasma although the plasma operated in a symmetric capacitively coupled reactor.
This can be achieved through the application of non-sinusoidal TVWs. Therefore, DC self-bias is generated due to what is called the electrical asymmetry effect (EAE). The preliminary results of DC bias voltages are obtained.

Peaks-type including peaks and valleys waveforms and sawtooth-type including sawtooth-up and sawtooth-down waveforms are used. These waveforms are applied on APPs and then their influences on the electron dynamics are discussed. The plasma is operated in a gas admixture consisting of helium as a feed gas with a small amount of argon used for optical analysis purposes and different amounts of nitrogen being varied from 0.05 % up to 0.5 %. The resultant electron impact excitation dynamics extracted by phase-resolved optical emission spectroscopy (PROES) are discussed. The DC self-bias resulting from applying peaks and valleys waveform are taken at different concentrations of nitrogen (0 %, 0.05 % and 0.1 %), representing the same trend which show an increase in in the DC self-bias until 3 harmonics and then decreases at four and five harmonics. Sawtooth-up and sawtooth-down waveforms show linear trends of the DC self-bias with the applied number of harmonics. The negative DC self-bias voltages obtained in peaks and sawtooth-up waveforms are greater than the positive DC self-bias voltages resulted from valleys and sawtooth-down waveforms. The electrical asymmetry obtained in the form of dc bias voltages occurred due to the asymmetry of electron heating.

Regarding the excitation dynamics obtained in peaks and valleys waveform, the main excitation structures occur during sheath expansion and sheath contraction at the grounded electrode and the powered electrode respectively. During the sheath collapse, a complex excitation process occurs due to the field reversal mechanism. The maximum excitation generated during sheath expansion in the application of both sawtooth up and sawtooth down takes place at the grounded electrode and sheath collapse at the powered electrode respectively both during sheath expansion. In all results, the excitation structure that has higher intensity is located at the powered electrode in the case of applying sawtooth up while the opposite is observed for the application of sawtooth-down waveforms.

The impact of increasing the nitrogen admixture on all used waveforms and the different harmonics numbers is studied. First, the excitation rate is reduced as the excited state is quenched by nitrogen and energy exploited in dissociating the molecular nitrogen. However, at each individual set of nitrogen admixtures, the excitation rate increases with increasing the harmonics numbers. Moreover, the plasma density decreases as observed through the reduction in the sheath thickness.

Chapter 5 The Electro-negative Character of He-O_2 RF-APPs Driven by TVWs

Atmospheric pressure plasmas driven by radio frequencies are known to be efficient sources for the production of chemically reactive species depending on the used gas component, the plasma volume and the operating parameters. If the plasma operated with a gas mixture consisting of He as a feed gas and oxygen makes it possible to produce high densities of reactive oxygen species (ROS), this allows a wide range of applications, particularly biomedical applications. Examples of the applications that are demonstrated are the killing of cancer cells and irradiating bacteria and biofilms [21, 102, 103]. Therefore, it is important to understand the essential plasma chemistry to have explicit optimisation for the desired applications.

In this chapter, the experimental results of an RF-μAPPJ operated in helium- oxygen driven by peaks-type and sawtooth-type tailored voltage waveforms with number of harmonics varied from 2 to 5 are presented. In particular, electron dynamics thorough PROES measurements taken with various concentrations of oxygen and the produced DC self-bias from the EAE are investigated. In addition, quantitative measurements of ozone density are involved.

5.1 Peak-type waveforms

5.1.1 Investigation of excitation dynamics

Electron impact excitation mechanisms are investigated from the discharge emission. The spatio-temporal electron-impact excitation into Ar ($2p_1$) state are obtained from applying peaks waveform on a gas mixture of He with 0.05 % Ar and different amounts of oxygen (0.05 % and 0.1 %) with the applied peak-to-peak voltages set at 480 V_{pp} and 490 V_{pp} as illustrated in figures 5.1 and 5.2 respectively. The fundamental frequency used is 13.56 MHz with its harmonics 2-5. In each image, the phase and space excitation is represented in the upper part and the colour bar at the top of each image shows the excitation rate where the higher rate is represented in dark red whereas the lower excitation rate shown in blue. The distance between the two electrodes is represented on the y-axis. The grounded electrode is located at 0 mm while the powered electrode is located at 1 mm. The x-axis, shared for the upper and the lower parts of each image, illustrates the time in ns, which include one cycle of the fundamental frequency. The lower part of each image includes the peak-to-peak voltage waveforms on the left y-axis as well as the current waveforms on the right y-axis. The voltage waveform represents the sheath motion in the plasma with the applied electric field. Three excitation maxima in each image are observed. One is located at the grounded electrode and the other two excitation structures are observed at the powered electrode. At the powered electrode, one excitation structure is closer to the powered electrode while the second one is nearly located in the plasma bulk. At the grounded electrode specifically at time between ~ 15 to ~ 35 ns, the voltage increases rapidly and then the sheath expands which, in turn, accelerates electrons toward the plasma bulk; therefore, a strong electron impact excitation occurs at the grounded electrode. Simultaneously, a denser excitation peak is initiated at the powered electrode during the rapid sheath collapse when the voltage decreases. During sheath

collapse, electrons cannot follow the fast change of the RF potential due to the collision condition; therefore, an electric field is initiated and hence accelerates electrons toward the powered electrode. This electric field is similar to the so-called field reversal, which has been observed in hydrogen plasmas at low pressure driven by a single frequency [54, 94] and using dual frequencies [95] as well as by multi frequencies [96]. It is also initiated by applying peaks and valleys waveforms on electronegative plasma (CF_4) [96]. This phenomenon is also observed in helium with nitrogen plasma carried out in the case of sine waveforms at atmospheric pressure [19]. The second excitation peak observed at the powered electrode at time between ~ 40 to ~ 55 occurs during sheath expansion when the voltage increases rapidly. Because the sheath is fully contracted at the grounded electrode, there is no field reversal produced at the grounded electrode. When the plasma operated in 0.05 % of oxygen, the amplitude of this excitation peak at the powered electrode gets smaller than the excitation peak at the grounded electrode in the case of n = 4. However, the opposite can be observed at n = 5 when using the same oxygen flux.

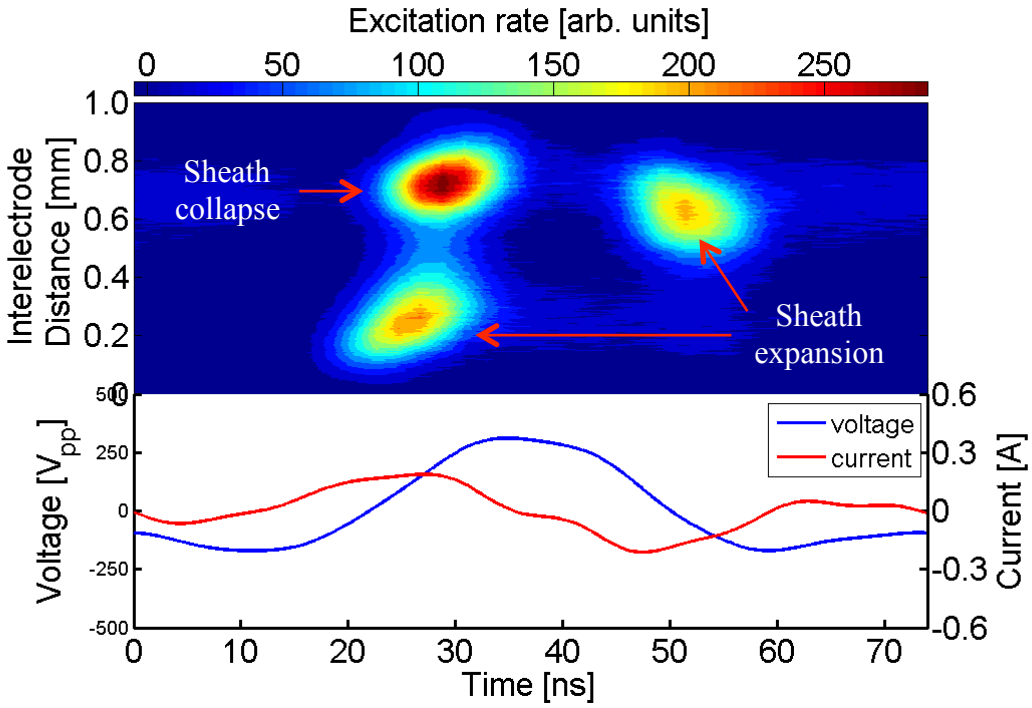
Excitation rate [arb. units]
0
50
100
150
200
250
Interelectrode Distance [mm]
1.0
0.8
0.6
0.4
0.2
0
Sheath collapse
Sheath expansion
Voltage [Vpp]
500
250
0
-250
-500
voltage
current
Current [A]
0.6
0.3
0
-0.3
-0.6
0
10
20
30
40
50
60
70
Time [ns]

n = 2

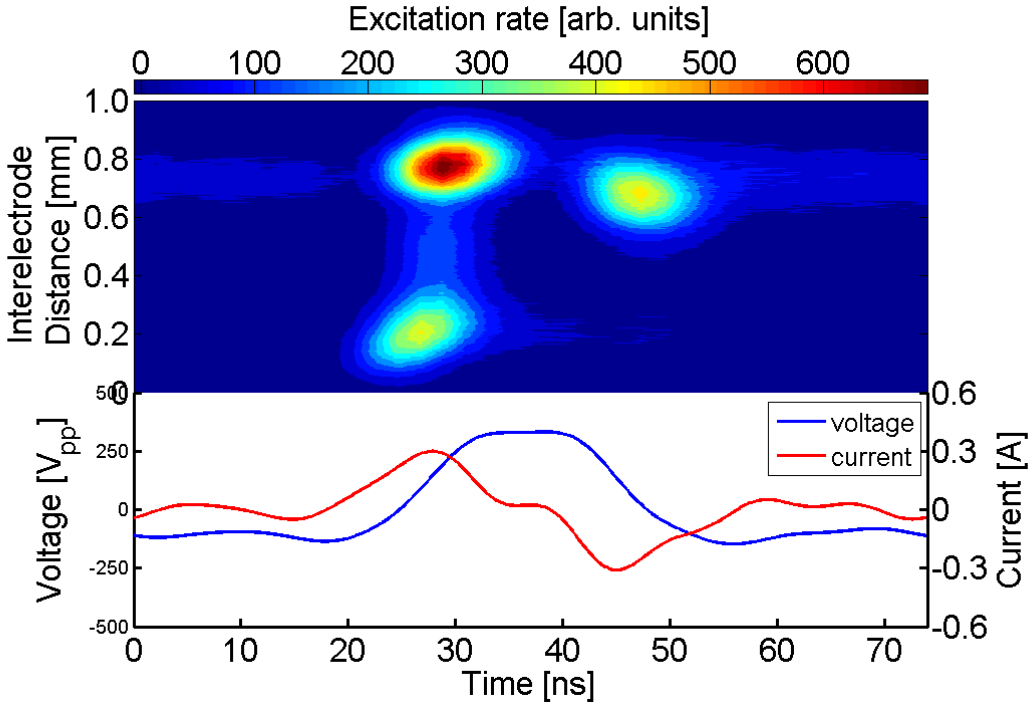
Excitation rate [arb. units]
0
100
200
300
400
500
600
Interelectrode Distance [mm]
1.0
0.8
0.6
0.4
0.2
0
Voltage [Vpp]
500
250
0
-250
-500
voltage
current
Current [A]
0.6
0.3
0
-0.3
-0.6
0
10
20
30
40
50
60
70
Time [ns]

n = 3

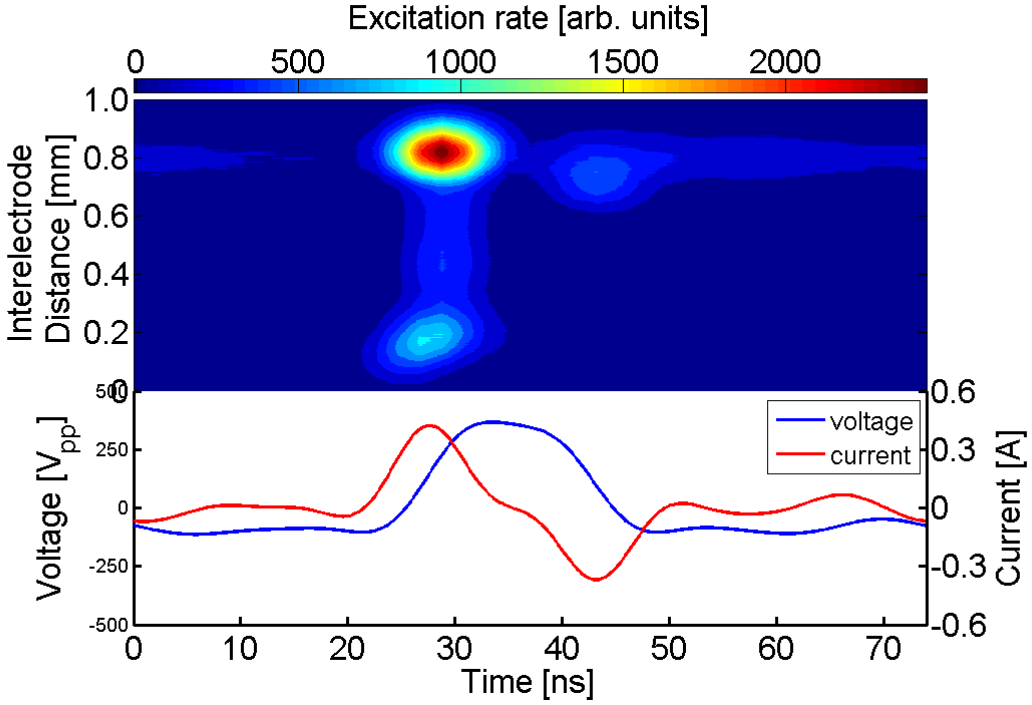

n = 4

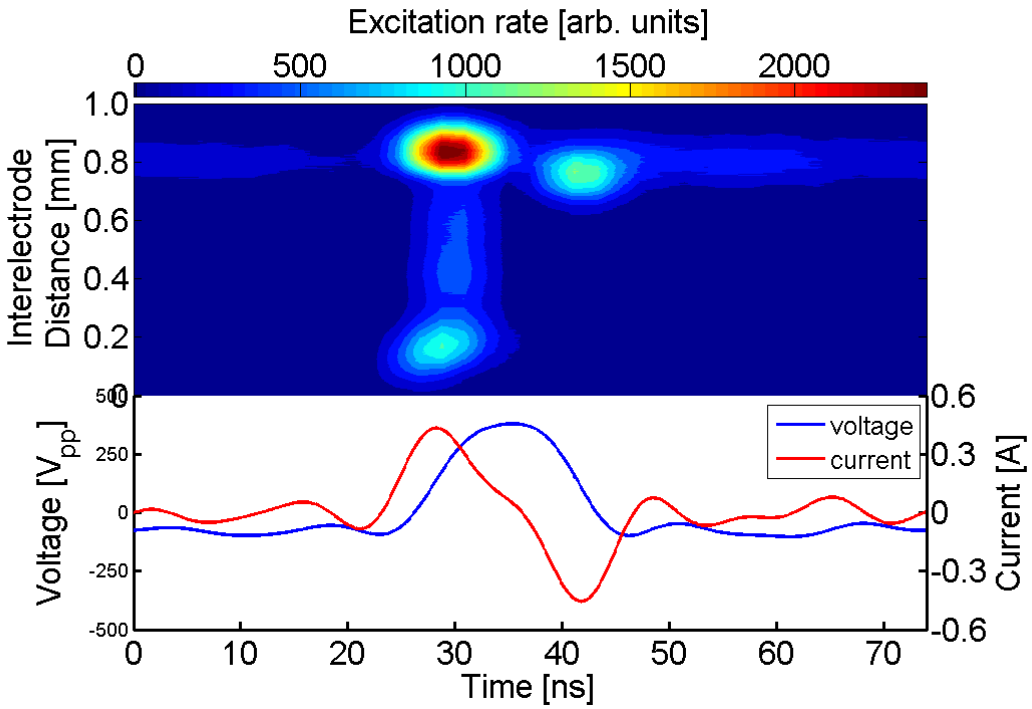

n = 5

Figure 5.1: Spatio-temporal excitation rates obtained from measurement of the emission line at 750.4 nm using PROES and applying peaks waveforms with n = 2-5 harmonics applied on a gas mixture of He with 0.05 % Ar and O_2 mixture 0.05 %. The peak-to-peak voltage waveform and the corresponding current waveforms for each harmonic are presented in the lower part of each image.

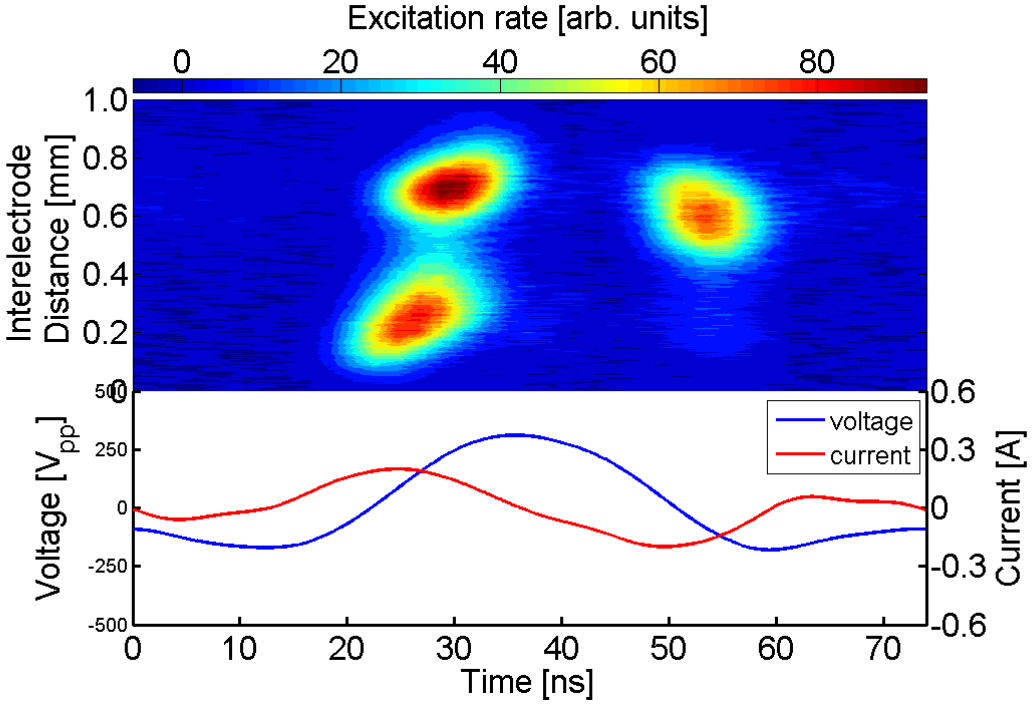
Excitation rate [arb. units]
0
20
40
60
80
Interelectrode Distance [mm]
1.0
0.8
0.6
0.4
0.2
0
500
250
0
-250
-500
Voltage [V_{pp}]
0.6
0.3
0
-0.3
-0.6
Current [A]
voltage
current
0
10
20
30
40
50
60
70
Time [ns]

n = 2

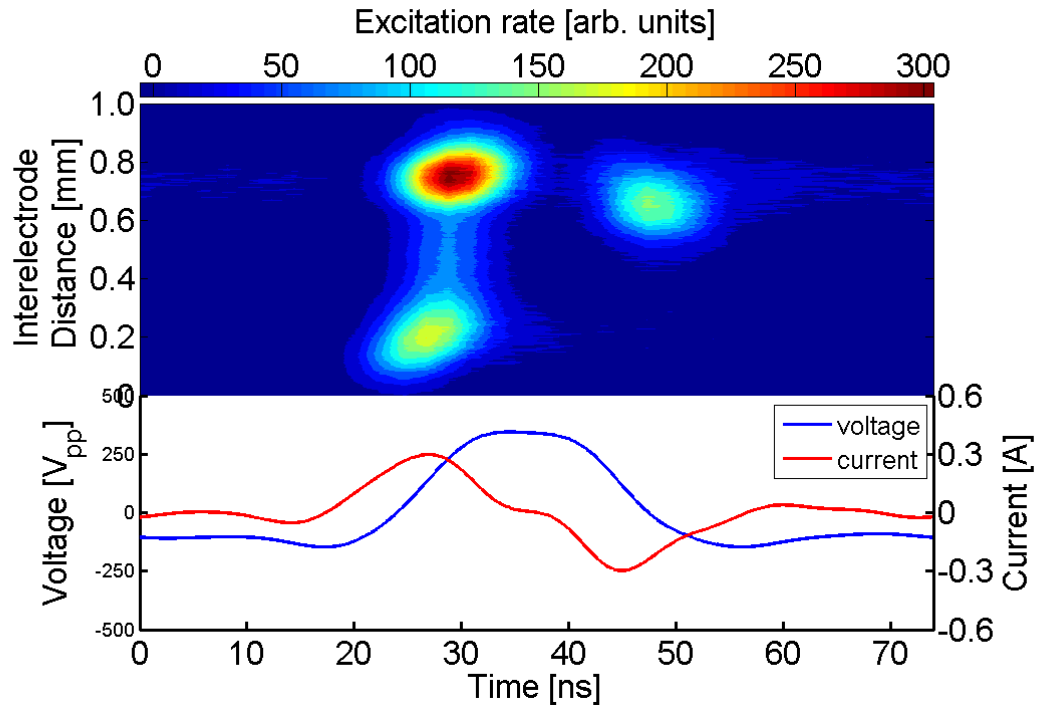
Excitation rate [arb. units]
0
50
100
150
200
250
300
Interelectrode Distance [mm]
1.0
0.8
0.6
0.4
0.2
0
500
250
0
-250
-500
Voltage [V_{pp}]
0.6
0.3
0
-0.3
-0.6
Current [A]
voltage
current
0
10
20
30
40
50
60
70
Time [ns]

n = 3

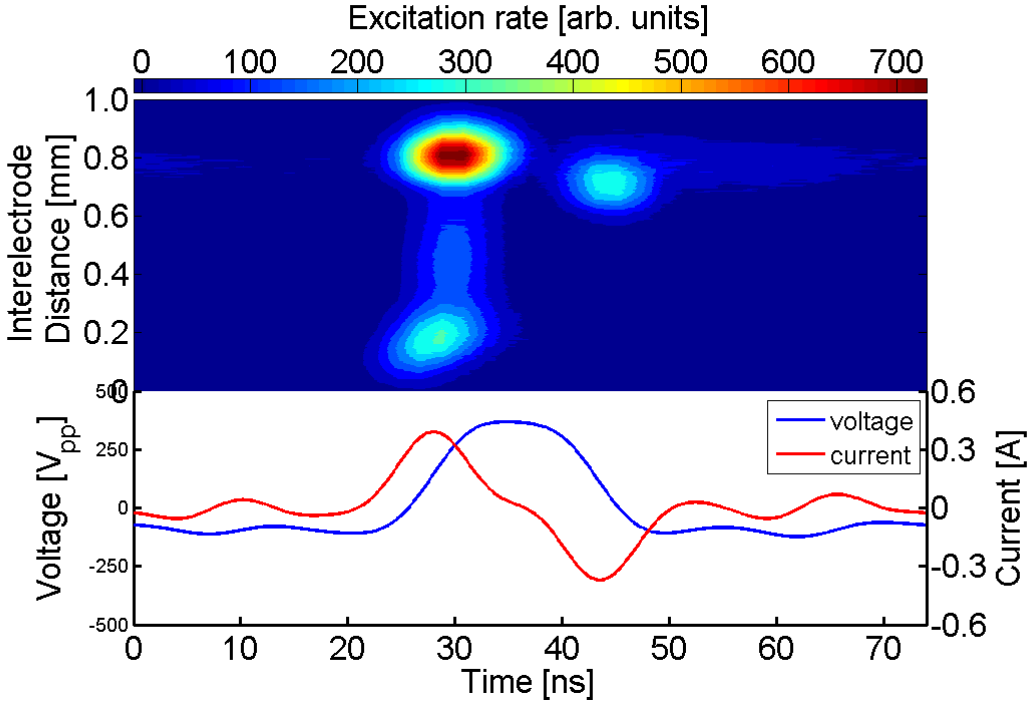

n = 4

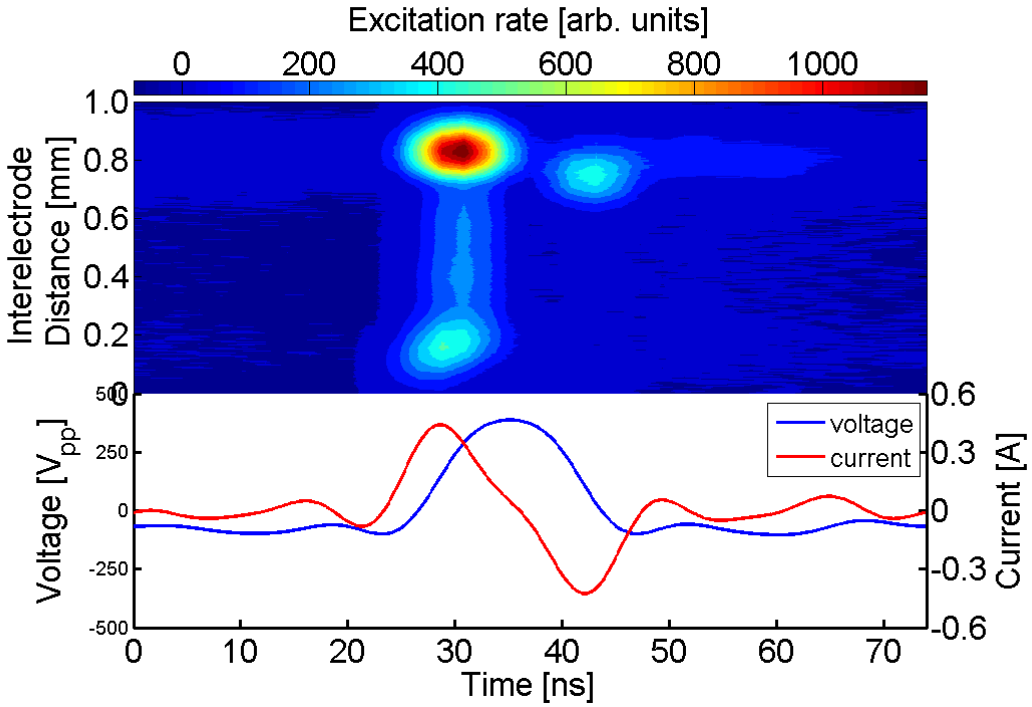

n = 5

Figure 5.2 Spatio-temporal excitation rates obtained from measurement of the emission line at 750.4 nm using PROES and applying peaks waveforms with n = 2-5 harmonics applied on a gas mixture of He with 0.05 % Ar and O_2 mixture 0.1 %. The peak-to-peak voltage waveform and the corresponding current waveforms for each harmonic are presented in the lower part of each image.

The amplitude of all of the excitation peaks mentioned above is correlated with the density of conduction current that represents the electron flux. The peak-to-peak current increases by increasing the number of harmonics; therefore, the intensity of the excitation maximum increases. Moreover, by increasing the number of harmonics, the distances between the excitation structures get larger, and they tend to get closer to the electrodes. Therefore, the thickness of plasma sheath gets smaller which indicates that the plasma density increases. Another factor affecting the excitation processes is increasing the amount of oxygen. As consequence, the excitation rate decreases, and this is due to the excited state being quenched by increasing the number of oxygen species in the discharge. These results are summarised and illustrated in figure 5.3.

In addition, the excitation peaks tend to be closer into the plasma bulk, which in turn increases the sheath thickness. There is a structure alongside the powered electrode being more obvious with n = 4 and n = 5 which might be described as a continuous excitation resulting from the minimum peaks of the applied voltage waveform. This structure also contracts when increasing the oxygen admixtures.

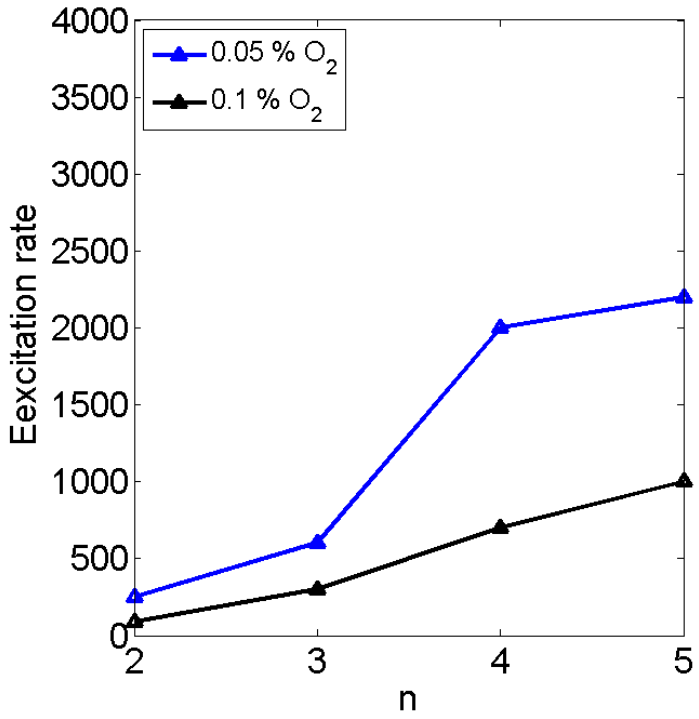

Figure 5.3 Summary of excitation rates as a function of the applied harmonics numbers 2-5 when peaks waveforms applied on the plasma with different percentages of O_2 admixtures.

Figures 5.4 and 5.5 show the space and phase electron impact excitation from applying valley waveforms with 480 Vpp and 490 Vpp on oxygen admixtures of 0.05 % and 0.1 % respectively. The behaviour of the plasma is almost the opposite of that in the case of peaks waveforms. It is also observed that there are three excitation peaks in each image: two of them at the grounded electrode while one is locate at the powered electrode in contrary to peaks waveforms. The first excitation structure at the grounded electrode at time between ~ 60 ns to ~ 74 ns occurs due to the fast sheath collapse due to the decrease in the voltage followed by fast sheath expansion at the powered electrode resulting in an excitation peak due to the field reversal as mentioned in the case of peaks waveforms. Another excitation peak originates when the voltage increases, inducing fast sheath expansion at the grounded electrode at time between 5 to 15 ns.

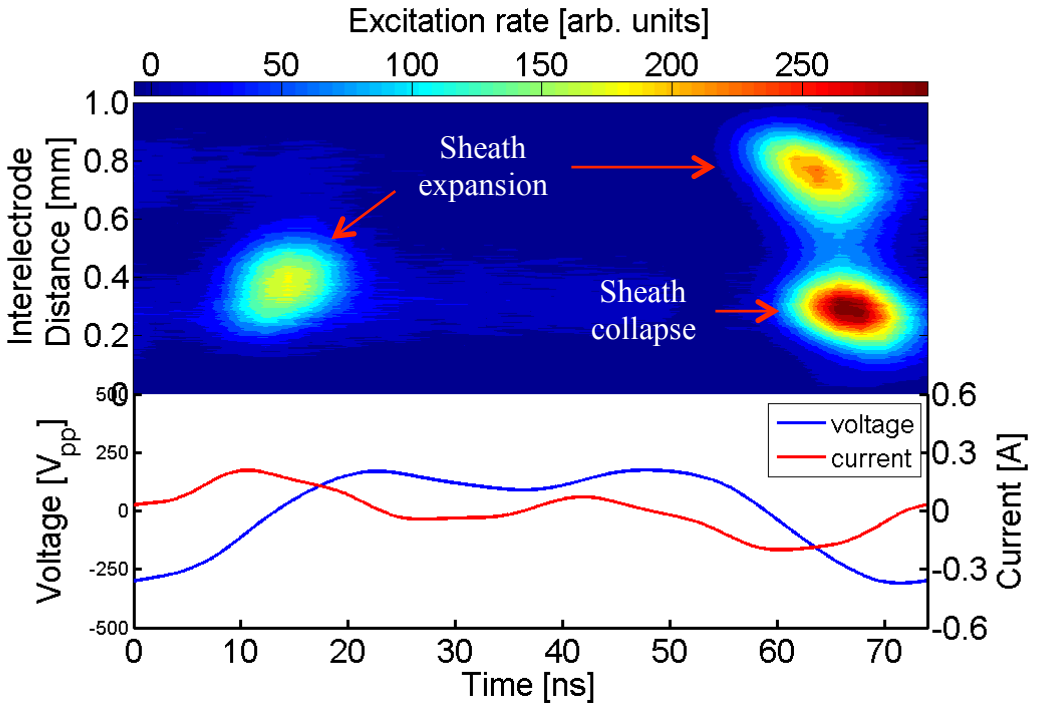
Excitation rate [arb. units]
0
50
100
150
200
250
Interelectrode Distance [mm]
1.0
0.8
0.6
0.4
0.2
0
Sheath expansion
Sheath collapse
Voltage [V_pp]
500
250
0
-250
-500
voltage
current
Current [A]
0.6
0.3
0
-0.3
-0.6
0
10
20
30
40
50
60
70
Time [ns]

n = 2

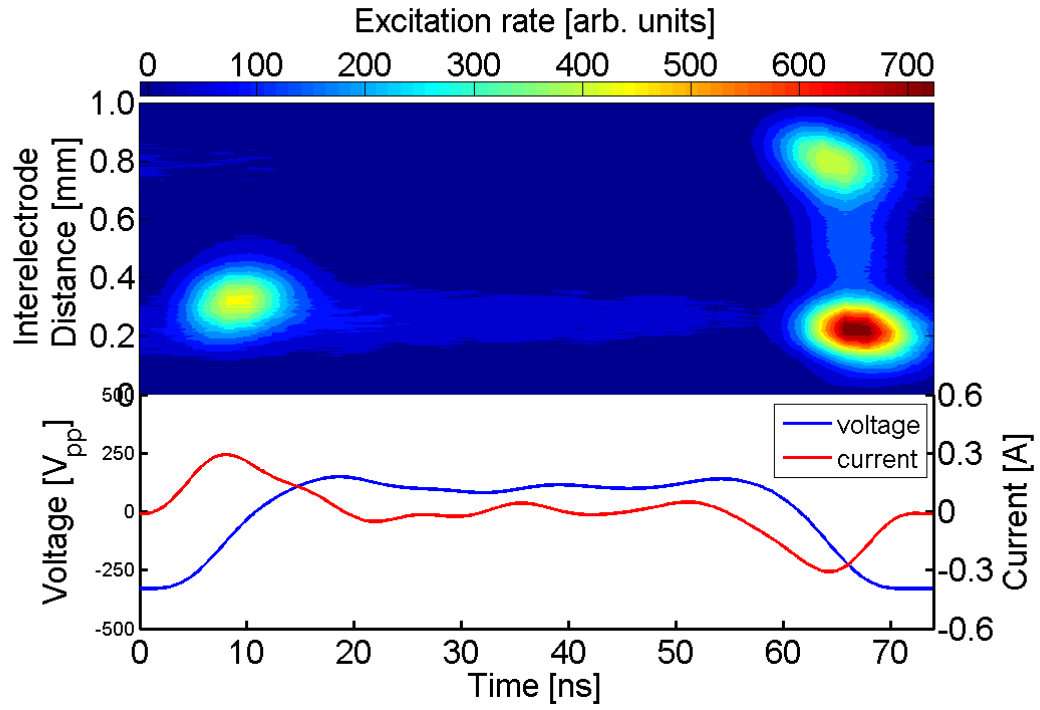
Excitation rate [arb. units]
0
100
200
300
400
500
600
700
Interelectrode Distance [mm]
1.0
0.8
0.6
0.4
0.2
0
Voltage [V_pp]
500
250
0
-250
-500
voltage
current
Current [A]
0.6
0.3
0
-0.3
-0.6
0
10
20
30
40
50
60
70
Time [ns]

n = 3

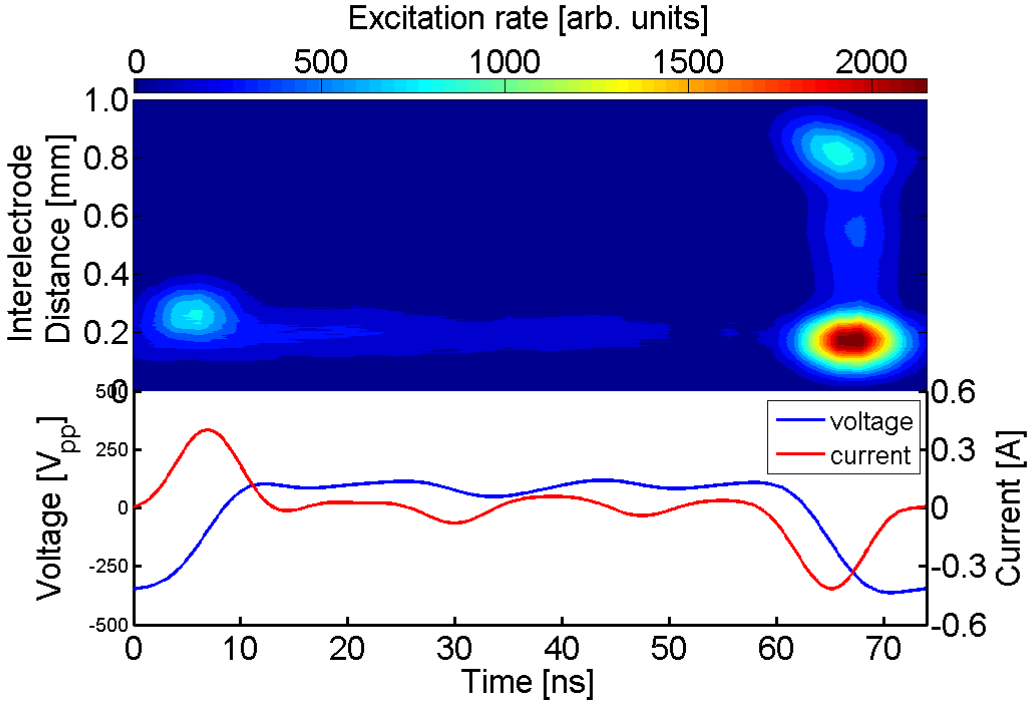

n = 4

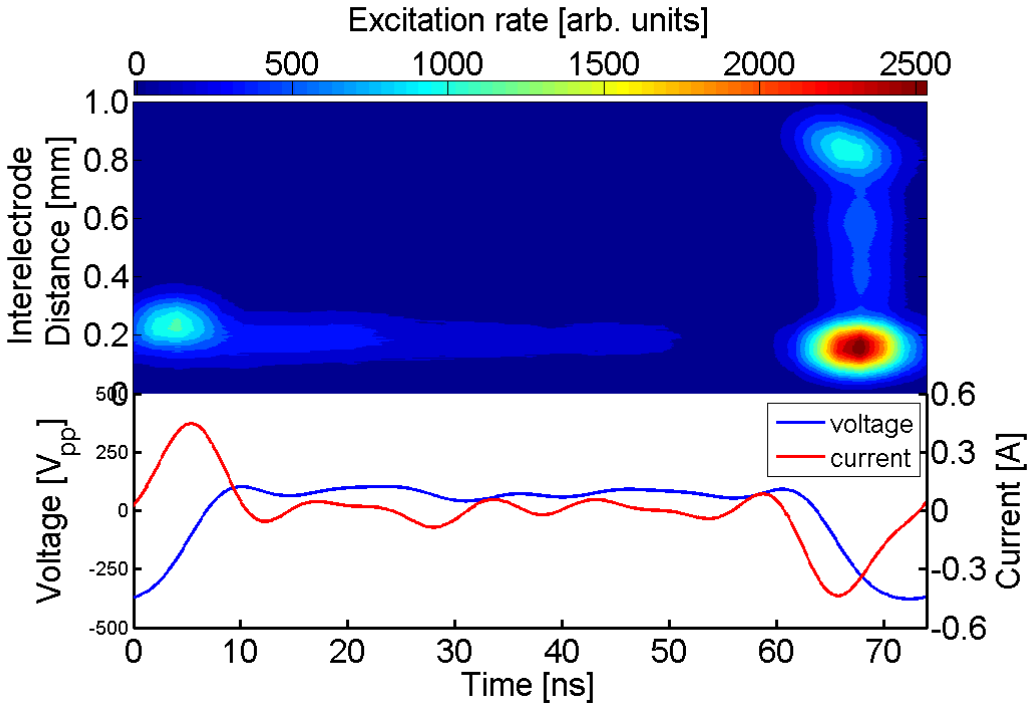

n = 5

Figure 5.4: Spatiotemporal excitation rates obtained from measurement of the emission line at 750.4 nm using PROES and applying valleys waveforms with n=2-5 harmonics applied on a gas mixture of He with 0.05 % Ar and O_2 mixture 0.05 %. The peak-to-peak voltage waveform and the corresponding current waveforms for each harmonic are presented in the lower part of each image.

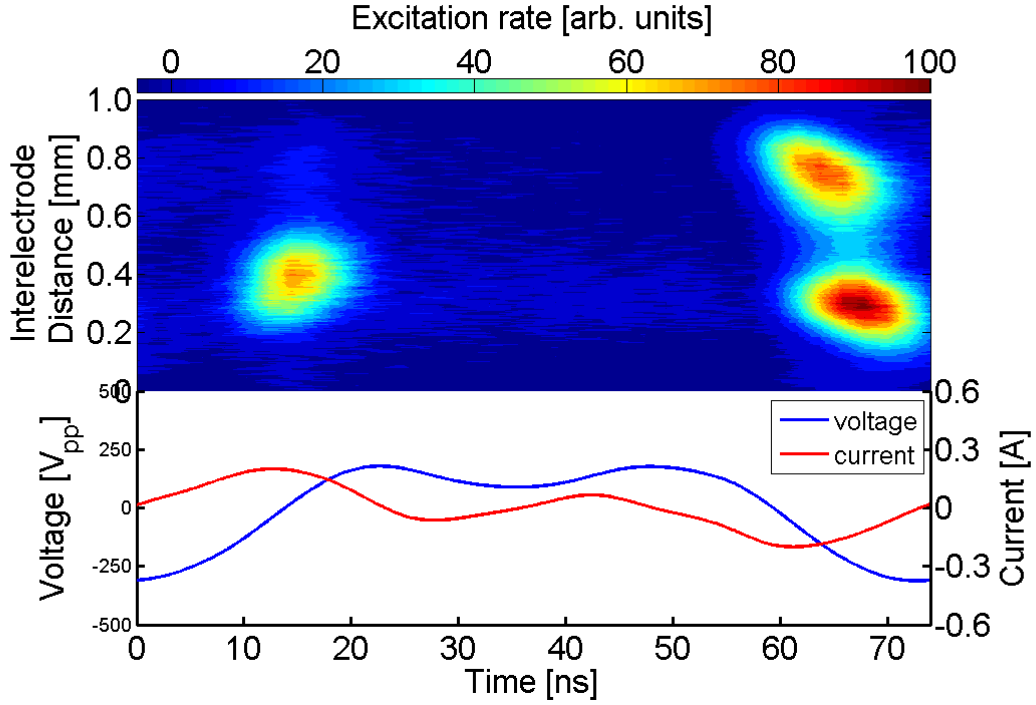
Excitation rate [arb. units]
0
20
40
60
80
100
Interelectrode Distance [mm]
1.0
0.8
0.6
0.4
0.2
0
500
250
0
-250
-500
Voltage [V_{pp}]
0.6
0.3
0
-0.3
-0.6
Current [A]
voltage
current
0
10
20
30
40
50
60
70
Time [ns]

n = 2

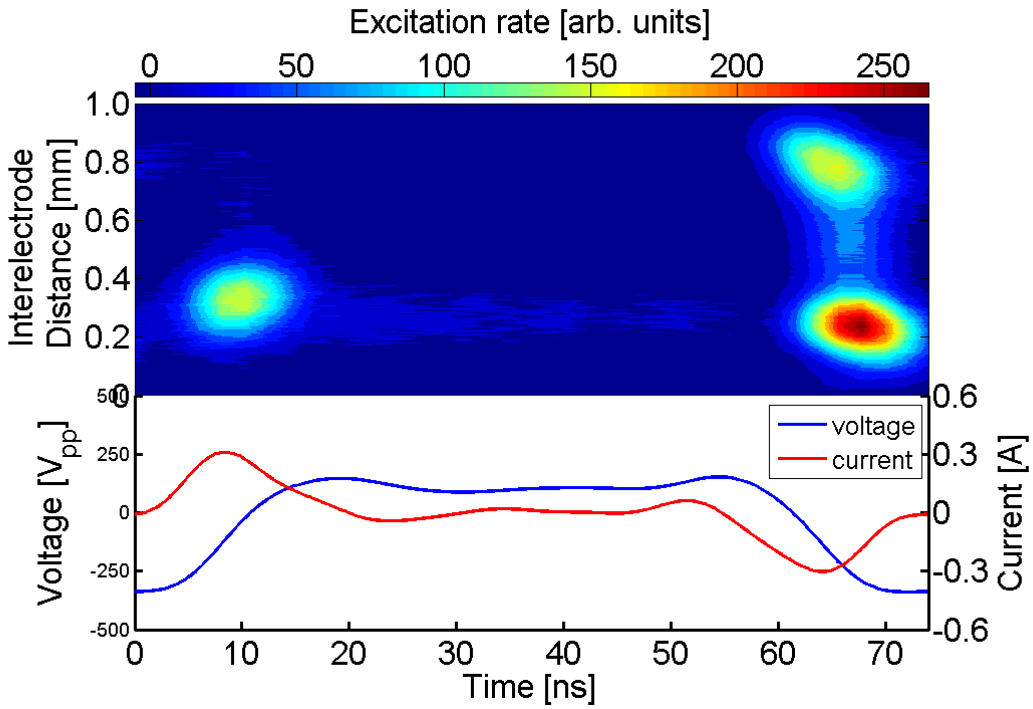
Excitation rate [arb. units]
0
50
100
150
200
250
Interelectrode Distance [mm]
1.0
0.8
0.6
0.4
0.2
0
500
250
0
-250
-500
Voltage [V_{pp}]
0.6
0.3
0
-0.3
-0.6
Current [A]
voltage
current
0
10
20
30
40
50
60
70
Time [ns]

n = 3

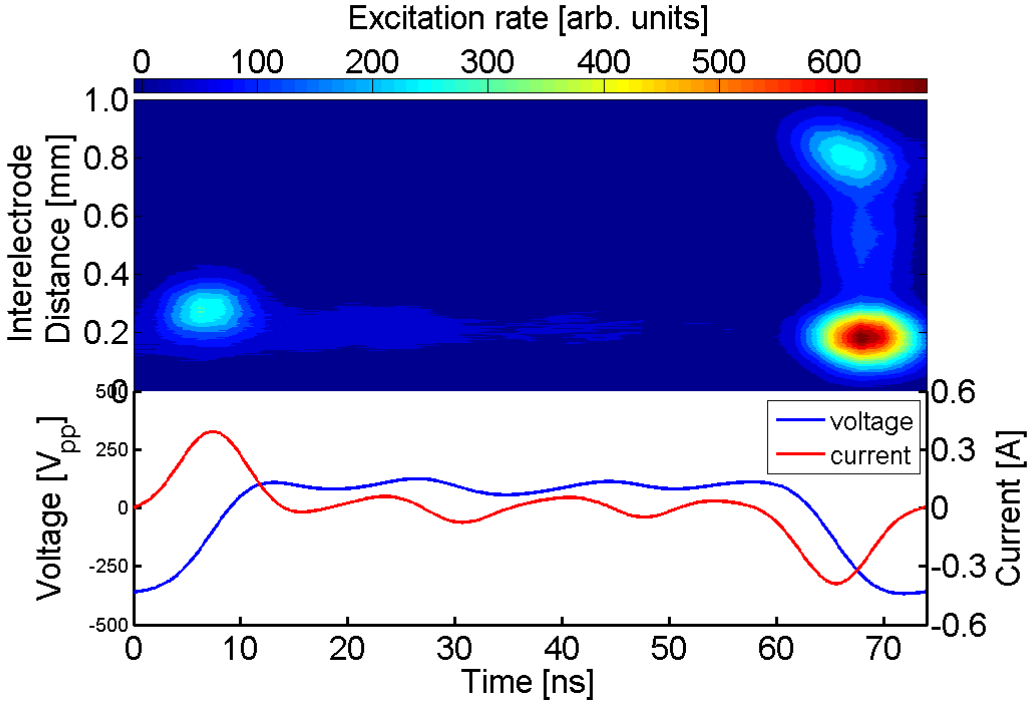

n = 4

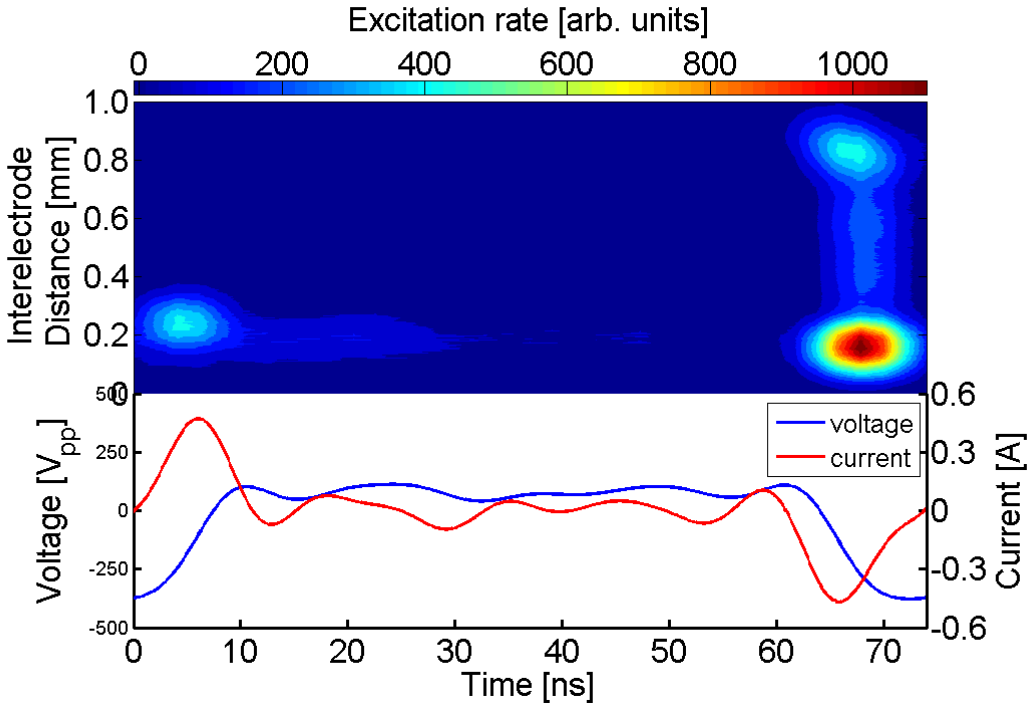

n = 5

Figure 5.5 Spatio-temporal excitation rates obtained from measurement of the emission line at 750.4 nm using PROES and applying valleys waveforms with n = 2-5 harmonics applied on a gas mixture of He with 0.05 % Ar and O_2 mixture 0.1 %. The peak-to-peak voltage waveform and the corresponding current waveforms for each harmonic are presented in the lower part of each image.

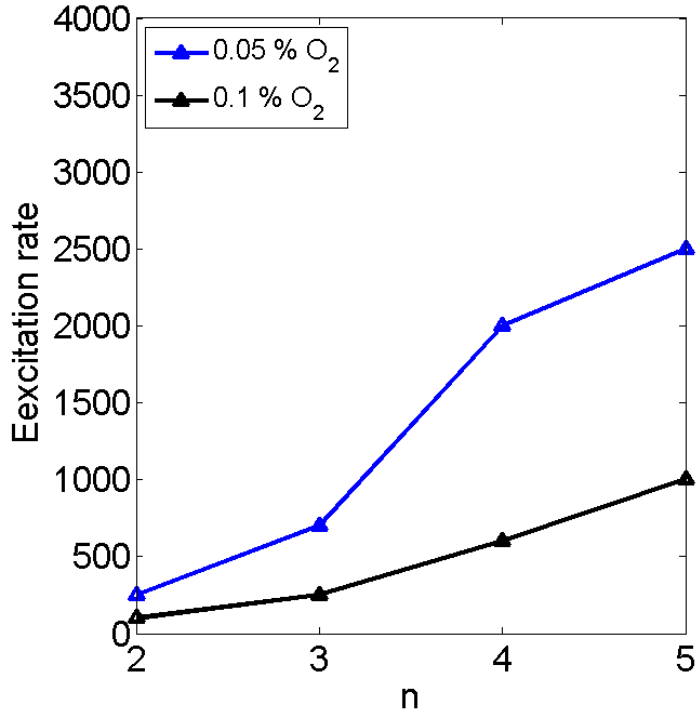

Figure 5.6 Summary of excitation rates as a function of the applied harmonics numbers 2-5 when valleys waveforms applied on the plasma with different percentages of O_2 admixtures.

The excitation dynamics in this case are affected by the same factor mentioned in the case of applying peaks waveforms. They are influenced by increasing the number of harmonics as the excitation rate increase. Also the plasma density increases as observed of the sheath thickness that is getting smaller with increasing the applied harmonics. However, the plasma density decreases with a greater concentration of oxygen being added to the discharge due to the influence of oxygen molecules on the excited state [104]. Moreover, the excitation rates decrease consequently. These results are extracted from figures 5.4 and 5.5 and shown in figure 5.6.

5.1.2 Electrical asymmetry effect of peaks-type waveforms on electronegative plasma

Driving APPs by TVWs, particularly peaks and valleys waveforms with different maximum and minimum excursions respectively, leads to the production of DC self-bias. The DC self-bias initiated due to the EAE but not geometrically as the APPJ used in this work is geometrically

symmetric. The plasma is operated in a gas mixture of helium with small amount of argon (0.05 %), used for optical diagnostic reasons and different amounts of oxygen. The driving RF voltage of 13.56 MHz with its harmonics up to five are used. The applied peak-to peak voltage was fixed at 480 V_{pp} and 490 V_{pp} for different admixtures of oxygen 0.05 % and 0.1 % respectively. The measured DC self-bias voltages resulted from the application of peaks waveform ($\theta = 0$) and valleys waveform ($\theta = \pi$) as a function of the applied harmonics are shown in figure 5.7.

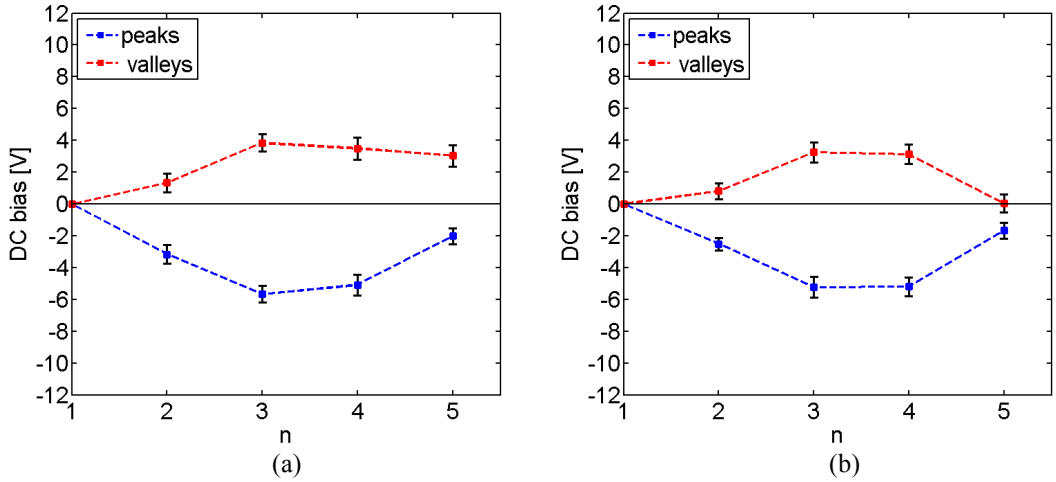

Figure 5.7: DC self-bias voltages measured as a function of harmonics varied between 1 to 5 harmonics for peaks waveforms (blue) and valleys waveforms (red) at (a) 480 V_{pp} with 0.05 % O_2 and (b) 490 V_{pp} with 0.1 % O_2.

The DC self-bias obtained from the peaks waveform represented in blue marks for each harmonic number while the red marks show the DC self-bias obtained from the application of valleys waveforms, and the lines between the marks are only for eye guide. Due to the uncertainty of the bias voltage probe, the measured DC self-bias for the first harmonic has been shifted up by ~ 0.65 V. The peaks waveforms represents negative self-bias while valleys waveforms show positive self-bias voltages. In all of these conditions, the DC bias almost follows the same trend starting with low values at n = 2 and increases to reach the maximum at n = 3 and then decreases at n = 4 down to n = 5. The higher DC bias voltage values are dominated by peaks waveforms although peaks and valleys waveforms both are operated at the same peak-to-peak voltages. By increasing

the concentration of oxygen, an obvious reduction in the DC self-bias voltages is observed in all conditions. This may due the influence of electronegativity of oxygen admixtures.

5.2 Sawtooth-type waveforms

5.2.1 Excitation dynamics

The plasma operated in a gas mixture of oxygen, with helium as a feed gas and a small amount of argon (0.05 %) used only for optical diagnostic purposes, and it is known that it does not affect the plasma interactions. Here, the spatio-temporal electron impact excitation is measured by applying sawtooth-type with adding different amounts of oxygen. Figures 5.8, 5.9, 5.10, 5.11 and 5.12 show the space and phase electron impact excitation by applying sawtooth-up waveforms on APPs using oxygen mixtures of 0.05 %, 0.1 %, 0.2 %, 0.3 % and 0.5 % as driven by 480 V_{pp} and 540 V_{pp}, 570 V_{pp} , 580 V_{pp} and 615 V_{pp} respectively. All images specification explained in the case of peaks-types waveforms are also represented here.

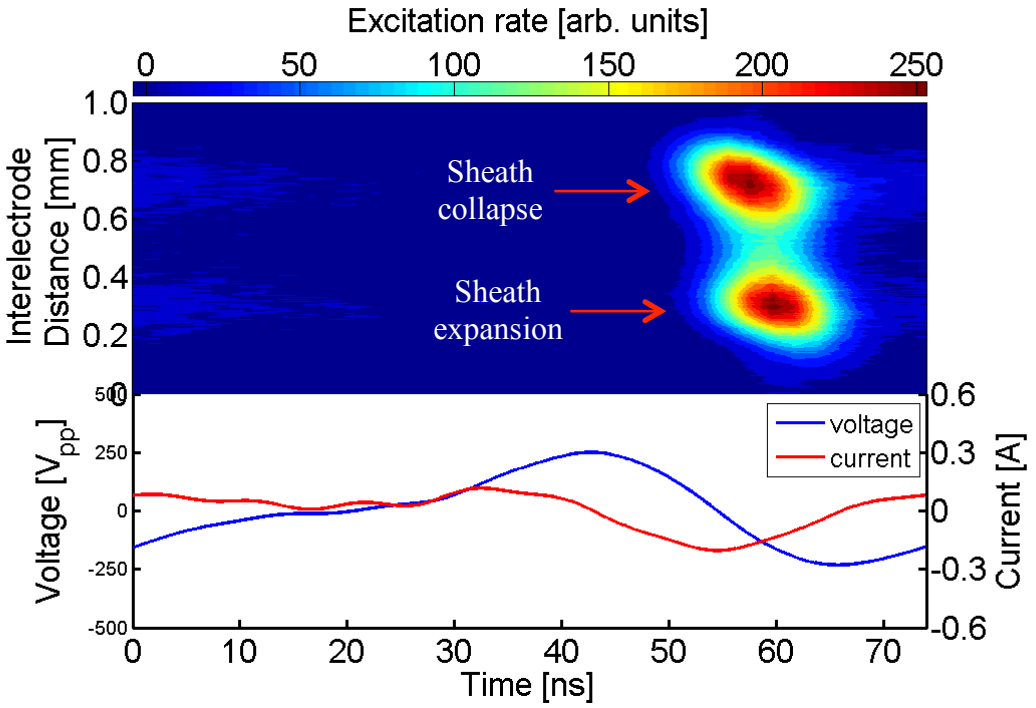
Excitation rate [arb. units]
0
50
100
150
200
250
Interelectrode Distance [mm]
1.0
0.8
0.6
0.4
0.2
0
Sheath collapse
Sheath expansion
Voltage [V_pp]
500
250
0
-250
-500
voltage
current
Current [A]
0.6
0.3
0
-0.3
-0.6
0
10
20
30
40
50
60
70
Time [ns]

n = 2

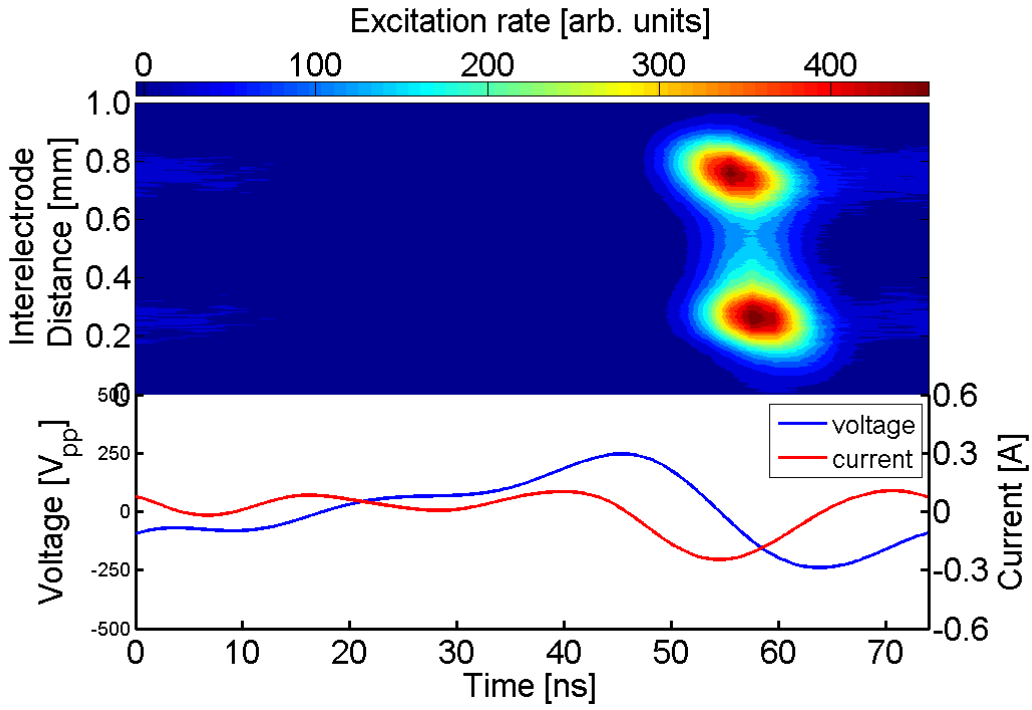
Excitation rate [arb. units]
0
100
200
300
400
Interelectrode Distance [mm]
1.0
0.8
0.6
0.4
0.2
0
Voltage [V_pp]
500
250
0
-250
-500
voltage
current
Current [A]
0.6
0.3
0
-0.3
-0.6
0
10
20
30
40
50
60
70
Time [ns]

n = 3

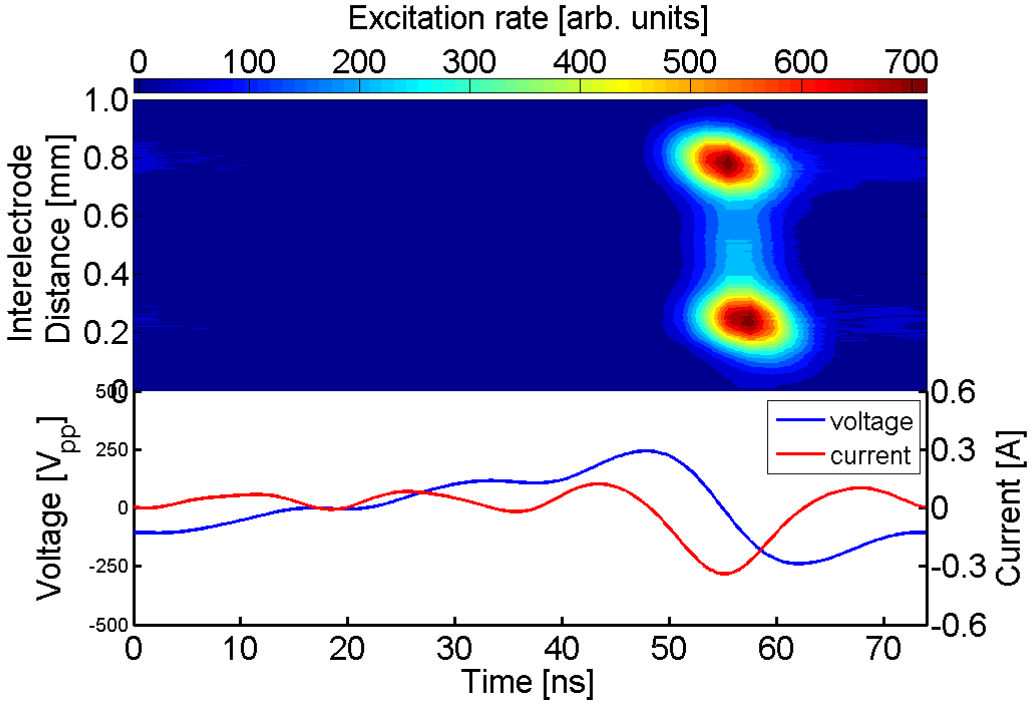

n = 4

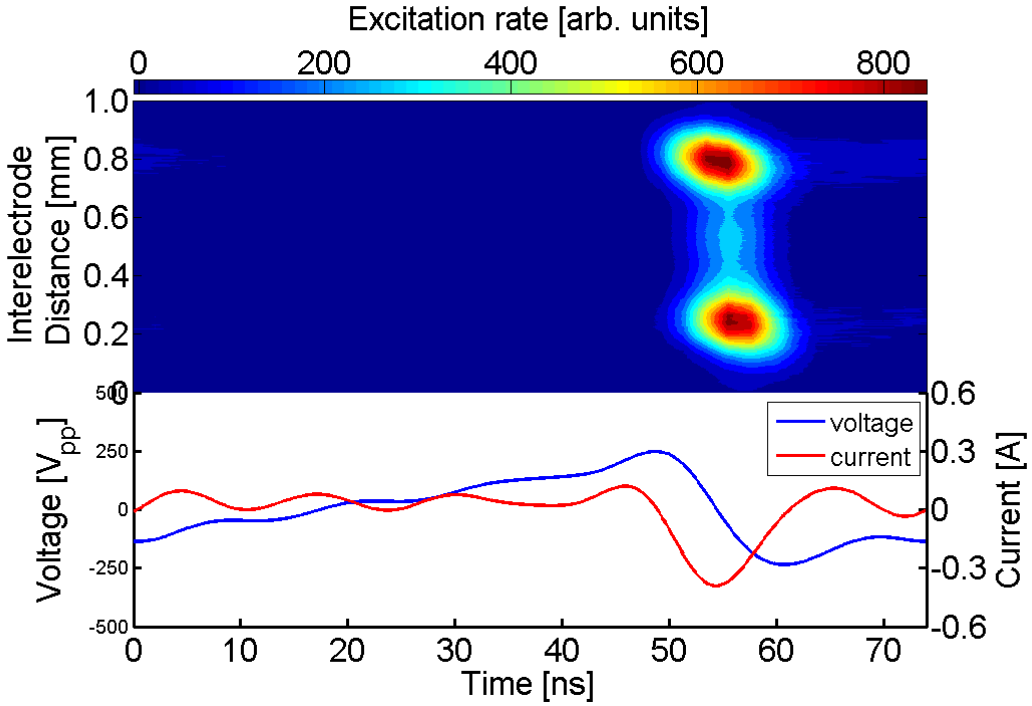

n = 5

Figure 5.8 Spatio-temporal excitation rates obtained from measurement of the emission line at 750.4 nm using PROES and applying sawtooth-up waveforms with n = 2-5 harmonics applied on a gas mixture of He with 0.05 % Ar and O_2 mixture 0.05 %. The peak-to-peak voltage waveform and the corresponding current waveforms for each harmonic are presented in the lower part of each image.

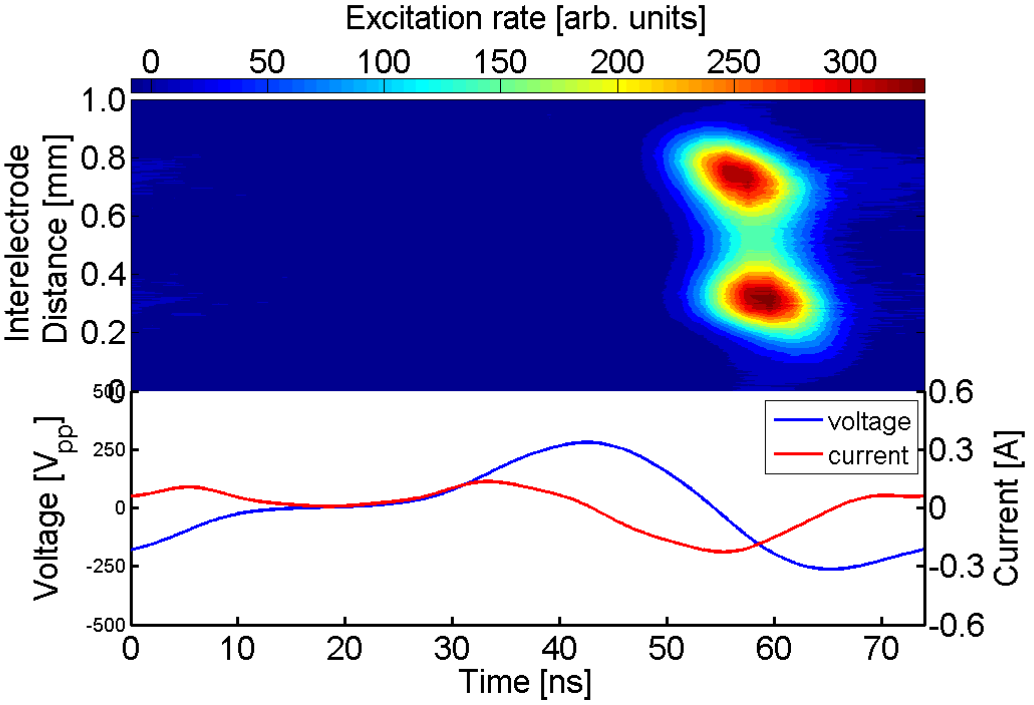
Excitation rate [arb. units]
0
50
100
150
200
250
300
Interelectrode Distance [mm]
1.0
0.8
0.6
0.4
0.2
0
Voltage [V_{pp}]
500
250
0
-250
-500
voltage
current
Current [A]
0.6
0.3
0
-0.3
-0.6
0
10
20
30
40
50
60
70
Time [ns]

n = 2

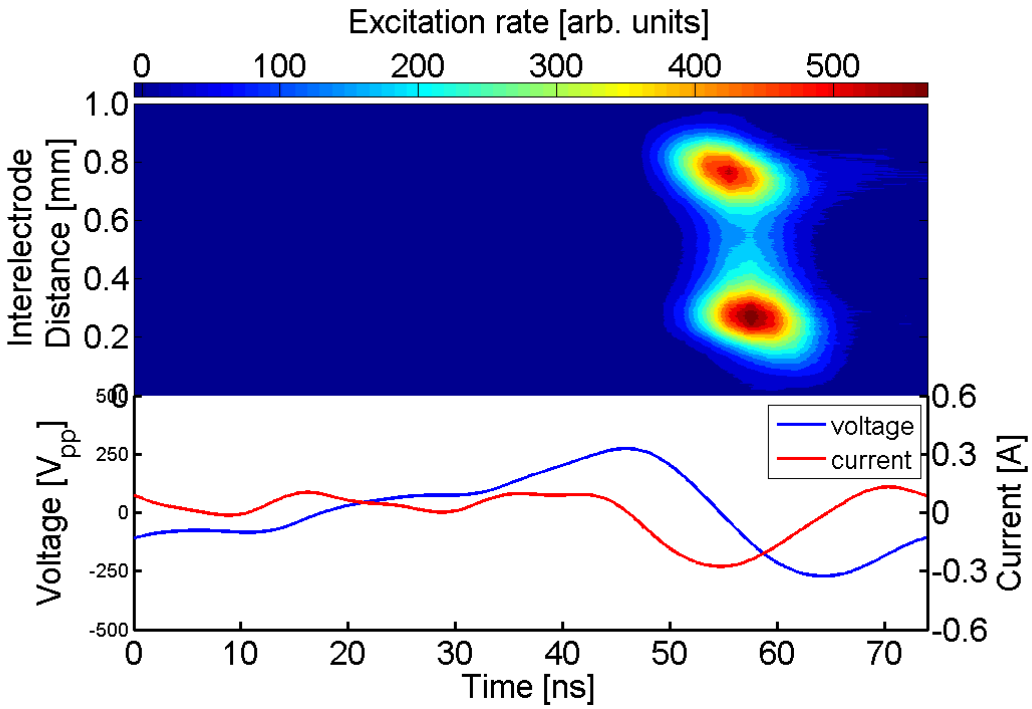
Excitation rate [arb. units]
0
100
200
300
400
500
Interelectrode Distance [mm]
1.0
0.8
0.6
0.4
0.2
0
Voltage [V_{pp}]
500
250
0
-250
-500
voltage
current
Current [A]
0.6
0.3
0
-0.3
-0.6
0
10
20
30
40
50
60
70
Time [ns]

n = 3

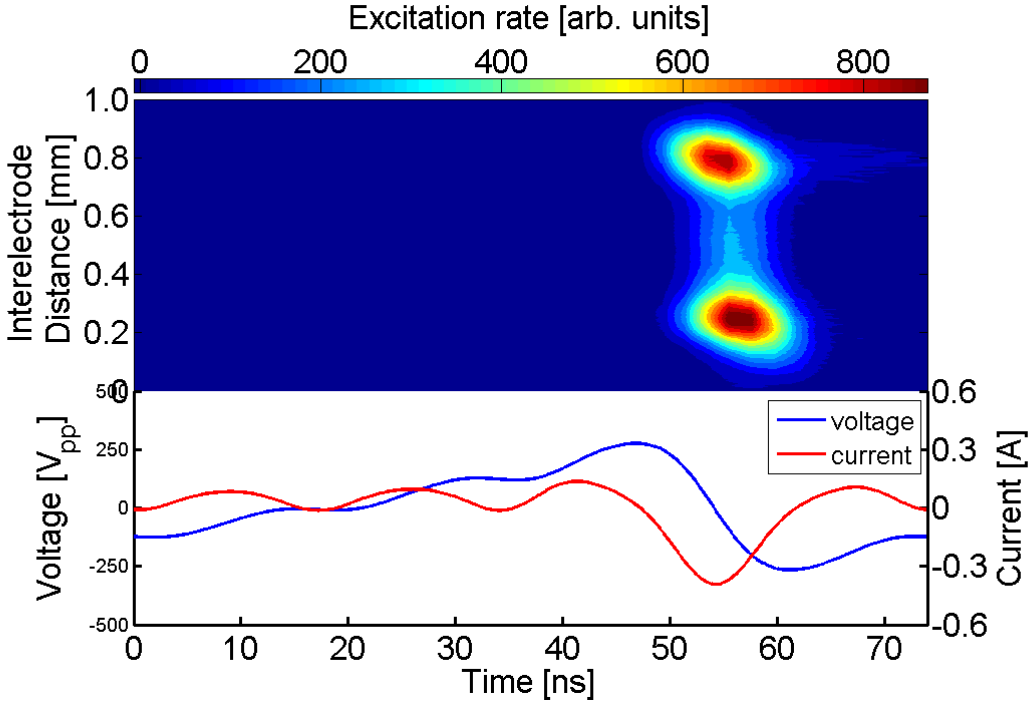

n = 4

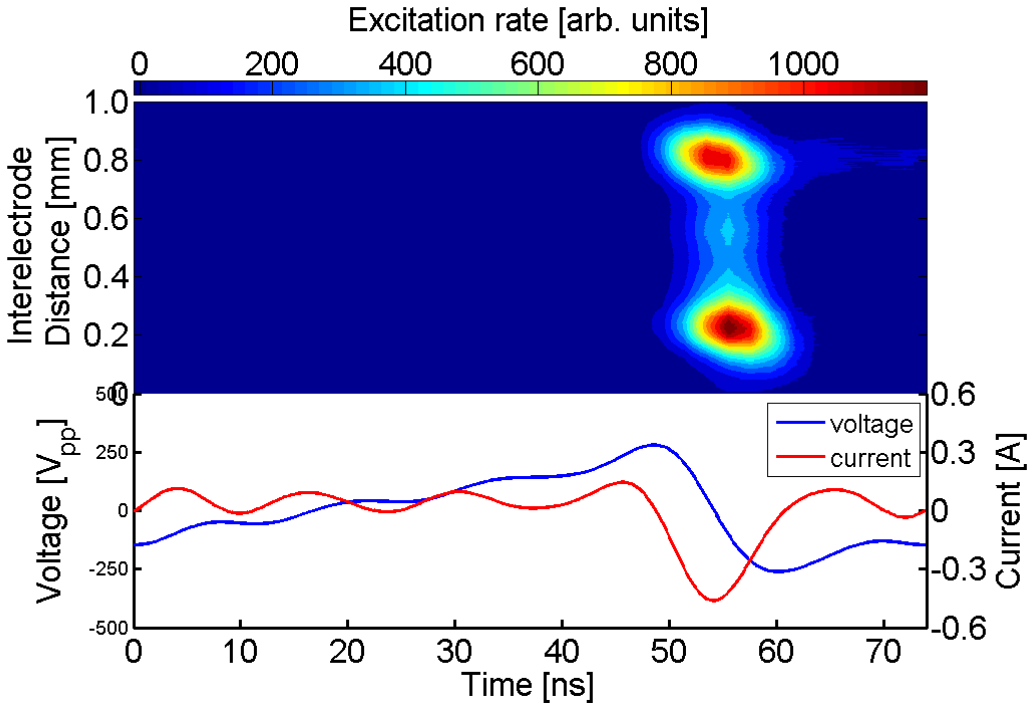

n = 5

Figure 5.9 Spatio-temporal excitation rates obtained from measurement of the emission line at 750.4 nm using PROES and applying sawtooth-up waveforms with n = 2-5 harmonics applied on a gas mixture of He with 0.05 % Ar and O_2 mixture 0.1 %. The peak-to-peak voltage waveform and the corresponding current waveforms for each harmonic are presented in the lower part of each image.

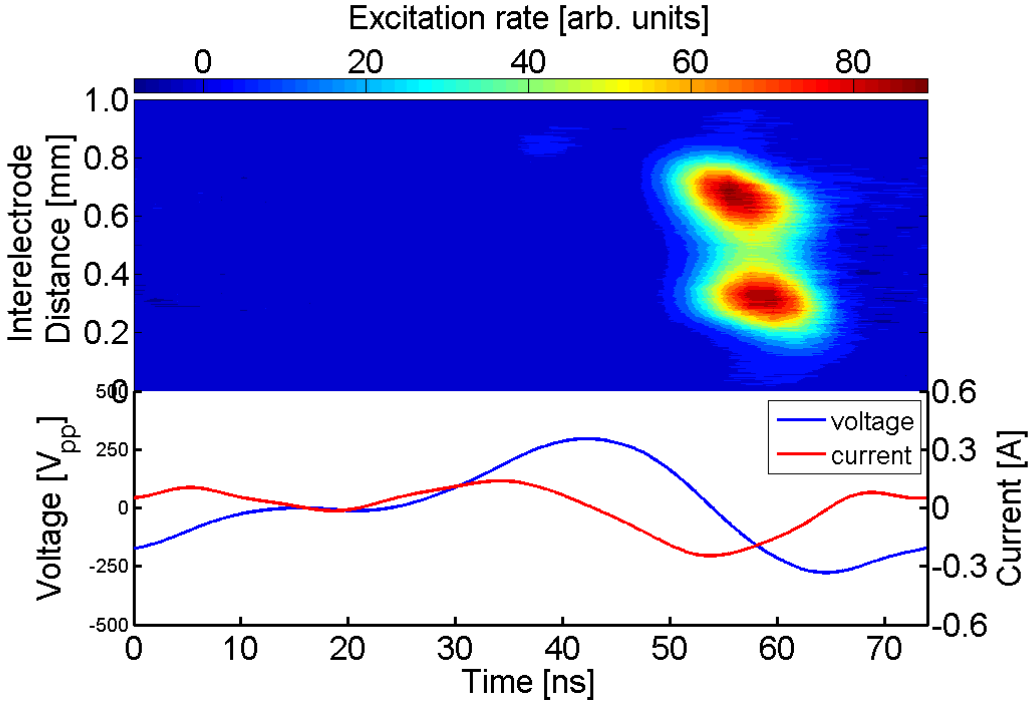
Excitation rate [arb. units]
0
20
40
60
80
Interelectrode Distance [mm]
1.0
0.8
0.6
0.4
0.2
0
voltage
current
Voltage [Vpp]
500
250
0
-250
-500
Current [A]
0.6
0.3
0
-0.3
-0.6
0
10
20
30
40
50
60
70
Time [ns]

n = 2

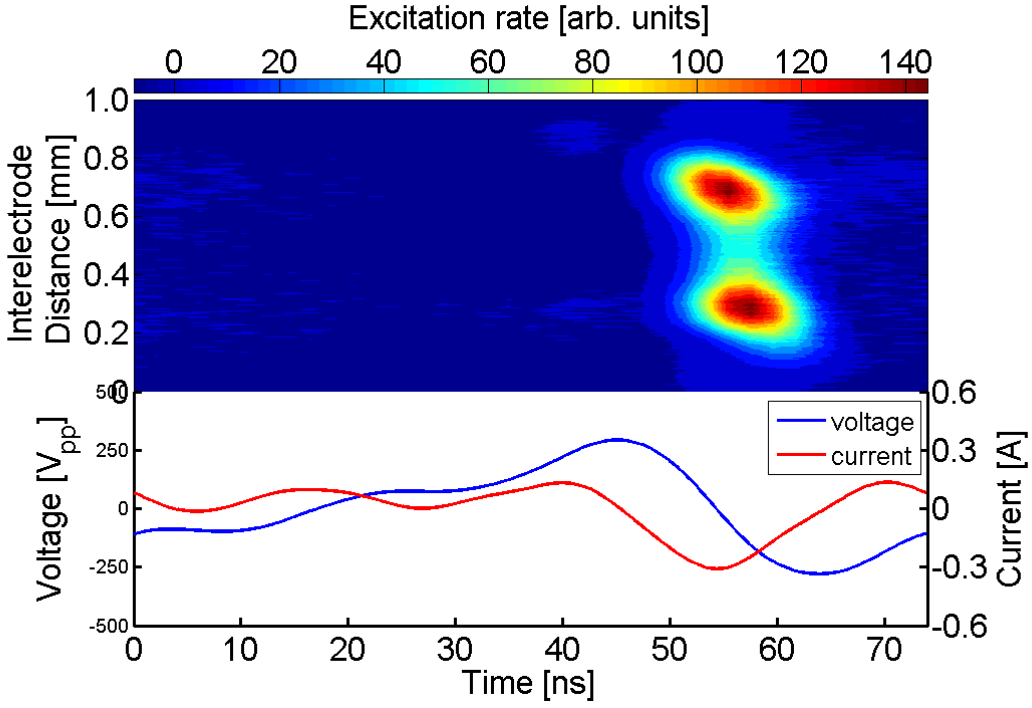
Excitation rate [arb. units]
0
20
40
60
80
100
120
140
Interelectrode Distance [mm]
1.0
0.8
0.6
0.4
0.2
0
voltage
current
Voltage [Vpp]
500
250
0
-250
-500
Current [A]
0.6
0.3
0
-0.3
-0.6
0
10
20
30
40
50
60
70
Time [ns]

n = 3

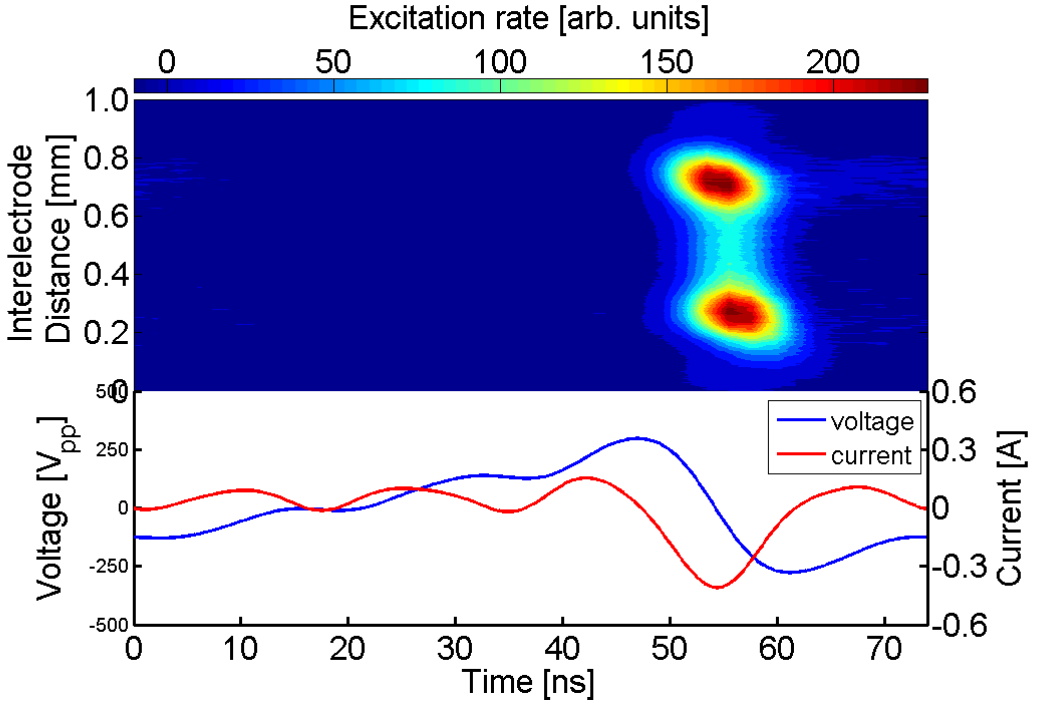

n = 4

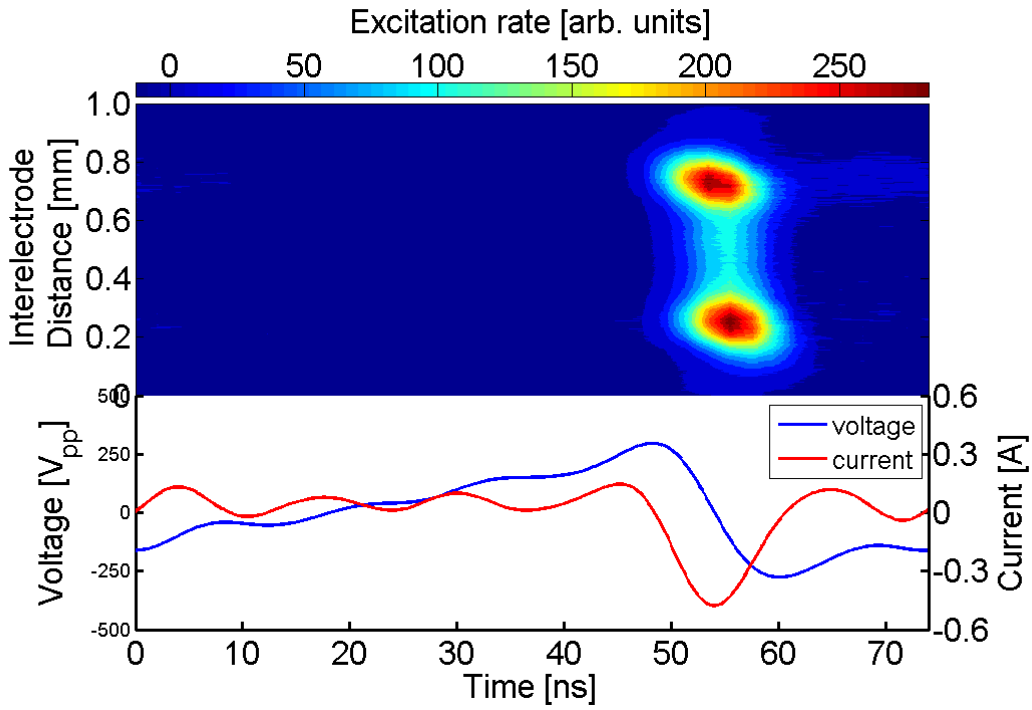

n = 5

Figure 5.10 Spatio-temporal excitation rates obtained from measurement of the emission line at 750.4 nm using PROES and applying sawtooth-up waveforms with n = 2-5 harmonics applied on a gas mixture of He with 0.05 % Ar and O_2 mixture 0.2 %. The peak-to-peak voltage waveform and the corresponding current waveforms for each harmonic are presented in the lower part of each image.

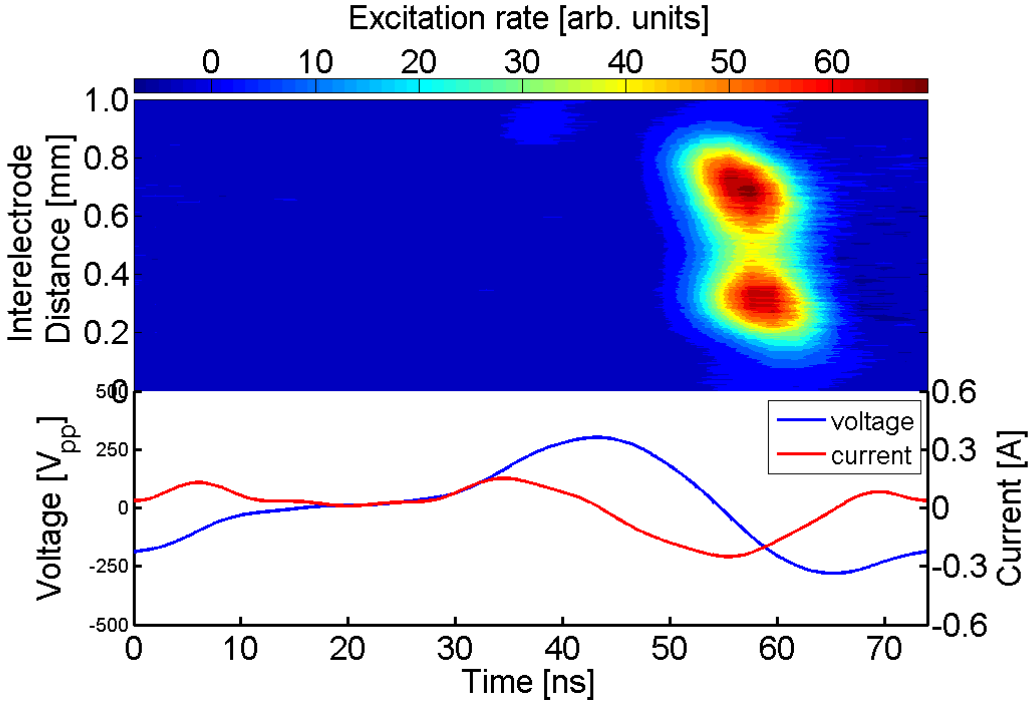
Excitation rate [arb. units]
0
10
20
30
40
50
60
Interelectrode Distance [mm]
1.0
0.8
0.6
0.4
0.2
0
Voltage [Vpp]
500
250
0
-250
-500
voltage
current
Current [A]
0.6
0.3
0
-0.3
-0.6
0
10
20
30
40
50
60
70
Time [ns]

n = 2

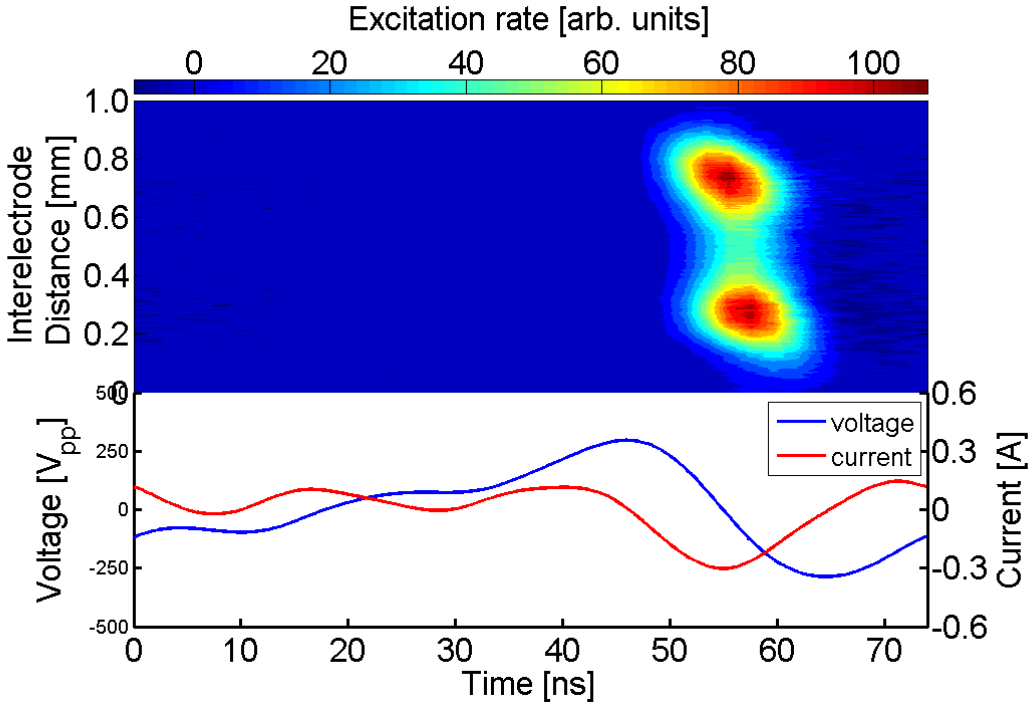
Excitation rate [arb. units]
0
20
40
60
80
100
Interelectrode Distance [mm]
1.0
0.8
0.6
0.4
0.2
0
Voltage [Vpp]
500
250
0
-250
-500
voltage
current
Current [A]
0.6
0.3
0
-0.3
-0.6
0
10
20
30
40
50
60
70
Time [ns]

n = 3

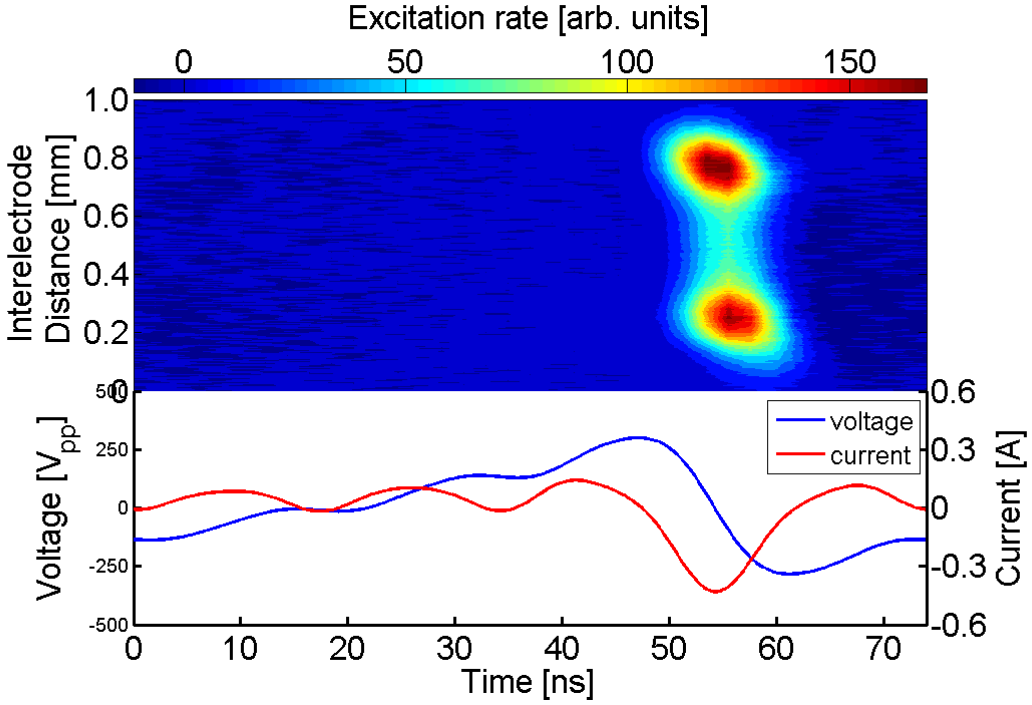

n = 4

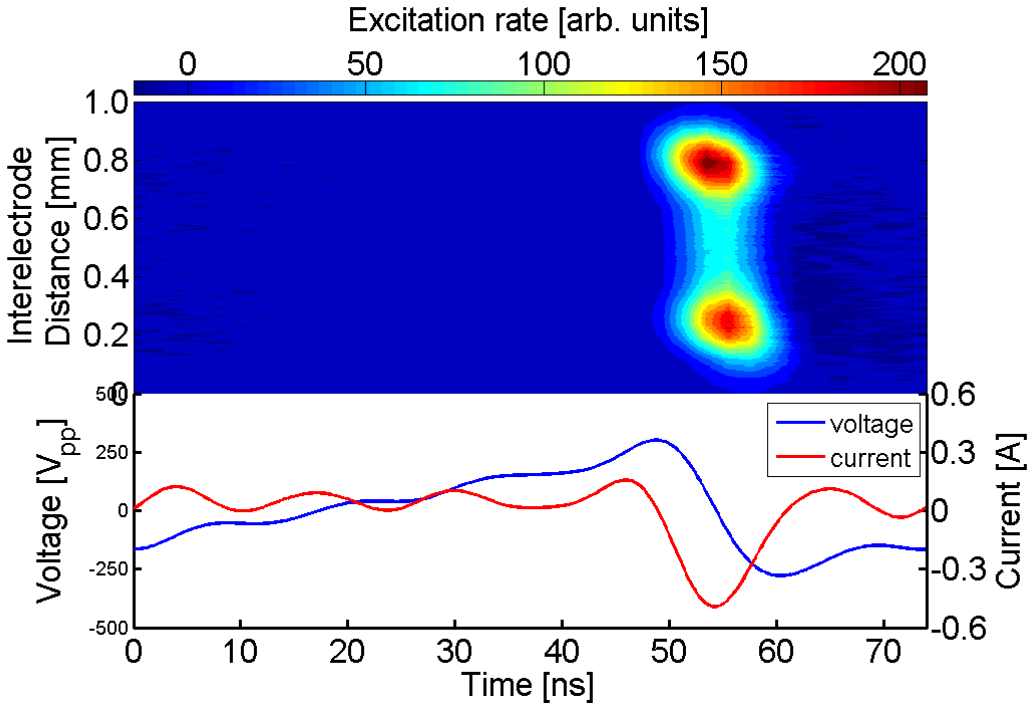

n = 5

Figure 5.11 Spatio-temporal excitation rates obtained from measurement of the emission line at 750.4 nm using PROES and applying sawtooth-up waveforms with n = 2-5 harmonics applied on a gas mixture of He with 0.05 % Ar and O_2 mixture 0.3 %. The peak-to-peak voltage waveform and the corresponding current waveforms for each harmonic are presented in the lower part of each image.

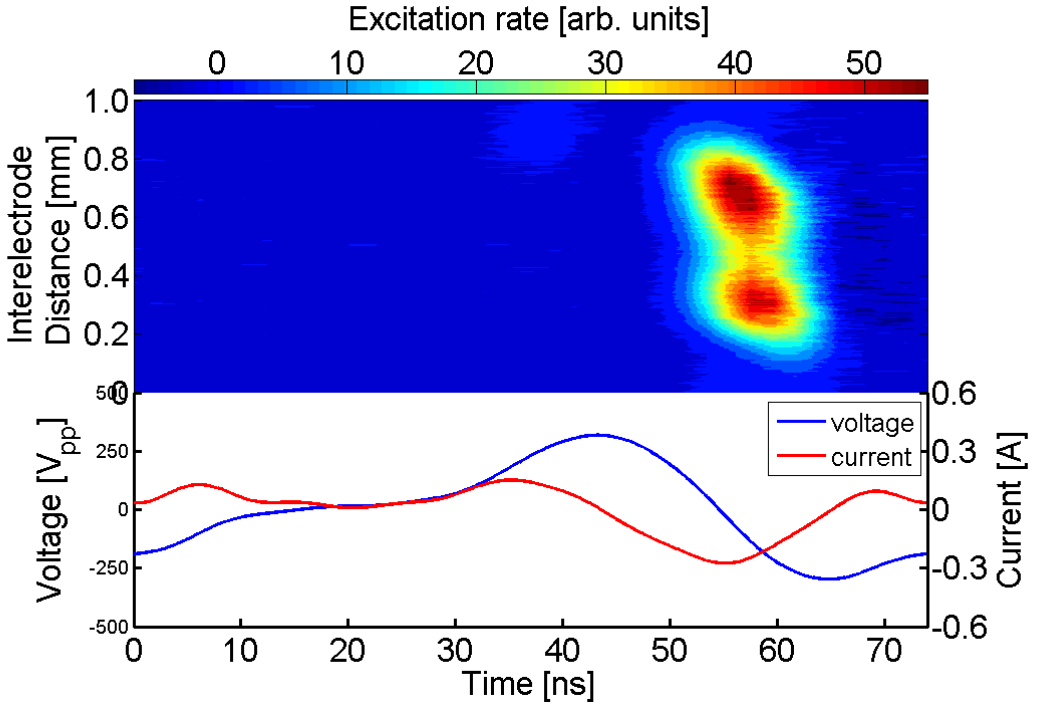
Excitation rate [arb. units]
0
10
20
30
40
50
Interelectrode Distance [mm]
1.0
0.8
0.6
0.4
0.2
0
Voltage [Vpp]
500
250
0
-250
-500
Current [A]
0.6
0.3
0
-0.3
-0.6
voltage
current
0
10
20
30
40
50
60
70
Time [ns]

n = 2

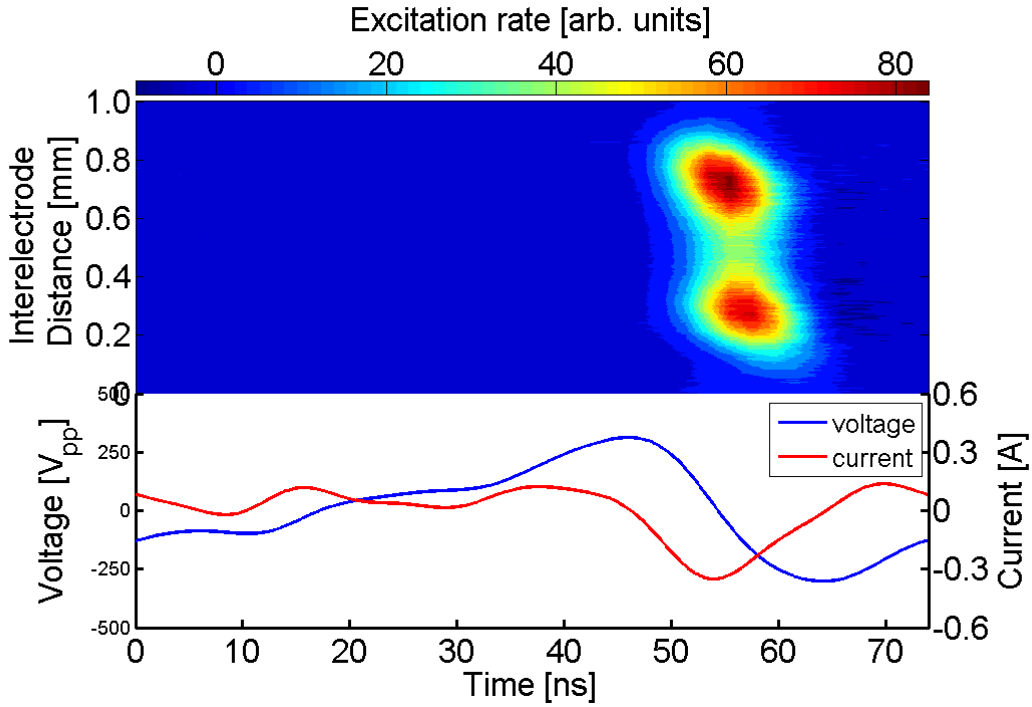
Excitation rate [arb. units]
0
20
40
60
80
Interelectrode Distance [mm]
1.0
0.8
0.6
0.4
0.2
0
Voltage [Vpp]
500
250
0
-250
-500
Current [A]
0.6
0.3
0
-0.3
-0.6
voltage
current
0
10
20
30
40
50
60
70
Time [ns]

n = 3

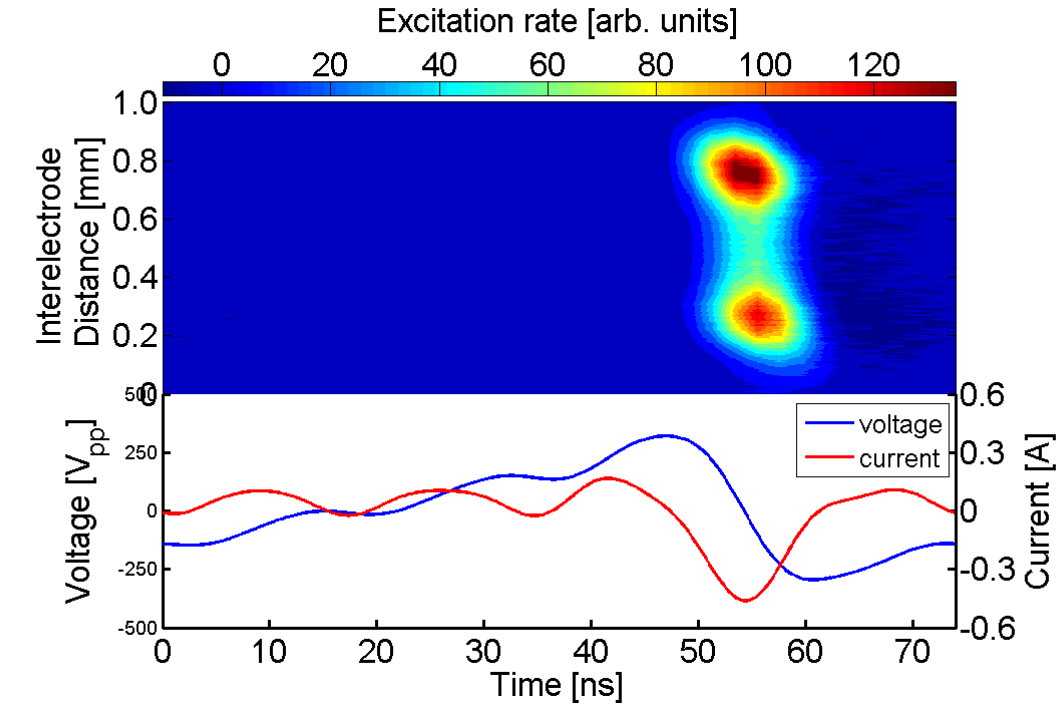

n = 4

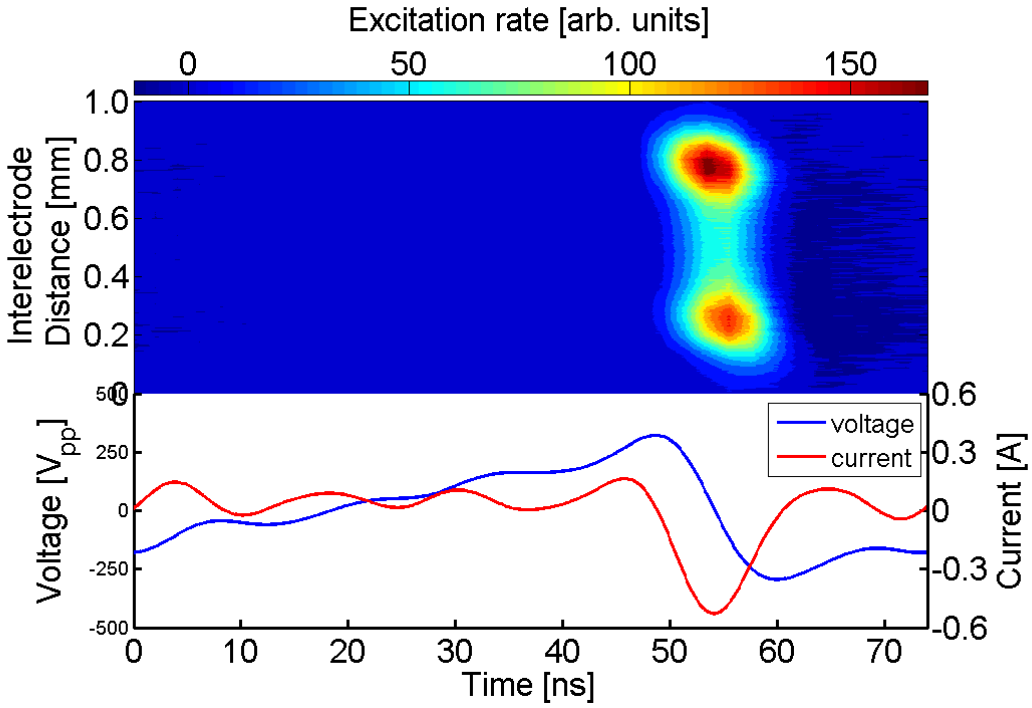

n = 5

Figure 5.12 Spatio-temporal excitation rates obtained from measurement of the emission line at 750.4 nm using PROES and applying sawtooth-up waveforms with n = 2-5 harmonics applied on a gas mixture of He with 0.05 % Ar and O_2 mixture 0.5 %. The peak-to-peak voltage waveform and the corresponding current waveforms for each harmonic are presented in the lower part of each image.

As one can see, in all cases, there are two excitation peaks: one at the grounded electrode while another excitation structure is located at the powered electrode. The rapid increase in the voltage at time between ~ 50 to ~ 65 ns induces a fast sheath expansion at the grounded electrode where electrons are accelerated away from the electrode toward the plasma bulk and then an excitation peak is initiated close to the grounded electrode. Simultaneously, another excitation peak located at the powered electrode occurs through the intensive sheath collapse, resulting from the rapid decrease in the voltage at the powered electrode. Increasing the number of harmonics from two to five affects the excitation dynamics. The peak-to-peak current increases by increasing the number of harmonics; therefore, the intensity of the excitation maximum increases. The excitation peaks approaching the electrode; therefore, the plasma sheaths are getting thinner, which means the plasma density increases. This character is applicable on all cases. There is also another parameter that can influence the excitation dynamics which is increasing the concentration of oxygen.

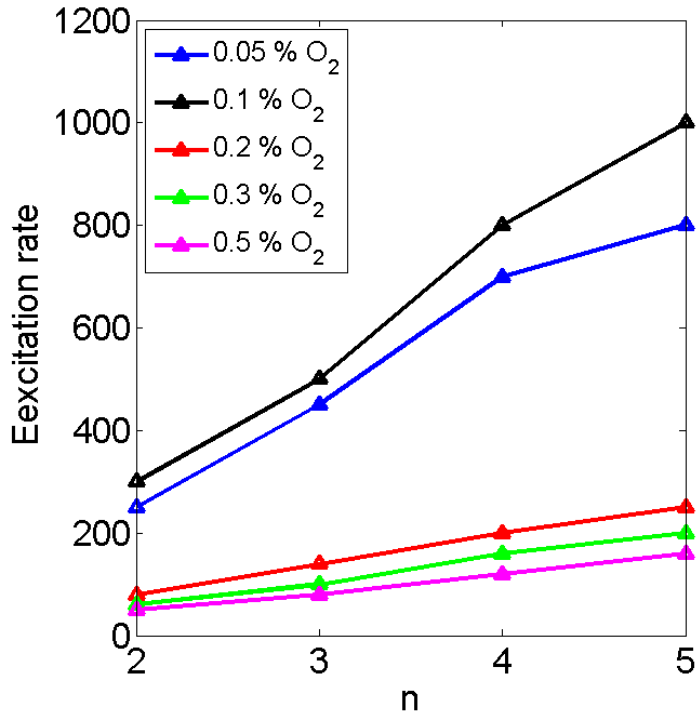

Figure 5.13 Summary of excitation rates as a function of the applied harmonics numbers 2-5 when sawtooth-up waveforms applied on the plasma with different percentages of O_2 admixtures.

The excitation rate is reduced with more oxygen being added to the plasma; however, the excitation rate increases when using 0.1 % of O_2 and this agrees with what it has been investigated in [101]. These results are illustrated in figure 5.13. Furthermore, the excitation peaks tend to approach the centre of the charge and hence the sheaths thicknesses rise. By focusing on the excitation peaks at higher harmonics with oxygen percentage being increased, the transition from sheath expansion dominated sheath collapse excitation as shown in figure 5.14. This is likely due to the change in electro-negativity with increasing admixtures of oxygen.

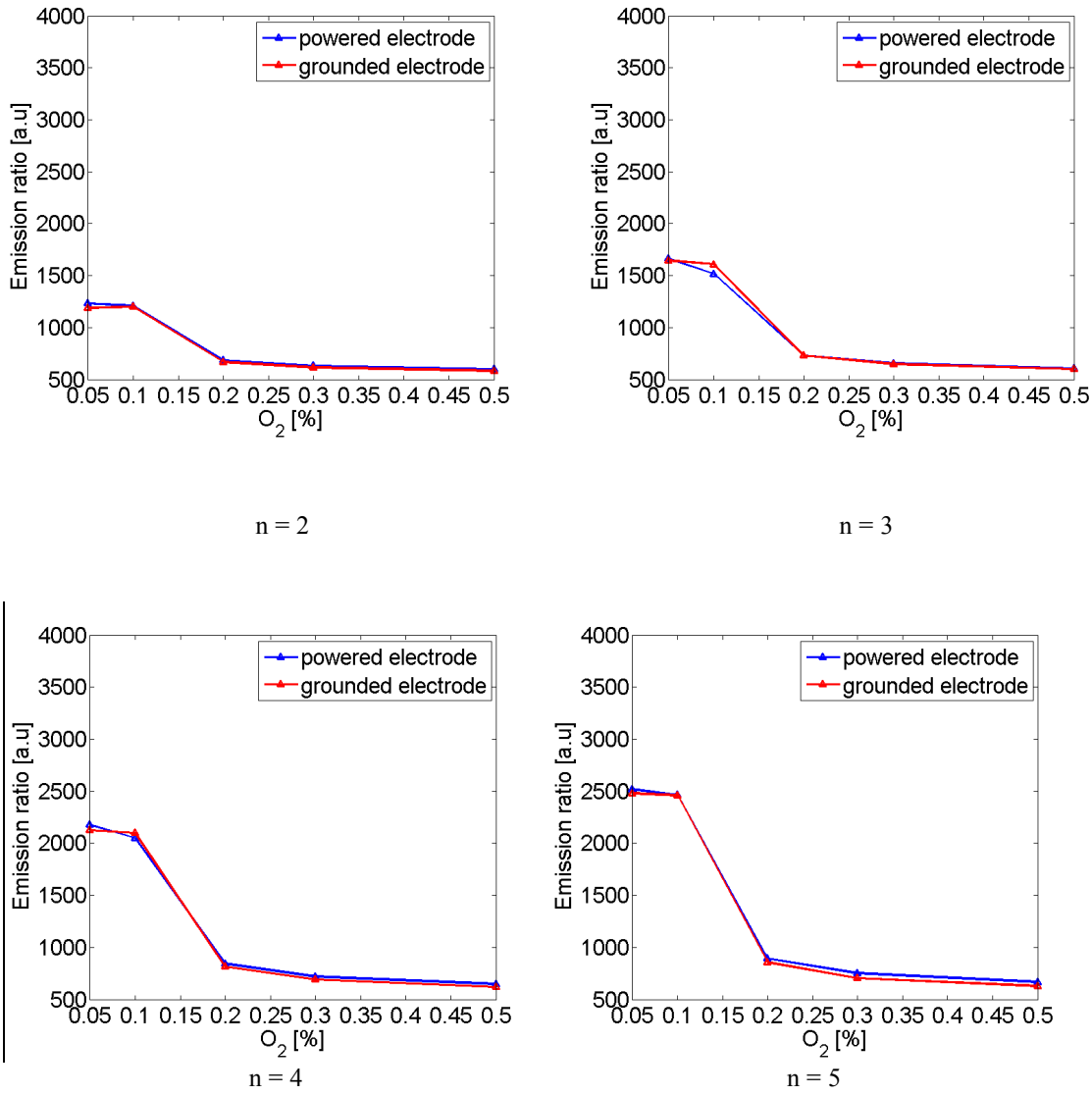

Figure 5.14 The emission ratio of the dense excitation structures as a function of O_2 admixture for the used harmonics in the application of sawtooth-up waveforms.

The same method of applying sawtooth up on the gas mixture with different concentrations of oxygen is also repeated but by driving the plasma through sawtooth-down waveforms. The electron impact excitation plots of these results are shown in figures 5.15 to 5.19 for the O_2 admixtures from 0.05 % to 0.5 % respectively. In all cases, two excitation maxima are represented, one at the grounded electrode while the other one is located at the powered electrode, and these structures are produced due to the action of sheath expansion and sheath collapse.

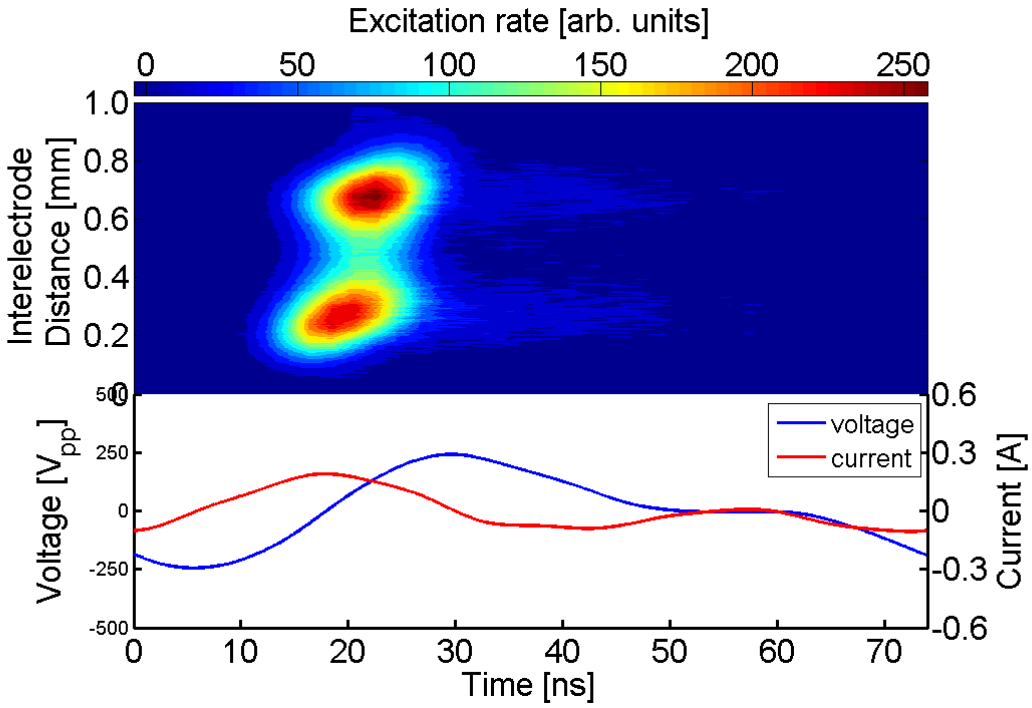
Excitation rate [arb. units]
0
50
100
150
200
250
Interelectrode Distance [mm]
1.0
0.8
0.6
0.4
0.2
0
Voltage [Vpp]
500
250
0
-250
-500
Current [A]
0.6
0.3
0
-0.3
-0.6
voltage
current
0
10
20
30
40
50
60
70
Time [ns]

n = 2

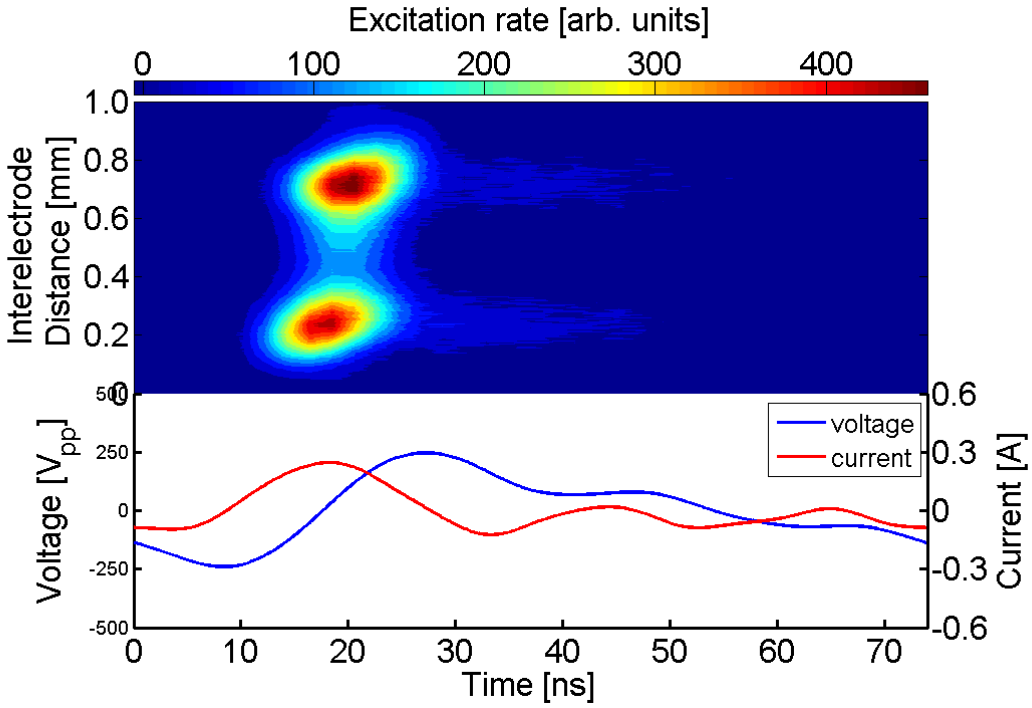
Excitation rate [arb. units]
0
100
200
300
400
Interelectrode Distance [mm]
1.0
0.8
0.6
0.4
0.2
0
Voltage [Vpp]
500
250
0
-250
-500
Current [A]
0.6
0.3
0
-0.3
-0.6
voltage
current
0
10
20
30
40
50
60
70
Time [ns]

n = 3

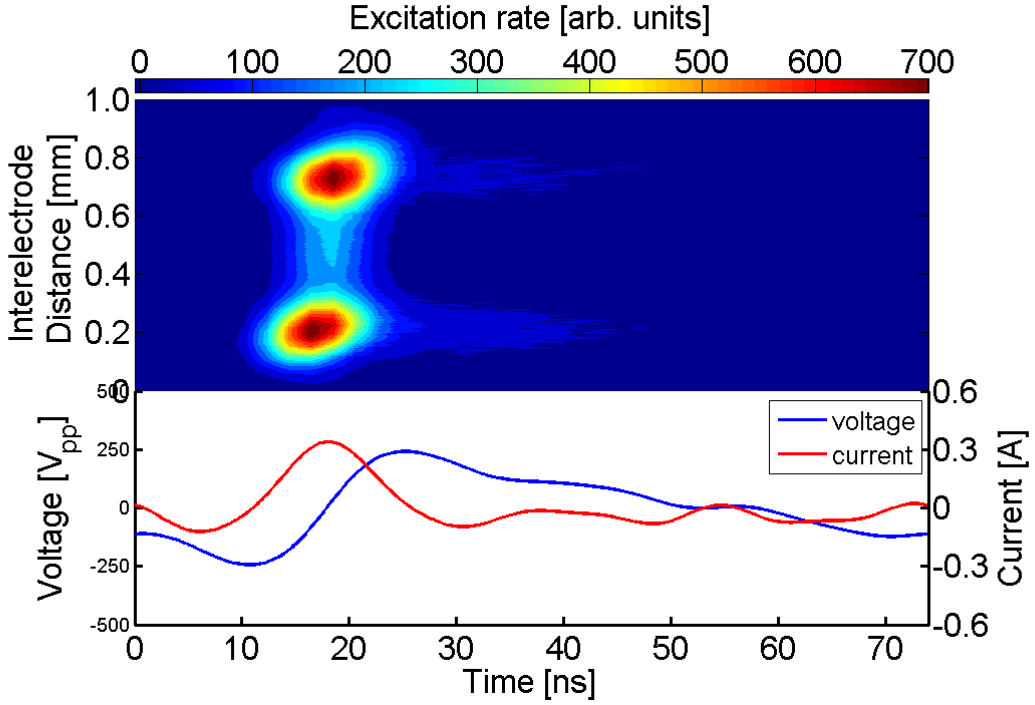

n = 4

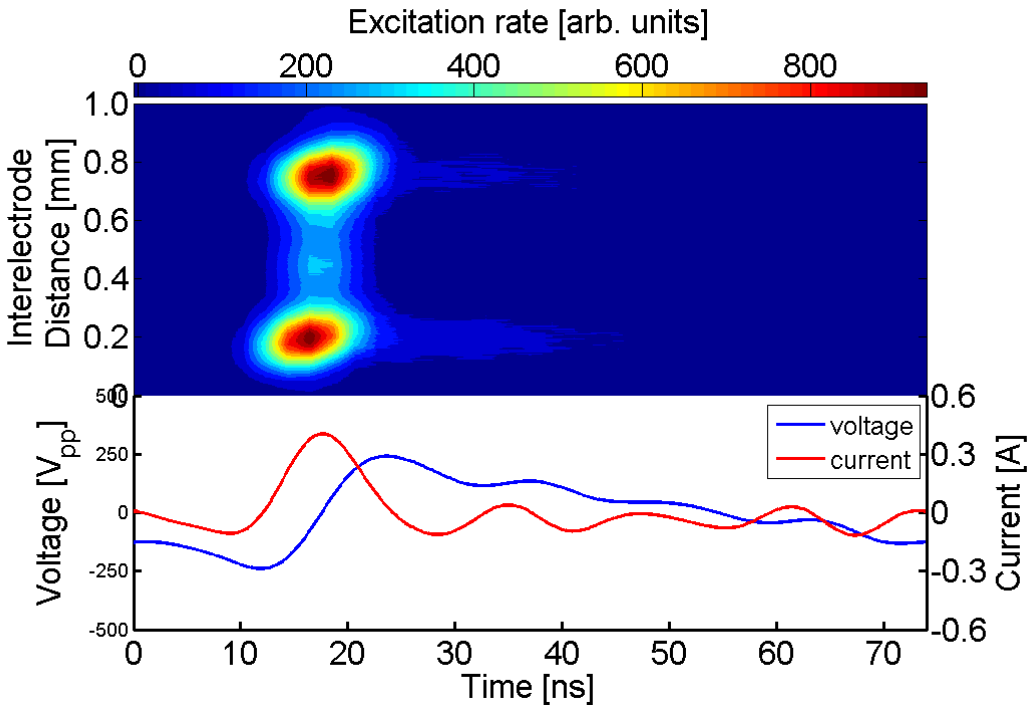

n = 5

Figure 5.15 Spatio-temporal excitation rates obtained from measurement of the emission line at 750.4 nm using PROES and applying sawtooth-down waveforms with n = 2-5 harmonics applied on a gas mixture of He with 0.05 % Ar and O_2 mixture 0.05 %. The peak-to-peak voltage waveform and the corresponding current waveforms for each harmonic are presented in the lower part of each image.

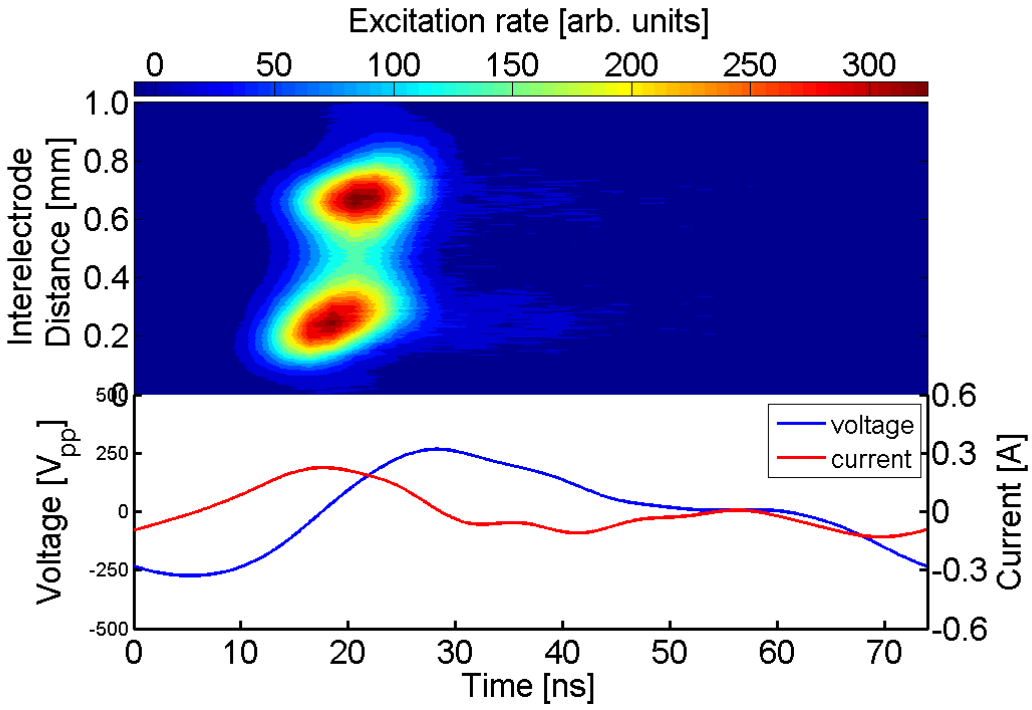
Excitation rate [arb. units]
0
50
100
150
200
250
300
Interelectrode Distance [mm]
1.0
0.8
0.6
0.4
0.2
0
Voltage [Vpp]
500
250
0
-250
-500
voltage
current
Current [A]
0.6
0.3
0
-0.3
-0.6
0
10
20
30
40
50
60
70
Time [ns]

n = 2

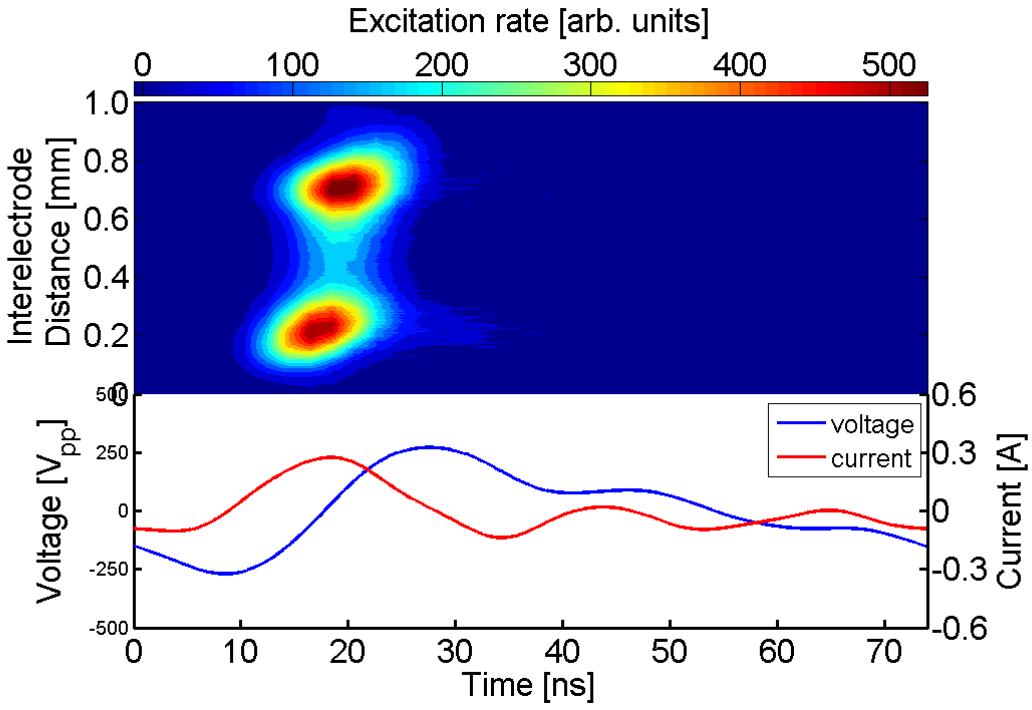
Excitation rate [arb. units]
0
100
200
300
400
500
Interelectrode Distance [mm]
1.0
0.8
0.6
0.4
0.2
0
Voltage [Vpp]
500
250
0
-250
-500
voltage
current
Current [A]
0.6
0.3
0
-0.3
-0.6
0
10
20
30
40
50
60
70
Time [ns]

n = 3

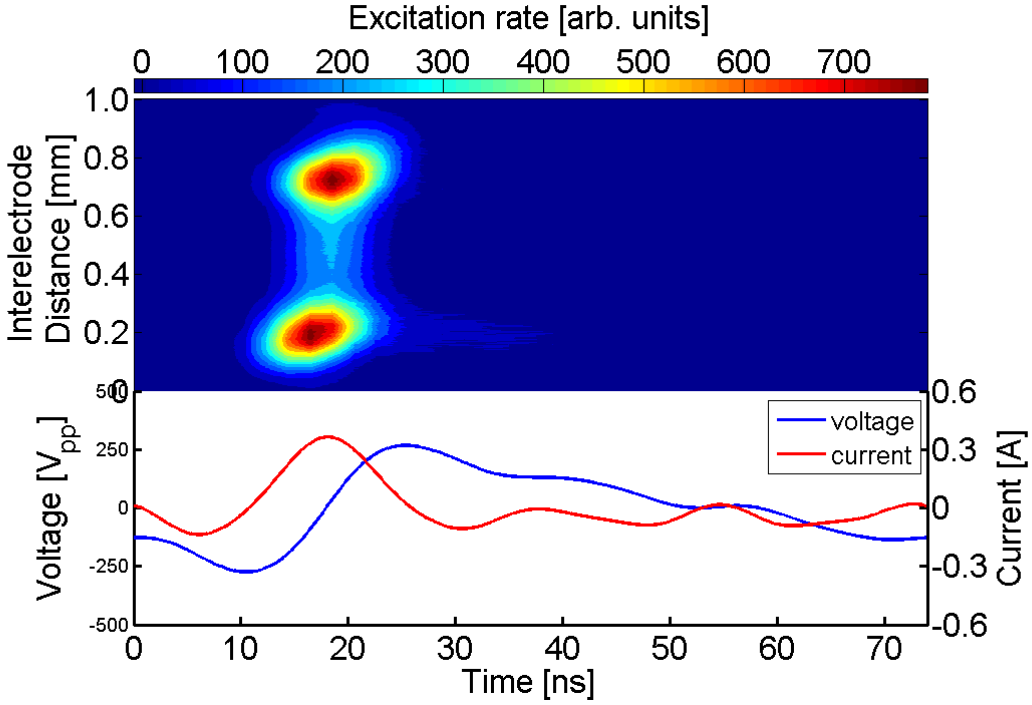

n = 4

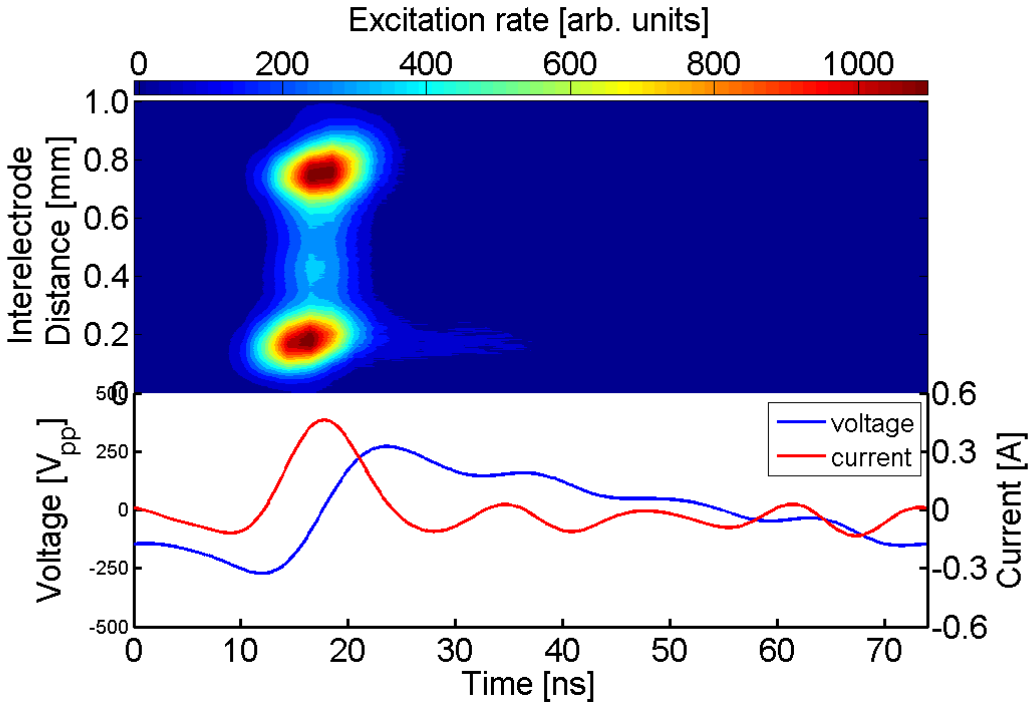

n = 5

Figure 5.16 Spatio-temporal excitation rates obtained from measurement of the emission line at 750.4 nm using PROES and applying sawtooth-down waveforms with n = 2-5 harmonics applied on a gas mixture of He with 0.05 % Ar and O_2 mixture 0.1 %. The peak-to-peak voltage waveform and the corresponding current waveforms for each harmonic are presented in the lower part of each image.

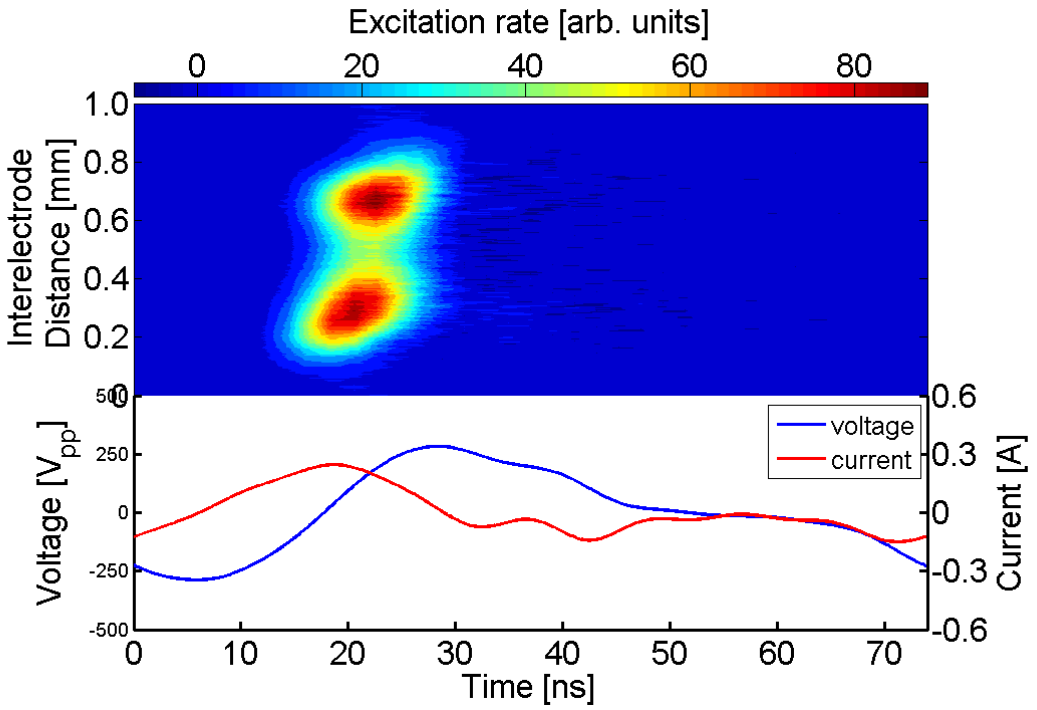
Excitation rate [arb. units]
0
20
40
60
80
Interelectrode Distance [mm]
1.0
0.8
0.6
0.4
0.2
0
Voltage [Vpp]
500
250
0
-250
-500
Current [A]
0.6
0.3
0
-0.3
-0.6
voltage
current
0
10
20
30
40
50
60
70
Time [ns]

n = 2

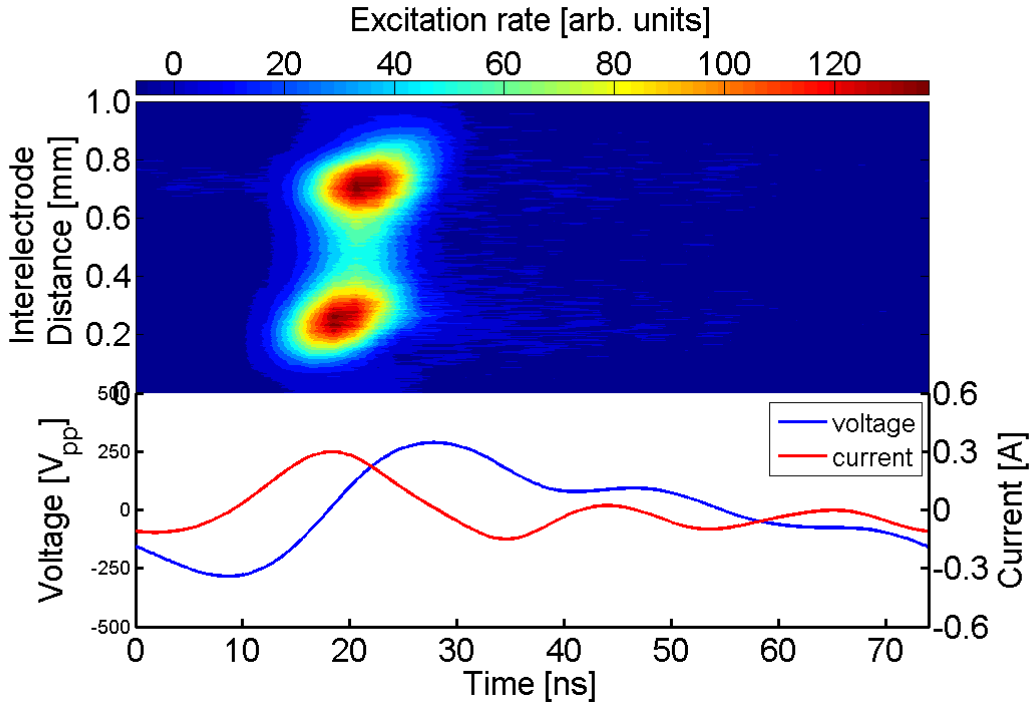
Excitation rate [arb. units]
0
20
40
60
80
100
120
Interelectrode Distance [mm]
1.0
0.8
0.6
0.4
0.2
0
Voltage [Vpp]
500
250
0
-250
-500
Current [A]
0.6
0.3
0
-0.3
-0.6
voltage
current
0
10
20
30
40
50
60
70
Time [ns]

n = 3

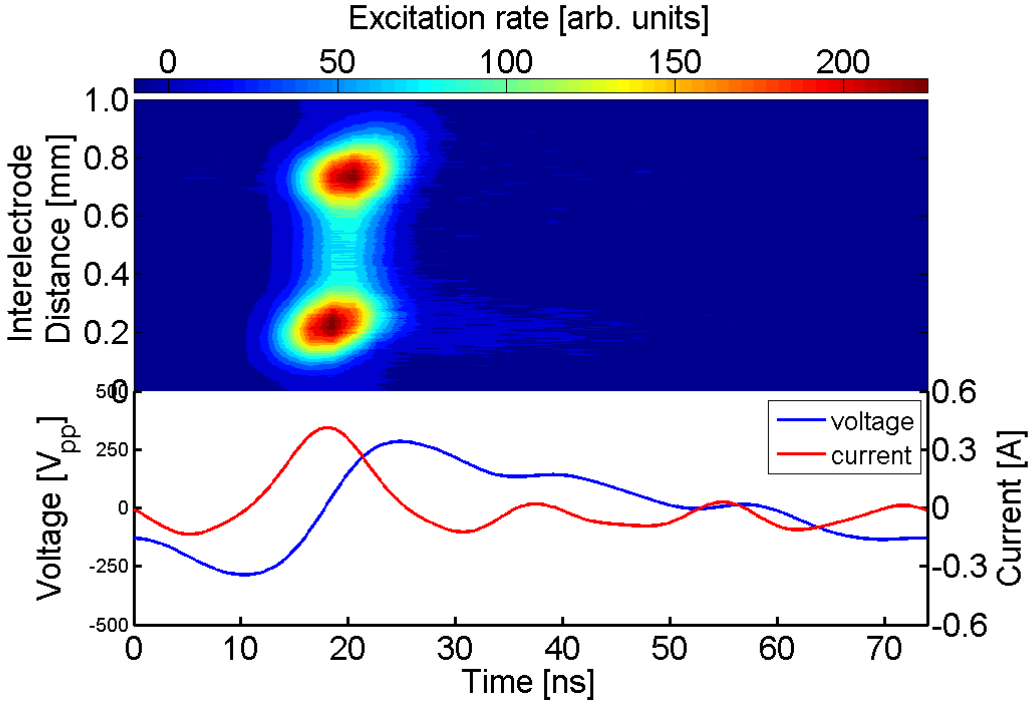

n = 4

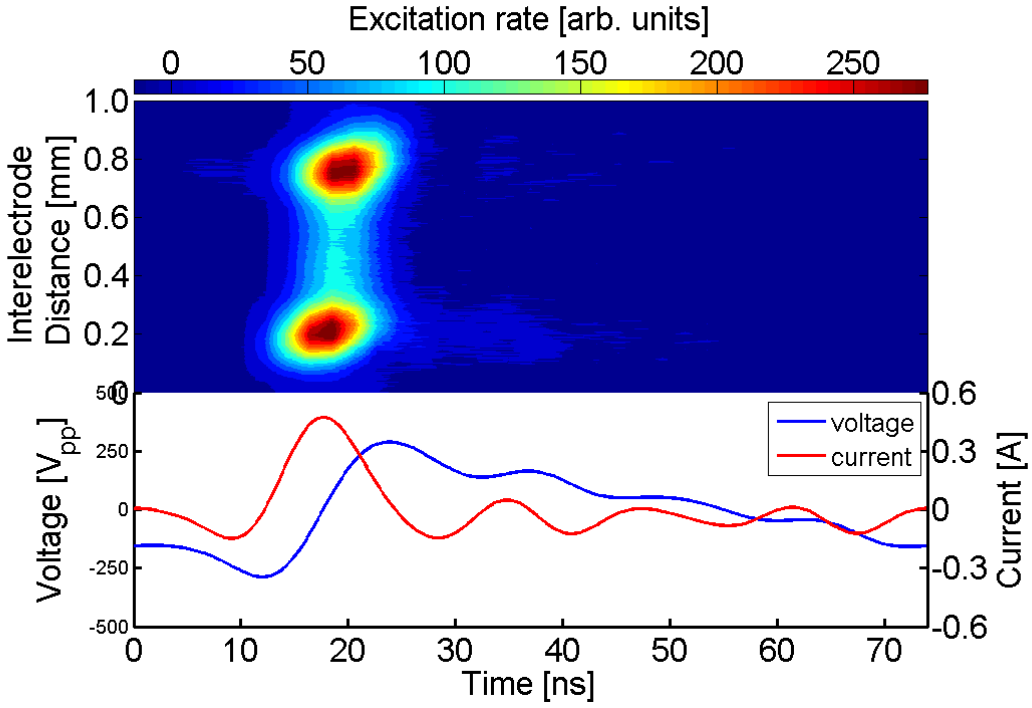

n = 5

Figure 5.17 Spatio-temporal excitation rates obtained from measurement of the emission line at 750.4 nm using PROES and applying sawtooth-down waveforms with n = 2-5 harmonics applied on a gas mixture of He with 0.05 % Ar and O_2 mixture 0.2 %. The peak-to-peak voltage waveform and the corresponding current waveforms for each harmonic are presented in the lower part of each image.

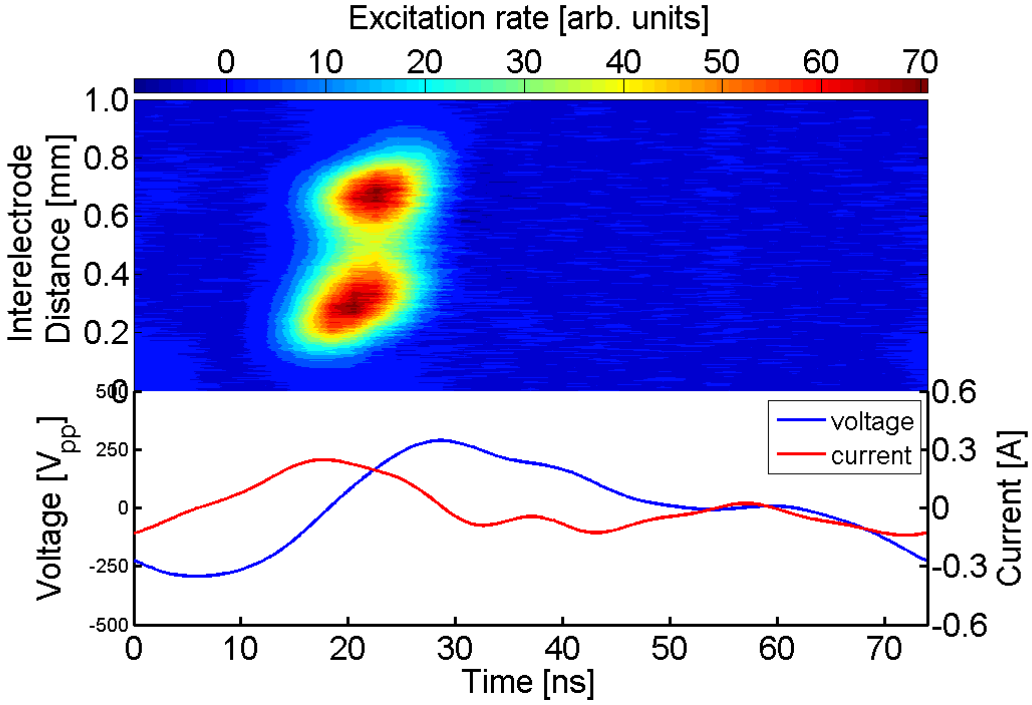
Excitation rate [arb. units]
0
10
20
30
40
50
60
70
Interelectrode Distance [mm]
1.0
0.8
0.6
0.4
0.2
0
Voltage [Vpp]
500
250
0
-250
-500
voltage
current
Current [A]
0.6
0.3
0
-0.3
-0.6
0
10
20
30
40
50
60
70
Time [ns]

n = 2

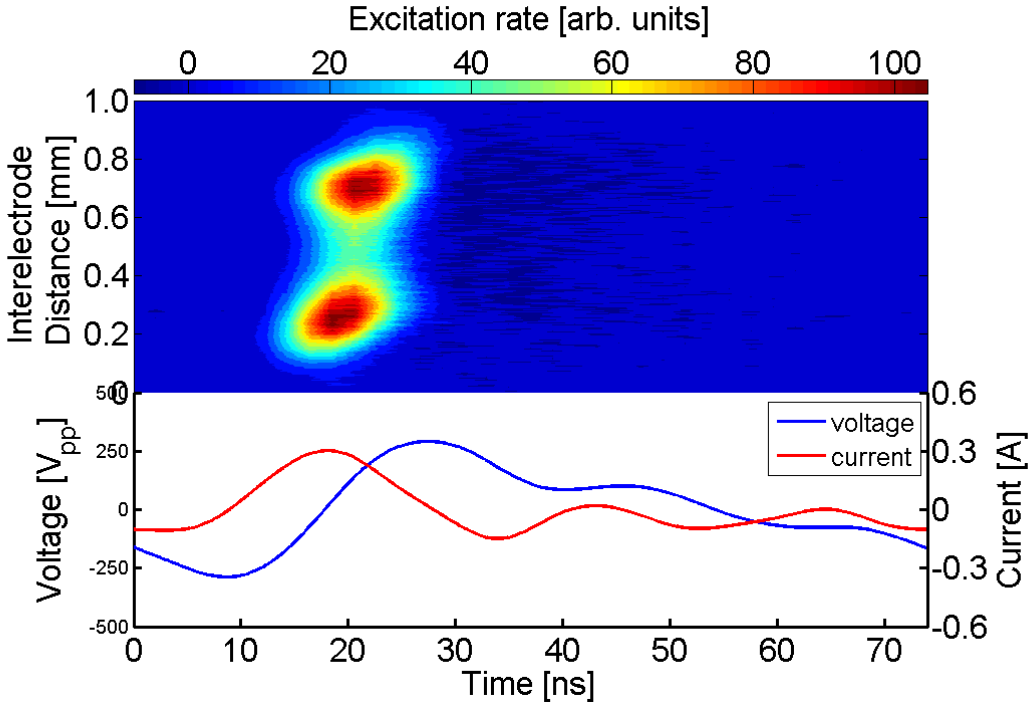
Excitation rate [arb. units]
0
20
40
60
80
100
Interelectrode Distance [mm]
1.0
0.8
0.6
0.4
0.2
0
Voltage [Vpp]
500
250
0
-250
-500
voltage
current
Current [A]
0.6
0.3
0
-0.3
-0.6
0
10
20
30
40
50
60
70
Time [ns]

n = 3

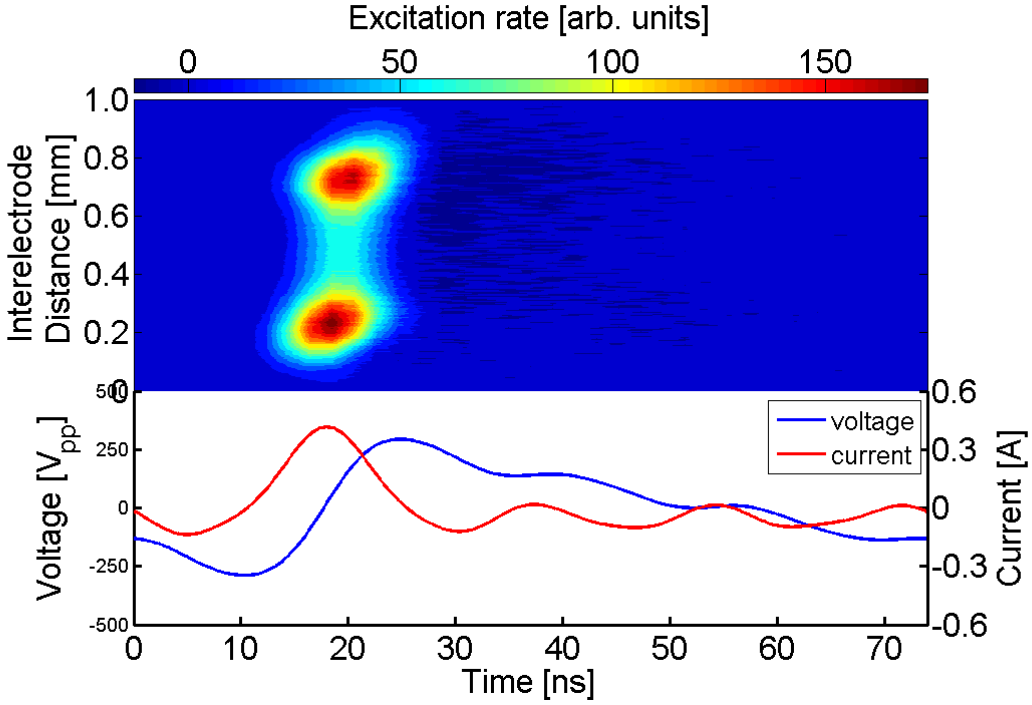

n = 4

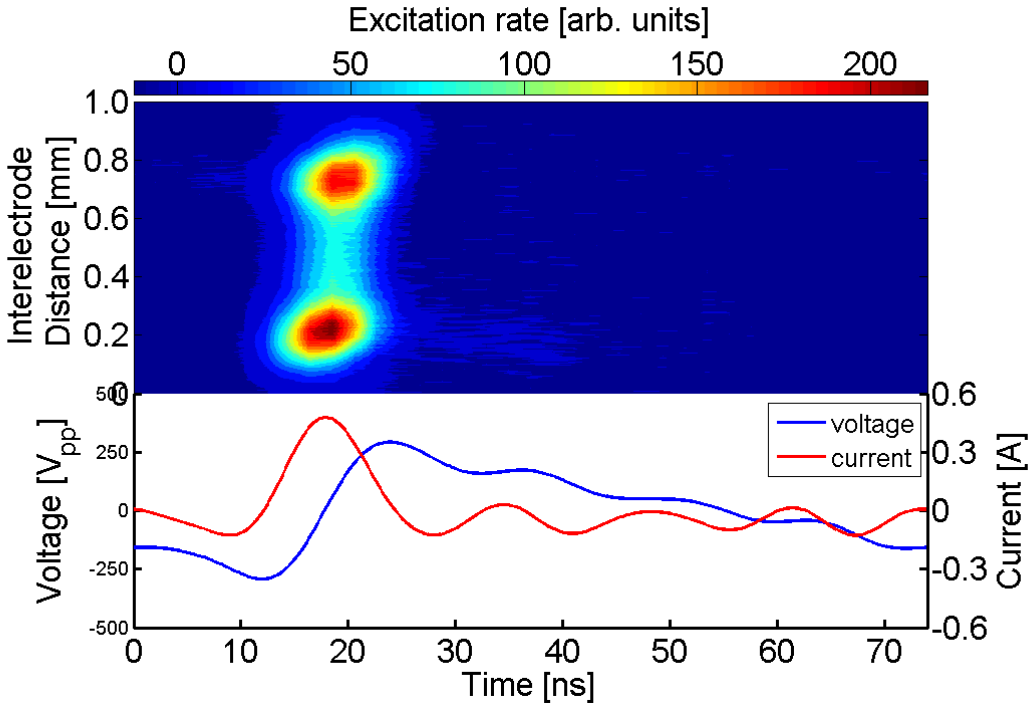

n = 5

Figure 5.18 Spatio-temporal excitation rates obtained from measurement of the emission line at 750.4 nm using PROES and applying sawtooth-down waveforms with n = 2-5 harmonics applied on a gas mixture of He with 0.05 % Ar and O_2 mixture 0.3 %. The peak-to-peak voltage waveform and the corresponding current waveforms for each harmonic are presented in the lower part of each image.

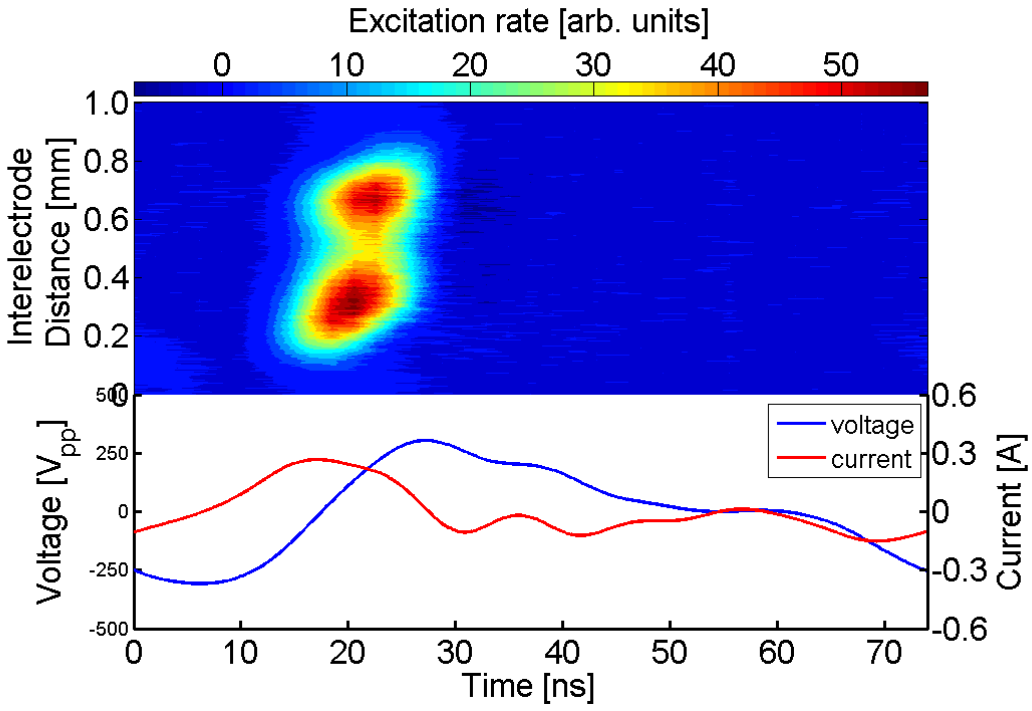
Excitation rate [arb. units]
0
10
20
30
40
50
Interelectrode Distance [mm]
1.0
0.8
0.6
0.4
0.2
0
Voltage [Vpp]
500
250
0
-250
-500
Current [A]
0.6
0.3
0
-0.3
-0.6
voltage
current
0
10
20
30
40
50
60
70
Time [ns]

n = 2

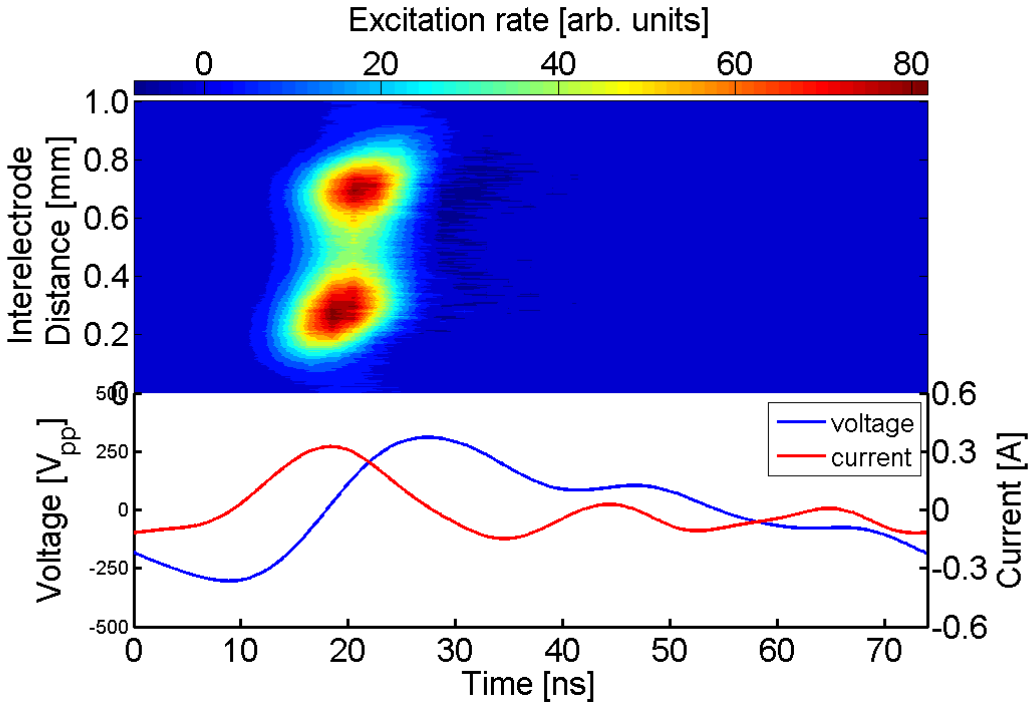
Excitation rate [arb. units]
0
20
40
60
80
Interelectrode Distance [mm]
1.0
0.8
0.6
0.4
0.2
0
Voltage [Vpp]
500
250
0
-250
-500
Current [A]
0.6
0.3
0
-0.3
-0.6
voltage
current
0
10
20
30
40
50
60
70
Time [ns]

n = 3

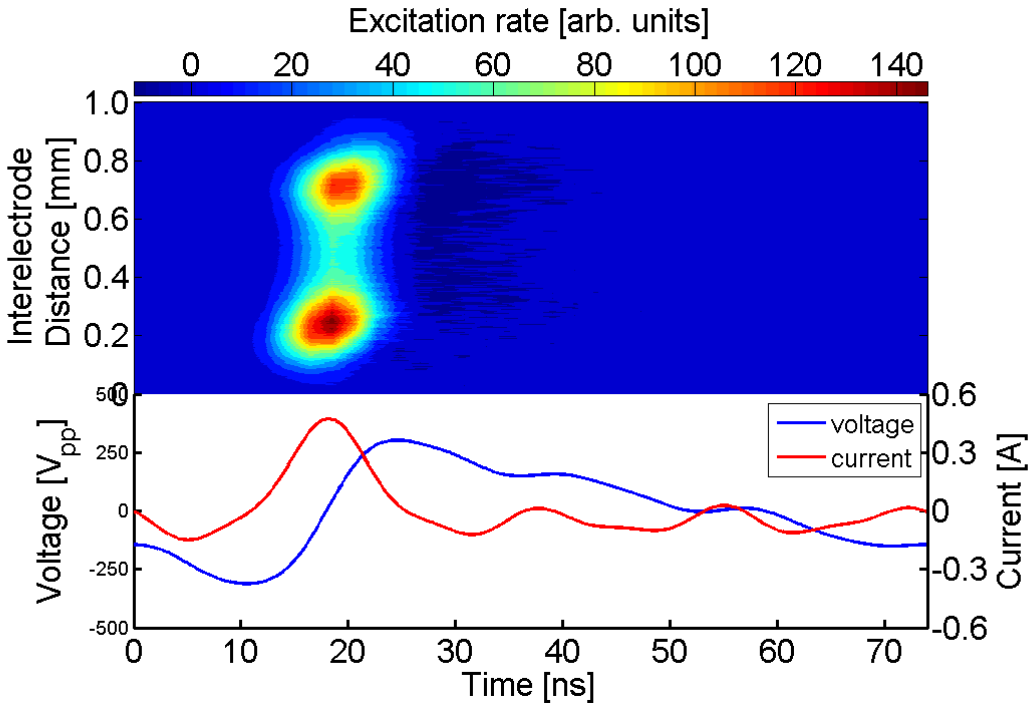

n = 4

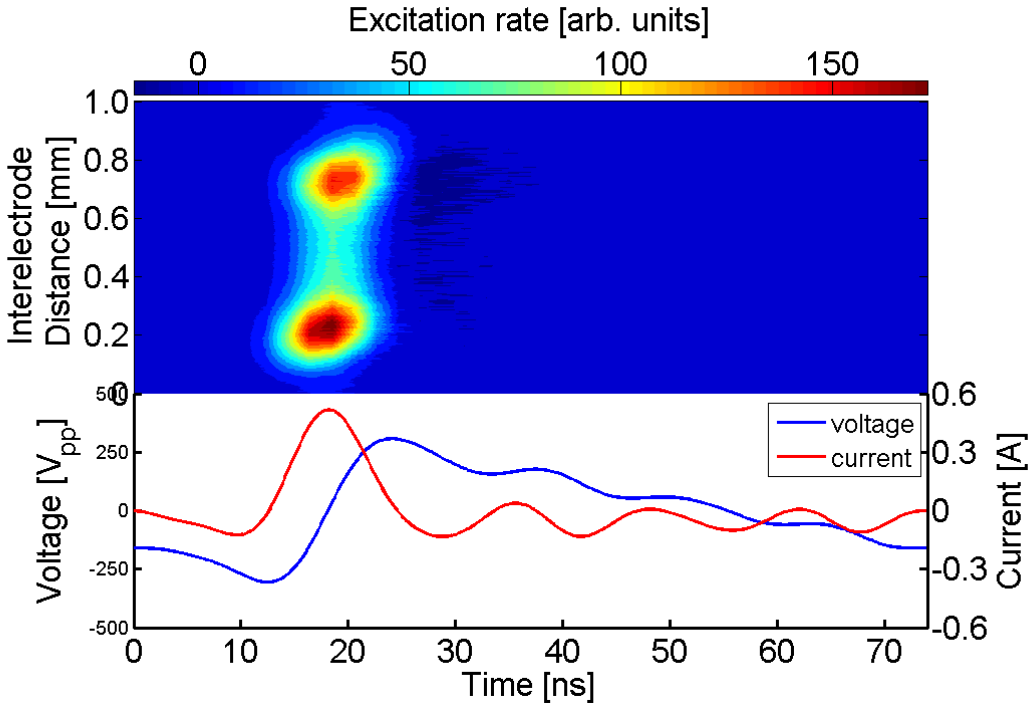

n = 5

Figure 5.19 Spatio-temporal excitation rates obtained from measurement of the emission line at 750.4 nm using PROES and applying sawtooth-down waveforms with n = 2-5 harmonics applied on a gas mixture of He with 0.05 % Ar and O_2 mixture 0.5 %. The peak-to-peak voltage waveform and the corresponding current waveforms for each harmonic are presented in the lower part of each image.

The excitation rate increases by increasing the number of harmonics as observed from the colour bar at the top of each image, and this can be summarised in figure 5.20. By increasing the concentration of oxygen, the excitation structures get closer to each other toward the centre of the discharge; therefore, the plasma sheathes get thicker at the two electrodes. This denotes that the plasma density decreases. The excitation rates are also diminished with higher percentages of oxygen being added to the plasma.

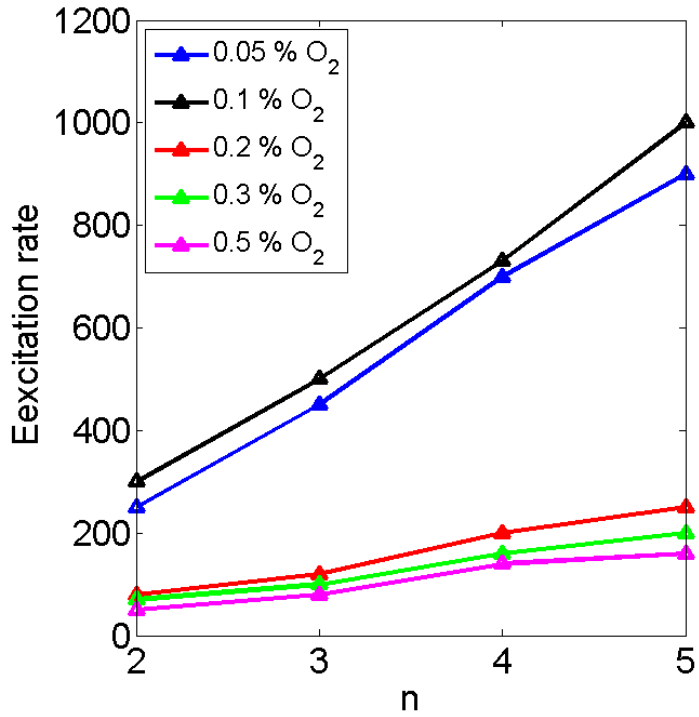

Figure 5.20 Summary of excitation rates as a function of the applied harmonics numbers 2-5 when sawtooth-down waveforms are applied on the plasma with different percentages of O_2 admixtures.

The transition from sheath collapse-dominated excitation to sheath expansion-dominated excitation is likely due to the change in electro-negativity with increasing admixtures of oxygen. This is observed in figure 5.21.

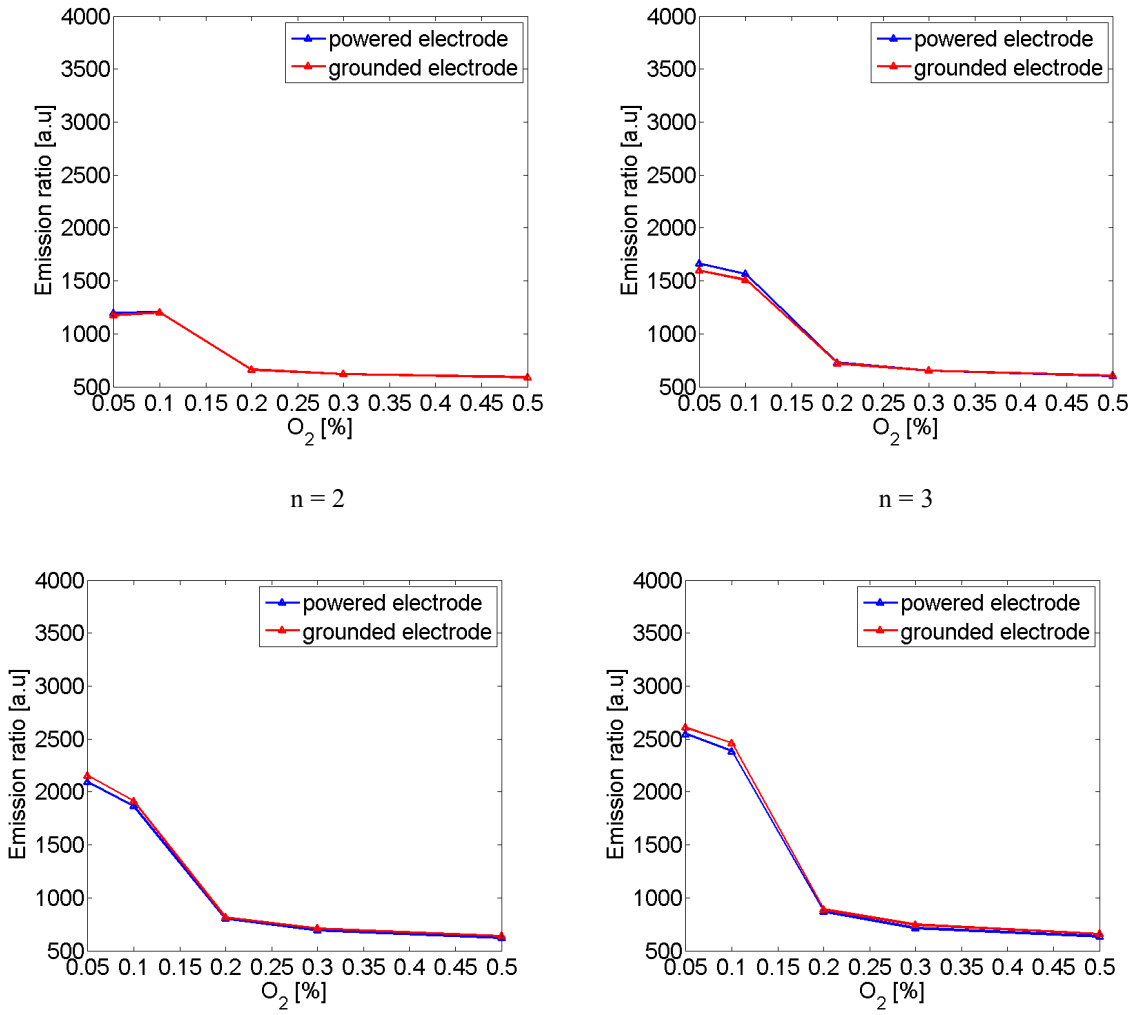

Figure 5.21 The emission ratio of the dense excitation structures as a function of O_2 admixture for the used harmonics in the application of sawtooth-down waveforms.

5.2.2 Electrical asymmetry effect

The sawtooth-type waveforms used in this chapter are sawtooth-up and sawtooth-down waveforms which have the same maximum and minimum excursions but different slopes as explained in chapter 4. They have been used to excite APPs with a fundamental frequency (13.56 MHz) and harmonics ranging from 1-5. The plasma operated in a gas mixture of helium with

0.05% of argon and different admixtures of oxygen 0.05 %, 0.1 %, 0.2 %, 0.3 % and 0.5 % and the applied peak to peak voltages are fixed at 480 V_{pp}, 540 V_{pp} , 570 V_{pp} , 580 V_{pp} and 615 V_{pp} respectively. The DC bias voltages as a function of the number of the applied harmonics varied from 1 to 5 as illustrated in figure 5.22.

The blue dashed line represents the DC self-bias obtained from the sawtooth-up waveform, while the red dashed line shows the DC self-bias resulted from the application of sawtooth-down waveform on the plasma. The measured self-bias for the first harmonic has been shifted up by ~ 0.57 V to correct for the uncertainty of the DC bias probe. The sawtooth-up waveforms show negative self-bias while sawtooth-down waveforms show positive self-bias voltages. The higher DC bias voltage values are dominated by sawtooth-up waveforms although sawtooth-up and sawtooth-down waveforms are both operated at the same peak-to peak voltages. In all of these conditions, the DC bias nearly follows the same trend starting with low values and increasing to reach a maximum at n = 5, and this shows a linear increase in the DC self-bias with respect to the number of harmonics. This trend is consistent with the DC self-bias obtained in some studies that were carried out in low pressure plasma such as hydrogen plasma [66] and argon [22]. The small values of the DC self-bias measured here are small in comparison with what were measured in argon; however, it is consistent with the small values obtained in hydrogen plasma [66]. The DC self-bias voltages mostly tend to decrease with more concentrations of O_2.

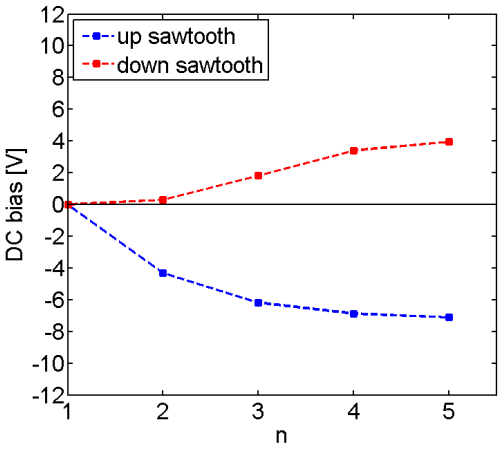

(a)

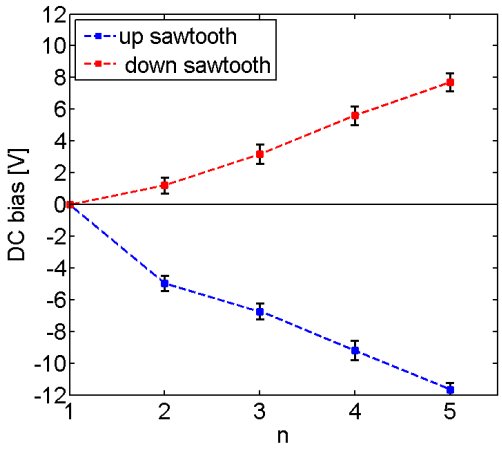

(b)

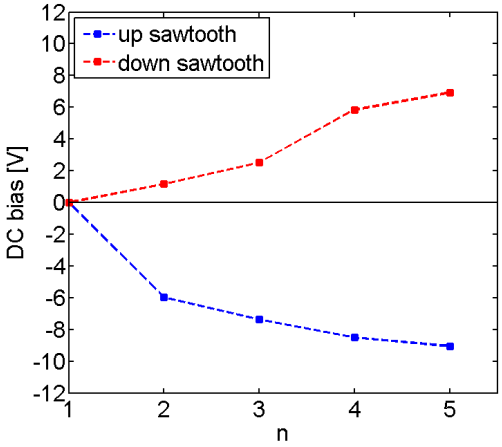

(a)

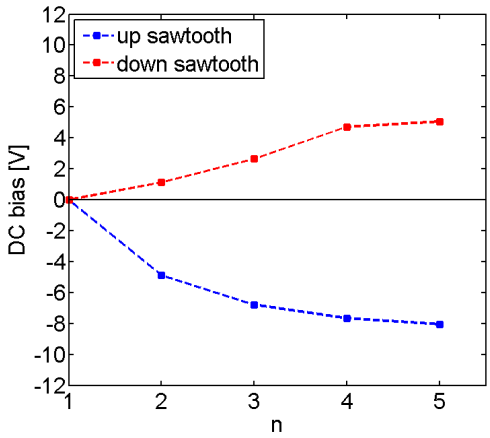

(d)

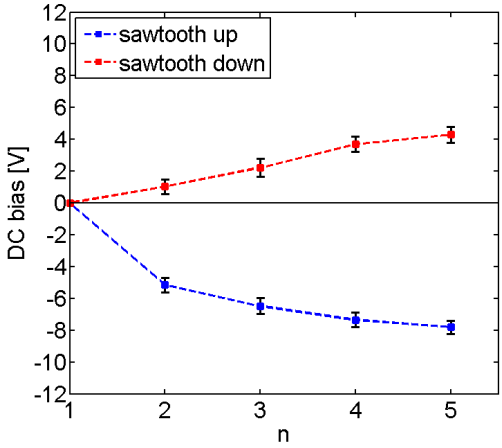

(e)

Figure 5.22: DC self-bias voltages measured as a function of n = 1-5 for sawtooth-up waveforms (blue) and sawtooth-down waveforms (red) at (a) 480 V_{pp} with 0.05 % O_2, (b) 540 V_{pp} with 0.1 % O_2, (c) 570 V_{pp} with 0.2 % O_2, (d) 580 V_{pp} with 0.3 % O_2 and (e) 615 V_{pp} with 0.5 % O_2.

5.3 Ozone species measurements

Non-thermal atmospheric pressure plasmas exhibit a unique property through the production of high density of oxygen and nitrogen chemically reactive species (RONS) at ambient pressures and close to room temperature. This makes them attractive for a wide variety of biomedical and technological applications. Plasma operated in helium with oxygen is considered a source for generating short- and long-lived species such as ozone (O_3), hydrogen peroxide (H_2O_2), atomic oxygen (O) and singlet delta oxygen. Measuring these species is crucial to understanding the fundamental processes behind their production and therefore their effects on applications.

Ozone is produced through the pathway of the three-body recombination reaction of O and O_2 while the main pathway is through the collision with $O_2(b^1\sum_u+)$ [105]

$$O + O_2 + He \rightarrow O_3 + He,$$

$$O_2\left(b^1\sum_u+\right) + O_3 \rightarrow 2O_2 + O$$

The plasma operated in helium with 0.05 % of argon and different admixtures of oxygen < 1 %. The small amount of argon does not affect the reactions held in the plasma. The plasma was driven by TVWs with a fundamental frequency (13.56 MHz) and its harmonics up to five. Peaks-type waveforms and sawtooth-type waveforms are applied on the plasma. Because the plasma operated in a gas mixture including oxygen, it was an opportunity to measure the density of the resulted species from the effluent. Ozone is a long-lived species which is important in many application such as sterilization. The ozone density was measured for each set of oxygen gas admixtures.

In the case of applying peak-type waveforms, the measured ozone densities as a function of harmonics number being applied for peaks waveforms and valleys waveforms are illustrated in figure 5.23.

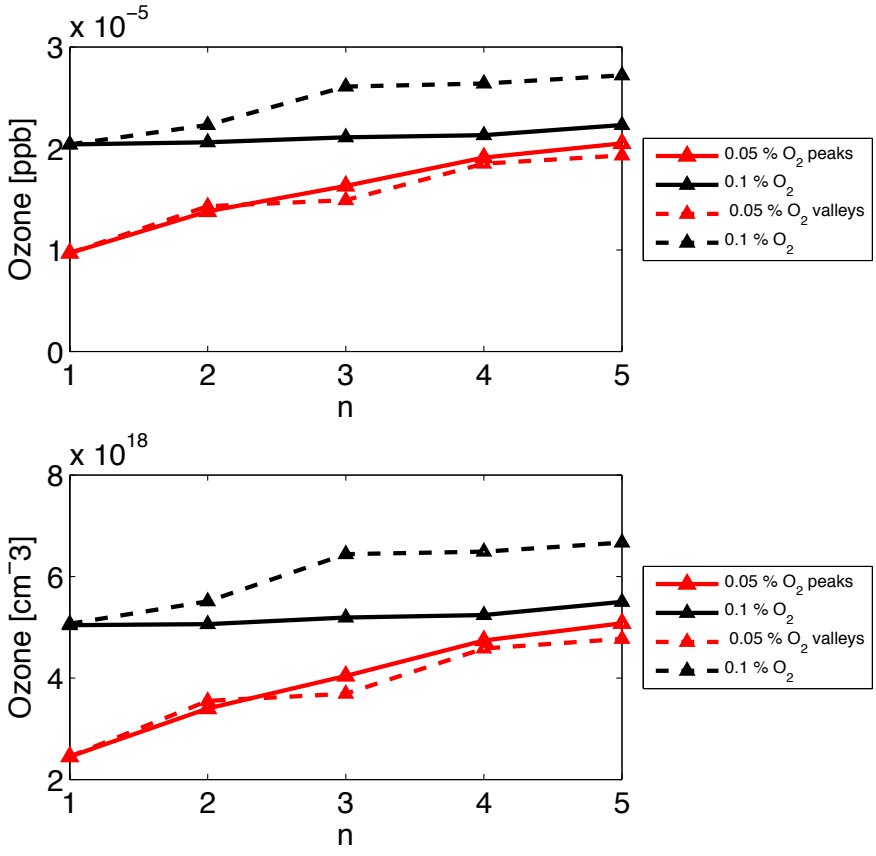

Figure 5.23: Ozone density as a function of the number of harmonics 1-5 by applying peaks and valleys waveforms using 0.05 % and 0.1 % of O_2.

As observed, the ozone densities increase gradually with more harmonics being applied. The same trend is shown for both cases. With higher oxygen admixtures, the ozone density increases.

In general, the ozone densities obtained through valleys waveforms with 0.1 % of oxygen is greater than that when peaks waveforms are applied. However, the opposite can be observed, as the ozone densities obtained through peaks waveforms with 0.05 % of oxygen is higher than the

ozone densities obtained through valleys waveforms. Ozone density also has been measured through the application of sawtooth up and sawtooth down as shown in figure 5.24.

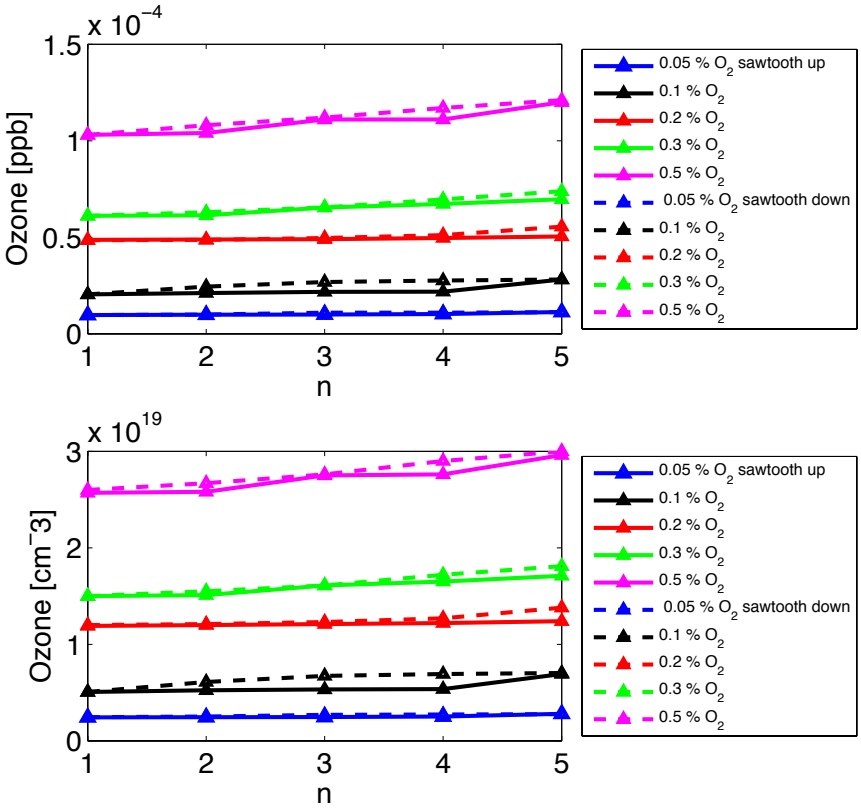

Figure 5.24: Ozone density as a function of the number of harmonics 1-5 by applying sawtooth-up waveforms with oxygen concentrations 0.05 %, 0.1 %, 0.2 %, 0.3 %, and 0.5 % O_2.

By applying sawtooth-up waveforms in the gas mixture including a variety of oxygen concentrations, the ozone density is measured. The ozone density increases dramatically by adding higher oxygen admixtures. The same trend is observed for all conditions when applying sawtooth-down waveforms either with increasing the number of harmonics or the oxygen admixtures.

5.4 Summary

In this chapter, peaks and sawtooth waveforms derive the plasma with using gas mixtures of helium, argon and different admixtures of oxygen < 1 %. These TVWs with number of harmonics are applied to APPs producing asymmetric plasma. The DC self-bias resulting from applying peaks and valleys waveform are taken at different concentrations of oxygen (0 %, 0.05 % and 0.1 %) representing the same trend which shows an increase in the DC self-bias until three harmonics and then decreases at four and five harmonics. Sawtooth-up and sawtooth-down waveforms show linear trends of the DC self-bias with the applied number of harmonics. The negative DC self-bias voltages obtained in peaks and sawtooth-up waveforms are greater than the positive DC self-bias voltages resulting from valleys and sawtooth-down waveforms. In order to achieve the excitation dynamics obtained in peaks and valleys waveforms, the main excitation structures occur during sheath expansion and sheath contraction at the grounded electrode and the powered electrode respectively. During the sheath collapse, a complex excitation process occurs due to the field reversal mechanism.

In the case of applying sawtooth waveforms, the maximum excitation is transferred between the two electrodes when increasing the number of harmonics and the oxygen admixtures due to the electronegativity feature. This distinguishes plasma driven by sawtooth waveforms from oxygen and shows a difference when nitrogen admixtures are used. Plasma driven with nitrogen admixtures shows that the maximum excitation in the application of sawtooth up and sawtooth down takes place at the powered electrode and at the grounded electrode respectively. The asymmetry in electron heating structures leads to tailoring electron energy distribution function and then influencing on the different applications [93].

The impact of increasing the oxygen admixtures on all used waveforms and the different harmonics numbers is studied. First, the excitation rate reduced as the excited state getting quenched by nitrogen. However, at each individual set of oxygen admixtures ,the excitation rate increases by increasing the harmonics numbers. Moreover, the plasma density decreases, and this is observed through the reduction in the sheath thickness. Ozone densities increase gradually with increasing oxygen admixtures in all cases. Also, they increase with more harmonics.

Chapter 6 Conclusion and Future Work

6.1 Conclusion

The experimental results carried out on APPs using tailored voltage waveforms (TVWs) are presented in this thesis. They have been proven to be capable of reproducing the pronounced electron dynamics in helium with nitrogen admixtures as well as in helium with oxygen admixtures. Excitation dynamics have been extracted from phase-resolved optical emission spectroscopy (PROES). The motion of non-linear plasma boundary sheaths following the change in the applied RF frequency has governed these dynamics. Two types of non-linear voltage waveforms have been used here to drive the APPs: peaks-type waveforms and sawtooth-type waveforms. All of these waveforms essentially comprise a sine wavefrorm of a fundamental frequency (13.56 MHz) summed with a number of its harmonics up to five. Peaks and valleys are waveforms wherein their amplitude change via an increasing in the number of harmonics whereas, in peaks waveforms, all peaks have the same phase angle ($\theta = 0$) while valleys waveform are exactly the opposite of the peaks waveforms but with phase shift of ($\theta = \pi$). On the other hand, sawtooth-up and sawtooth-down waveforms have the same phase but different slopes. When TVWs with these asymmetric characteristics drive capacitively coupled symmetric plasma, DC self-bias voltage is produced due to the electrically asymmetric effect (EAE), which means the plasma is getting electrically asymmetric rather than being geometrically asymmetric. In this thesis, the excitation dynamics have been investigated through studying the effect of the different

types of TVWs, their harmonics and the concentration of nitrogen and oxygen admixtures. Different behaviours of the dynamics of He-N_2 and He-O_2 plasmas have been observed depending on the chemistry.

He-O_2 plasmas are an important source for producing chemically reactive species which are very important in many application, including biomedicine. The produced ozone densities are measured from the plasma effluent.

6.2 Future work

First and foremost, TVWs were, in this thesis, operated in atmospheric pressure plasma for the first time, and this in turn will open new fields for research. Therefore, more research is needed to provide a clear understanding of plasma parameters and their impact on applications.

Future work on (He-N_2) atmospheric pressure plasma with water or air admixtures driven by tailored voltage waveforms would be carried out to measure the produced reactive species such as NO and NO_2. In the case of He-O_2 plasma, the density of atomic oxygen (O) should also be measured. Further, electron dynamics would be studied by doing simulations to simulate the experimental results obtained in this thesis on He- O_2 atmospheric pressure plasma TVW driven.

List of symbols Abbreviations

RF	radio frequency
K	Kelvin
APPs	Atmospheric pressure plasmas
APPJ	Atmospheric pressure plasma jet
PROES	Phase resolved optical emission spectroscopy
CCP	Capacitively coupled plasma
TVW	Tailored voltage waveforms
λ_D	Debye length
ε_0	Permittivity of free vacuum
k_B	Boltzmann constant (1.3807×10^{-23} J. K $^{-1}$)
e	Electron charge
n_e	Electron number density
T_e	Electron temperature
m_e	Electron mass
ω_p	Plasma frequency
I	Degree of ionization
Γ_{-i}	Negative ion flux
Γ_{+i}	Positive ion flux
Γ_e	Electron flux
DC	Direct current
AC	Alternating current
γ	Gamma
α	Alpha

d	Distance between electrodes
p	Pressure
TALIF	Two-photon Absorption Laser Induced Fluorescence
i	Observed excitation state
n_0	Ground state population density
E_i	Electron impact excitation
A_{ik}	Einstein coefficient from the excited state *i* to a lower energy level *k*
$\sigma_i(\epsilon)$	Cross section of the energy dependant electron impact excitation
τ_i	Radiative lifetime
A_{ci}	Transition rate from the cascade level *c* to the level *i*
n_c	Population density of cascade state *c*
E_{mi}	Electron impact excitation out of metastable state *m*
g_{ik}	Escape factor
k_q	Quenching coefficient
EEDF	Electron energy distribution function
EAE	Electrical asymmetry effect
MFC	Mass flow controller
He	Helium
N_2	Nitrogen
O_2	Oxygen
Ar	Argon
slm	Standard litre per minute
sccm	Standard cubic centimetre per minute
AFG	Arbitrary function generator
ICCD	intensified charge-coupled device
k	Harmonic index
ϕ_k	Amplitude of every individual harmonic
θ_k	Phase shift
AAE	Amplitude asymmetry effect
SAE	Slope asymmetry effect
τ_{eff}	Effective lifetime

References list

1. Francis, F.C., *Introduction to plasma physics and controlled fusion*. Plasma Physics, 1984.
2. Schouten, J.C., *Micro Systems and Devices for (Bio) chemical Processes*. Vol. 38. 2010: Academic Press.
3. Lancaster, J.F., *The physics of welding*. Physics in technology, 1984. **15**(2): p. 73.
4. Goldston, R.J. and P.H. Rutherford, *Introduction to plasma physics*. 1995: CRC Press.
5. Bellan, P.M., *Fundamentals of plasma physics*. 2008: Cambridge University Press.
6. Freidberg, J.P., *Plasma physics and fusion energy*. 2008: Cambridge university press.
7. Mogab, C., A. Adams, and D.L. Flamm, *Plasma etching of Si and SiO2—the effect of oxygen additions to CF4 plasmas*. Journal of applied physics, 1978. **49**(7): p. 3796-3803.
8. Capezzuto, P. and A. Madan, *Plasma deposition of amorphous silicon-based materials*. 1995: Academic Press.
9. Foest, R., et al., *Non-thermal atmospheric pressure discharges for surface modification*. Plasma physics and controlled fusion, 2005. **47**(12B): p. B525.
10. Desmet, T., et al., *Nonthermal plasma technology as a versatile strategy for polymeric biomaterials surface modification: a review*. Biomacromolecules, 2009. **10**(9): p. 2351-2378.
11. Iza, F., J.K. Lee, and M.G. Kong, *Electron kinetics in radio-frequency atmospheric-pressure microplasmas*. Physical review letters, 2007. **99**(7): p. 075004.
12. Li, L., et al., *OH radicals distribution in an Ar-H2O atmospheric plasma jet*. Physics of plasmas, 2013. **20**(9): p. 093502.
13. Li, X., et al., *Characteristics of an atmospheric-pressure argon plasma jet excited by a dc voltage*. Plasma Sources Science and Technology, 2013. **22**(4): p. 045007.
14. Park, J., et al., *An atmospheric pressure plasma source*. Applied Physics Letters, 2000. **76**(3): p. 288-290.
15. Gans, T., V. Schulz-von der Gathen, and H. Döbele, *Prospects of Phase Resolved Optical Emission Spectroscopy as a Powerful Diagnostic Tool for RF-Discharges*. Contributions to Plasma Physics, 2004. **44**(5-6): p. 523-528.
16. Liu, D., F. Iza, and M.G. Kong, *Electron heating in radio-frequency capacitively coupled atmospheric-pressure plasmas*. Applied Physics Letters, 2008. **93**(26): p. 261503.
17. Schaper, L., et al., *Electron Dynamics in a Radio-Frequency-Driven Microatmospheric Pressure Plasma Jet*. IEEE Transactions on Plasma Science, 2011. **39**(11): p. 2370-2371.

18. Waskoenig, J. and T. Gans, *Nonlinear frequency coupling in dual radio-frequency driven atmospheric pressure plasmas*. Applied Physics Letters, 2010. **96**(18): p. 181501.

19. Waskoenig, J., *Numerical simulations of the electron dynamics in single and dual radio-frequency driven atmospheric pressure plasmas and associated plasma chemistry in electro-negative He-O2 mixtures*. Ph.D. thesis, Queen's University Belfast, 2011.

20. O'Neill, C., J. Waskoenig, and T. Gans, *Tailoring electron energy distribution functions through energy confinement in dual radio-frequency driven atmospheric pressure plasmas*. Applied Physics Letters, 2012. **101**(15): p. 154107.

21. Dwivedi, S., et al., *Reactive oxygen species mediated bacterial biofilm inhibition via zinc oxide nanoparticles and their statistical determination*. PloS one, 2014. **9**(11): p. e111289.

22. Bruneau, B., et al., *Strong ionization asymmetry in a geometrically symmetric radio frequency capacitively coupled plasma induced by sawtooth voltage waveforms*. Physical review letters, 2015. **114**(12): p. 125002.

23. Langmuir, I., *Oscillations in ionized gases*. Proceedings of the National Academy of Sciences, 1928. **14**(8): p. 627-637.

24. Dendy, R., *Plasma dynamics*. 1990: Oxford University Press Oxford.

25. Chabert, P. and N. Braithwaite, *Physics of radio-frequency plasmas*. 2011: Cambridge University Press.

26. Lieberman, M.A. and A.J. Lichtenberg, *Principles of plasma discharges and materials processing*. 2005: John Wiley & Sons.

27. Chapman, B.N., *Glow discharge processes: sputtering and plasma etching*. 1980: Wiley.

28. You, H.-X., N.M. Brown, and K.F. Al-Assadi, *Radio-frequency (RF) plasma etching of graphite with oxygen: a scanning tunnelling microscope study*. Surface science, 1993. **284**(3): p. 263-272.

29. Śmietana, M., R. Mroczyński, and N. Kwietniewski, *Effect of sample elevation in radio frequency plasma enhanced chemical vapor deposition (RF PECVD) reactor on optical properties and deposition rate of silicon nitride thin films*. Materials, 2014. **7**(2): p. 1249-1260.

30. Felmetsger, V., M. Mikhov, and P. Laptev, *Effect of pre-deposition rf plasma etching on wafer surface morphology and crystal orientation of piezoelectric AlN thin films*. IEEE transactions on ultrasonics, ferroelectrics, and frequency control, 2015. **62**(2): p. 387-391.

31. Godyak, V.A. and N. Sternberg, *Dynamic model of the electrode sheaths in symmetrically driven rf discharges*. Physical Review A, 1990. **42**(4): p. 2299.

32. Keller, J.H., J.C. Forster, and M.S. Barnes, *Novel radio-frequency induction plasma processing techniques*. Journal of Vacuum Science & Technology A: Vacuum, Surfaces, and Films, 1993. **11**(5): p. 2487-2491.

33. Godyak, V. and A. Khanneh, *Ion Bombardment Secondaty Electron Maintenance of Steady RF Discharge*. IEEE transactions on plasma science, 1986. **14**(2): p. 112-123.

34. Farouk, T., et al., *Atmospheric pressure radio frequency glow discharges in argon: effects of external matching circuit parameters*. Plasma Sources Science and Technology, 2008. **17**(3): p. 035015.

35. Ono, K., et al., *Measurements of the Cl atom concentration in radio-frequency and microwave plasmas by two-photon laser-induced fluorescence: Relation to the etching of Si*. Journal of Vacuum Science & Technology A: Vacuum, Surfaces, and Films, 1992. **10**(4): p. 1071-1079.

36. Stoffels, E., I. Kieft, and R. Sladek, *Superficial treatment of mammalian cells using plasma needle*. Journal of Physics D: Applied Physics, 2003. **36**(23): p. 2908.

37. Riès, D., et al. *LIF and fast imaging atmospheric pressure plasma jet characterization relevant to NTP biomedical applications*. in *International Workshop on Diagnostics and Modelling for Plasma Medicine (DMPM2014)*. 2014.

38. Selwyn, G.S., *Atmospheric-pressure plasma jet*. 1999, Google Patents.

39. Šimor, M., et al., *Atmospheric-pressure plasma treatment of polyester nonwoven fabrics for electroless plating*. Surface and Coatings Technology, 2003. **172**(1): p. 1-6.

40. Wagner, H.-E., et al., *The barrier discharge: basic properties and applications to surface treatment*. Vacuum, 2003. **71**(3): p. 417-436.

41. Kakiuchi, H., et al., *Characterization of intrinsic amorphous silicon layers for solar cells prepared at extremely high rates by atmospheric pressure plasma chemical vapor deposition*. Journal of non-crystalline solids, 2005. **351**(8-9): p. 741-747.

42. Jeong, J., et al., *Etching materials with an atmospheric-pressure plasma jet*. Plasma Sources Science and Technology, 1998. **7**(3): p. 282.

43. Jeong, J., et al., *Etching polyimide with a nonequilibrium atmospheric-pressure plasma jet*. Journal of Vacuum Science & Technology A: Vacuum, Surfaces, and Films, 1999. **17**(5): p. 2581-2585.

44. Babayan, S., et al., *Deposition of silicon dioxide films with an atmospheric-pressure plasma jet*. Plasma Sources Science and Technology, 1998. **7**(3): p. 286.

45. Babayan, S., et al., *Deposition of silicon dioxide films with a non-equilibrium atmospheric-pressure plasma jet*. Plasma Sources Science and Technology, 2001. **10**(4): p. 573.

46. Massines, F., et al., *Atmospheric pressure plasma deposition of thin films by Townsend dielectric barrier discharge*. Surface and Coatings Technology, 2005. **200**(5-6): p. 1855-1861.

47. Arndt, S., et al., *Cold atmospheric plasma, a new strategy to induce senescence in melanoma cells*. Experimental dermatology, 2013. **22**(4): p. 284-289.

48. Hirst, A.M., et al., *Low temperature plasmas as emerging cancer therapeutics: the state of play and thoughts for the future*. Tumor Biology, 2016. **37**(6): p. 7021-7031.

49. Schulz-von der Gathen, V., et al., *Optical diagnostics of micro discharge jets*. Contributions to Plasma Physics, 2007. **47**(7): p. 510-519.

50. Schulz-Von Der Gathen, V., et al., *Spatially resolved diagnostics on a microscale atmospheric pressure plasma jet*. Journal of Physics D: Applied Physics, 2008. **41**(19): p. 194004.

51. Winter, J., R. Brandenburg, and K. Weltmann, *Atmospheric pressure plasma jets: an overview of devices and new directions*. Plasma Sources Science and Technology, 2015. **24**(6): p. 064001.

52. Fantz, U., *Basics of plasma spectroscopy*. Plasma sources science and technology, 2006. **15**(4): p. S137.

53. Kunze, H.-J., *Introduction to plasma spectroscopy*. Vol. 56. 2009: Springer Science & Business Media.

54. Gans, T., et al., *Phase-resolved emission spectroscopy of a hydrogen rf discharge for the determination of quenching coefficients*. Physical Review A, 2003. **67**(1): p. 012707.

55. Greb, A., *Dynamics of The Plasma Surface Interface In Capacitively Coupled Radio-Frequency Oxygen Plamsmas: Coupling Numerical Simulations With Optical Diagnostics*, in *Department of physics*. 2013, University of York.

56. Boyle, P., A. Ellingboe, and M. Turner, *Independent control of ion current and ion impact energy onto electrodes in dual frequency plasma devices*. Journal of Physics D: Applied Physics, 2004. **37**(5): p. 697.

57. Donkó, Z., et al., *The effect of secondary electrons on the separate control of ion energy and flux in dual-frequency capacitively coupled radio frequency discharges*. Applied Physics Letters, 2010. **97**(8): p. 081501.

58. Löwe, H.D., H.H. Goto, and T. Ohmi, *Control of ion energy and flux in a dual radio frequency excitation magnetron sputtering discharge*. Journal of Vacuum Science & Technology A: Vacuum, Surfaces, and Films, 1991. **9**(6): p. 3090-3099.

59. Donkó, Z. and Z.L. Petrović, *Analysis of a capacitively coupled dual-frequency CF4 discharge*. Japanese journal of applied physics, 2006. **45**(10S): p. 8151.

60. Heintze, M., R. Zedlitz, and G. Bauer, *Analysis of high-rate a-Si: H deposition in a VHF plasma*. Journal of Physics D: Applied Physics, 1993. **26**(10): p. 1781.

61. Oda, S., *Frequency effects in processing plasmas of the VHF band*. Plasma Sources Science and Technology, 1993. **2**(1): p. 26.

62. Pang, S., et al., *Damage induced in Si by ion milling or reactive ion etching*. Journal of applied physics, 1983. **54**(6): p. 3272-3277.

63. Turner, M.M. and P. Chabert, *Collisionless heating in capacitive discharges enhanced by dual-frequency excitation*. Physical review letters, 2006. **96**(20): p. 205001.

64. Kawamura, E., M. Lieberman, and A. Lichtenberg, *Electron heating in low pressure capacitive discharges revisited*. Physics of Plasmas, 2014. **21**(12): p. 123505.

65. Lafleur, T., *Tailored-waveform excitation of capacitively coupled plasmas and the electrical asymmetry effect*. Plasma Sources Science and Technology, 2015. **25**(1): p. 013001.

66. Bruneau, B., et al., *Capacitively coupled hydrogen plasmas sustained by tailored voltage waveforms: excitation dynamics and ion flux asymmetry*. Plasma Sources Science and Technology, 2016. **25**(4): p. 045019.

67. Niemi, K., et al., *Diagnostic based modelling of radio-frequency driven atmospheric pressure plasmas*. Journal of Physics D: Applied Physics, 2010. **43**(12): p. 124006.

68. Waskoenig, J., et al., *Atomic oxygen formation in a radio-frequency driven micro-atmospheric pressure plasma jet*. Plasma Sources Science and Technology, 2010. **19**(4): p. 045018.

69. O'Neill, C., J. Waskoenig, and T. Gans, *Electron Heating in Dual-Radio-Frequency-Driven Atmospheric-Pressure Plasmas*. IEEE Transactions on Plasma Science, 2011. **39**(11): p. 2588-2589.

70. Park, S., et al., *Electron Information in Single-and Dual-Frequency Capacitive Discharges at Atmospheric Pressure*. Scientific reports, 2018. **8**(1): p. 7516.

71. mksinstruments. *Gas Correction Factors for Thermal-based Mass Flow Controllers*. [cited 2017; Available from: https://http://www.mksinst.com/docs/ur/MFCGasCorrection.aspx.

72. Niemi, K., et al., *Diagnostic based modeling for determining absolute atomic oxygen densities in atmospheric pressure helium-oxygen plasmas*. Applied Physics Letters, 2009. **95**(15): p. 151504.

73. SOLAYL, *SOLAYL RF Measurement and Control*. 2017.

74. Bilodeau, T., W. Dunbar, and W. Sarjeant, *High-voltage and partial discharge testing techniques for space power systems*. IEEE Electrical Insulation Magazine, 1989. **5**(2): p. 12-21.

75. Awakowicz, P., *Diagnostics of reactive low temperature-low pressure plasmas with probe measurement, optical emission spectroscopy and energy-mass spectrometry*. VIDE-PARIS-, 1999: p. 1-7.

76. Ovsyannikov, A. and M.F. Zhukov, *Plasma diagnostics*. 2000: Cambridge Int Science Publishing.

77. Schulze, J., et al., *Phase resolved optical emission spectroscopy: a non-intrusive diagnostic to study electron dynamics in capacitive radio frequency discharges*. Journal of Physics D: Applied Physics, 2010. **43**(12): p. 124016.

78. Karakas, E., V.M. Donnelly, and D.J. Economou, *Optical emission spectroscopy and Langmuir probe diagnostics of CH3F/O2 inductively coupled plasmas*. Journal of Applied Physics, 2013. **113**(21): p. 213301.

79. Meshcheryakova, E., et al., *Langmuir probe diagnostics of low-pressure inductively coupled argon plasmas in a magnetic field*. Physics Procedia, 2015. **71**: p. 121-126.

80. Harshbarger, W., et al., *A study of the optical emission from an RF plasma during semiconductor etching*. Applied spectroscopy, 1977. **31**(3): p. 201-207.

81. Coburn, J. and M. Chen, *Optical emission spectroscopy of reactive plasmas: A method for correlating emission intensities to reactive particle density*. Journal of applied physics, 1980. **51**(6): p. 3134-3136.

82. Nemschokmichal, S., K. Dittmann, and J. Meichsner, *Spatial and phase-resolved optical emission patterns in capacitively coupled radio-frequency plasmas*. IEEE Transactions on Plasma Science, 2008. **36**(4): p. 1360-1361.

83. Gans, T., D. O'Connell, and V. der Gathen, *The challenge of revealing and tailoring the dynamics of radio-frequency plasmas*. Plasma Sources Science and Technology, 2010. **19**(3).

84. Mahony, C., R. Al Wazzan, and W. Graham, *Sheath dynamics observed in a 13.56 MHz-driven plasma*. Applied physics letters, 1997. **71**(5): p. 608-610.

85. Sadeghi, N., et al., *Quenching rate constants for reactions of Ar (4p'[1/2] 0, 4p [1/2] 0, 4p [3/2] 2, and 4p [5/2] 2) atoms with 22 reagent gases*. The Journal of Chemical Physics, 2001. **115**(7): p. 3144-3154.

86. Andrew Thomas West, *Optical and Electrical Diagnosis of Atmospheric Pressure Plasma Jets*. Ph.D. thesis, University of York, 2016.

87. Gibson, A.R., et al., *Interactions of a non-thermal atmospheric pressure plasma effluent with PC-3 prostate cancer cells*. Plasma Processes and Polymers, 2014. **11**(12): p. 1142-1149.

88. Ma, Y., et al., *Non-thermal atmospheric pressure plasma preferentially induces apoptosis in p53-mutated cancer cells by activating ROS stress-response pathways*. PloS one, 2014. **9**(4): p. e91947.

89. Witte, M.B. and A. Barbul, *Role of nitric oxide in wound repair*. The American Journal of Surgery, 2002. **183**(4): p. 406-412.

90. Luo, J.-d. and A.F. Chen, *Nitric oxide: a newly discovered function on wound healing*. Acta Pharmacologica Sinica, 2005. **26**(3): p. 259.

91. Guimond, S. and M.R. Wertheimer, *Surface degradation and hydrophobic recovery of polyolefins treated by air corona and nitrogen atmospheric pressure glow discharge*. Journal of Applied Polymer Science, 2004. **94**(3): p. 1291-1303.

92. Golubovskii, Y.B., et al., *Modelling of the homogeneous barrier discharge in helium at atmospheric pressure*. Journal of Physics D: Applied Physics, 2002. **36**(1): p. 39.

93. Gibson, A.R., et al., *Disrupting the spatio-temporal symmetry of the electron dynamics in atmospheric pressure plasmas by voltage waveform tailoring*. Plasma Sources Science and Technology, 2018.

94. O'Connell, D., et al., *Plasma ionization through wave-particle interaction in a capacitively coupled radio-frequency discharge*. Physics of plasmas, 2007. **14**(3): p. 034505.

95. Mohr, S., et al., *Field reversals in electrically asymmetric capacitively coupled radio-frequency discharges in hydrogen*. Journal of Physics D: Applied Physics, 2013. **46**(43): p. 435201.

96. Bruneau, B., *Control of radio frequency capacitively coupled plasma asymmetries using Tailored Voltage Waveforms*. Ph.D. thesis. LPICM-University Paris Saclay, 2015.

97. Colmenares, F., J.G. McCaffrey, and O. Novaro, *Quenching of excited 1 P 1 state atomic zinc by molecular nitrogen: A matrix-isolation spectroscopy/quantum chemical calculation study*. The Journal of Chemical Physics, 2001. **114**(22): p. 9911-9918.

98. Diomede, P., et al., *Radio-frequency capacitively coupled plasmas in hydrogen excited by tailored voltage waveforms: comparison of simulations with experiments*. Plasma Sources Science and Technology, 2014. **23**(6): p. 065049.

99. Delattre, P.-A., et al., *Radio-frequency capacitively coupled plasmas excited by tailored voltage waveforms: comparison of experiment and particle-in-cell simulations*. Journal of Physics D: Applied Physics, 2013. **46**(23): p. 235201.

100. Chandhok, M. and J.W. Grizzle, *Modeling the pressure dependence of DC bias voltage in asymmetric, capacitive RF sheaths*. IEEE transactions on plasma science, 1998. **26**(2): p. 181-189.

101. Arkhipenko, V., et al., *Influence of nitrogen impurities on an electron-excited helium atoms concentration in the self-sustained normal dc glow discharge at atmospheric pressure*. arXiv preprint physics/0411037, 2004.

102. Cabiscol Català, E., J. Tamarit Sumalla, and J. Ros Salvador, *Oxidative stress in bacteria and protein damage by reactive oxygen species*. International Microbiology, 2000, vol. 3, núm. 1, p. 3-8, 2000.

103. Alexandre, J., et al., *Novel action of paclitaxel against cancer cells: bystander effect mediated by reactive oxygen species*. Cancer research, 2007. **67**(8): p. 3512-3517.

104. Zalesskaya, G. and A. Kuchinskii, *Role of charge-transfer complexes in oxygen quenching of excited states of anthracene derivatives in the gas phase*. Journal of Applied Spectroscopy, 2008. **75**(1): p. 36-42.

105. Wijaikhum, A., et al., *Absolute ozone densities in a radio-frequency driven atmospheric pressure plasma using two-beam UV-LED absorption spectroscopy and numerical simulations*. Plasma Sources Science and Technology, 2017. **26**(11): p. 115004.